

REPORT NO 127

SEPTEMBER 1963

PRELIMINARY SYSTEMS ANALYSIS AND SIMULATION

AD 645997



ARCHIVE COPY

DDC AVAILABILITY NOTICES

1. Distribution of this document is unlimited.
2. This document is subject to special export controls and each transmittal to foreign governments or foreign nationals may be made only with prior approval of US Army Aviation Materiel Laboratories, Fort Eustis, Virginia 23604.
3. In addition to security requirements which must be met, this document is subject to special export controls and each transmittal to foreign governments or foreign nationals may be made only with prior approval of USAAVLABS, Fort Eustis, Virginia 23604.
4. Each transmittal of this document outside the agencies of the US Government must have prior approval of US Army Aviation Materiel Laboratories, Fort Eustis, Virginia 23604.
5. In addition to security requirements which apply to this document and must be met, each transmittal outside the agencies of the US Government must have prior approval of US Army Aviation Materiel Laboratories, Fort Eustis, Virginia 23604.
6. Each transmittal of this document outside the Department of Defense must have prior approval of US Army Aviation Materiel Laboratories, Fort Eustis, Virginia 23604.
7. In addition to security requirements which apply to this document and must be met, each transmittal outside the Department of Defense must have prior approval of US Army Aviation Materiel Laboratories, Fort Eustis, Virginia 23604.
8. This document may be further distributed by any holder only with specific prior approval of US Army Aviation Materiel Laboratories, Fort Eustis, Virginia 23604.
9. In addition to security requirements which apply to this document and must be met, it may be further distributed by the holder only with specific prior approval of US Army Aviation Materiel Laboratories, Fort Eustis, Virginia 23604.

DISCLAIMER

10. The findings in this report are not to be construed as an official Department of the Army position unless so designated by other authorized documents.
11. When Government drawings, specifications, or other data are used for any purpose other than in connection with a definitely related Government procurement operation, the United States Government thereby incurs no responsibility nor any obligation whatsoever; and the fact that the Government may have formulated, furnished, or in any way supplied the said drawings, specifications, or other data is not to be regarded by implication or otherwise as

in any manner licensing the holder or any other person or corporation, or conveying any rights or permission, to manufacture, use, or sell any patented invention that may in any way be related thereto.

12. Trade names cited in this report do not constitute an official endorsement or approval of the use of such commercial hardware or software.

DISPOSITION INSTRUCTIONS

13. Destroy this report when no longer needed. Do not return it to originator.

14. When this report is no longer needed, Department of the Army organizations will destroy it in accordance with the procedures given in AR 380-5.

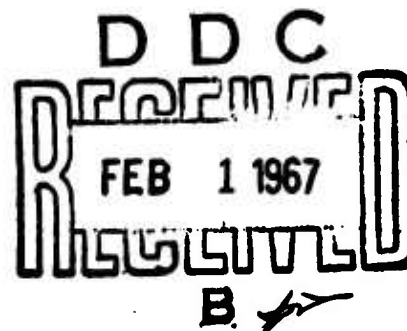
Report No. 127

September 1963

PRELIMINARY SYSTEMS ANALYSIS AND SIMULATION

XV-5A LIFT FAN

FLIGHT RESEARCH AIRCRAFT PROGRAM



Contract Number DA44-177-TC-715

ADVANCED ENGINE AND TECHNOLOGY DEPARTMENT
GENERAL ELECTRIC COMPANY
CINCINNATI 15, OHIO

5 APR 1966

MF

ACCESSION for	
CRSTI	WHITE SECTION <input checked="" type="checkbox"/>
DOC	BUFF SECTION <input type="checkbox"/>
RESEARCH/DEVELOPMENT	<input type="checkbox"/>
CLASSIFICATION	
BY	
DISTRIBUTION/AVAILABILITY CODES	
DISC.	AVAIL. and/or SPECIAL
/	

CONTENTS

SECTION	PAGE
1.0 INTRODUCTION	1
2.0 SIX-DEGREE-OF-FREEDOM HOVER SIMULATION	3
3.0 LONGITUDINAL THREE-DEGREE-OF-FREEDOM TRANSITION SIMULATION	29
4.0 LONGITUDINAL THREE-DEGREE-OF-FREEDOM CONVERSION SIMULATION	81
5.0 SIX-DEGREE-OF-FREEDOM PERTURBATION CONVENTIONAL FLIGHT SIMULATION	111
6.0 GAS GENERATOR CONTROL ANALYSIS	131
7.0 LIFT-FAN ROLL-YAW CONTROL COUPLING ANALYSIS	157
8.0 LIFT-FAN PITCH CONTROL STRUCTURAL FEED- BACK ANALYSIS	177
9.0 YAW-ROLL-PITCH EULER ANGULAR AND DEFLOREZ DISPLAY RATES DERIVATION	205
10.0 STABILIZATION SYSTEM BRIDGE NETWORK DEVELOPMENT	219

LIST OF FIGURES

FIGURE		PAGE
1	Rate Gyro Concept for Damping and Reference	4
2	Derivation of Linear and Angular Accelerations	15
3	Computer Diagram	23
4	Computer Diagram	25
5	Computer Diagram	27
6	Required Per Cent Stick from Full Forward for Trim vs Equivalent Airspeed	39
7	One Engine Out Speed-Altitude Envelope for 10 FPS or Less Sink Rate at Touchdown	40
8	Velocity vs Angle of Attack at Constant Vector Angle	41
9	Tail Incidence for Trim vs Equivalent Airspeed, Knots	42
10	Dynamic Check Hand-Calculation - Response for Impulse of δ_p , for Small Perturbation Transfer Function	43
11	Plot of Analog Computer Record for Dynamic Check Initial Conditions	43
12	Estimated Normal and Longitudinal Force Coefficients	57
13	Estimated Force and Moment Coefficients at High Angles of Attack $T_c^S = .99$	59
14	Lift and Drag Parameters for Vector Effectiveness	61
15	Lift and Drag Parameters for Stagger Effectiveness	62
16	Estimated Pitch Fan Performance	63
17	Estimated Moment Coefficient about C. G.	65
18	Estimated Moment Coefficient about C. G.	67
19	Effect of Exit Louver Vectoring on Pitching Moment	68
20	Effect of Stagger on Pitching Moment Coefficient	68
21	Estimated Downwash Angle at Horizontal Tail	69
22	Fan Power Coefficient	69
23	Incremental Change in Fan Power Coefficient due to Stagger at Constant Power	70
24	Variation of Wing-Fan Thrust and Power with Gas Generator RPM	70
25	Estimated Performance for Pitch Fan Thrust Reverser Static	71
26	Estimated Pitch Fan Force and Moment Coefficients	72

FIGURE		PAGE
27	$F_1(V)$ vs Velocity	72
28	Stick Control vs Pitch Fan Door Position	73
29	Estimated Wing and Nose Fan Thrust for Single Engine Operation	74
30	Nose Fan Power Characteristics	75
31	Computer Diagram, 3° Longitudinal Transition	77
32	Computer Diagram, 3° Longitudinal Transition	79
33	Net Horizontal Force with Trim Lift and Moment vs Velocity for Both Engines in Fan Mode	86
34	Net Horizontal Force with Trim Lift and Moment vs Velocity for One Engine in Turbojet Mode and One Engine in Fan Mode	87
35	Net Horizontal Force with Trim Lift and Moment vs Velocity for Both Engines in Fan Mode	88
36	Nominal Fan to Conventional Conversion - With and Without Pilot Control	89
37	Nominal Conventional to Fan Conversion - Pilot Control	90
38	Nominal Single Engine Fan to Conventional Conversion With and Without Pilot Control	91
39	Nominal Single Engine Conventional to Fan Conversion - Pilot Control	92
40	Stability Axis Coordinate System	95
41	Effect of Wing Closure Doors - Power Off	97
42	Longitudinal Characteristics During Conversion	99
43	Corrections to Drag for Ram Drag and Landing Gear	101
44	Longitudinal Characteristics in Conversion	102
45	Thrust vs Time from Diverter Actuation for Nose Fan and Main Fan Runup	103
46	Variation of Nose Fan Ram Drag Following Diverter Valve Operation	103
47	J-85 Thrust Transient Following Diverter Valve Switch	104
48	Wing Fan Thrust vs Time for 1 Second Diverter Switch	104
49	Drag Coefficient Increment Due to Fan Thrust at $R_q = .046, .105, .295$ and $.46$	105
50	Lift Coefficient Increment Due to Fan Thrust at $R_q = .046, .105, .295$ and $.46$	106
51	Pitching Moment Coefficient Increment Due to Fan Thrust at $R_q = .046, .105, .295$ and $.46$	106
51A	3° Conversion Longitudinal Computer Diagram	107
52	Axis Transformation	125
53	6° of Freedom Simulation Conventional Flight	127
54	DeFlorez Display Input Computer Diagram	129

FIGURE		PAGE
55	Simplified J-85 Computer Wiring	134
56	Further Simplified J-85 Computer Wiring	134
57A	Step Response of Network for $R_2 = \frac{R_1}{3}$	135
57B	Schematic Diagram of Lead Network	135
58	Step Input Responses with 100% Ng Command Limit for 1% ΔN_g Input	136
59	Step Input Responses with 102% Ng Command Limit for 1% ΔN_g Input	137
60	Computer Output Records for Bare Engine Plus Fan Response for 1% ΔN_g Input	139
61	Computer Output Records for 100% Ng Limit with 1% ΔN_g Command	141
62	Computer Output Records for 102% Ng Limit with 1% ΔN_g Command	141
63	P_{s3} vs N (% RPM)	143
64	W_f vs N (% RPM)	143
65	$\frac{W_f}{P_3}$ vs N (% RPM)	145
66	Operational Line and Schedule for 2500' Hot Day	147
67	Block Diagram of J-85 Engine and Fuel Control System	149
68	Reduced Block Diagram of J-85 Engine and Fuel Control System	150
69	Further Reduced Block Diagram of J-85 Engine and Fuel Control System	150
70	Further Reduced Block Diagram of J-85 Engine and Fuel Control System	151
71	Further Reduced Block Diagram of J-85 Engine and Fuel Control System	151
72	Final Engine Closed-Loop Small Disturbance Transfer Function	152
73	Final Engine Closed-Loop Small Disturbance Transfer Function (Factored)	152
74	Plot of Angle of Resulting Moments for Roll and Yaw Inputs	169
75	Damping and Natural Frequency vs Yaw Gain	170
76	Damping and Natural Frequency vs Yaw Gain	171
77	Damping and Natural Frequency vs Yaw Gain	172
78	Damping and Natural Frequency vs Yaw Gain	173
79	Effect of Exit Louver Stagger on Longitudinal Characteristics	174

FIGURE		PAGE
80	Exit Louver Vector Effectiveness	175
81	Determination of Axis of Resultant Moment for a Combination of Rolling and Yawing Moments	176
82	Location of Rate Gyros and Nose Fan with Respect to Airplane C. G.	186
83	Block Diagram of Flexible Body Plus SA System	187
84	Nose Fan Door Rigging - One Side	189
85	Gyro Station 90, θ_g/δ_p Response Less NWB Response	190
86	Gyro Station 120, θ_g/δ_p Response Less NWB Response	191
87	Gyro Station 150, θ_g/δ_p Response Less NWB Response	192
88	$F/F_0/\delta_p$ Command Response	193
89	Gyro Station 120, θ_g/δ_p Response, No Notch Network	194
90	Gyro Station 120, θ_g/δ_p Response Including Notch Network at 100 Rad/Sec	195
91	Gyro Station 150, θ_g/δ_p Response, No Notch Network	196
92	Gyro Station 150, θ_g/δ_p Response Including Notch Network at 100 Rad/Sec	197
93	Normalized Deflection vs Fuselage Station for 1st and 2nd Free-Free Body Modes	198
94	Normalized Deflection vs Fuselage Station for 3rd and 4th Free-Free Body Modes	198
95	Normalized Deflection vs Fuselage Station for 5th and 6th Free-Free Body Modes	199
96	Normalized Deflection vs Fuselage Station for 7th and 8th Free-Free Body Modes	199
97	Response of Rate Gyro, Servo and NWB	200
98	Response of Rate Gyro, Servo, NWB and Notch Network	201
99	Pitch Loop for Rate Gyro at Station 90	202
100	Pitch Loop for Rate Gyro at Station 120	202
101	Pitch Loop for Rate Gyro at Station 150	202
102	Determination of Distance Between Nose Fan Door C. G. and Hinge Line	203
103	Yaw Rotation	218
104	Roll Rotation	218
105	Pitch Rotation	218
106	Block Diagram of SA Components and Input Network	221
107	Servo Input Network with Leakage	222
108	Package Yaw Channel Response, Position #6	225

1.0 INTRODUCTION

This report describes the systems analysis and simulation from the start of the XV-5A Program through 1 May 1963. It also includes information on certain related topics which were not explicitly a part of the program. This task was performed as authorized by Contract No. DA-44-177-TC-715.

The analog work performed included the six-degree-of-freedom hover simulation; the longitudinal three-degree-of-freedom transition simulation; the longitudinal three-degree-of-freedom conversion simulation, the six-degree-of-freedom perturbation conventional flight simulation, and the simulation of gas generator control for wing-fan thrust.

Supporting analyses included roll-yaw coupling and structural feedback in the pitch mode.

Further work accomplished involved the stability augmentation system specification; the development of the bridge concept for roll and yaw louver control; support of various hardware tests; the generation of the specification for the DeFlorez point light source visual display; furnishing consolation services during the DeFlorez display installation and testing, and developing the yaw, roll and pitch direction cosine relationships.

This report is divided into sections corresponding to the various subjects mentioned above.

BLANK PAGE

2.0 SIX-DEGREE-OF-FREEDOM HOVER SIMULATION

2.1 Discussion

The hovering simulation utilized a six-degree of freedom representation of the XV-5A in the hovering regime, and included the effects of fan ram drag, as well as estimated values of induced lift and pitching moment.

The philosophy of using only rate gyros for both damping and reference was carried through from the original proposal. The original concept is shown in Figure 1. A separate "Lagged-Rate Integrator" was used as a short-term attitude reference.

In this configuration, the time constant of the "approximate" integrator was chosen as 10 seconds, and the values K_R and K_P , referring to "rate" and "position" gain, were independently variable. By combining the two transfer functions, K_R and K_P an interesting result is obtained.

When combining transfer functions of parallel elements, the transfer functions of the original items are simply added, thus the feedback terms become:

$$\frac{K_R + K_P}{1 + \tau S} = \frac{K_R + K_P + K_R \tau S}{1 + \tau S} \quad (1)$$

$$= \frac{(K_R + K_P) \left(1 + \frac{K_R \tau S}{K_R + K_P}\right)}{1 + \tau S} \quad (2)$$

Further, letting $K_R + K_P = K$, and letting $\frac{K_R}{K_R + K_P} = R$, the transfer functions becomes:

$$\frac{(K_R + K_P) \left(1 + \frac{K_R \tau S}{K_R + K_P}\right)}{1 + \tau S} = \frac{K (1 + R \tau S)}{1 + \tau S} \quad (3)$$

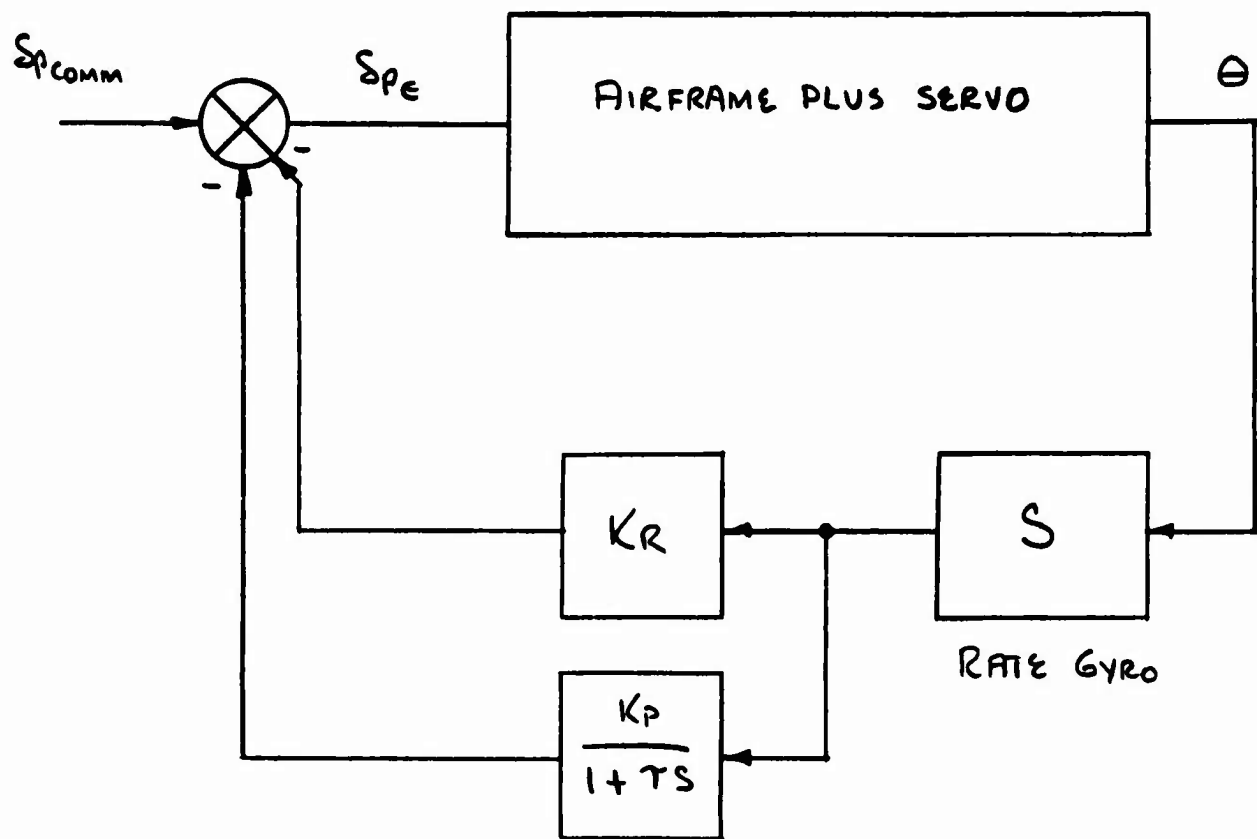


Figure 1 Rate Gyro Concept for Damping and Reference

In this case, the system gain becomes K , and R is defined as the ratio of the numerator and denominator time constants. Since R is always <1 , this transfer function, which is identical to the original parallel combination, has a "lag-lead" characteristic, and gives the effect for short periods of position plus rate, when fed with a rate gyro. This network is easily mechanized with two resistors and one capacitor. Its use is discussed in another section of this report.

The hovering simulation was utilized to give a preliminary justification for the lagged rate concept as applied to the XV-5A, as well as to the selected stability augmentation (SA) system authority of 25 percent of the manual input. A preliminary investigation of handling qualities in the hovering regime as well as an evaluation of hovering thrust control were further objectives of the simulation.

The equations of motion and the development of the forces used in this study are indicated in the following Section 2.3.

All evaluations of the SA system and hovering flying qualities were made using a fixed-base cockpit and a somewhat marginal display. Past experience indicates that results obtained, using this display, have been conservative, since various vehicles have been easier to fly than their simulation indicated. The only problem inherent in a marginal display is that the SA system can be "over-designed".

All of the hovering analysis and simulation used an assumed transfer function for the electrohydraulic servos. This transfer function was assumed to be a first order lag with a $1/10$ second time constant, although it was known that the servo would be at least third order. As far as aircraft handling qualities are concerned, the $1/10$ second lag is dominant, and the higher frequency additional second order response affects only the servo mode. Later, the measured servo response to electrical inputs was determined to be a first order with a $1/20$ second time constant and a second order with a natural frequency of 20 cps. As mentioned, the use of a simple first order lag resulted in essentially equivalent handling qualities; but the point of high-gain system instability was not accurate. This was not important to this preliminary investigation.

Hovering flights were made to evaluate the handling qualities of the vehicle, within the limitations imposed by the display.

The SA system includes means to facilitate maneuvering. This involves using stick/pedal motion switches which modify the compensation network whenever the control inputs exceed a certain percent of full scale deflection. The compensation network configuration with the control inputs

near zero is called the "Holding" configuration. When the control inputs are displaced beyond a given amount the SA system is in the "Maneuvering" configuration.

In the holding configuration, the compensation network provides the approximate attitude stability previously described. Both the ratio, R , and the gain, K_H , are variable in the primary system. In the maneuvering configuration, simple rate damping is provided, and the maneuvering gain, K_M , is variable from zero up to 3% of the maximum holding gain.

As a result of these investigations, "nominal" parameters of about $K_H = 20$, $R = 1$ were chosen for further evaluation.

The SA system as presently planned has authority equal to 25 percent of the manual authority in the various control axes. It was necessary to evaluate the effects of this authority limit on the operation of the system. The authority limit has two effects. These are:

1. The size of the transient generated by a SA system hard-over failure is reduced proportionally to the reduction in authority.
2. The ability of the SA system to recover the vehicle from large transients is also reduced proportionally to authority.

There are two different types of SA system hard-over failures which can occur. They are:

1. The amplifier driving the SA system actuator inputs can have a hard-over output.
2. The torque motor in a specific actuator can have a hard-over failure.

The two types of hard-over failures thus have different results on the vehicle.

An amplifier hard-over in any axis merely results in a 25 percent maximum displacement of that axis actuator(s). This difficulty can be overcome by either switching to the other SA system channel or by displacing the stick to restore trim. If the SA system is not switched to the other channel, the axis with the failure will have no SA, and the pilot control task becomes more difficult.

A torque-motor failure in the pitch axis results in a complete loss of SA in the pitch axis, and the stick will have to be displaced an amount equal to the authority of the torque motor. Stick inputs will still operate the pitch buckets, but no SA is available on primary or standby.

A single torque-motor hard-over failure in a wing fan louver actuator results in a $1/8$ full stick roll mis-trim and a simultaneous $1/16$ of full pedal yaw mis-trim. The mechanical inputs have no cross-coupling induced by this failure. However, the SA inputs are active only in 3 of the 4 torque motors, and cross-coupling results. A full roll signal would result in $3/4$ of the normal roll authority and would couple a $1/4$ full authority yaw signal also. The opposite would be the same for a full yaw input.

As far as either of these failure modes is concerned, the 25 percent limitation on SA torque motor authority limits the effect of the transient to fairly small values. It is easy to either switch to the standby system or to re-trim the vehicle about the new reference.

The second result of the SA authority limitation involves the magnitude of transients which the SA system will damp out. One kind of transient which is easily induced is derived from pushing the stick forward, building up a translational velocity, and then releasing the stick. This is not an expected transient, because it is not likely the pilot would ever do this. It does, however, indicate the efficacy of the 25 percent authority limitation.

It was determined that the SA system configuration used with 25 percent authority would take care of a transient of this nature up to +45 feet/second forward velocity.

The effect of possible de-stabilizing ground effects was also considered. The worst ground effect would be to cause a first-order divergence in roll. If this divergence built up to double-amplitude too rapidly, it would be beyond pilot capability to control it.

The SA system cannot eliminate a ground effect of this type, but it can raise the time constant to an arbitrarily high value, and thus reduce the divergence to a controllable value.

The reason the chosen SA compensation network cannot remove a pure divergence is due to the fact that it is a rate system, and this leads to a zero at the origin on the complex plane. A pure divergence is repre-

sented by a pole on the positive real axis. From root locus analysis, as the system gain is increased, the roots of the closed loop move from the poles of the open loop transfer function toward the zeros of the open loop transfer function. Since the divergent real root moves along the real axis toward the zero from the rate gyro at the origin, it is seen that the divergent root can never migrate to the stable portion of the complex plane. It can only be moved to an arbitrarily small distance from the origin, along the positive real axis. The time to double-amplitude of the response of a positive real root equals $.693/\alpha$, where α is the location of the root on the positive X axis. Thus, the smaller the value of α , the longer the time to double-amplitude becomes.

2.2 List of Symbols

m	Vehicle mass, slugs
\dot{m}	Flow rate, slugs/sec
I_x	Moment of inertia about the body X-axis, slug ft. ²
I_y	Moment of inertia about the body Y-axis, slug ft. ²
I_z	Moment of inertia about the body Z-axis, slug ft. ²
I_{xz}	Product of inertia, slug ft. ²
H_x	Component of engine and fan angular momentum about the body X-axis, slug-ft. ² /sec.
H_z	Component of engine and fan angular momentum about the body Z-axis, slug ft. ² /sec.
g_o	Acceleration of gravity, ft./sec. ²
l_z	Direction cosine between the inertial Z and body X-axes.
m_z	Direction cosine between the inertial Z and body Y-axes.
n_z	Direction cosine between the inertial Z and body Z-axes.
x	Distance along body X-axis (positive forward of the center of gravity), ft.
y	Distance along body Y-axis (positive out the right wing), ft.
z	Distance along body Z-axis (positive down), ft.
h	Altitude (measured along inertial Z-axis), ft.
mf	Subscript, denotes main fans.

ℓ	Subscript, denotes left main fan.
r	Subscript, denotes right main fan.
nf	Subscript, denotes nose fan.
c	Subscript, denotes commanded value.
T	Thrust, lbs.
T_o	Main fan thrust for rpm, zero vector and stagger angle and zero speed, lb
T_x	Component of main fan thrust along the body X-axis, lbs.
T_z	Component of main fan thrust along the body Z-axis, lbs.
T_{nf}	Nose fan thrust (only along the body Z-axis), lbs.
L	Rolling moment (positive for right wing down), ft.-lbs.
M	Pitching moment (positive for nose up), ft.-lbs.
N	Yawing moment (positive for right wing back), ft.-lbs.
D	Force along body X-axis (positive aft), lbs.
Y	Force along body Y-axis (positive out right wing) lbs.
Z	Force along body Z-axis (positive down), lbs.
u	Velocity along body X-axis, ft./sec.
v	Velocity along body Y-axis, ft./sec.
w	Velocity along body Z-axis, ft./sec.
p	Angular velocity about the body X-axis, rad./sec.
V	Total velocity, fps

q	Angular velocity about the body Y-axis, rad./sec.
r	Angular velocity about the body Z-axis, rad./sec.
K_L	Fan, induced lift, lbs.
K_M	Fan, induced moment, ft.-lbs.
D_R	Ram drag along the body X-axis, lbs.
Y_R	Ram drag along the body Y-axis, lbs.
δ_B	Pitch control bucket angle, deg
β_1	Louver position, aft set, main fans, degrees.
β_2	Louver position, forward set, main fans, degrees.
β_s	Stagger angle, main fan louvers, degrees.
β_v	Vane angle, main fan louvers, degrees.
σ	Collective stagger stick position (positive for increasing altitude), radians.
Γ	Roll control stick deflection (positive for right roll), radians.
λ	Collective vane stick position (positive for forward acceleration), radians.
ξ	Yaw control stick deflection (positive for right yaw), radians.
ν	Pitch control stick deflection (positive for pitch up), radians.
K_σ	Commanded stagger angle per stick deflection, rad./rad.
K_w	Commanded stagger angle per w, rad./ft./sec.

K_{ϕ}	Commanded stagger angle per roll angle, rad./rad.
K_{Γ}	Commanded stagger angle per roll control deflection, rad./rad.
K_u	Commanded vane angle per throttle position, rad./rad.
K_{ψ}	Commanded vane angle per yaw angle, rad./rad.
$K_{\dot{\psi}}$	Commanded vane angle per rate of yaw, rad./rad./sec.
K_{ξ}	Commanded vane angle per yaw control deflection, rad./rad.
K_{ν}	Commanded bucket angle per pitch control deflection, rad./rad.
K_{θ}	Commanded bucket angle per pitch angle, rad./rad.
$K_{\dot{\theta}}$	Commanded bucket angle per rate of pitch, rad./rad./sec.

2.3 Analysis

The forces and moments for the hover flight regime were calculated in the body axis system, and the body coordinates were referenced to earth coordinates by means of a Yaw, Roll, Pitch set of Euler angles and direction cosines.

The body axis equations of motion are given below:

$$\dot{u} = rv - qw + \frac{T_x \ell + T_x r}{m} + X_u u + \ell_z g_0 \quad (1)$$

(Continued)

$$\dot{w} = qu - pv - \left(\frac{T_{z\ell} + T_{zr}}{m} \right) - T_{nf}/m + Z_w w + Z_q q + Z_u u + n_z g_o \quad (2)$$

$$\begin{aligned} \dot{q} = & \frac{I_{xz}}{I_y} (r^2 - p^2) + \frac{I_x - I_z}{I_y} pr + (T_{z\ell} + T_{zr}) \frac{X_{mf}}{I_y} + \frac{T_{nf} X_{nf}}{I_y} \\ & + \frac{H_z p}{I_y} + \frac{H_x r}{I_y} + M_q q + M_w w + M_u u \end{aligned} \quad (3)$$

$$\dot{v} = pw - ru + Y_v v + Y_r r + m_z g_o \quad (4)$$

$$\dot{p} = \frac{I_{xz}}{I_x} (\dot{r} + pq) + \frac{I_y - I_z}{I_x} qr + \left(\frac{T_{z\ell} - T_{zr}}{I_x} \right) Y_{mf} - \frac{H_z q}{I_x} + L_p p \quad (5)$$

$$\dot{r} = \frac{I_{xz}}{I_z} (\dot{p} - qr) + \frac{I_x - I_y}{I_z} pq + \left(\frac{T_{x\ell} - T_{xr}}{I_z} \right) Y_{mf} + \frac{H_x q}{I_z} + N_v v + N_r r \quad (6)$$

The Euler angular relationships used are described in Section 9.0 of this report.

2.3.1 Thrust Functions

The fan thrust data was based on the original General Electric powerplant specification. These data were later corrected to conform with subsequent data furnished by General Electric. For the condition of 2500 foot altitude and a standard hot day ($\rho = .00205$),

$$T_o = 5000 - 300 (100 - \% N_g) \text{ per fan.} \quad (7)$$

BLANK PAGE

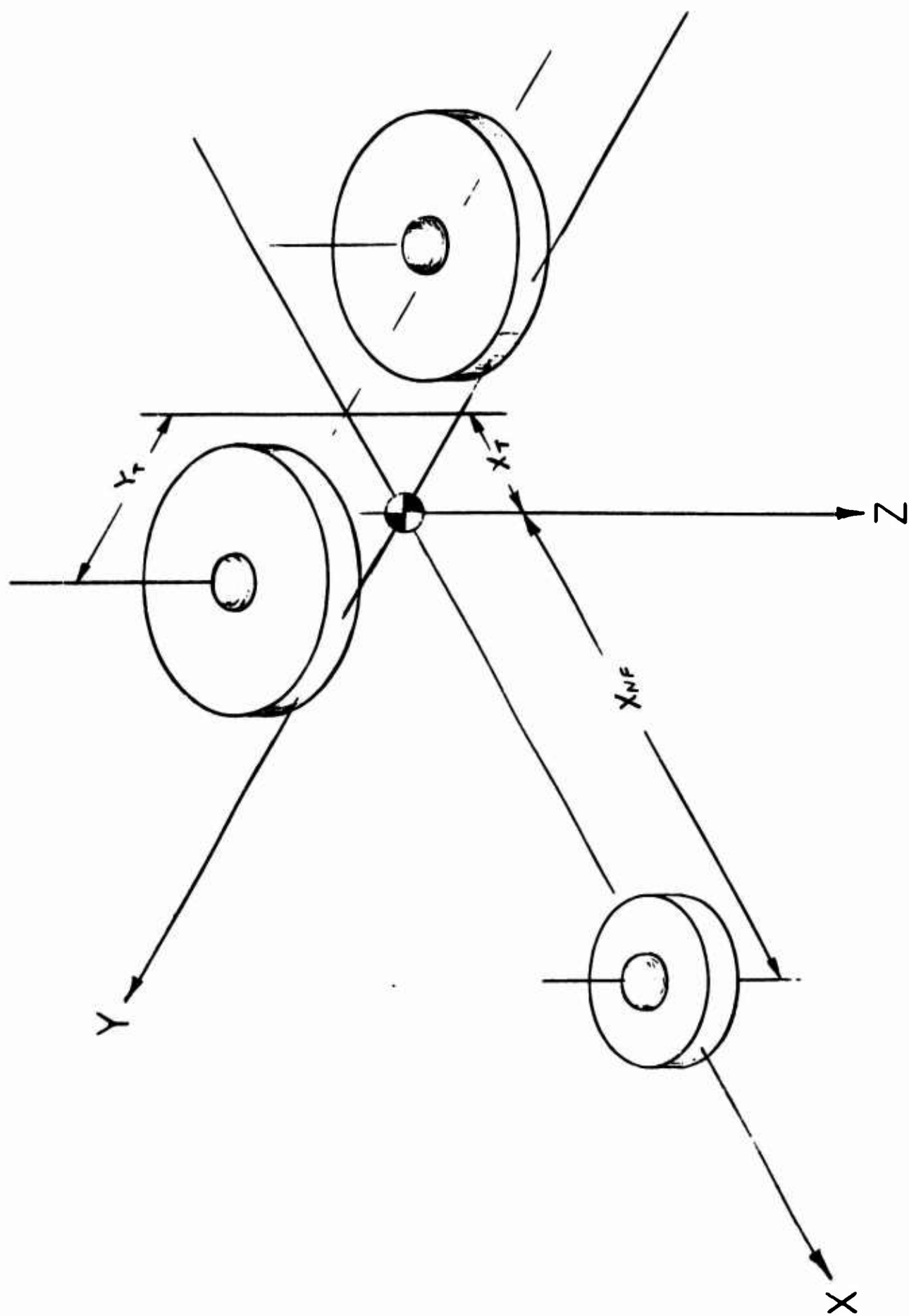


Figure 2 Derivation of Linear and Angular Accelerations

For small changes in altitude (< 500 ft.) the thrust was modified by the density ratio so that

$$T_o = \left[5000 - 300 (100 - \% N_g) \right] \left[1 - .000026 \Delta h \right] \text{ per fan} \quad (8)$$

The axial and thrust fan forces were modified by vector and stagger angle as below:

$$T_z = T_o (1.000189 \beta_v^2) (1 - .00466 \beta_s) \quad (9)$$

$$T_x = T_o (.0174 - .0001133 \beta_s) \beta_v \quad (10)$$

The nose fan thrust was assumed to be a linear function of nose fan bucket (thrust reverser) position, measured from -200 lb. of thrust. The nose fan thrust was assumed to vary linearly from -200 to + 1500 lbs. thrust at 100% N_g for δ_p variation from 0 to 65°.

The linear and angular accelerations due to the thrust forces are derived from the geometry of Figure 2, and are thus represented in the body axis equation of motion.

2.3.2 Stability Derivatives

Since the study was concerned primarily with small perturbation velocities around zero (± 50 ft/sec), the aerodynamic characteristics of the airframe were ignored, and all stability derivatives were derived from momentum considerations of the fan flow.

Available data was plotted to give the linear variations of ram drag with forward velocity as a function of total thrust vector. Assuming the fan reaction forces to be due to simple momentum change, $\dot{m} \Delta V$, the variation of ram drag with velocity is simply the mass flow rate through the fan. Based upon these assumptions the mass flow rate of each main fan is:

$$\dot{m}_{mf} = .214 \sqrt{T_o} \text{ per fan.} \quad (11)$$

For the nose fan, using the previously established relationship between nose fan and main fan total thrust vector,

$$\dot{m}_{nf} = .0545 \sqrt{T_o} \quad (12)$$

The mass flow rate was assumed constant at a nominal thrust of 4850 lbs/fan which was approximately that required to hover, so that:

$$\dot{m}_{nf} = 3.86 \text{ slugs/sec.} \quad (13)$$

$$\dot{m}_{mf} = 15.15 \text{ slugs/sec.} \quad (14)$$

The forces due to momentum changes can be expressed as:

$$\bar{F}_1 = - \dot{m}_1 (\bar{V}_1 + \bar{\omega} \times \bar{R}_1) \quad (15)$$

Where $\bar{\omega} \times \bar{R}_1$ is the velocity due to rotation, $\bar{\omega}$, and $\bar{R}_1 = x_1 \hat{i} + y_1 \hat{j} + z_1 \hat{k}$.

In body axes, then

$$\bar{F}_1 = - \dot{m}_1 \left[u \hat{i} + v \hat{j} + w \hat{k} + \bar{\omega} \times \bar{R}_1 \right] \quad (16)$$

$$\begin{aligned} \text{Now, } \bar{\omega} \times \bar{R}_1 &= \begin{bmatrix} \hat{i} & \hat{j} & \hat{k} \\ p & q & r \\ x_1 & y_1 & z_1 \end{bmatrix} = \hat{i} (qz_1 - ry_1) + \hat{j} (rx_1 - pz_1) \\ &\quad + \hat{k} (py_1 - qx_1) \end{aligned} \quad (17)$$

in our case, $z_1 = 0$, so eq. (16) becomes, when expanded,

$$\bar{F}_1 = \dot{m}_1 \left[\hat{i} (u - ry_1) + \hat{j} (v + rx_1) + \hat{k} (w + py_1 - qx_1) \right] \quad (18)$$

For our system, the fan coordinates are:

$$x_{nf} = 15.45'$$

$$x_{mfr} = -1.0$$

$$x_{mfl} = -1.0$$

$$y_{nf} = 0$$

$$y_{mfr} = +5$$

$$y_{mfl} = -5$$

So that, if we define the dimensional derivative as acceleration/velocity;

$$X_u = Y_v = Z_w = - \left(\frac{\dot{m}_{nf} + 2\dot{m}_{mf}}{m} \right) = -.118/\text{sec.} \quad (19)$$

$$Z_q = -Y_r = \frac{\dot{m}_{nf} x_{nf} + Z \dot{m}_{mf} x_{mf}}{m} = -.101/\text{sec.} \quad (20)$$

The moments due to these forces can be expressed as $\bar{R}_i \times \bar{F}_i$.
Thus, taking the cross product of \bar{R}_i and equa. (18), \bar{F}_i , we get

$$\bar{R}_i \times \bar{F}_i = \dot{m}_i \begin{bmatrix} \hat{i} & \hat{j} & \hat{k} \\ x_i & y_i & z_i \\ (u-ry_i) & (v+rx_i) & (w+py_i-qx_i) \end{bmatrix} \quad (21)$$

and expanding,

$$\begin{aligned} \frac{\mathbf{R}_i \mathbf{X} \mathbf{F}_i}{\dot{m}_i} = & \hat{i} \left[y_i (w + p y_i - q x_i) - z_i (v + r x_i) \right] \\ & + \hat{j} \left[z_i (u - r y_i) - x_i (w + p y_i - q x_i) \right] \\ & + \hat{k} \left[x_i (v + r x_i) - y_i (u - r y_i) \right] \end{aligned} \quad (22)$$

and letting $Z_i = 0$

$$\begin{aligned} M = -\dot{m}_i \left[\hat{i} (w y_i + p y_i^2 - q x_i y_i) + \hat{j} (-w x_i + q x_i^2 - p x_i y_i) \right. \\ \left. + \hat{k} (v x_i + r x_i^2 - u y_i + r y_i^2) \right] \end{aligned} \quad (23)$$

and we can calculate the dimensional derivatives for rotation

$$L_p = \frac{2 \dot{m}_{mf} x_{mf}}{I_x} = -.0427/\text{sec.} \quad (24)$$

$$M_w = \frac{\dot{m}_{nf} x_{nf} + 2 \dot{m}_{mf} x_{mf}}{I_y} = -.00172/\text{ft. sec.} \quad (25)$$

$$M_q = - \frac{\dot{m}_{nf} x_{nf}^2 + 2 \dot{m}_{mf} x_{mf}^2}{I_y} = -.0562/\text{sec.} \quad (26)$$

$$N_v = - \frac{\dot{m}_{nf} x_{nf} + 2 \dot{m}_{mf} x_{mf}}{I_z} = -.00155/\text{ft. /sec.} \quad (27)$$

$$N_r = - \frac{\dot{m}_{nf} x_{nf}^2 + 2 \dot{m}_{mf} (x_{mf}^2 + y_{mf}^2)}{I_z} = -.0906/\text{ft. sec.} \quad (28)$$

and because of symmetry in the x - y plane:

$$X_r = Z_p = L_w = L_q = M_p = N_u = 0.$$

The only additional stability derivatives considered were those due to induced lift and those due to control motion. The induced lift and moment derivatives were taken as:

$$Z_u = \frac{-.275 \left| \sqrt{2T_o} \right|}{M} = -.0954/\text{sec. at 4850 lbs. thr.} \quad (29)$$

$$M_u = \frac{1.078 \sqrt{2T_o}}{I_y} = .00637/\text{ft. sec. at 4850 lbs. thr.} \quad (30)$$

The control derivatives were continuously computed as shown in equations (9) and (10). For small perturbations around hover, and the thrust per fan of 4850 lbs.

$$Z_{\beta_s} = \frac{57.3 \times .00932 T_o}{m} = 9.1 \text{ ft/sec}^2 \quad (31)$$

$$I_{\beta_{s \text{ diff}}} = \frac{57.3 \times .00932 T_o y_{mf}}{I_x} = 3.71/\text{sec}^2 \quad (32)$$

$$M_{\beta_v} = \frac{57.3 (.0174 - .0001133 \beta_s)}{I_y} 2 y_{mf} T_o = 2.4/\text{sec}^2 \quad (33)$$

This is calculated at $12^\circ \beta_s$ on each fan, which is required to hover at 4850 lbs. thrust.

Similarly -

$$X_{\beta_v} = 57.3 \frac{(.0174 - .000113 \beta_s) 2T_o}{m} = 31.3 \text{ ft/sec}^2 \quad (34)$$

$$Z_{\delta_B} = \frac{57.3 (26.2)}{m} \frac{T_o}{T_o_{100\%}} = -4.17 \text{ ft/sec}^2 \quad (35)$$

$$M_{\delta_B} = \frac{57.3 (26.2) \times_{nf} T_o}{I_y T_o_{100\%}} = 1.11/\text{sec}^2 \quad (36)$$

2.3.3 Control Command Equations

The command equations comprise the total control surface position commanded as a function of the inputs from the pilot and from the SA system sensors.

The SA system utilizes a three axis rate gyro package and associated networks to provide "pseudo position" and rate feedback signals.

The SA compensation networks have the transfer function,

$$\frac{\theta_o}{\theta_i} = K \frac{(1 + R\tau S)}{1 + \tau S} \quad (37)$$

And thus the total control command equations can be written:

$$\delta_{B_C} = K_{\nu} \nu + K_{\theta} \frac{(1 + R_{\theta} \tau S)}{1 + \tau S} q \quad (38)$$

$$\beta_{B_{C_r}} = K_{\sigma} \sigma - K_{\phi} \frac{(1 + R_{\phi} \tau S)}{1 + \tau S} p + K_{\Gamma} \Gamma \quad (39)$$

$$\beta_{vC_r} = K_\lambda \lambda + K_\phi \left(\frac{1 + R_\phi \tau S}{1 + \tau S} \right) r - K_z \dot{z} \quad (40)$$

$$\beta_{sC_\ell} = K_\tau \tau + K_\phi \left(\frac{1 + R_\phi \tau S}{1 + \tau S} \right) p - K_\Gamma \Gamma \quad (41)$$

$$\beta_{vC_\ell} = K_\lambda \lambda - K_\phi \left(\frac{1 + R_\phi \tau S}{1 + \tau S} \right) r + K_z \dot{z} \quad (42)$$

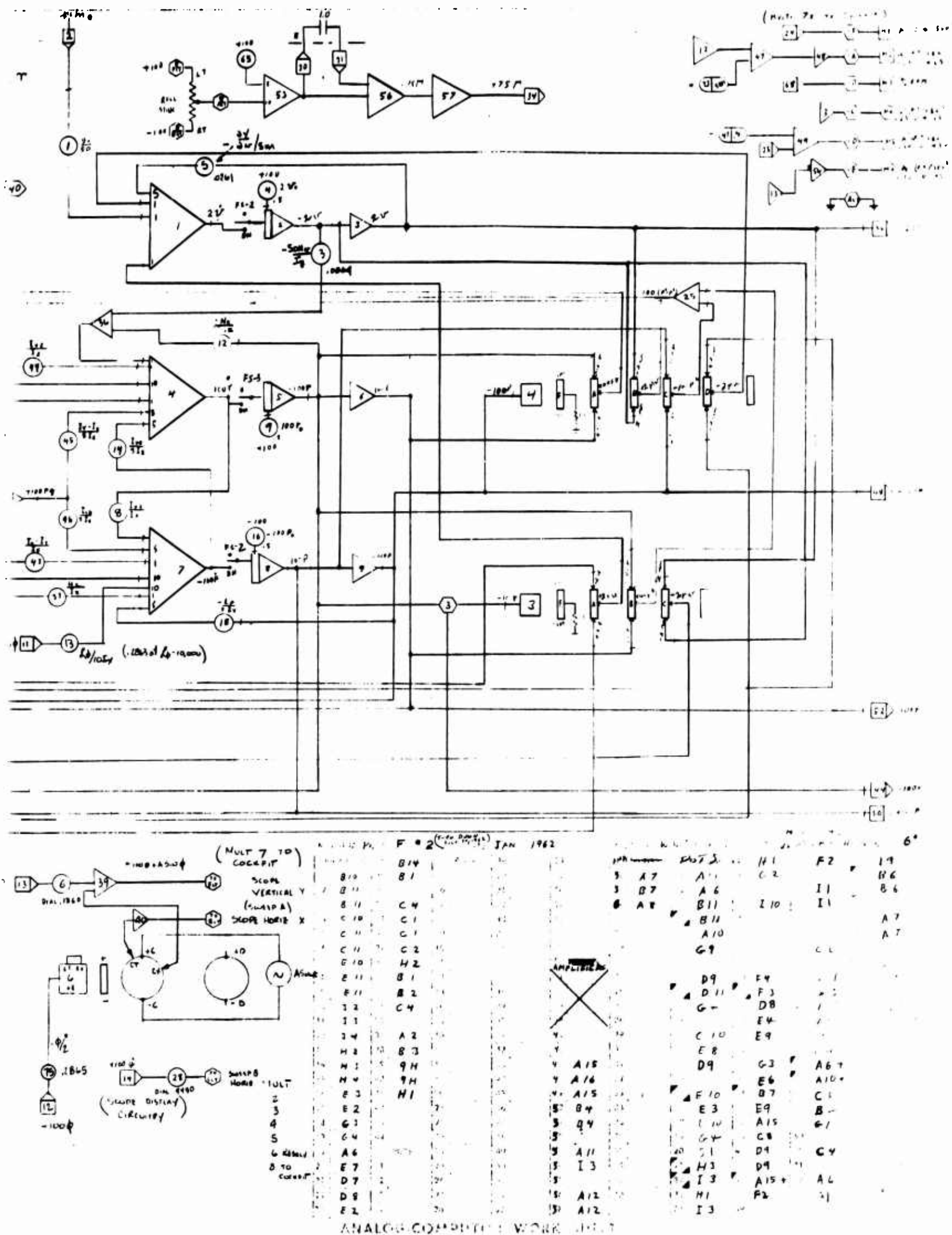
Control motions commanded by the SA system were limited to 25% of the total authority, around trim. These limits were:

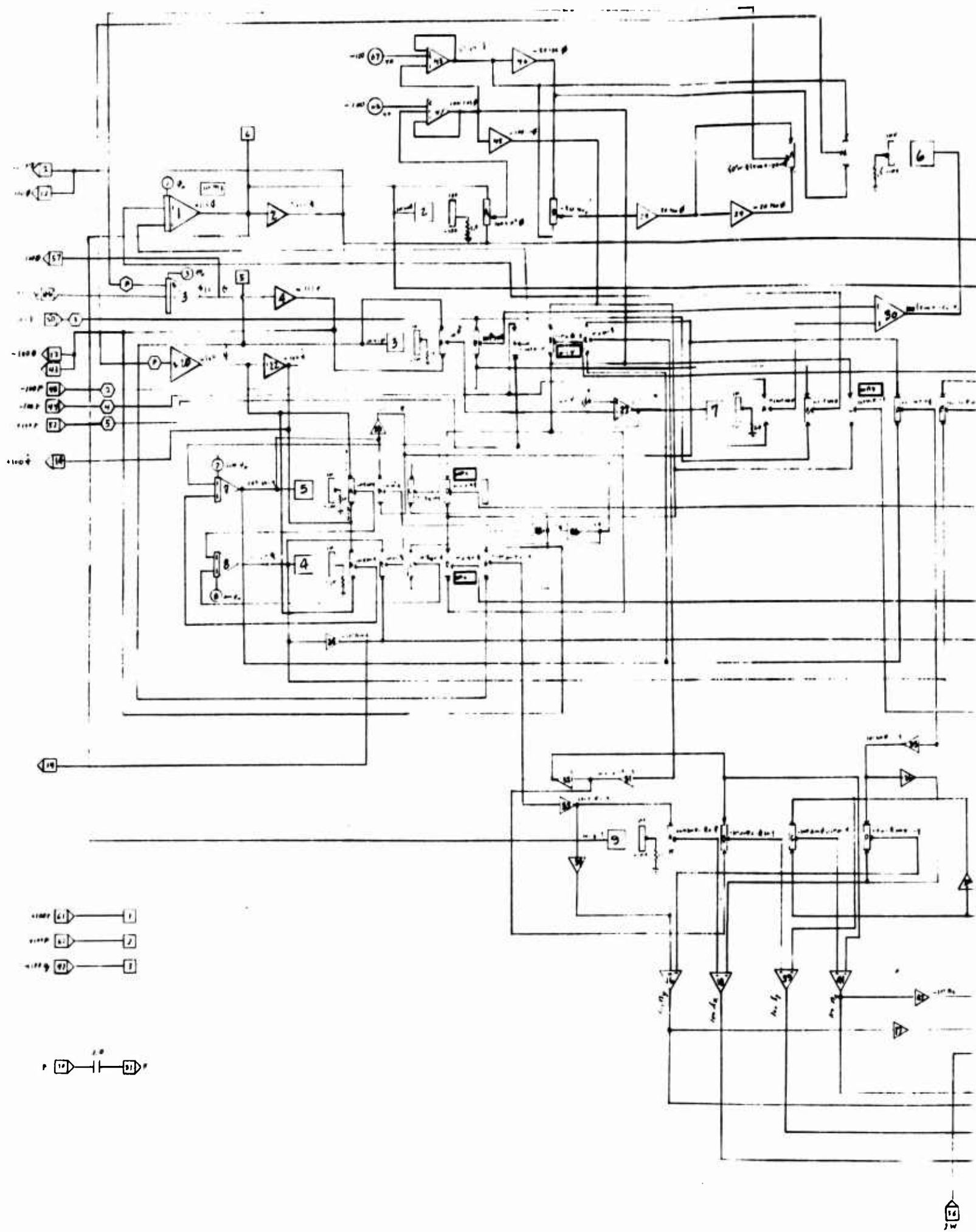
$$\Delta \delta_{B_{Lim}} = \pm 8.125 \text{ deg.}$$

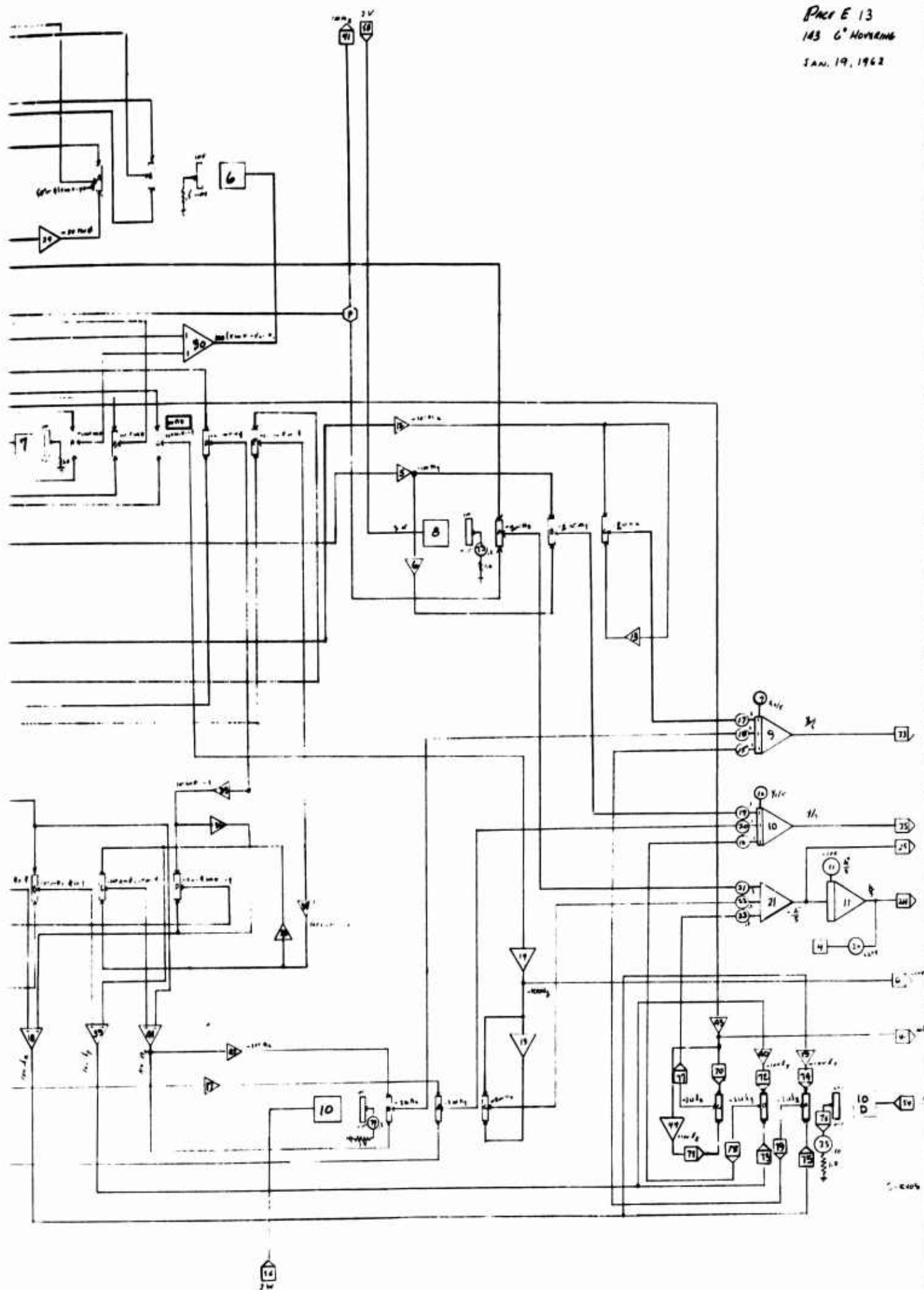
$$\Delta \beta_{s_{Lim}} = \pm 3.5 \text{ deg.}$$

$$\Delta \beta_{v_{Lim}} = \pm 3 \text{ deg.}$$

Figures 3, 4, and 5 are the computer diagrams used to mechanize the hovering equation of motion.

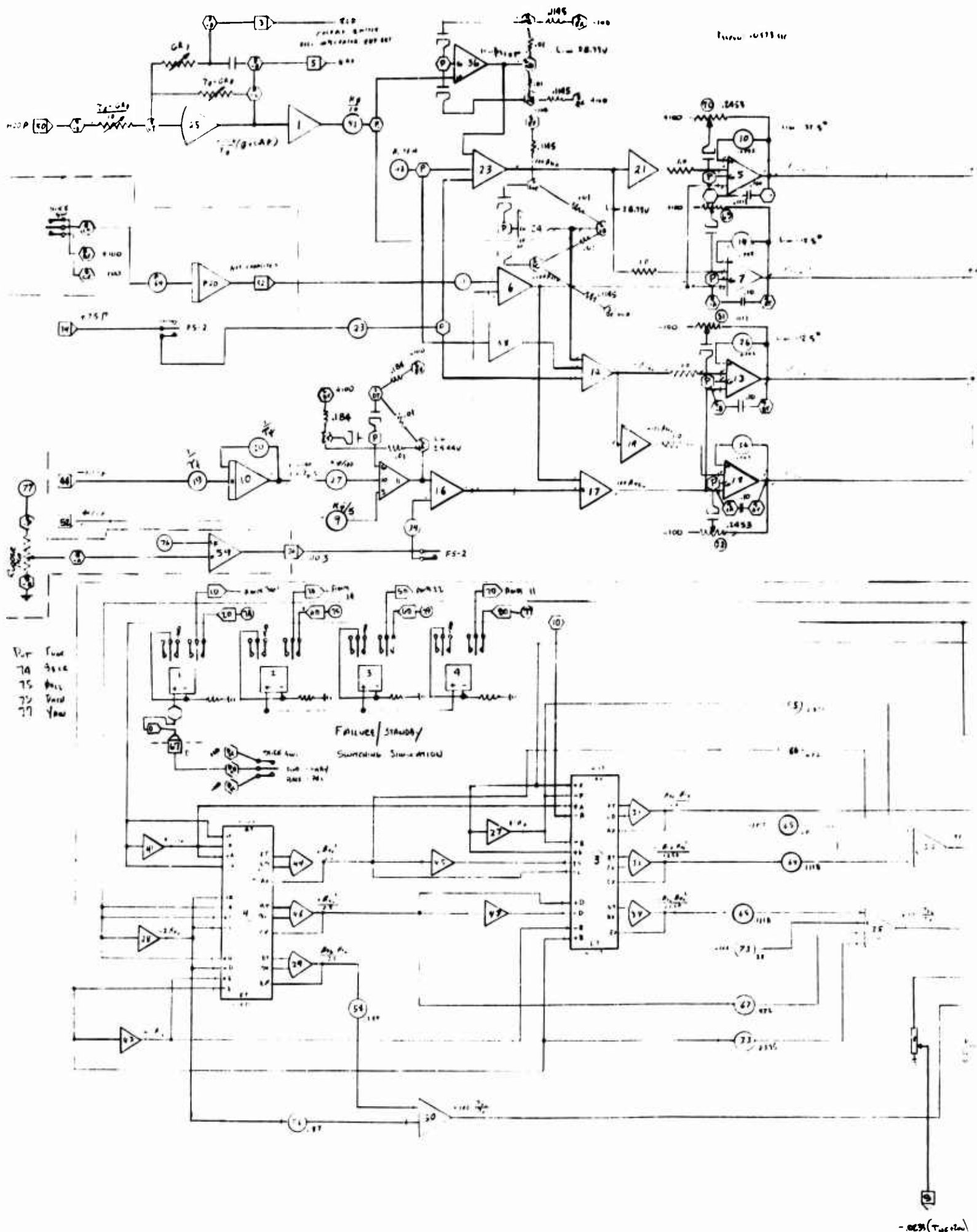




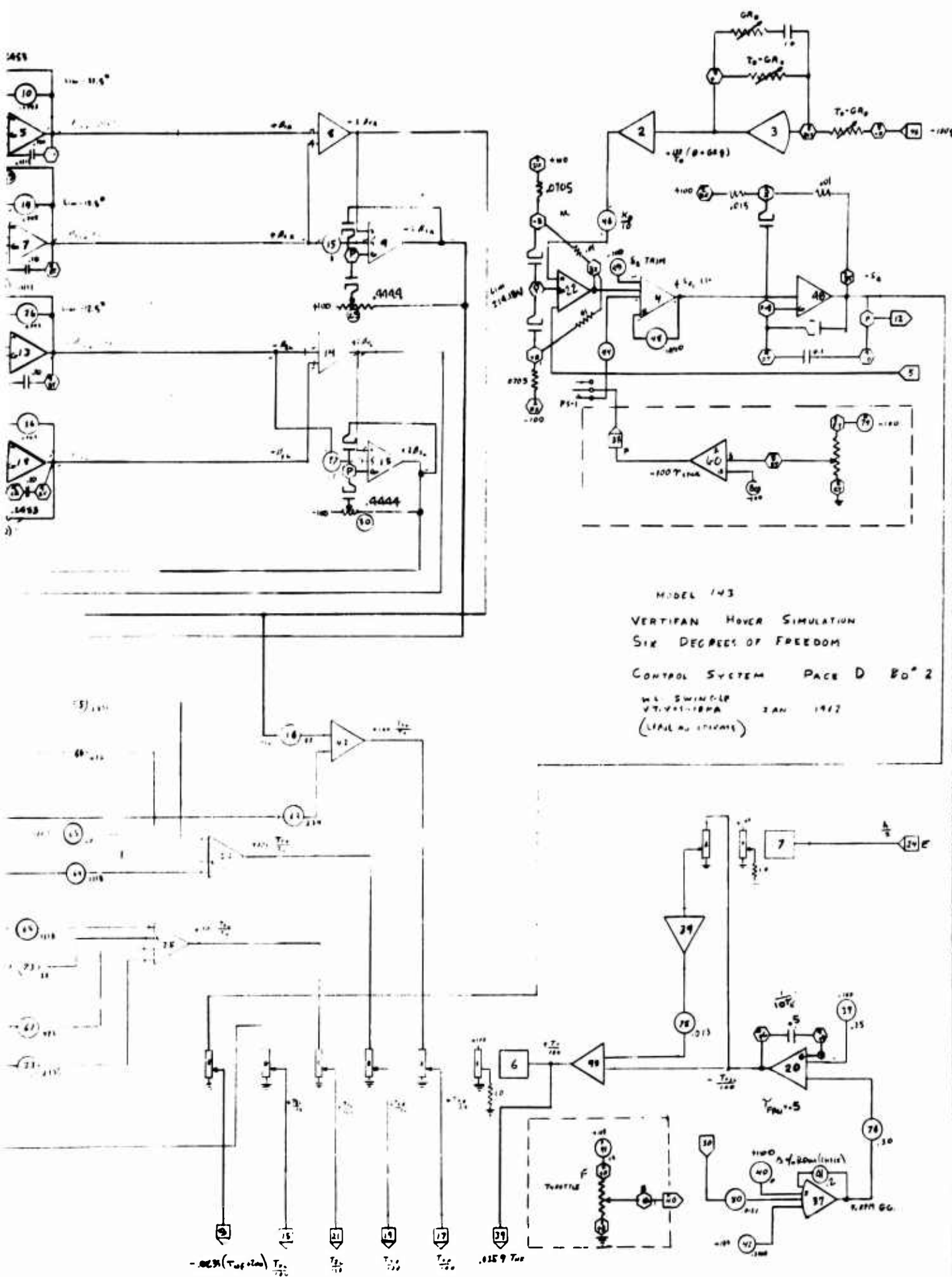


Legend			
	INVERTER		AND GATE
	OR GATE		NAND GATE
	NOR GATE		XOR GATE
	RELAY		SWITCH
	POWER SOURCE		GROUND
Component List			
BL	118	39	
BS	119	310	
CS	120	315	
DS	121	316	
ES	122	317	
FS	123	318	
GS	124	319	
HS	125	320	
IS	126	321	
JS	127	322	
KS	128	323	
LS	129	324	
MS	130	325	
NS	131	326	
OS	132	327	
PS	133	328	
QS	134	329	
RS	135	330	
TS	136	331	
US	137	332	
VS	138	333	
WS	139	334	
XS	140	335	
YS	141	336	
ZS	142	337	
AS	143	338	
BS	144	339	
CS	145	340	
DS	146	341	
ES	147	342	
FS	148	343	
GS	149	344	
HS	150	345	
IS	151	346	
JS	152	347	
KS	153	348	
LS	154	349	
MS	155	350	
NS	156	351	
OS	157	352	
PS	158	353	
QS	159	354	
RS	160	355	
TS	161	356	
US	162	357	
VS	163	358	
WS	164	359	
XS	165	360	
YS	166	361	
ZS	167	362	
AS	168	363	
BS	169	364	
CS	170	365	
DS	171	366	
ES	172	367	
FS	173	368	
GS	174	369	
HS	175	370	
IS	176	371	
JS	177	372	
KS	178	373	
LS	179	374	
MS	180	375	
NS	181	376	
OS	182	377	
PS	183	378	
QS	184	379	
RS	185	380	
TS	186	381	
US	187	382	
VS	188	383	
WS	189	384	
XS	190	385	
YS	191	386	
ZS	192	387	
AS	193	388	
BS	194	389	
CS	195	390	
DS	196	391	
ES	197	392	
FS	198	393	
GS	199	394	
HS	200	395	
IS	201	396	
JS	202	397	
KS	203	398	
LS	204	399	
MS	205	400	
NS	206	401	
OS	207	402	
PS	208	403	
QS	209	404	
RS	210	405	
TS	211	406	
US	212	407	
VS	213	408	
WS	214	409	
XS	215	410	
YS	216	411	
ZS	217	412	
AS	218	413	
BS	219	414	
CS	220	415	
DS	221	416	
ES	222	417	
FS	223	418	
GS	224	419	
HS	225	420	
IS	226	421	
JS	227	422	
KS	228	423	
LS	229	424	
MS	230	425	
NS	231	426	
OS	232	427	
PS	233	428	
QS	234	429	
RS	235	430	
TS	236	431	
US	237	432	
VS	238	433	
WS	239	434	
XS	240	435	
YS	241	436	
ZS	242	437	
AS	243	438	
BS	244	439	
CS	245	440	
DS	246	441	
ES	247	442	
FS	248	443	
GS	249	444	
HS	250	445	
IS	251	446	
JS	252	447	
KS	253	448	
LS	254	449	
MS	255	450	
NS	256	451	
OS	257	452	
PS	258	453	
QS	259	454	
RS	260	455	
TS	261	456	
US	262	457	
VS	263	458	
WS	264	459	
XS	265	460	
YS	266	461	
ZS	267	462	
AS	268	463	
BS	269	464	
CS	270	465	
DS	271	466	
ES	272	467	
FS	273	468	
GS	274	469	
HS	275	470	
IS	276	471	
JS	277	472	
KS	278	473	
LS	279	474	
MS	280	475	
NS	281	476	
OS	282	477	
PS	283	478	
QS	284	479	
RS	285	480	
TS	286	481	
US	287	482	
VS	288	483	
WS	289	484	
XS	290	485	
YS	291	486	
ZS	292	487	
AS	293	488	
BS	294	489	
CS	295	490	
DS	296	491	
ES	297	492	
FS	298	493	
GS	299	494	
HS	300	495	

Figure 4 Computer Diagram



A



A3	B4	I1
B14	C13	H1
B15	H5	A1
C14	C4	I1
B1	A1	I1
C4	H5	I1
B11	I2	D15
C11	I3	
B3	K5	
B1	K7	
I4	I7	
D11	I10	
B11	I7	
I5	A5	
B4	I15	
I4	D5	
I7	I14	
I15	I13	

P	D11	G7
P	E11	M3
P	C4	T4
P	F4	
P	F5	
E4	F4	H14
I4	F11	I4
C5	P	H1
P	I14	H1
P	L15	I4
C4	A15	I4
C11	A18	P1
G10	B5	A1
	D14	
B3	C13	I4
F3	D14	F2
P	C	K1
C4		P4
		I14
D8	A4	F5
F1		I15

A14
D16

A3	D1
A4	C2
	C1
L10	F4
	F15
	E12
	I17
	L18
	H2

E10	F1
E12	F1
L11	I16
L11	C1
B16	A1
	F1

Computer Diagram

B

3.0 LONGITUDINAL THREE-DEGREE-OF-FREEDOM TRANSITION SIMULATION

3.1 Discussion

The basis for the longitudinal transition work described in this section was the 2500 foot, hot day, flight condition; an aircraft with the cg at station 246; and a weight of 9200 pounds. The analog computer simulation work involved the use of a fixed base oscilloscope display cockpit for providing pilot inputs to the simulation, as well as for obtaining pilot evaluation of system operation.

This simulation included investigation or development of the following items:

1. Altitude Control and Transition Procedures. Pitch control with and without stabilization system
2. Single engine recovery and speed-altitude envelope for 10 fps sink rate
3. Selection of vector rate for pilot command during transition
4. Trimmed flight at various α , β_v and V_T
5. Methods of controlling horizontal tail trim during transition
6. Nose fan phase-out with β_v , evaluation, and nose-fan and tail malfunctions during transition
7. Variation of $\partial C_{p_{pf}} / \partial \delta_p$ on handling qualities
8. Pitch auto stabilization authority, gains, and concept in the transition regime
9. Hand calculation dynamic check of simulation

The mechanics of the simulation, as well as the limitation of the simulation are included in the following Section 3.15. (Shown are approximation, data, data fits (separation of data), limitations, etc.)

3.2 Accelerating Transition

The accelerating transitions require that the control stick be displaced to a nose-down position during the entire sequence, which in turn means the maneuvering gain switch on the stick will be energized. The maneuvering gain in the pitch mode must thus be chosen to afford damping according to the pilot's wishes. In the transition simulation, energizing the maneuvering switch cuts the pitch channel gain to zero. The transition offered no control problems in the absence of auto-stab signals, so the results should be conservative. Figure 6 is a plot of % stick position versus velocity for trimmed velocities at various β_v .

A fast accelerating transition required more forward stick than a slow accelerating transition, because in the fast transition higher vector angles are obtained at lower speeds, which means the tail contribution opposing the pitch-up tendency is less. The "fast" transition required twice the forward stick for a trimmed transition.

There are two limits placed upon the maximum allowable vector rate during the accelerating transition. They are: (1) the fact that the higher the vector rate, the more forward stick is required to hold the nose down, and (2) the fact that a higher vector rate results in a higher thrust level being required to hold lift equals weight. If the gas generators are already at 100% and the louvers are already at maximum lift, the vector rate must be slow enough so the induced and aerodynamic lift components increase sufficiently to compensate for the loss of lift due to thrust vectoring. In general, the maximum vector rate limit due to insufficient lift occurs before the limit due to insufficient longitudinal control power.

To determine the maximum allowable vector rate during an accelerating transition, a high gain autopilot was synthesized and connected into the pitch mode. Pitch angle was fed to the control stick input, and rate-of-climb was fed to collective stagger. N_g was set at 100%. Collective vector was set to operate at a preset rate. The computer was then turned

on, and several transitions were made to determine the maximum vector rate which required no less than 13° collective stagger and resulted in no change of altitude or pitch attitude. As simulated, this maximum vector rate was found to be 2° per second.

Other considerations dictated a faster rate than this, and 3° per second was chosen. This means that the pilot must "beep" the vector button to attain an average vector rate of around 2° per second, maximum.

3.2.1 Preferred Technique for Accelerating Transition

The preferred accelerating transition technique was developed to be as follows:

1. Set stagger at maximum lift.
2. Increase throttle to $100\% N_g$.
3. After lift-off immediately begin vectoring until rate of climb goes to zero on IVSI.
4. Control rate-of-climb with reference to the IVSI (Instantaneous Vertical Speed Indicator) by beeping vector until rate-of-climb becomes negative. As rate-of-climb goes to zero, again resume beeping.

Using this procedure, accelerating transitions can be consistently made within a ± 10 ft. altitude band.

3.3 Decelerating Transition

The decelerating transition requires a different approach. During this maneuver, the aerodynamic lift is appreciable, and it is indeed necessary to reduce thrust to slow down. Reduction of gas generator RPM also reduces the nose-up pitching moment caused by the fans at intermediate vector angles, and thus allows more rapid removal of collective vector. The decelerating transition can be accomplished at the maximum 3° /second vector rate.

The preferred decelerating transition procedure was developed to be as follows:

1. Reduce speed to conversion speed at $90\% N_g$.
- 1a. Set lift control at maximum lift.

2. Convert.
3. Vector towards $\beta_v = 0$, until a rate-of-climb shows on the IVSI.
4. Cease vectoring until a sink rate appears on the IVSI, and then resume vectoring. Repeat this operation as often as required.
5. At 40-50 knots IAS begin applying power to keep sink rate zero. The vector angle will be around zero at this time.
6. Hover or land.

The same ± 10 ft. altitude corridor is possible with this transition also.

These techniques result in the fastest transition possible with zero altitude loss or gain. Transition may be made at as low a rate as desired, and lower rate transitions require less forward stick.

The fastest accelerating transition requires 80% forward stick at intermediate vector angles, whereas a slow transition which does not deviate appreciably from thrust=drag can be accomplished with 40% forward stick.

The decelerating transition requires less forward stick because it is accomplished mostly at higher speeds where the tail and elevator effectiveness are appreciable.

True hovering ($\pm 360^\circ \alpha$) was not possible in this simulation due to the method used of resolving body rates into angle of attack. Due to the extensive hovering simulation already conducted, it was felt that rearward flight was not important to the transition investigations. The system used allowed true vertical flight, with α being limited to $\pm 140^\circ$.

3.4 One-Engine Out Operation

For evaluation of single-engine fan powered flight, the fan thrust data was modified to give 59% of the two-engine main fan thrust and 56% of the two-engine nose fan thrust.

A speed-altitude envelope was determined by flying at a given speed and zero sink rate, and then reducing fan thrust by means of a switch to the single engine value, taking into account the fan dynamics.

An indicated airspeed of 45 knots or above allows 10 fps sink rate or less to be established and held. The criterion of a successful recovery was to determine how much altitude must be lost to reduce the sink rate to ten feet per second. The technique of recovery varies with the initial altitude. For the high-altitude recovery, assuming low vector angle and low velocity, the recovery technique involves immediate increase of the remaining Ng to 100%, dropping of the nose, and immediate initiation of vectoring toward 45° vector angle. From the high altitude one-engine out recovery aspect, it is evident that the highest vector rate possible is desirable.

The low altitude recovery in the hovering regime involves merely applying maximum power to the remaining engine and holding on. At 30 knots or so IAS, it is desirable to vector towards 45° β_v and attempt to gain velocity.

A plot of the one-engine out speed altitude envelope for 10 fps sink rate is shown in Figure 7.

3.5 Choice of Pilot - Commanded Collective Vector Rate During Fan-Powered Flight

As has been discussed, two conflicting requirements have affected the choice of collective vector rate during the transition. They are:

1. The rate of vectoring during the accelerating transition is limited by the requirement to be able to perform zero altitude change transitions. This limit is 2° per second.
2. A higher rate of vectoring is useable during the decelerating transition, and an even higher rate of vectoring is desirable to accomplish a high-altitude one-engine recovery.

It was decided that the pilot should have a capacity of vectoring in excess of the maximum allowable for the accelerating transition, but that the excess should be limited so that all inadvertent steady vectoring to maximum vector would not be catastrophic.

3.6 Computer Derived Trim Conditions

During the longitudinal transition simulation, a number of trim conditions were arrived at by manually "flying" the simulation to a given indicated air-speed at a given vector angle, and then going to "hold" on

the computer and reading the various flight parameters out. It should be noted that for this simulation $\sin \theta$ was defined equal to θ in radians, so high angles of pitch (and α) resulted in errors in the trim condition. The data is reasonable up to $\pm 10^\circ$ angle of attack. The results of this work are plotted in Figure 8.

3.7 Tail Trim During Transition

Several schemes to position the horizontal tail during the transition were investigated.

For the accelerating transition, a considerable nose-up moment from the fans must be balanced by control inputs. Figure 9 is a computer-derived plot of required tail incidence versus velocity for trimmed fan-powered flight.

It would appear that a simple program of tail incidence versus β_v would suffice for transition operation (untrimmed fan-powered flight). This is not true however, since the vector angle-velocity relationship is different for accelerating and decelerating transitions. Furthermore, the decelerating transition occurs at a different gas generator RPM than the accelerating transition. The tail incidence turns out to be a function of velocity and power setting, and since transitions are made under varying flight conditions, an open-loop program of tail versus β_v is unsatisfactory. Many open-loop tail programs were tested, and they universally were wrong for one or the other of the transitions. A program of tail incidence which was a function of vector angle and power setting worked reasonably well at the 2500 foot hot day condition, but would be wrong for S. L. std. day conditions.

For the above reasons, programmed open-loop tail incidence was discarded. Some form of closed loop (pilot input) scheme was indicated, and the following were tested:

1. Pilot manual Beeper control.
2. Integral control based on returning the elevator position to zero in the steady state.
3. Automatic beeper control using elevator position by means of control stick position-actuated switches. Using this system, the tail moves at a fixed rate if the control stick is displaced more than a predetermined amount.

4. Automatic beeper control using a combination of elevator position sensing and stability augmentation system output sensing. This system commands a fixed tail rate if the sum of control stick plus auto stab output (δ_{psa}) exceeds a certain predetermined value.

The Cooper pilot rating was used to classify these various systems. During these runs, the pilot made no specific maneuvers, but just gave opinions on his feelings toward the handling qualities. The Ryan Racer, a fixed base cockpit, was used for these tests.

In general, the results of these tests were as follows:

1. The manual beeper system had a best rating of 4 obtained with a $3^\circ/\text{sec}$ tail rate. Other tail rates had poorer ratings.
2. Integral control had a best rating of 3.
3. Elevator alone beeping the tail had a best rating of 3-4 with a $1^\circ \delta_e$ dead band and $2^\circ/\text{sec}$ tail rate.
4. Elevator alone with a two rate system and two dead bands, a small one for the small rate and a large one for the larger rate, had ratings of 5 or worse.
5. A combination of δ_e and δ_p commanding a given tail rate when the sum of the two exceeded a given dead band, had a best rate of 3.

As a result of these tests, the method used in test 4 was discarded. Since the method of test 2 would mean a different tail trim system, and the Cooper rating was not appreciably higher than tests 1, 3, and 5, the integral control was discarded.

The method of test 5 gave good results, but required the mixing of electrical (auto stab output) and mechanical (control stick position) information. It was not discarded, but just put in abeyance.

The manual beeper system and the control stick switch beeper system had about the same rating, but method 3 had certain advantages. They are:

1. Due to the requirement of forward stick displacement during transition, the horizontal tail is automatically positioned at the full up position by the time it begins to be effective.
2. The requirement of pilot manual beeping would detract from the ability of the pilot to hold zero rate of climb by selective vector beeping. He only has one thumb on the right hand. The control stick beeping allows the pilot to devote nearly full time to his transition requirements.

Using either system 1 or system 2, it is possible to trim the airplane with stick centered so that full auto stab nose fan authority is being commanded. If the stab system is thus saturated, the auto stab system is effectively imperative until the hard-over bleeds away. Due to the high system gain possible, this effect could easily occur. On the other hand, this problem only presents itself at the higher transition speeds, where auto stab operation is not really required.

System 5 eliminates this effect, but until evidence to the contrary is available, this effect will be considered unimportant.

System 3 has been deemed the most attractive on the combined basis of simplicity, reliability, and operational effectiveness.

3.8 Nose Fan Phase-Out With β_v

As vector angle is increased, the pilot stick input to the nose-fan thrust reverser doors is phased out, and the nose fan thrust level goes to zero, although the auto stab inputs still have the original 25% of stick authority. Transitions were accomplished with various programs of pitch fan phase-out with vector angle, and no difference could be noted in aircraft response. For this reason, the pitch fan phase-out program incorporated into the airplane was deemed satisfactory.

3.9 Tail Incidence Actuator Malfunction During Fan-Powered Flight

If the tail actuator fails hard over in the up-trim position, nose down control power runs out at $20^\circ \beta_v$ (55 Knots EAS).

If the actuator fails in the nose-down trim position, the transition can be successfully completed, but considerable back stick is required.

The minimum tail incidence allowable for a successful transition is from 5° to 7° up.

If the tail fails full up at higher than conversion speed, sufficient back stick might not be available.

3.10 Nose Fan Door Failure

In the case of a nose fan door failure, the vehicle, of course, cannot be hovered. For a hard-over in the maximum thrust direction, stick control runs out at 75 Knots EAS.

If the doors fail in a closed position while the fan is running, we are indeed in deep trouble.

A failure resulting in zero nose fan thrust results in all pitch control resulting from the elevators and tail; 30 Knots would be considered a minimum speed for this condition, and control is very mushy.

3.11 Variation of $\delta C_{p_{nf}} / \delta \delta_p$ on Handling Qualities

This coefficient causes the nose fan RPM to vary with nose fan thrust reverser door position. The value of this coefficient was increased by a factor of 10 with no apparent effect.

3.12 Pitch Channel Auto Stab Authority, Gains and Concept in the Transition Regime

Of all the work to date, the transition regime seemed to be the least critical, at least in the longitudinal mode as far as the auto stab system is concerned. Most of the transitions were accomplished with maneuvering gain. Since the stick is displaced outside the holding gain limits for practically the entire transition, maneuvering gain was set to zero for all transition work. At transition flight trim speeds, the dynamic response of the airplane alone and airplane and auto stab was recorded. The autopilot reduced the characteristic divergent character of the airplane response to a considerable degree.

3.13 Dynamic Check of Simulation

As with all analog simulation work, some sort of independent dynamic response check is required if the maximum confidence of valid

results is to be obtained.

Due to the difficulty of calculating this check, a single case, $35^\circ \beta_v$, 100 % RPM at angle of attack equals zero was picked for calculation. The calculations were made by a small perturbation analysis around trim points. For this condition θ / δ_p was derived to be:

$$\theta / \delta_p = \frac{-1.32 (S+.227) (S+.628)}{(S-.219) (S+.45) (S^2 + 2(.614) (1.32) S + 1.32^2)}$$

The transient response of this system to an impulse of $\delta \rho$ was derived to be as follows; for a unit $\delta \rho$ impulse

$$\theta(t) = -1.32 \left[.2639e^{-.219t} + .0492e^{-.45t} + .752e^{-.81t} \sin(1.04t - 24.6^\circ) \right]$$

A plot of this response is shown in Figure 10 and a plot of the computer derived response for the same condition is shown in Figure 11.

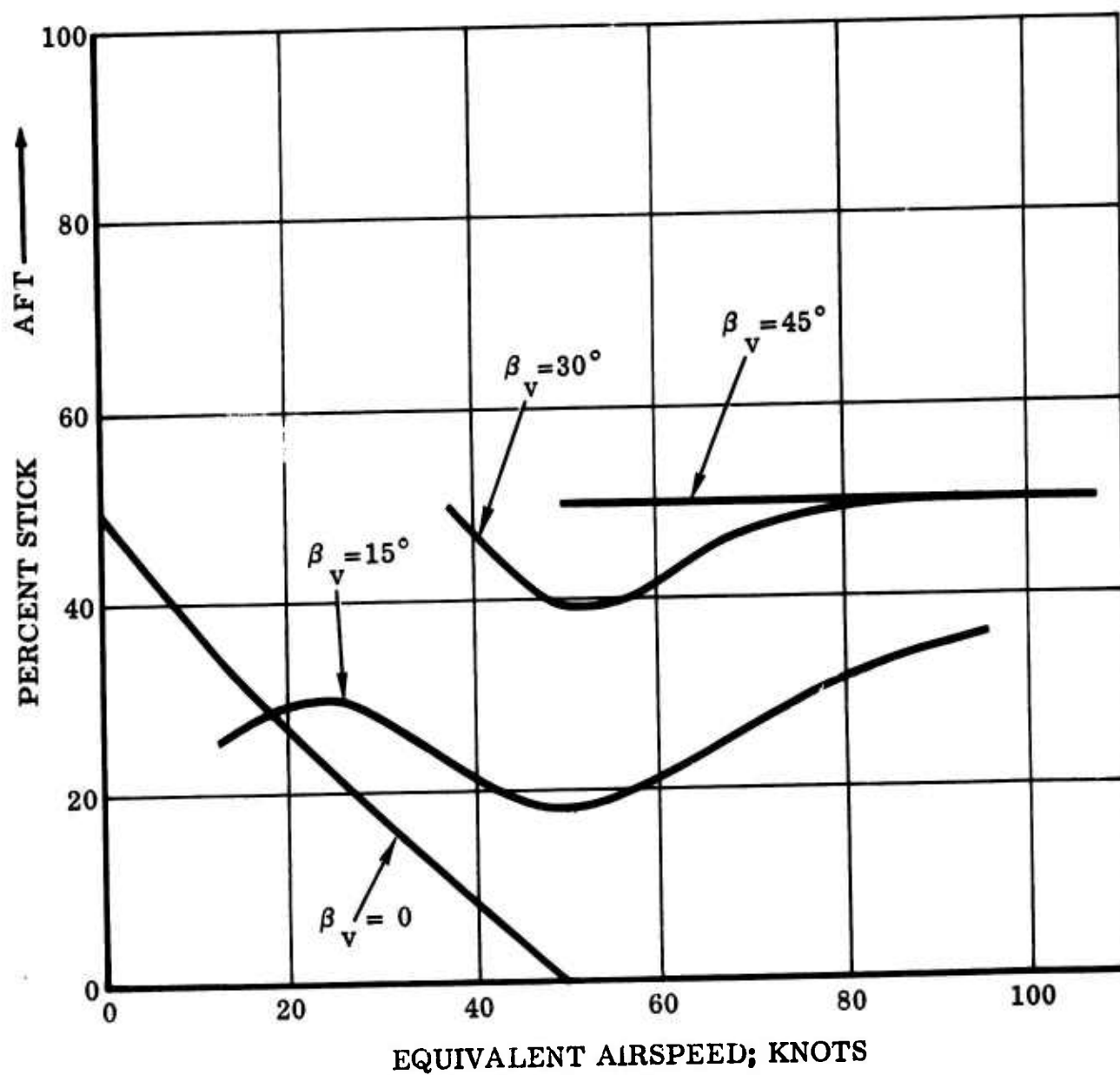


Figure 6 Required Per Cent Stick from Full Forward for Trim vs Equivalent Airspeed

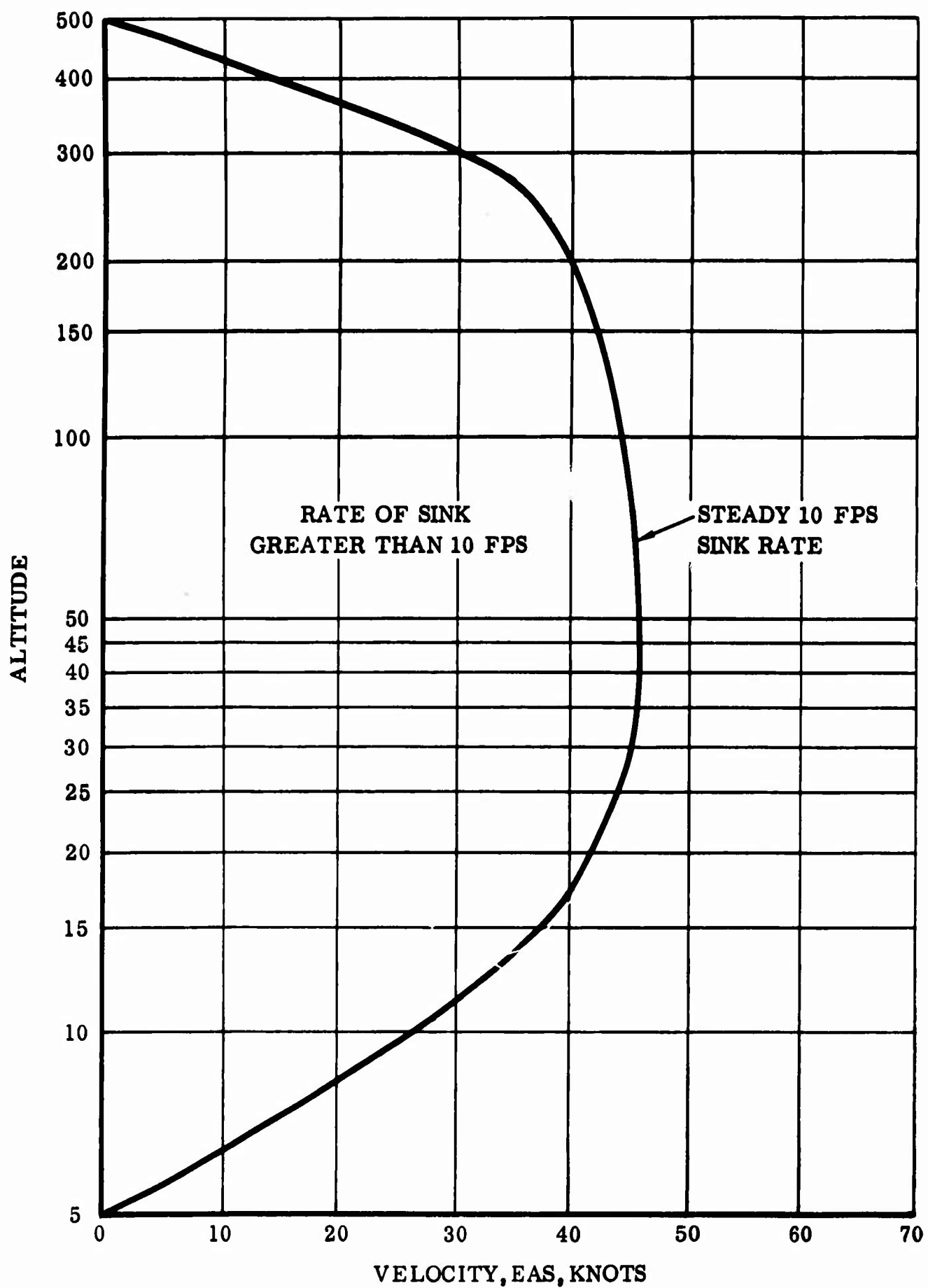


Figure 7 One Engine Out Speed-Altitude Envelope for 10 FPS or Less Sink Rate at Touchdown

2500 FT, HOT DAY
 $\delta_f = 45^\circ$, $\beta_s = 13^\circ$, 9200 LBS

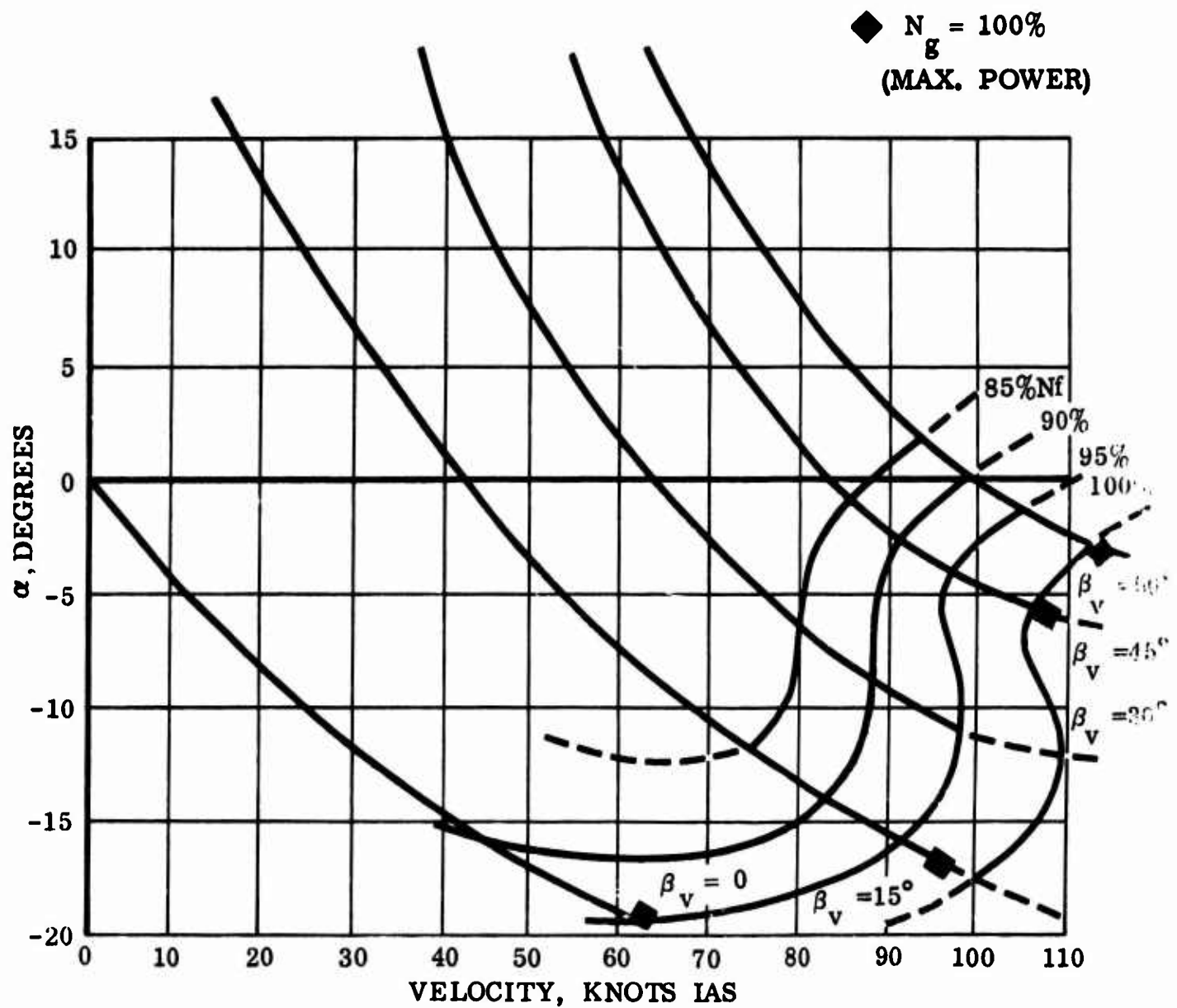


Figure 8 Velocity vs Angle of Attack at Constant Vector Angle

ANGLE OF ATTACK = ZERO
TRIM CONDITIONS

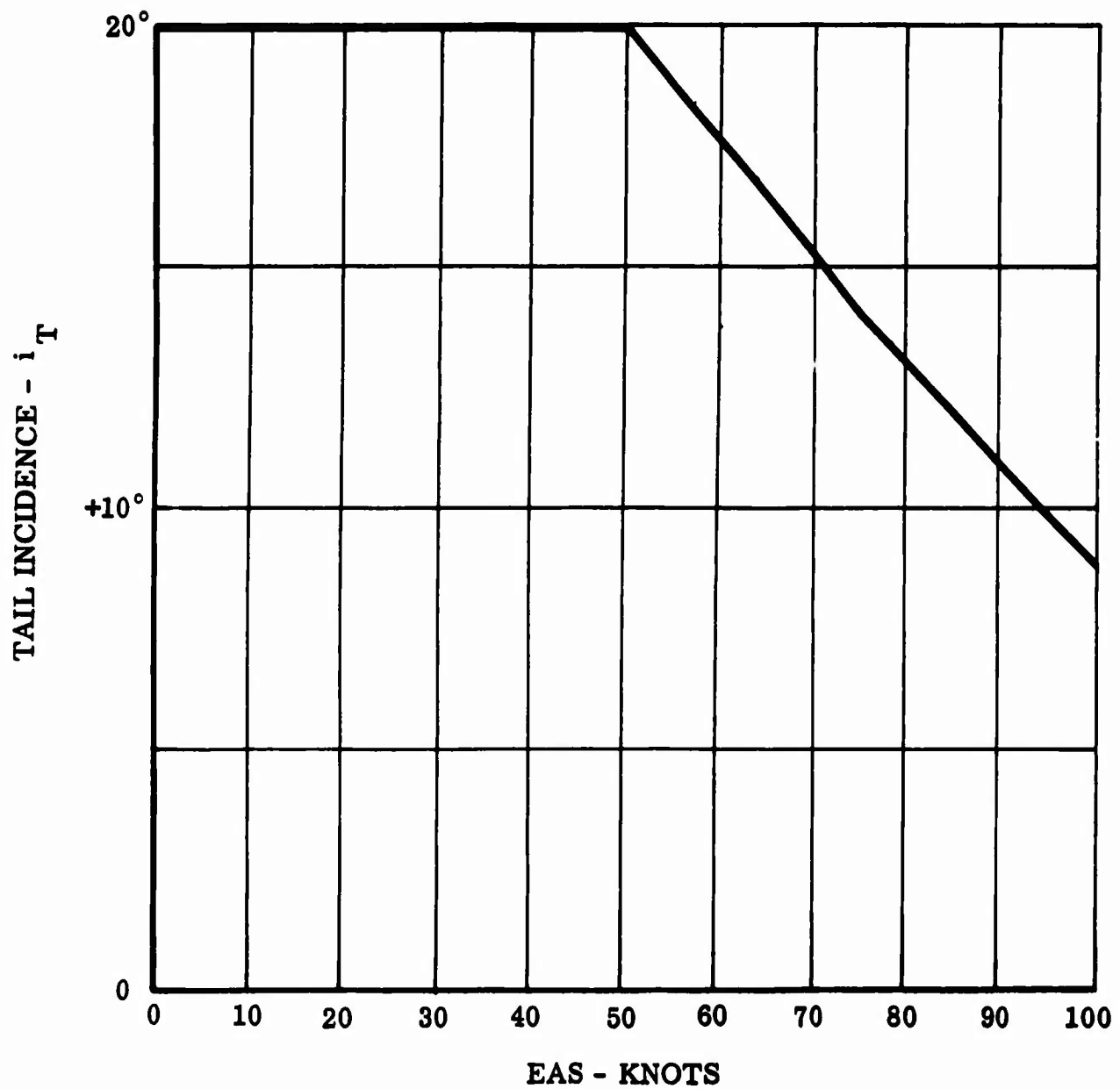


Figure 9 Tail Incidence for Trim vs Equivalent Airspeed, Knots

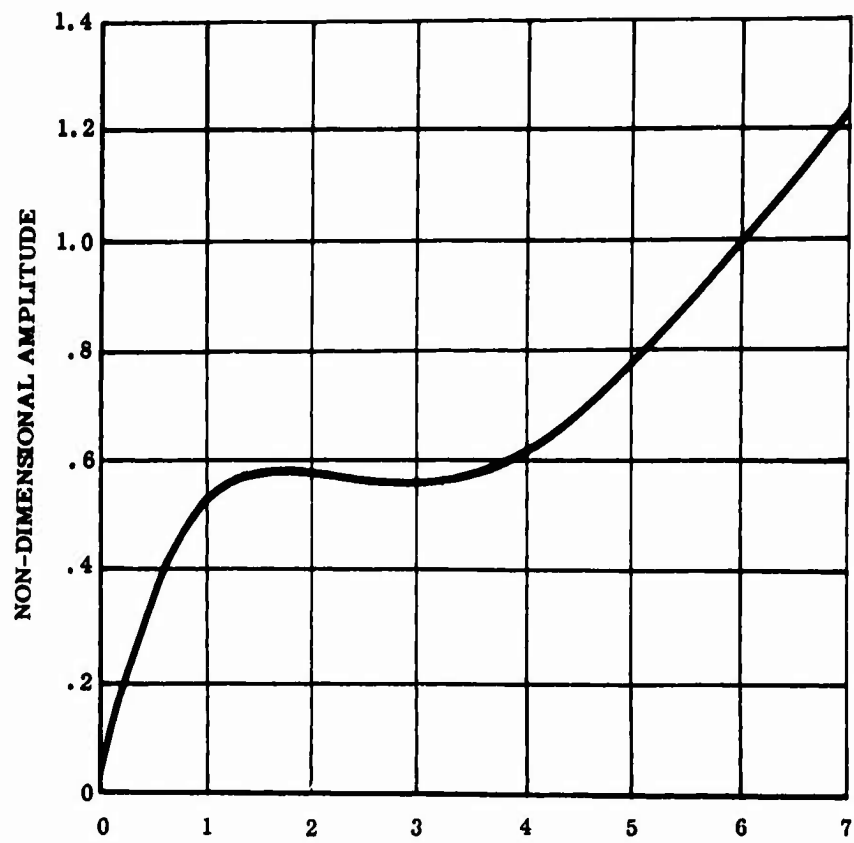


Figure 10 Dynamic Check Hand-Calculation Response for impulse of δp , for Small Pert. Transfer Function

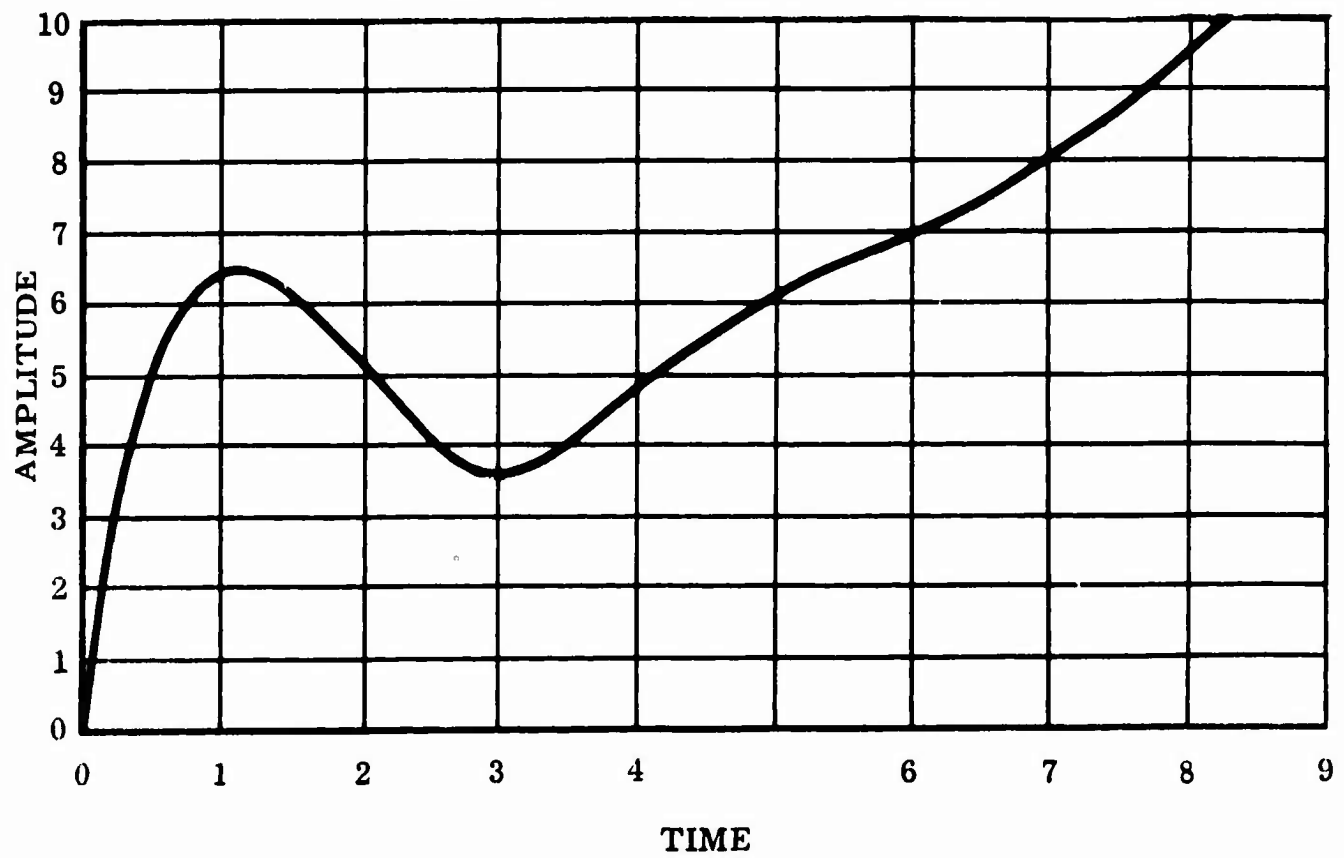


Figure 11 Plot of Analog Computer Record for Dynamic Check Initial Conditions

3.14 List of Symbols

u	Velocity along vehicle X axis, ft/sec.
w	Velocity along vehicle Z axis, ft/sec.
θ	Pitch angle, radians
\dot{A}	Time derivative of arbitrary quantity, A.
\ddot{A}	Second time derivative of A
F_x	Force along vehicle X axis, lbs.
F_z	Force along vehicle Z axis, lbs.
M	Pitching moment, ft. lbs.
m	Mass, slugs.
g	32.2 ft/sec ²
I_y	Pitch moment of inertia, slug ft ²
L	Lift, perpendicular to velocity vector/lbs.
V_T	Total velocity, ft/sec.
q^s	Slipstream dynamic pressure, $q + T_{\infty}/A_f$, PSF.
q	$\rho / 2 V_T^2$, PSF
ρ	Density of air, slugs/cu. ft.
A_f	Total wing fan area, ft ²
C_N^s	Slipstream normal force coefficient $\frac{N}{q^s A_f}$

N	Normal force, $-F_z$, lb.
\bar{X}_T	Tail moment arm, feet.
$C_{N_o}^s$	C_N^s at $\alpha = 0$
A_{PF}	Pitch fan area, ft^2 ; and Axial force, lb.
D_f	Main fan diameter, ft
α	Angle of attack, degrees or radians, as specified.
β_v	Collective vector angle, degrees.
β_s	Collective stagger angle, degrees.
R_q	$1 - T_c^s$
T_c^s	$\frac{T_{ooo}/AF}{q + T_{ooo}/AF}$
T_{ooo}	Wing fan thrust at $\beta_v = \beta_s = V_T = 0$
A	Axial Force = $-F_x$, lbs.
C_A^s	Slipstream axial force coefficient $\frac{A}{q^s A_f}$
D_{NF}	Nose fan ram drag, considered as a body axis term here, lbs.
C_m^s	Slipstream pitching moment coefficient $\frac{M}{q^s A_f D_f}$
M_{PF}	Pitch fan pitching moment, $M_{OP_F} + N_{PF} \bar{X}_{PF}$, ft. lbs.

$M_{O_{PF}}$	Pitch fan pitching moment about fan hub ft. lbs.
ϵ	Downwash angle at horizontal tail, degrees.
i_t	Tail incidence angle w/respect to body X axis, degrees.
δ_e	Elevator deflection, degrees.
S_t	Horizontal tail area, ft ²
l_t	Tail moment arm, ft.
$M_{\dot{\theta}}$	Damping moment due to $\dot{\theta}$, ft. lbs./rad./sec.
$M_{\dot{\alpha}}$	Damping moment due to $\dot{\alpha}$, ft. lbs./rad./sec.
C_P^s	Fan power coefficient. $\frac{P_F \rho^{1/2}}{A_f \left(\frac{T_{000}}{A_f} \right)^{3/2}}$
P_F	Fan power.
N_g	Gas generator RPM, %
δ_f	Flap deflection, degrees
N	$1 - \frac{\%N_g}{100}$
T_g	Gross thrust

3.15 Analysis

The equations of motion used for the longitudinal three-degree-of-freedom transition simulation are shown below. The equations are in body axis form, and are related to the inertial axes by the pitch angle, θ .

$$\dot{u} = \frac{\Sigma F_x}{m} - \frac{g \sin \theta}{m} - qw \quad (1)$$

$$\dot{w} = \frac{\Sigma F_z}{m} + \frac{g \cos \theta}{m} + qu \quad (2)$$

$$\ddot{\theta} = \frac{\Sigma M}{I_y} \quad (3)$$

Where:

$$\Sigma F_x = -L_{tail} \sin \left(\frac{\alpha}{2} - \epsilon_o \right) - A_{PF} - C_A^s q^s A_F \quad (4)$$

$$\Sigma F_z = -L_{tail} \cos \left(\frac{\alpha}{2} - \epsilon_o \right) - C_N^s q^s A_F - N_{PF} \quad (5)$$

$$\Sigma M = M_{PF} + C_m^s q^s A_f D_f - 99qu - 875q \quad (6)$$

$$-L_T \overline{X_T}$$

where $-99qu$ is equal to the tail pitching moment due to pitch rate, and $-875q$ is the damping moment due to the fans. The drag of the tail is ignored as a pitching moment contribution.

3.15.1 NORMAL FORCE

$$F_N = -F_Z$$

$$C_N^s = C_{N_o}^s + \Delta C_{N_\alpha}^s + \Delta C_{N_{\beta_v}}^s + \Delta C_{N_{\beta_s}}^s \quad (7)$$

Where

$$C_{N_o}^s = C_{N_\alpha=0}^s \text{ less the } \Delta C_N^s \text{ due to } 45^\circ \text{ flap (Figure 12, Figure 13)}$$

$$\Delta C_{N_\alpha}^s = \text{Change in normal force coeff. due to angle of attack.}$$

$$C_{N_{\beta_v}}^s = -C_{N_o}^s \left[1 - K_{\beta_{vL}} \right] \quad (\text{Figure 14}) \quad (8)$$

$$\Delta C_{N_{\beta_s}}^s = -C_{N_o}^s K_{\beta_{sL}} \quad (\text{Figure 15}) \quad (9)$$

$$N_{PF} = \text{Normal force due to the pitch fan} \quad (10)$$

$$\Delta C_{N_{\delta_F=45^\circ}}^s = 3 R_q \quad (11)$$

3.15.2 AXIAL FORCE

$$F_A = -F_x$$

$$C_A^s = C_{A_o}^s + \Delta C_{A_\alpha}^s + \Delta C_{A_{\beta_v}}^s + \Delta C_{A_{\beta_s}}^s \quad (12)$$

$$C_{A_o}^s = C_A^s \text{ at } \alpha = 0$$

$$\Delta C_{A_\alpha}^s = \text{change in } C_A^s \text{ due to } \alpha \quad (\text{Figure 12, Figure 13})$$

$$C_{A_{\beta_v}}^s = - C_{N_o}^s (K_{\beta_v}) \quad (\text{Figure 14}) \quad (13)$$

$$\Delta C_{A_{\beta_s}}^s = - C_{N_o}^s (K_{\beta_s}) \quad (\text{Figure 15}) \quad (14)$$

$$D_{PF} = \text{Nose Fan Ram Drag} \quad (\text{Figure 16})$$

3.15.3 PITCHING MOMENT (At c.g. Sta. 246)

$$M = C_m^s q A_F D_F + M_t + M_{PF} + M_{\dot{\theta}} q + M_{\dot{\alpha}} \dot{\alpha} \quad (15)$$

$$C_m^s = C_{m_o}^s + \Delta C_{m_{\alpha}}^s \alpha + \Delta C_{m_{\beta_v}}^s \beta_v + \Delta C_{m_{\beta_s}}^s \beta_s \quad (16)$$

$$C_{m_o}^s = C_{m_{\alpha}}^s = 0 \quad (\text{Figure 17, 18})$$

$$\Delta C_{m_{\alpha}}^s = \text{Change in moment coeff. due to } \alpha \quad (\text{Figure 17, 18})$$

$$\Delta C_{m_{\beta_v}}^s = \text{vector pitching effectiveness} \quad (\text{Figure 19})$$

$$M_t = \text{Tail pitching moment}$$

$$\Delta C_{m_{\beta_s}}^s = \text{Stagger pitching effectiveness.} \quad (\text{Figure 20})$$

$$M_{PF} = \text{Nose fan pitching moment.}$$

$$M_{\dot{\theta}} = \text{Damping moment due to fans and horizontal tail.}$$

$$M_{\dot{\alpha}} = \text{Moment due to rate of change of } \alpha .$$

3.15.4 Force and Moment Equations for the Horizontal Tail

For the transition simulation, the drag of the tail was assumed negligible, and the only contribution to pitching moment from the tail was the tail lift. This also held true for the tail contributions to F_x and F_z .

With this in mind, the equation for lift and pitching moment from the tail are:

$$L_t = \left[\left(\frac{dC_{L_t}}{d\alpha} \right) \left(\alpha \left(1 - \frac{d\epsilon}{d\alpha} \right) - \epsilon_o + i_t \right) + \frac{dC_{L_t}}{d\delta_e} \delta_e \right] \frac{\rho}{2} V_T^2 S_t \quad (17)$$

$$M_t = - L_t \ell_t \quad (18)$$

Where:

$$\frac{dC_{L_t}}{d\alpha} = .052/\text{deg.}$$

$$\frac{d\epsilon}{d\alpha} = .5$$

$$\epsilon_o = f(T_c^S) \quad (\text{Figure 21})$$

i_t = Tail incidence

$$\frac{dC_{L_t}}{d\delta_e} = .027/\text{deg.}$$

$$\delta_e = \pm 25^\circ$$

$$S_t = 50.66 \text{ ft}^2$$

$$\ell_t = 20.6 \text{ ft.}$$

The tail lift force is in tail stability axes, which is removed from the body axis system by the angle α_{tail} , which is equal to $\alpha \left(1 - \frac{d\epsilon}{d\alpha}\right) - \epsilon_o$.

Since $\frac{d\epsilon}{d\alpha} = .5$, the angle of attack of the tail is equal to $\frac{\alpha}{2} - \epsilon_o$.

We can thus write.

$$F_{z \text{ tail}} = -L_t \cos \left(\frac{\alpha}{2} - \epsilon_o \right) \quad (19)$$

$$F_{x \text{ tail}} = + L_t \sin \left(\frac{\alpha}{2} - \epsilon_o \right) \quad (20)$$

$$M_t = -20.66 L_t \quad (21)$$

The damping terms in pitch, $M_{\dot{\theta}}$ and $M_{\dot{\alpha}}$ are given below:

$$M_{\dot{\theta}} = -66V_T \text{ ft lbs/rad/sec.}$$

$$M_{\dot{\alpha}} = -33V_T \text{ ft lbs/rad/sec.}$$

Where V_T is total velocity in feet/second.

We assumed $\dot{\alpha} \approx \dot{\theta}$, so we could multiply the sum of $M_{\dot{\theta}}$ and $M_{\dot{\alpha}}$ by $V_T q$ to get the damping moment.

3.15.5 Calculation of Thrust Coefficient for the Fans and Forces and Moments for the Nose Fan

Main Fan Thrust Coefficient, T_c^s .

(Continued)

The main fan thrust coefficient, T_c^s , is defined:

$$T_c^s = \frac{T_{ooo}/A_F}{\frac{\rho V_T^2}{2} + T_{ooo}/A_F} \quad (22)$$

Where T_{ooo} is defined as the thrust which would occur at a given fan RPM if β_v , β_s and Velocity were suddenly all made equal to zero.

In slipstream notation, q^s is defined as the free stream dynamic pressure plus the disc loading.

It can be easily shown that $\frac{q}{q^s} = 1 - T_c^s$

$1 - T_c^s$ has been called R_q for simulation purposes. This is the ratio of free-stream to slipstream dynamic pressures.

The curves presented in Figures 22, 23, and 24 are required in the computation of T_c^s .

The equation governing C_p^s and T_{ooo} is:

$$C_p^s = \frac{P_F \rho^{1/2}}{\left(\frac{T_{ooo}}{A_f} \right)^{3/2} A_f} \quad (23)$$

C_p^s is a function of T_c^s , β_v and β_s , as shown in Figures 22 and 23.

P_F is a function of N_g , as is shown in Figure 24.

We can solve equation (23) for T_{ooo}/A_f

$$\frac{T_{ooo}}{A_f} = \left[\frac{P_F \rho^{1/2}}{C_p^s A_f} \right]^{2/3} \quad (24)$$

We note also in Figure 24 that gross thrust, T_g , is equal to:

$$A_f \left(\frac{P_F \rho^{1/2}}{C_p^s A_f} \right)_{i.c.}^{2/3}$$

By assuming variations of T_{ooo}/A_f around some initial value, we can write T_{ooo}/A_f as a function of the initial value plus an increment due to ΔC_p^s .

Therefore

$$\frac{dT_{ooo}/A_f}{dC_p^s} = \frac{2}{3} \left(\frac{P_F \rho^{1/2}}{A_f C_p^s} \right) \left[-1 \left(\frac{1}{C_p^s} \right)^2 \left(\frac{P_F \rho^{1/2}}{A_f} \right) \right] \quad (25)$$

$$\frac{dT_{ooo}/A_f}{dC_p^s} = -\frac{2}{3} \left(\frac{P_F \rho^{1/2}}{C_p^s A_f} \right)^{2/3} \left(\frac{1}{C_p^s} \right) \quad (26)$$

Thus, we can write the expression

$$\frac{T_{ooo}}{A_f} = \left(\frac{P_F \rho^{1/2}}{C_p^s A_f} \right)^{2/3} \left[1 - \frac{2 \Delta C_p^s}{3 C_p^s} \right]_{i.c.} \quad (27)$$

where i.c. stands for the initial condition chosen to operate about.

Noting, as before, that $T_g = \left(\frac{P_F \rho^{1/2}}{C_p^s A_f} \right)^{2/3}_{i.c.} A_f$

we can write:

$$\frac{T_{ooo}}{A_f} \approx \frac{T_g}{A_f} \left[1 - \frac{2 \Delta C_p^s}{3 C_p^s}_{i.c.} \right] \quad (28)$$

This is a more convenient form since T_g is easier to curve fit than P_F .

$$\text{Letting } N = 1 - \frac{\%N_g}{100},$$

we find

$$T_g = 10,000 - 62,500N + 125,000N^2 \text{ lbs.} \quad (29)$$

$$C_p^s = .64 - (.813 - .000231 \beta_v^2) R_q - .000069 \beta_v^2 - 2 \times 10^{-5} \beta_s^2 \quad (30)$$

$$\text{OR, } \Delta C_p^s = - (.813 - .000231 \beta_v^2) R_q - .000069 \beta_v^2 - 2 \times 10^{-5} \beta_s^2 \quad (31)$$

Once T_{ooo}/A_f was computed, it was possible to calculate T_c^s . We did not calculate T_c^s , but the value $1 - T_c^s$. This is equal to q/q_s , and is called " R_q ". All of the T_c^s data were fitted using R_q instead of T_c^s . R_q is desirable because at $T_c^s = 1.0$, $R_q = 0$, and is more accurately calculated on the analog computer. The variations of T_{ooo}/A_f with T_c^s ,

β_v and β_s were applied through a circuit with a 0.6 sec. time lag, to simulate the fan dynamic response.

3.15.6 Nose Fan Force and Moment Data

The same technique as used for determination of main fan T_{ooo}/A_f was applied to the nose fan forces and moments.

The variation of nose fan lift with δ_p , thrust reverser door position, was assumed a linear function of δ_p , with $\delta_p = 0$ corresponding to maximum lift. The nose fan maximum normal force was calculated as a function of airspeed, N_g , and δ_p , and then multiplied by $\delta_p/67$, where 67° δ_p was the point of maximum negative thrust. Figure 25 is a plot of per cent maximum lift versus δ_p .

$T_{o_{PF}}$, which is the thrust of the pitch fan at $\delta_p = 0$, is given in Figure 16.

The lift for this is:

$$T_{o_{PF}} = 1500 + .1306V + .0045V^2 - 12100N + 3400N^2 \quad (32)$$

and using the previous technique

$$N_{PF \max.} = T_{o_{PF}} \left[\frac{2 \Delta C_{p_{PF}}^s}{1 - \frac{3 C_{p_{i.c.}}^s}{3 C_{p_{i.c.}}^s}} \right] \quad (\text{Figure 30}) \quad (33)$$

$$\Delta C_{p_{PF}}^s = .000665 \delta_p - 4.17 \times 10^{-7} \delta_p^3 \quad (\delta_p \text{ in deg.}) \quad (34)$$

$$N_{PF} = N_{PF \max.} (1 - .0172 \delta_p) + 3.5w \quad (35)$$

The pitch fan axial force, X_{PF} ,

$$X_{PF} = - (4.2-14N) u \left[\frac{2 \Delta C_{p_{PF}}^s}{1 - \frac{3 C_{p_{i.c.}}^s}{3 C_{p_{i.c.}}^s}} \right] \quad (36)$$

The moment about the pitch fan hub, $M_{O_{PF}}$, was calculated using

Figure 26 and is equal to

$$M_{O_{PF}} = (1.766N + 18.4N^2) F_1 (V) \quad (37)$$

Where $F_1 (V)$ is given in Figure 27.

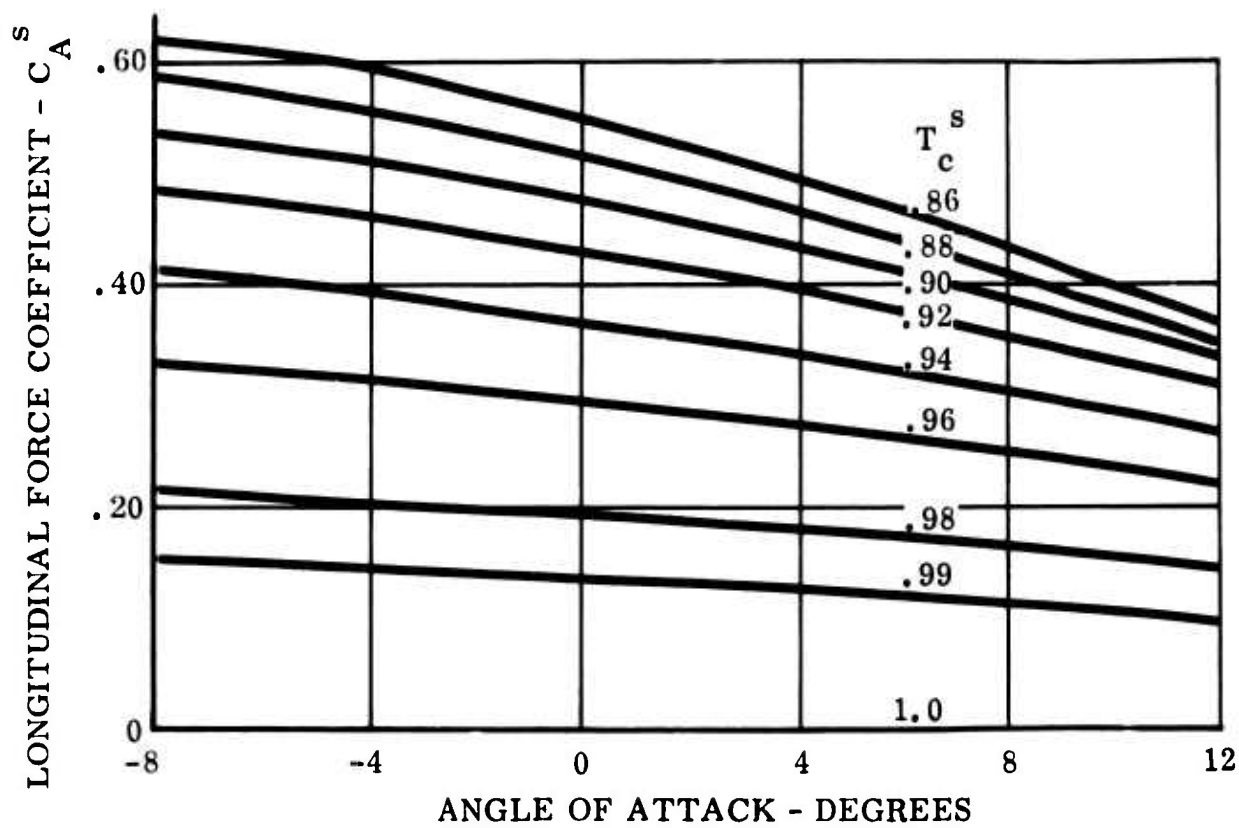
The effect of vectoring on the δ_p values is shown in Figure 28. It is seen that the nose fan δ_p phases out to zero thrust at maximum vector angle.

Figure 29 shows the thrust versus N_g for single engine operation for the nose fan and main fans.

Figures 31 and 32 are the computer wiring diagrams for the 3° transition simulation.

TAIL OFF

$$\beta_v = 0, \beta_s = 0, \delta_f = 45^\circ$$



Fig

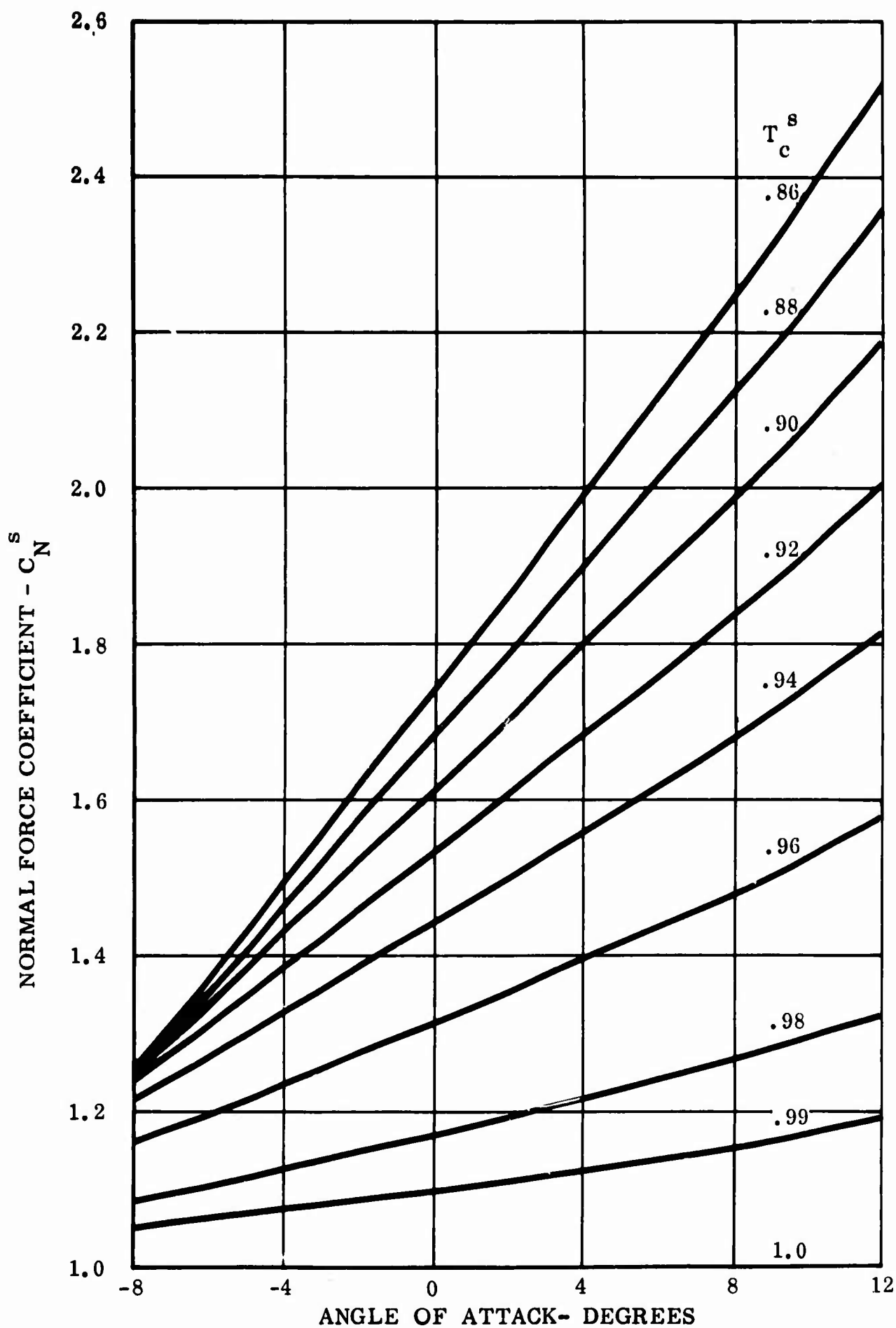
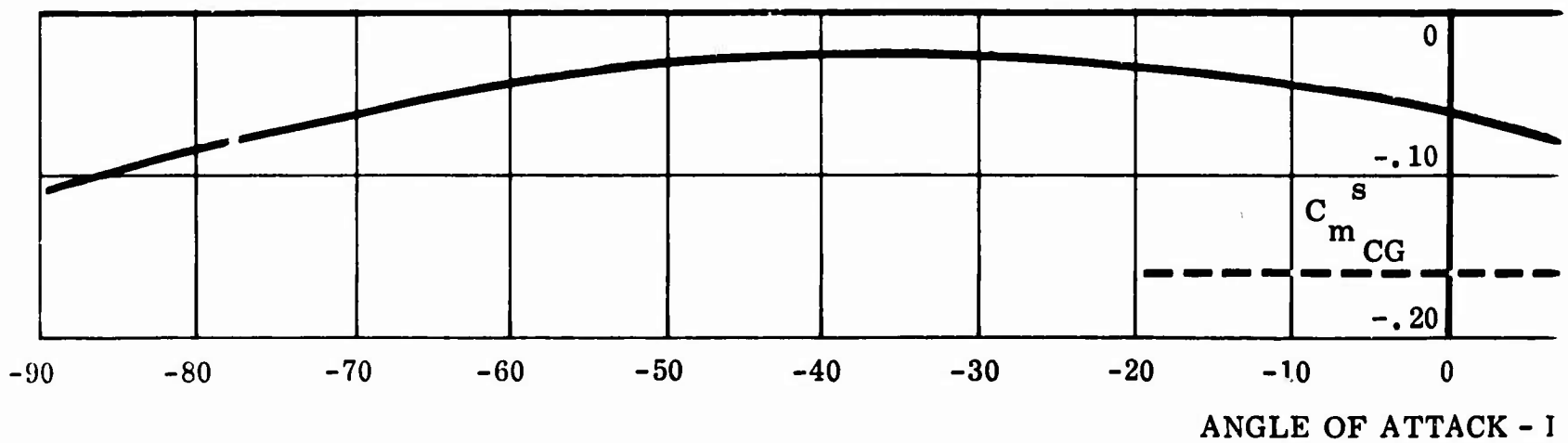
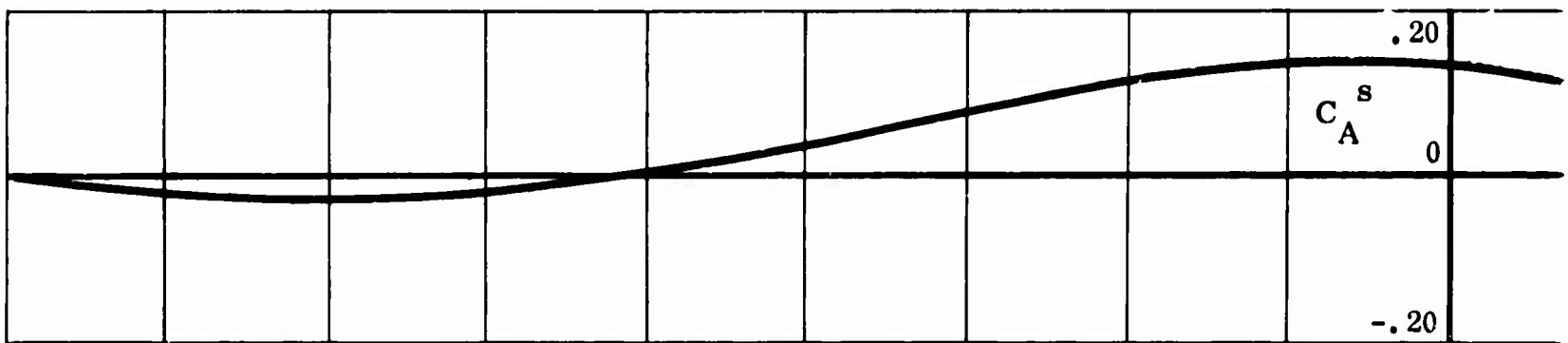
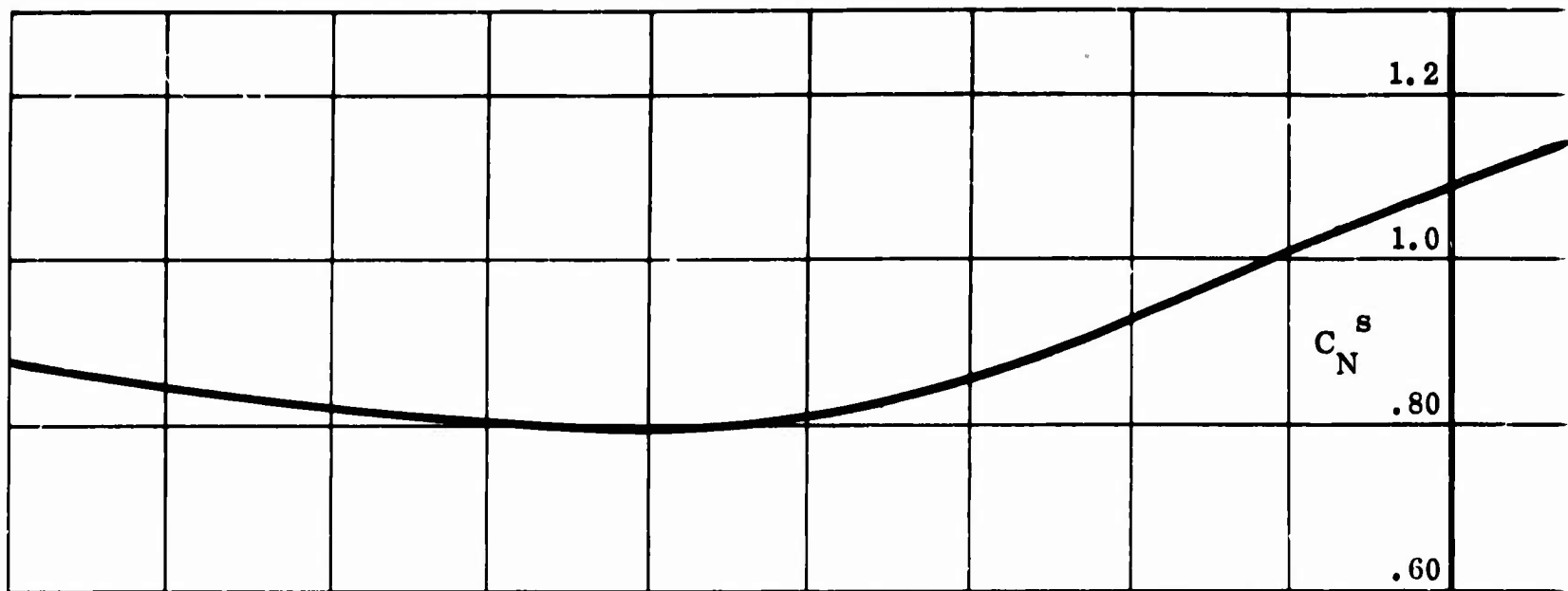


Figure 12 Estimated Normal and Longitudinal Force Coefficients



A

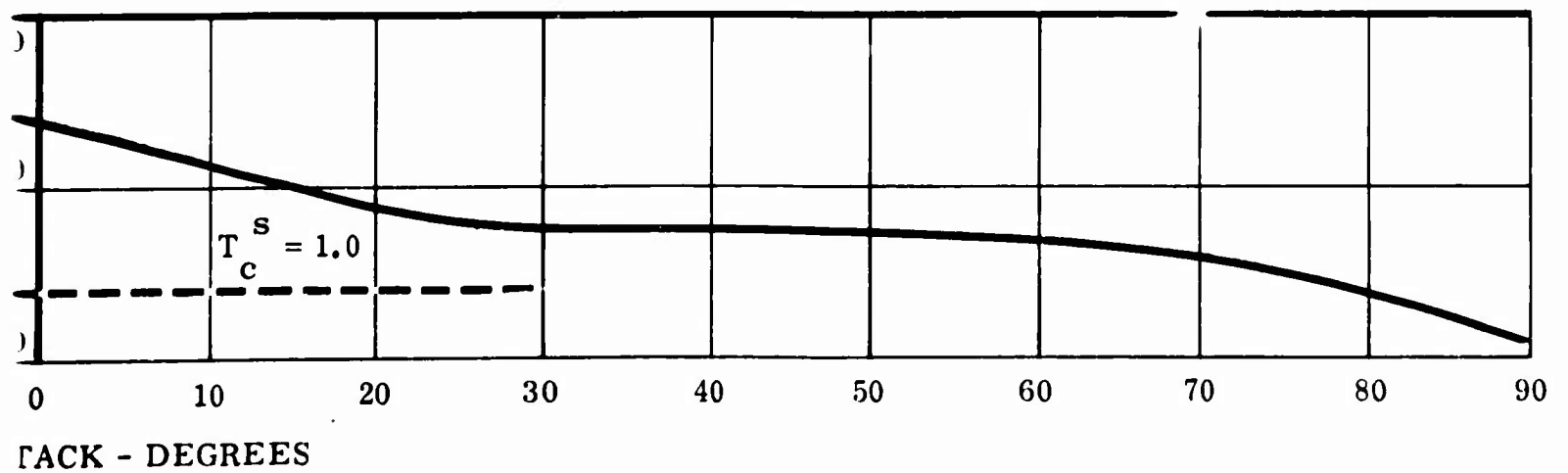
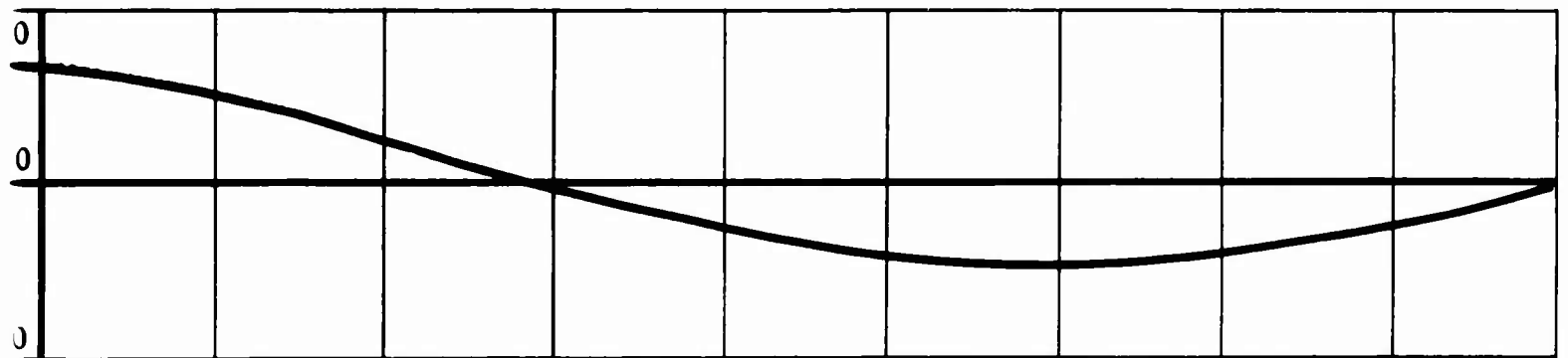
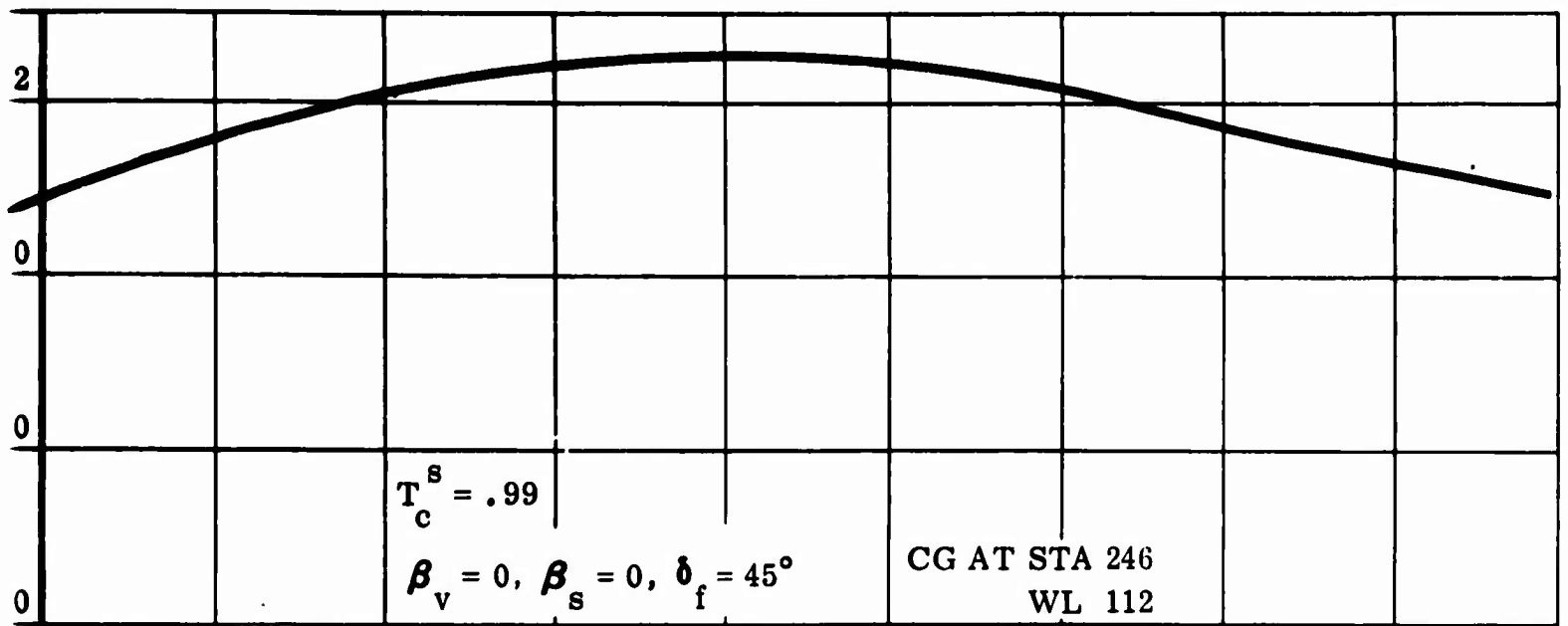


Figure 13 Estimated Force and Moment Coefficients at High Angles of Attack $T_c^s = .99$

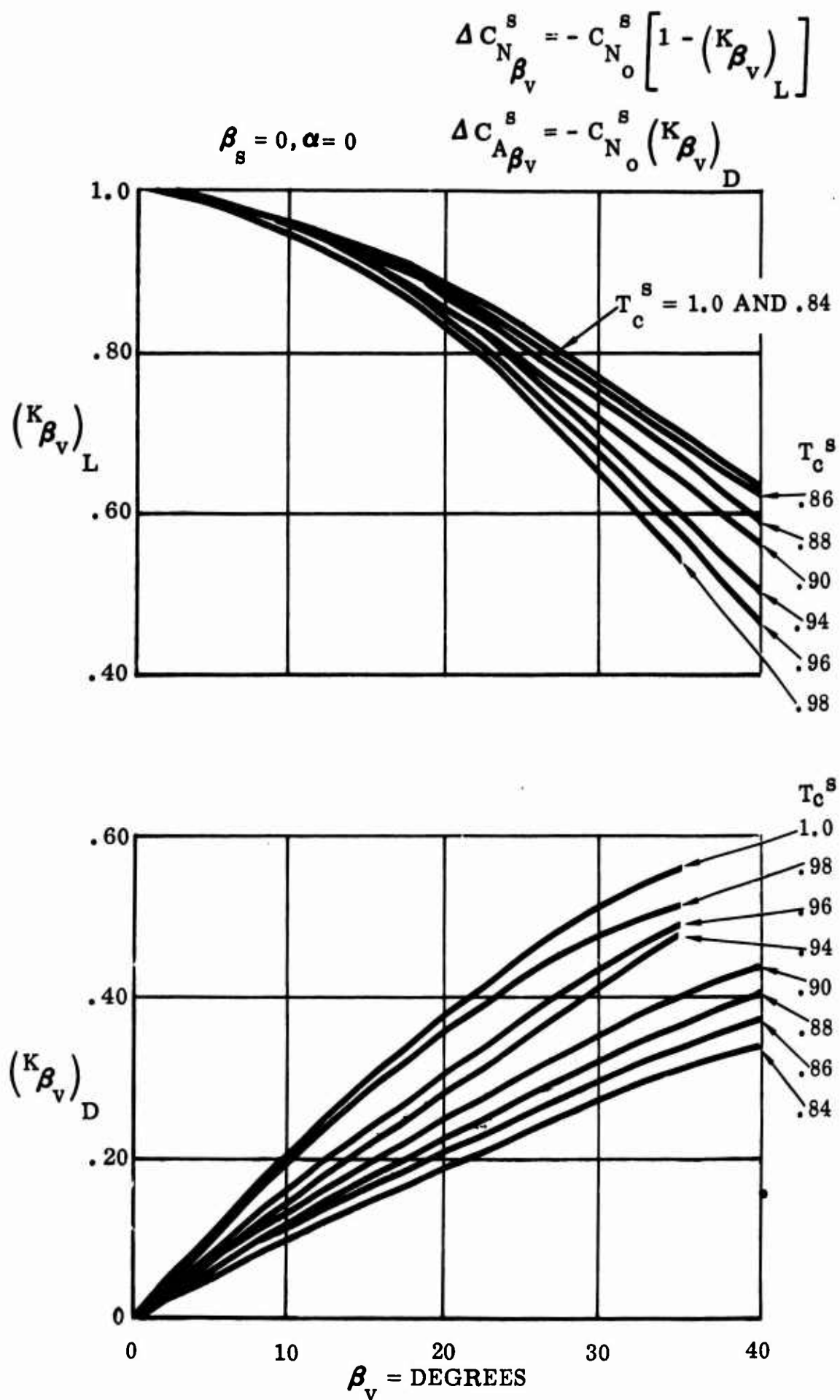


Figure 14 Lift and Drag Parameters for Vector Effectiveness

$$\Delta C_{N_{\beta_s}}^s = -C_{N_o}^s \left[1 - (K_{\beta_s})_L \right]$$

$$\alpha = 0$$

$$\Delta C_{A_{\beta_s}}^s = -C_{N_o}^s (K_{\beta_s})_D$$

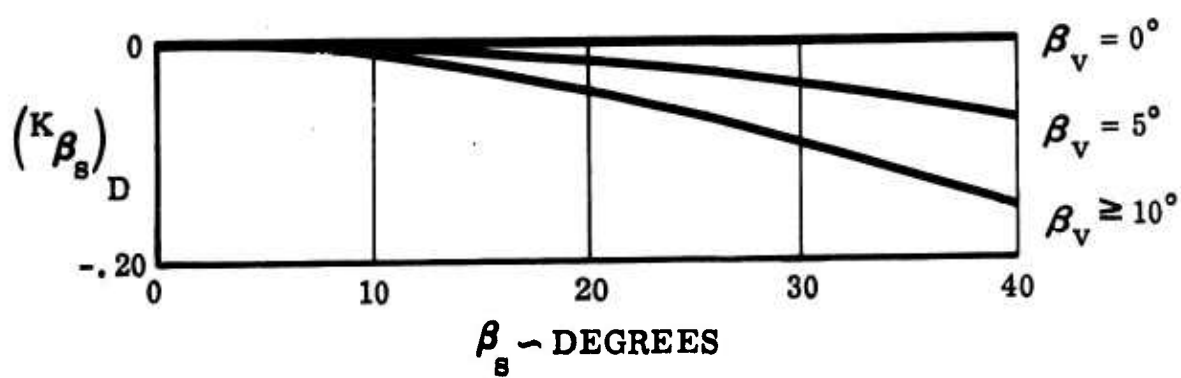
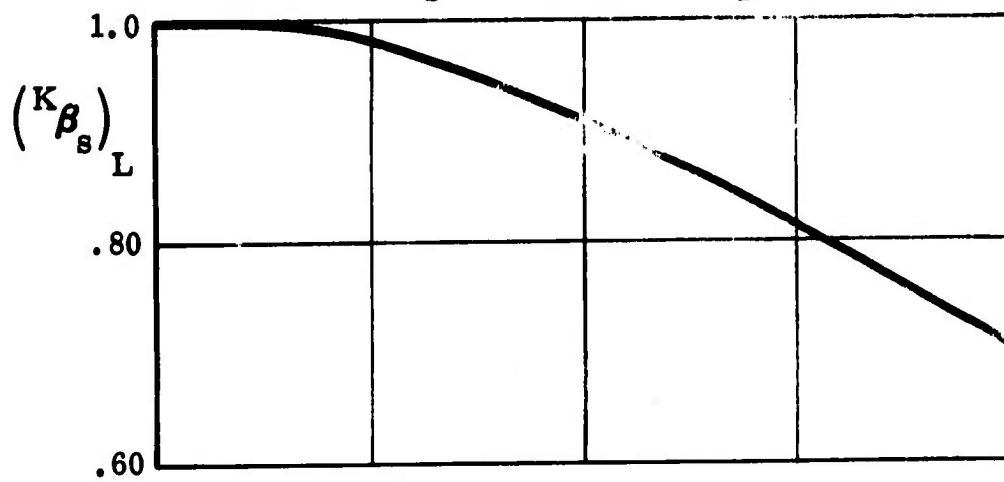


Figure 15 Lift and Drag Parameters for Stagger Effectiveness

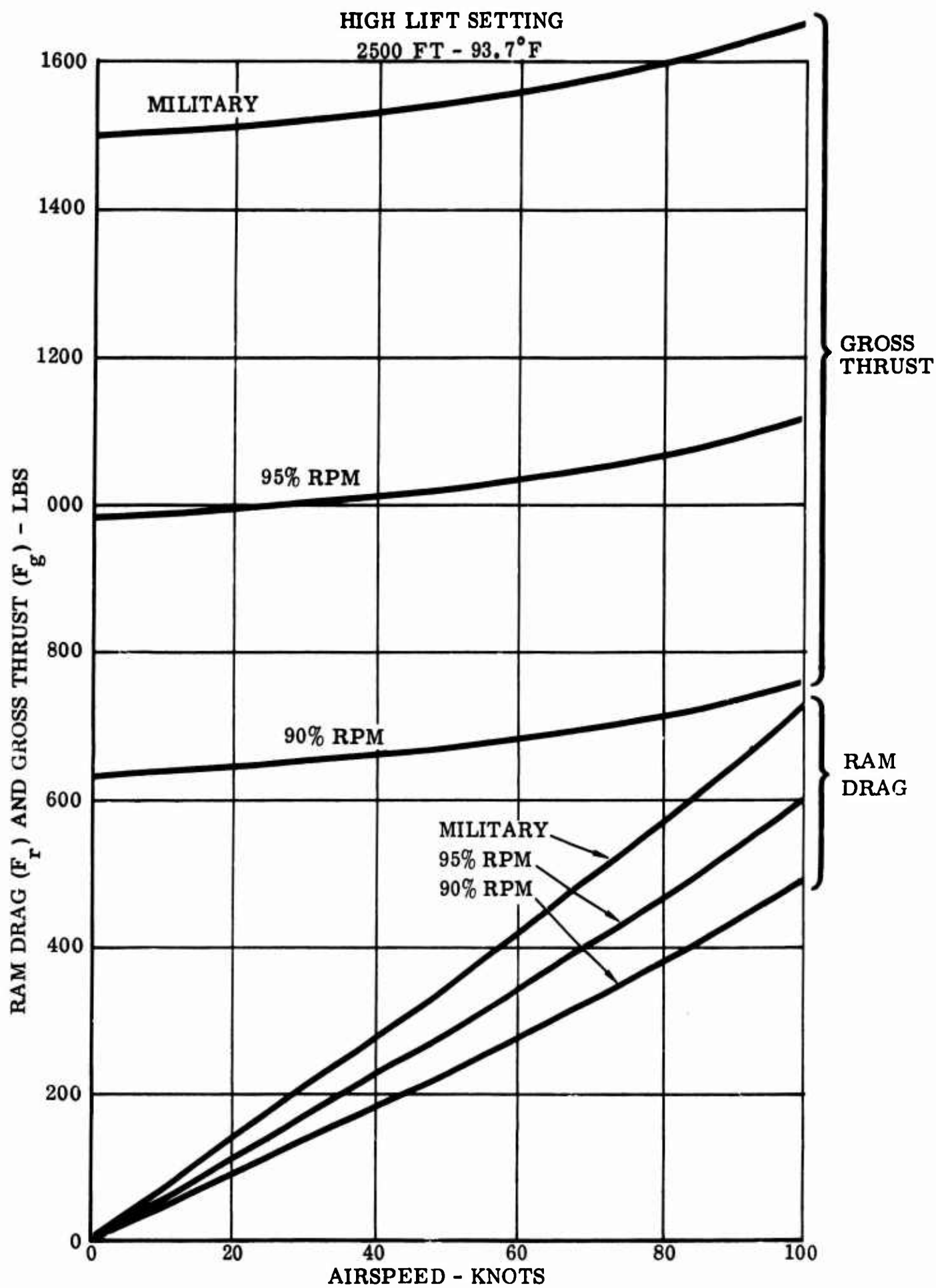


Figure 16 Estimated Pitch Fan Performance

CG AT FS 246, WL 112
 TAIL OFF, PITCH FAN OFF
 $\beta_v = 0^\circ$, $\beta_s = 0^\circ$, $\delta_f = 45^\circ$

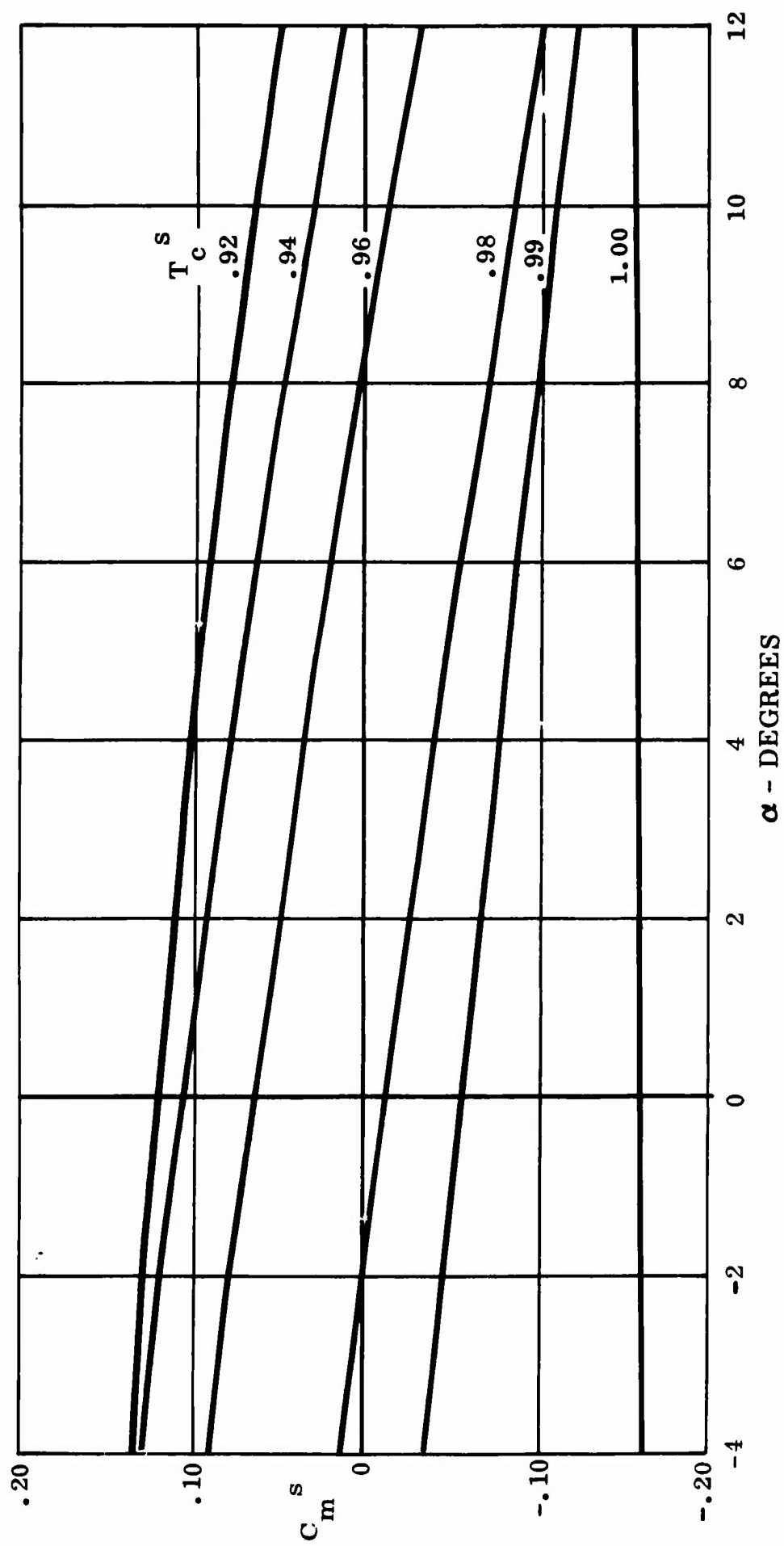


Figure 17 Estimated Moment Coefficient About C. G.

CG AT FS 246, WL 112
 TAIL OFF, PITCH FAN OFF
 $\beta_v = 0^\circ, \beta_s = 0^\circ, \delta_f = 45^\circ$

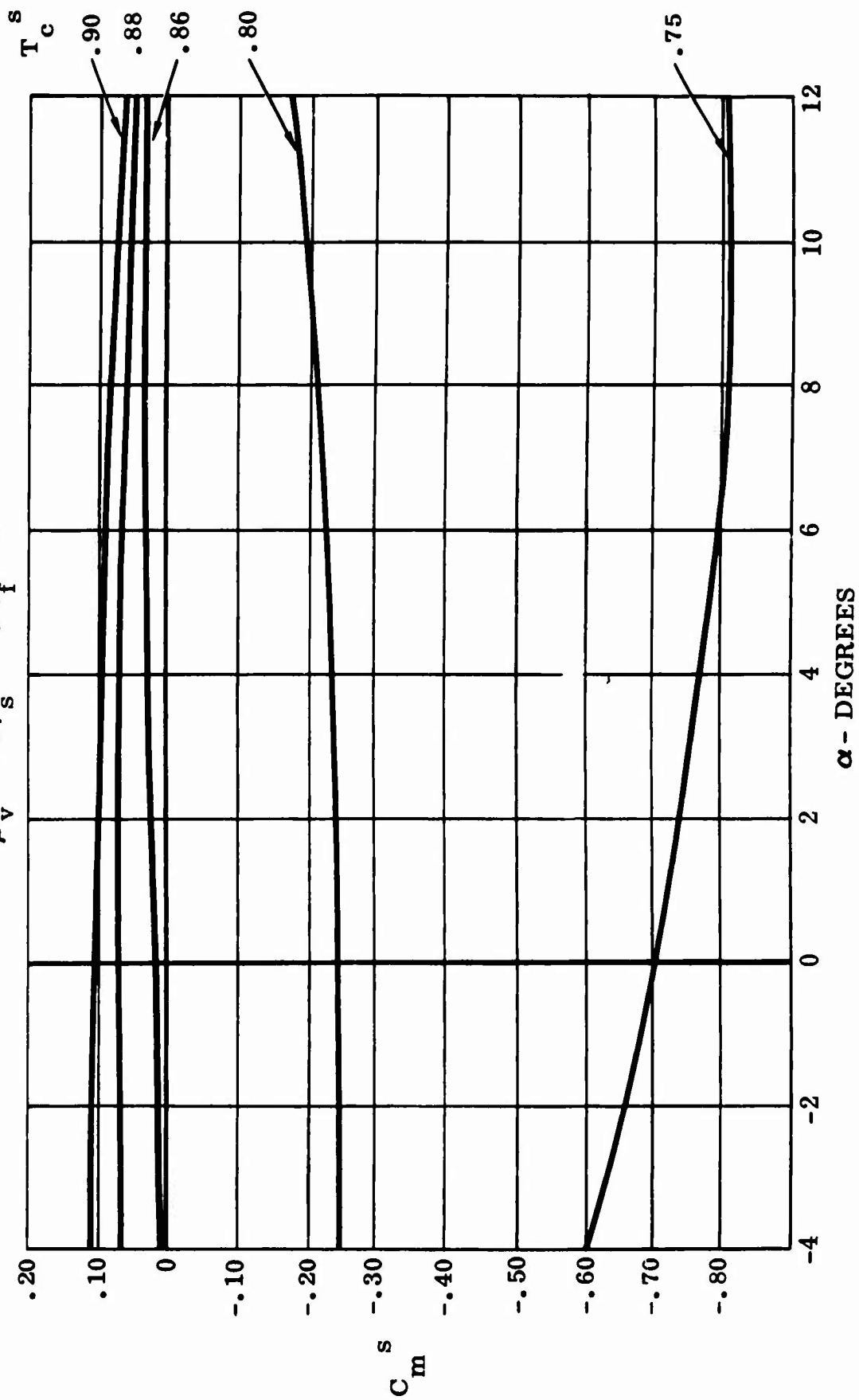


Figure 18 Estimated Moment Coefficient About C. G.

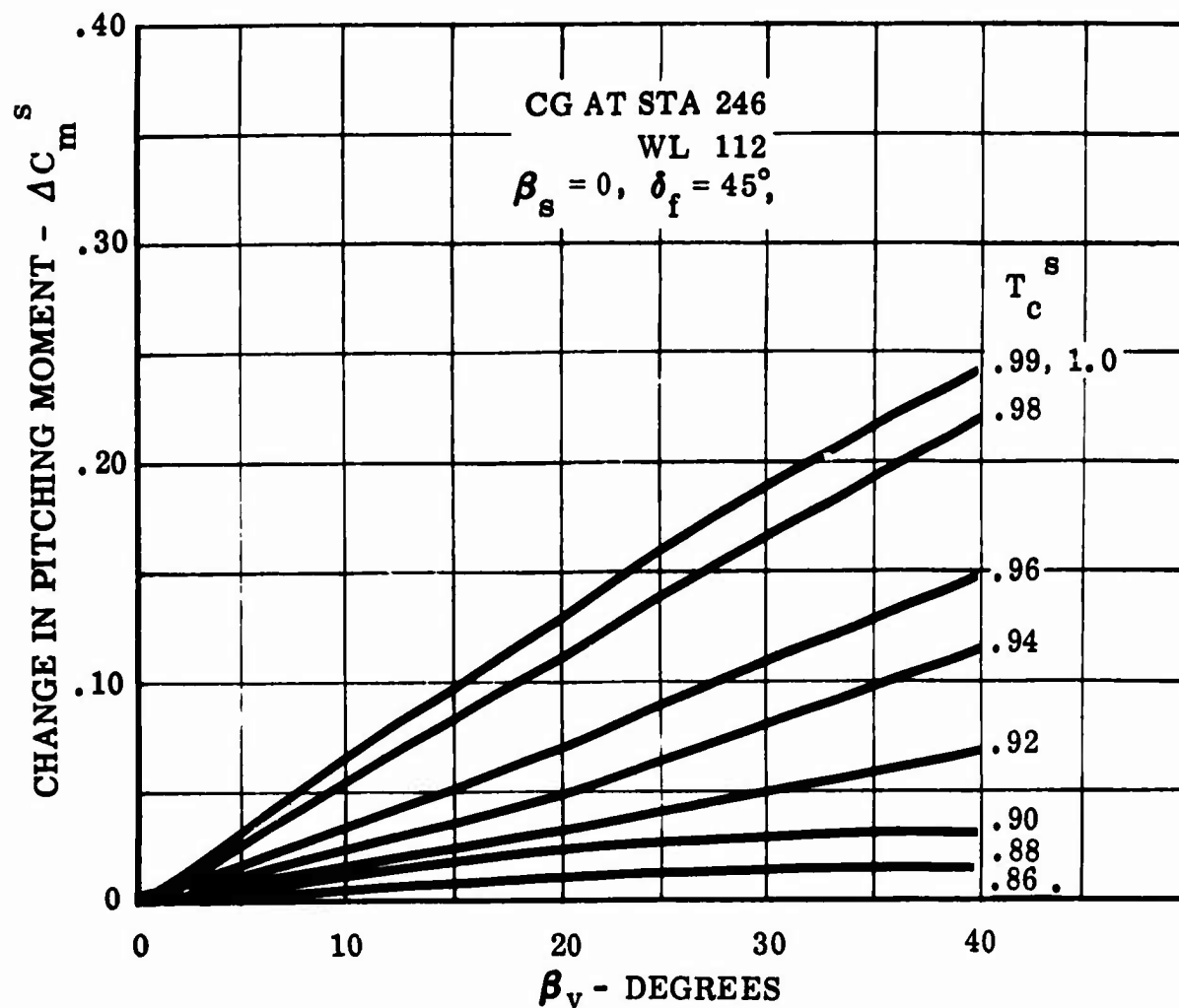


Figure 19 Effect of Exit Louver Vectoring on Pitching Moment

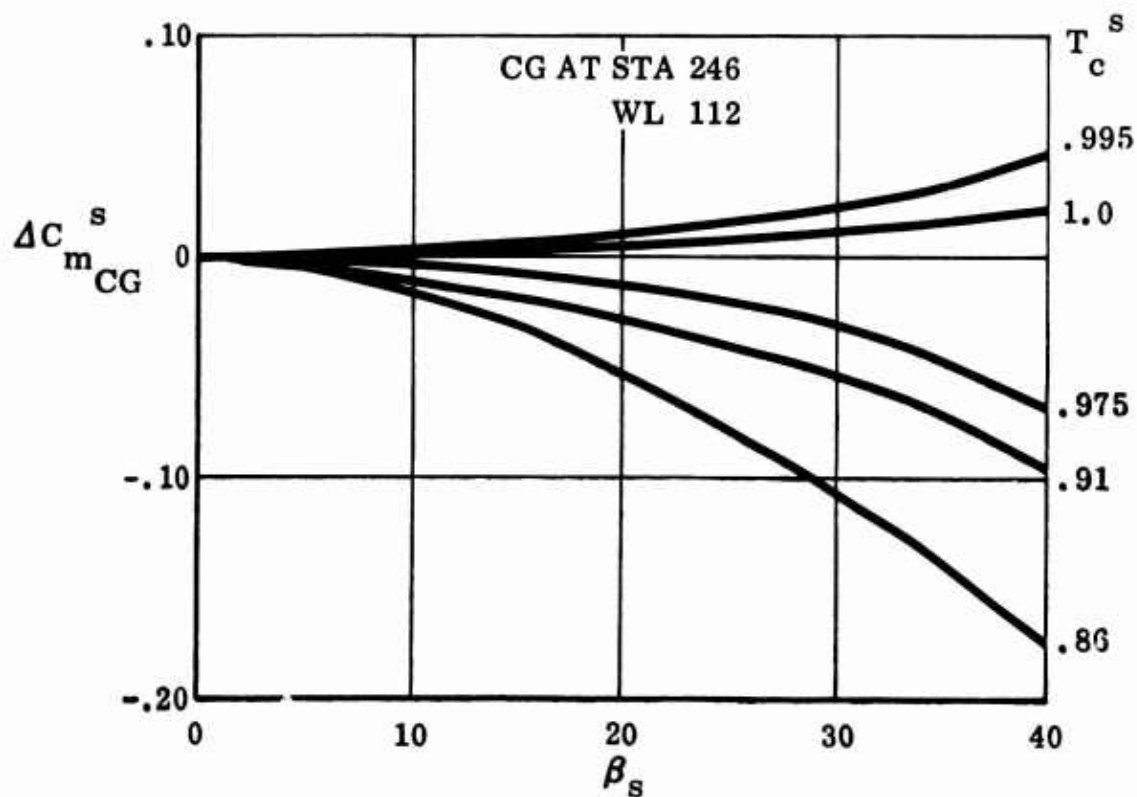


Figure 20 Effect of Stagger on Pitching Moment Coefficient

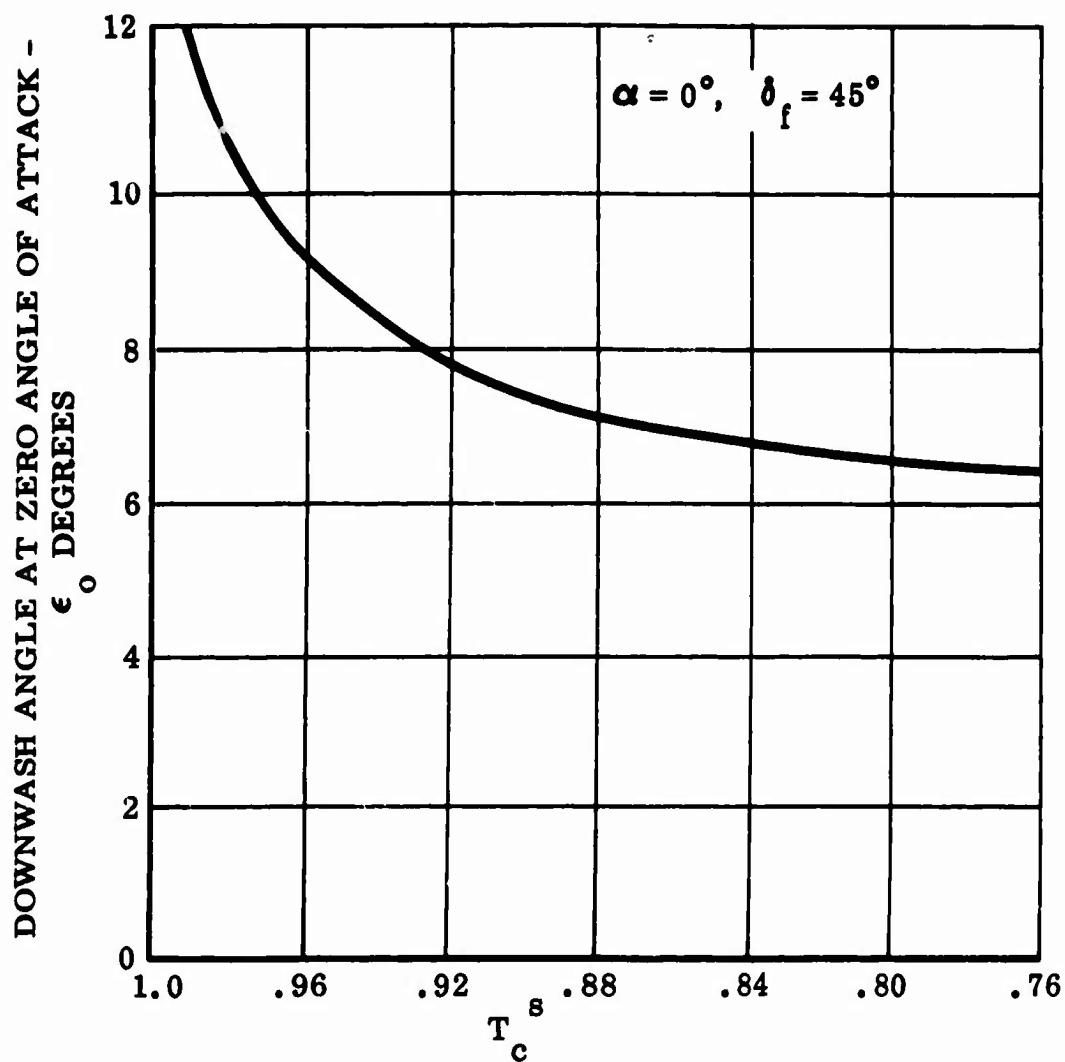


Figure 21 Estimated Downwash Angle at Horizontal Tail

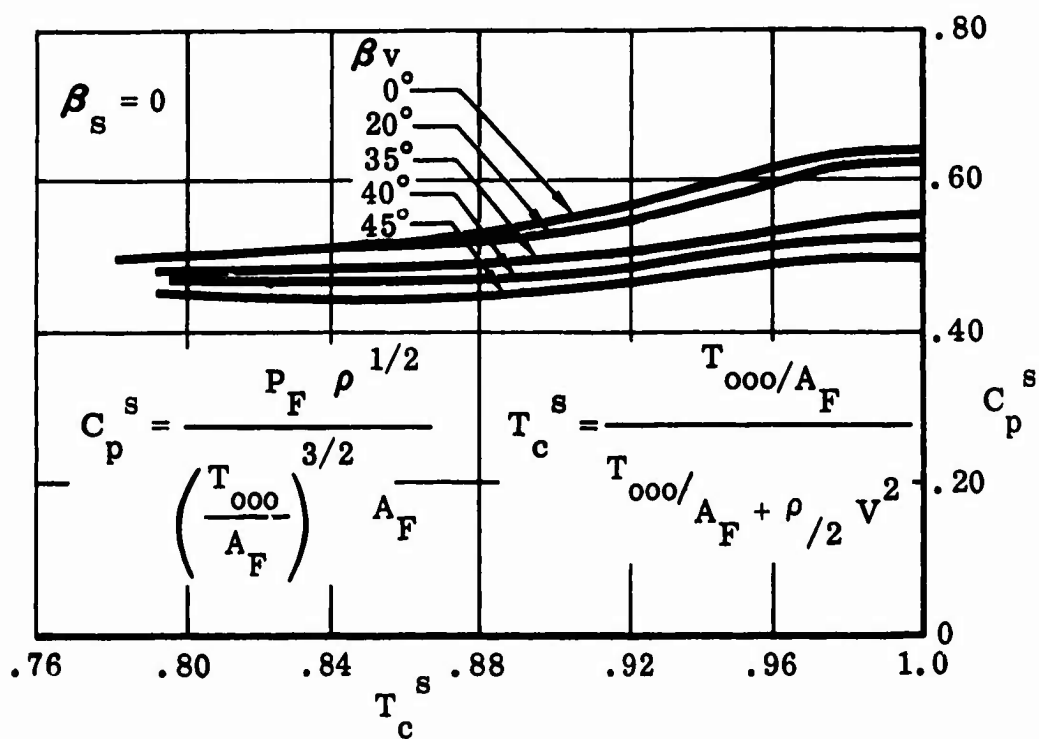


Figure 22 Fan Power Coefficient

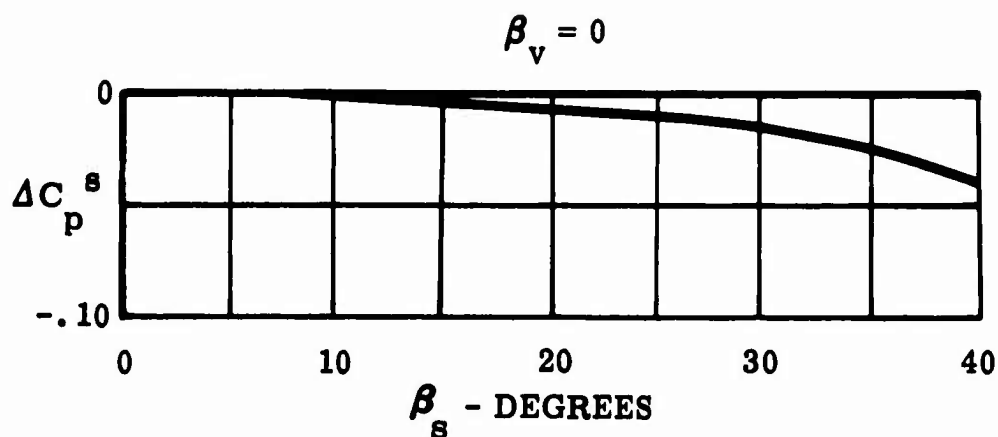


Figure 23 Incremental Change in Fan Power Coefficient Due to Stagger at Constant Power

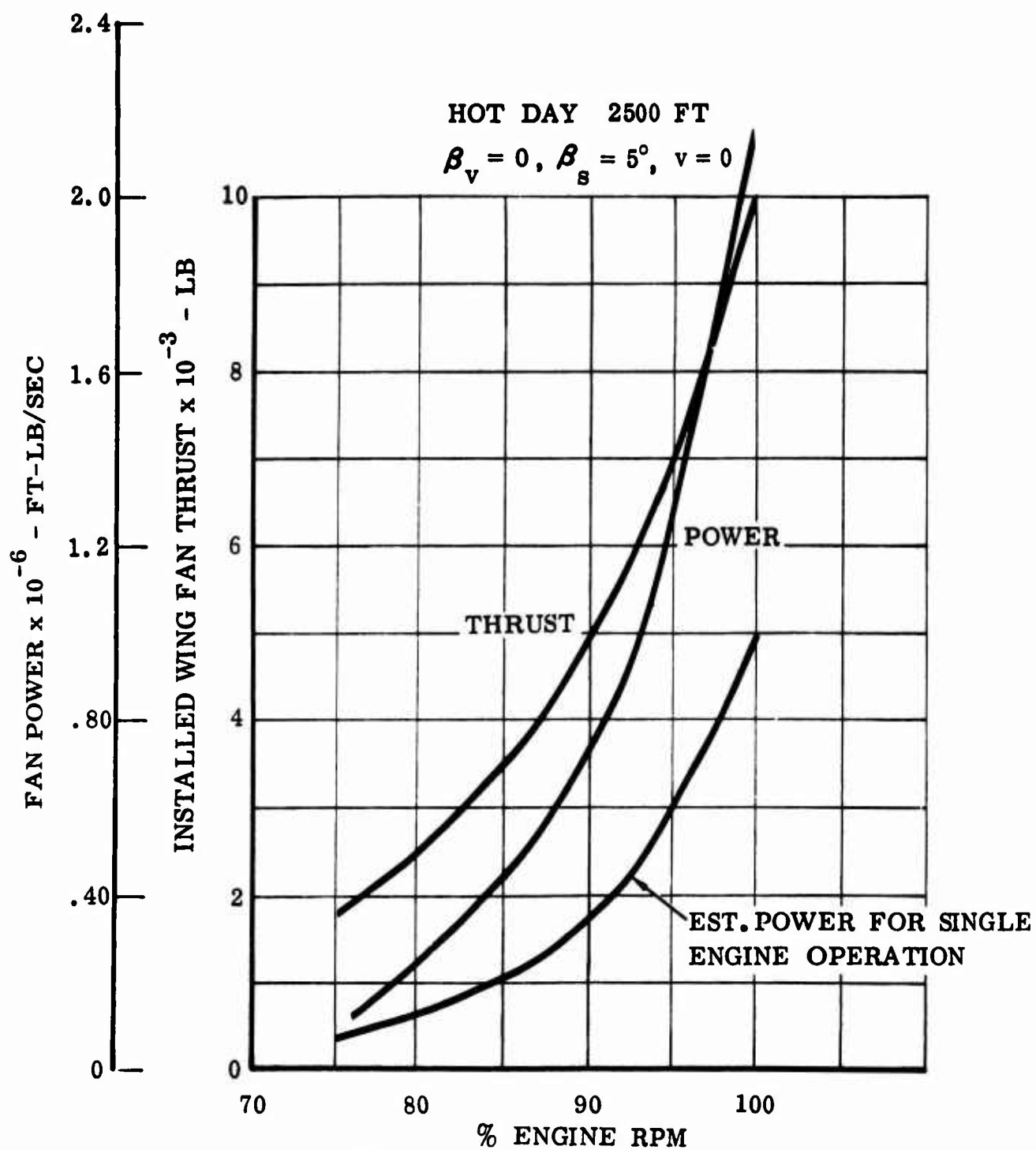


Figure 24 Variation of Wing-Fan Thrust and Power with Gas Generator RPM

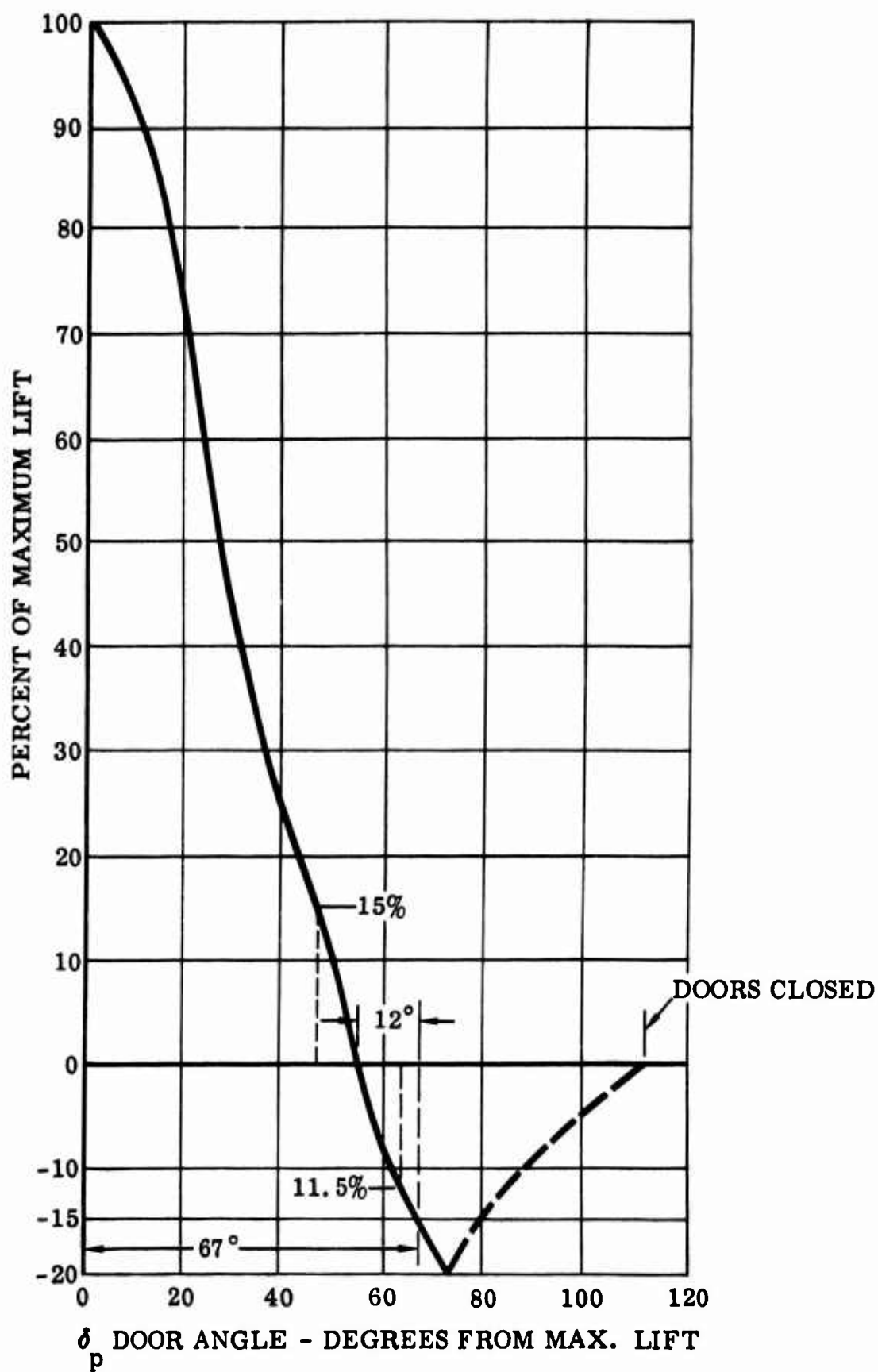


Figure 25 Estimated Performance for Pitch Fan Thrust Reverser-Static

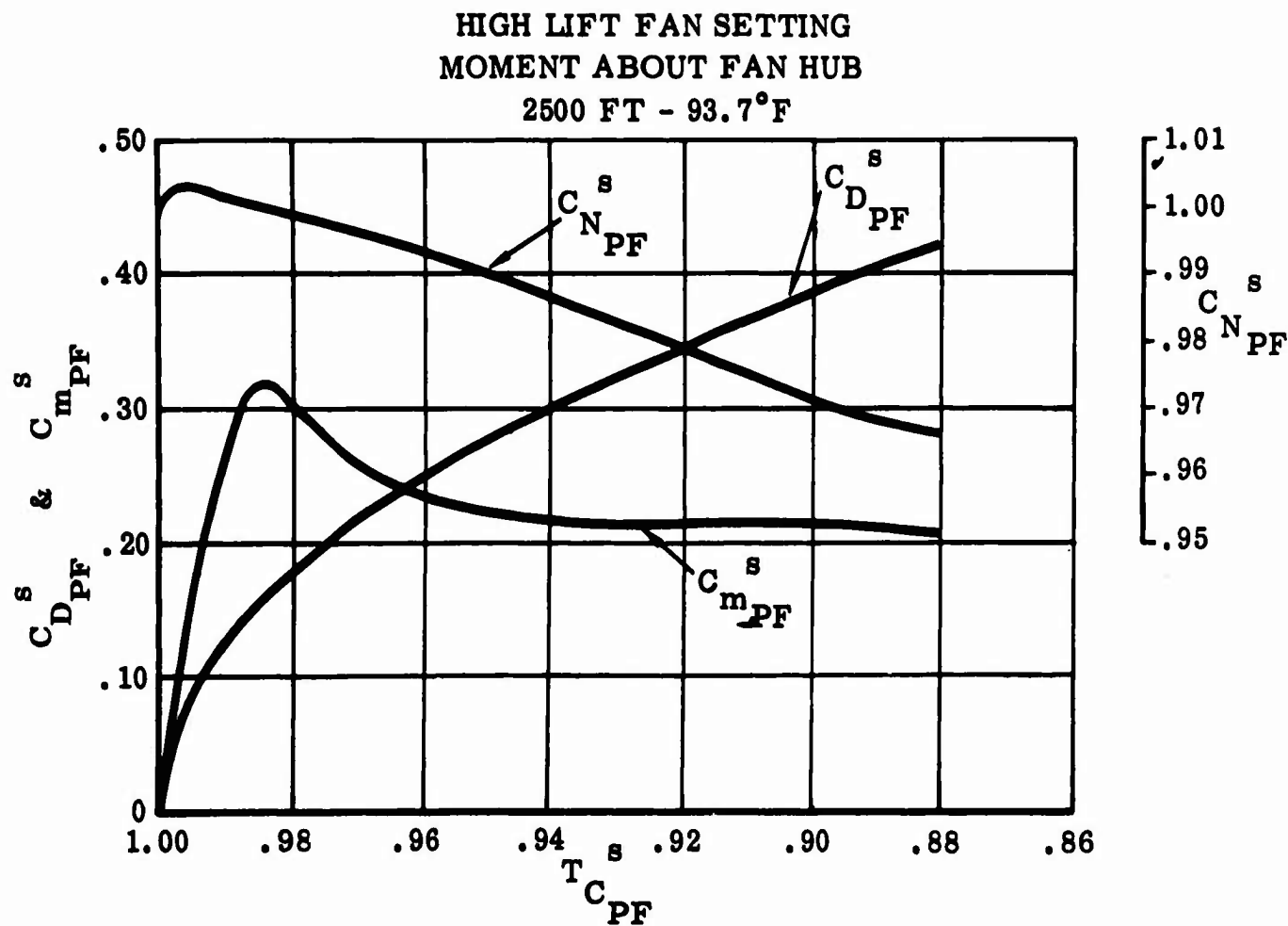


Figure 26 Estimated Pitch Fan Force and Moment Coefficients

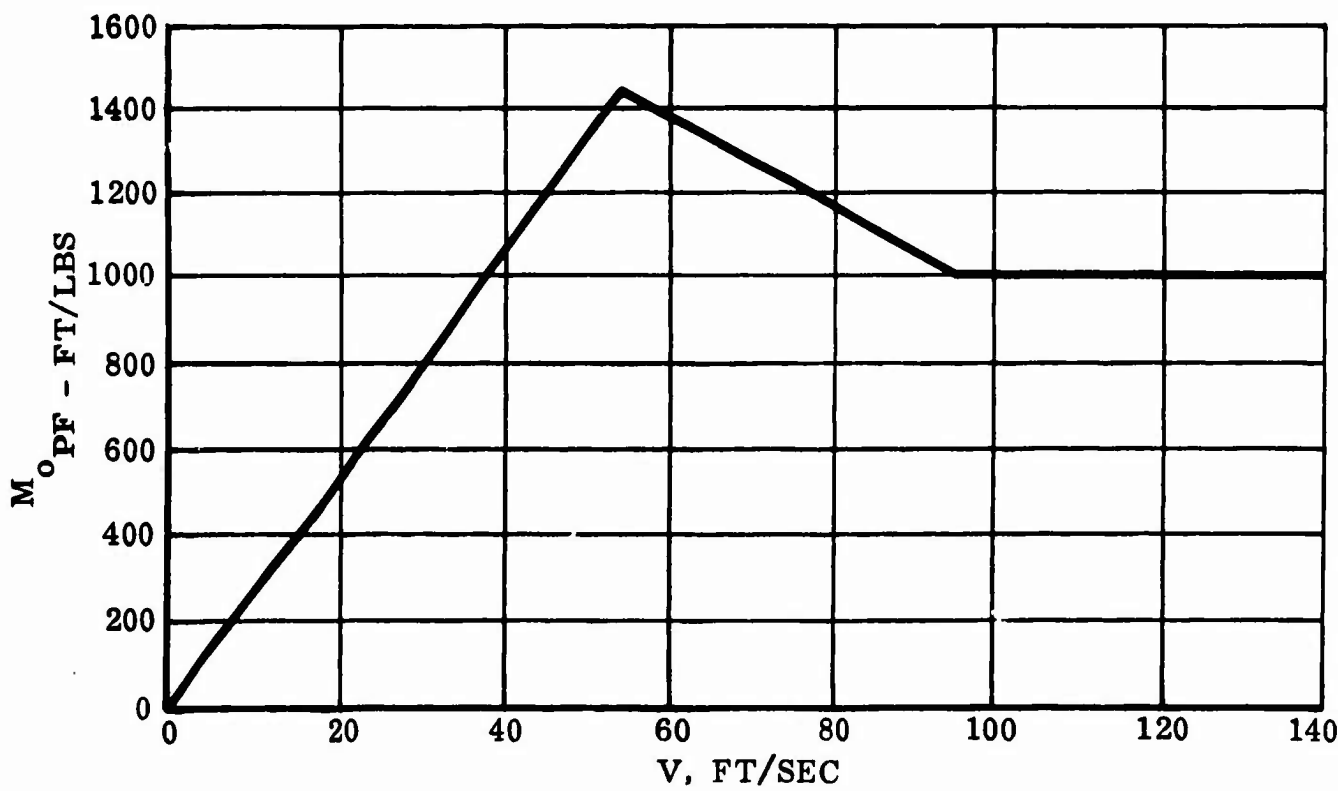


Figure 27 $F_1(V)$ vs Velocity

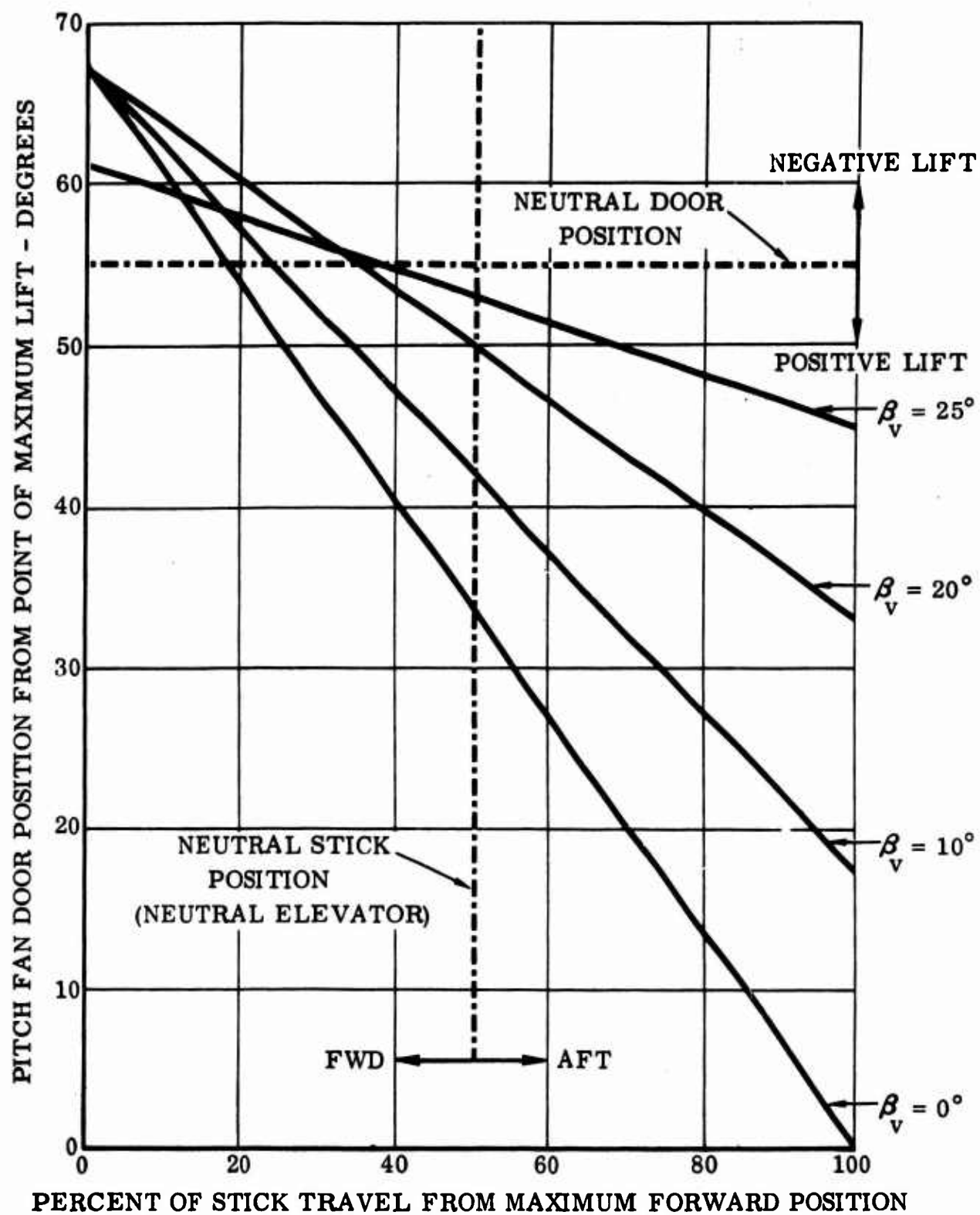


Figure 28 Stick Control vs Pitch Fan Door Position

2500 FT HOT DAY

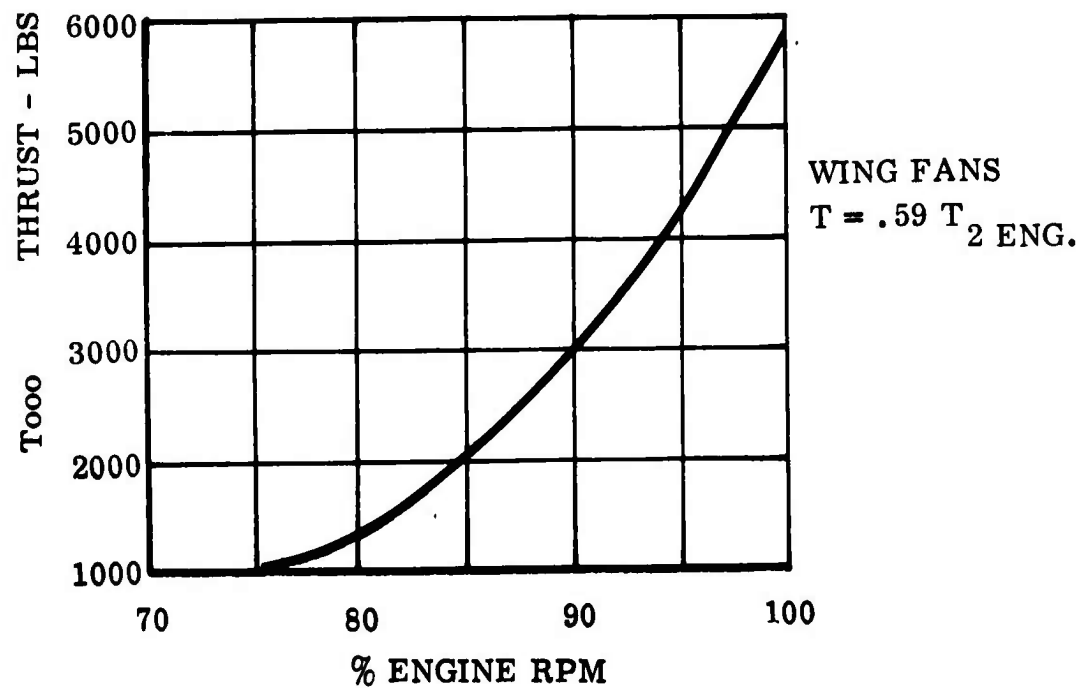
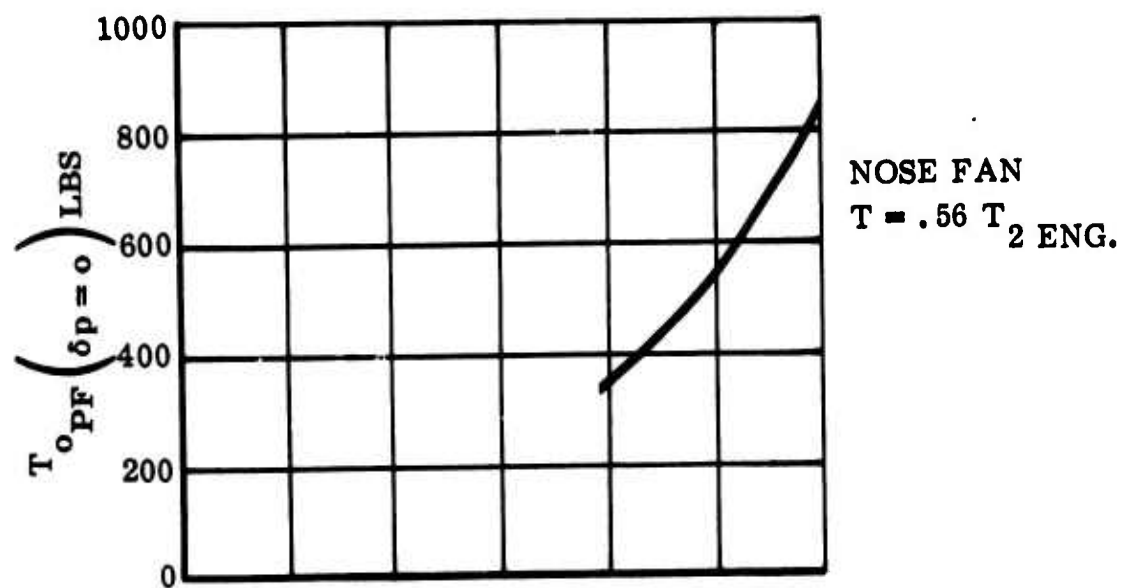


Figure 29 Estimated Wing and Nose Fan Thrust for Single Engine Operation

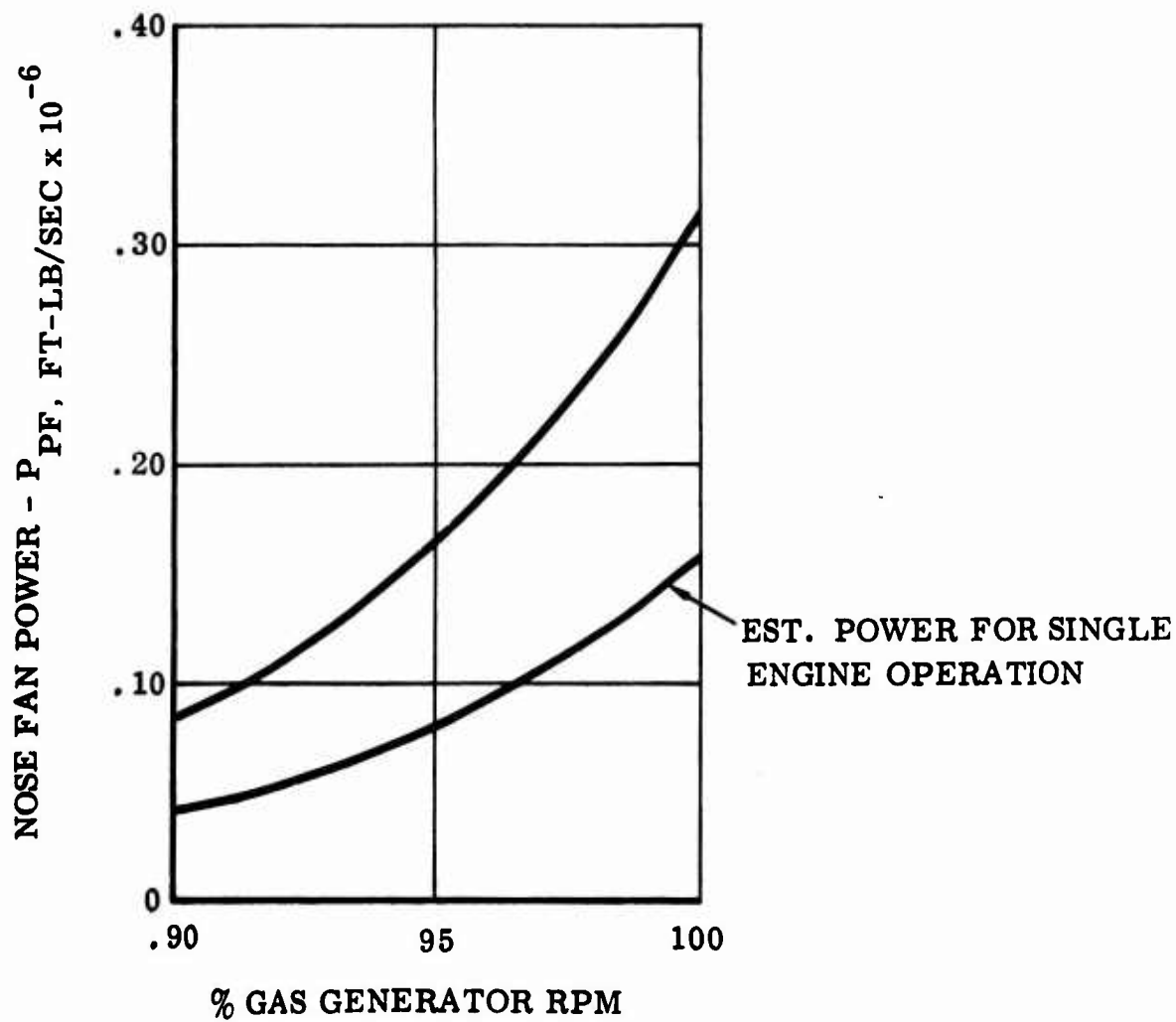
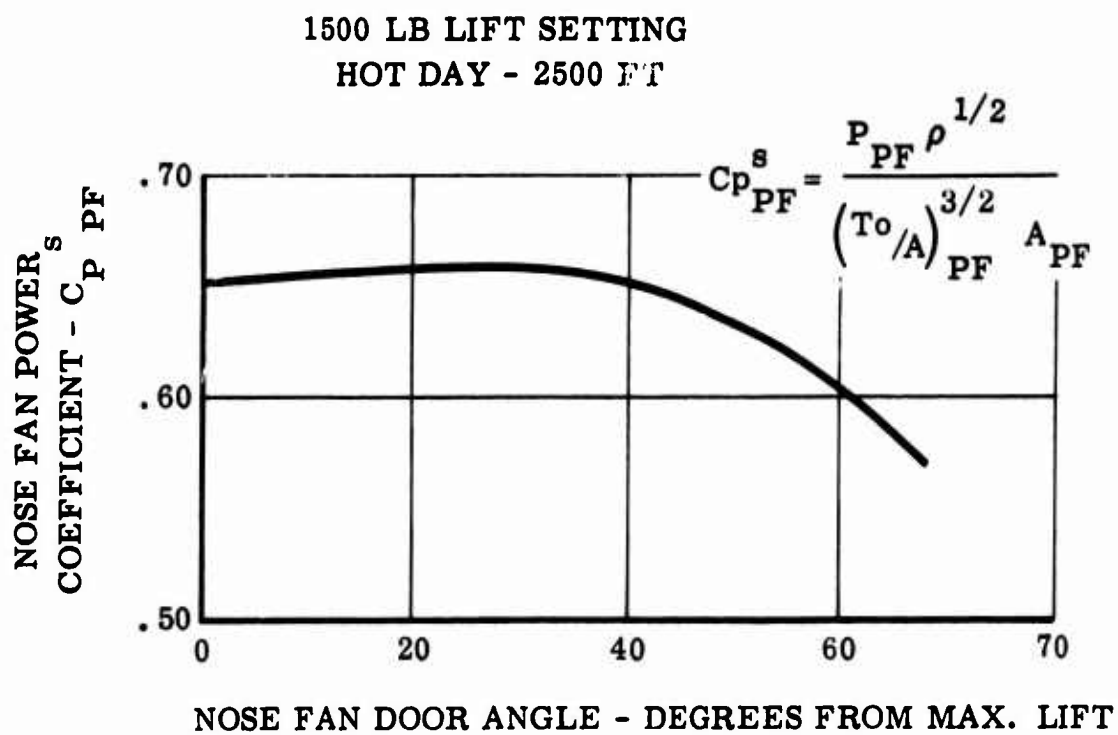


Figure 30 Nose Fan Power Characteristics

$$m(\ddot{u} + f_{ur}) = m\dot{q}_r + \Sigma F_r$$

$$m(\dot{u} - q_u) = m\dot{q}_z + \Sigma F_z$$

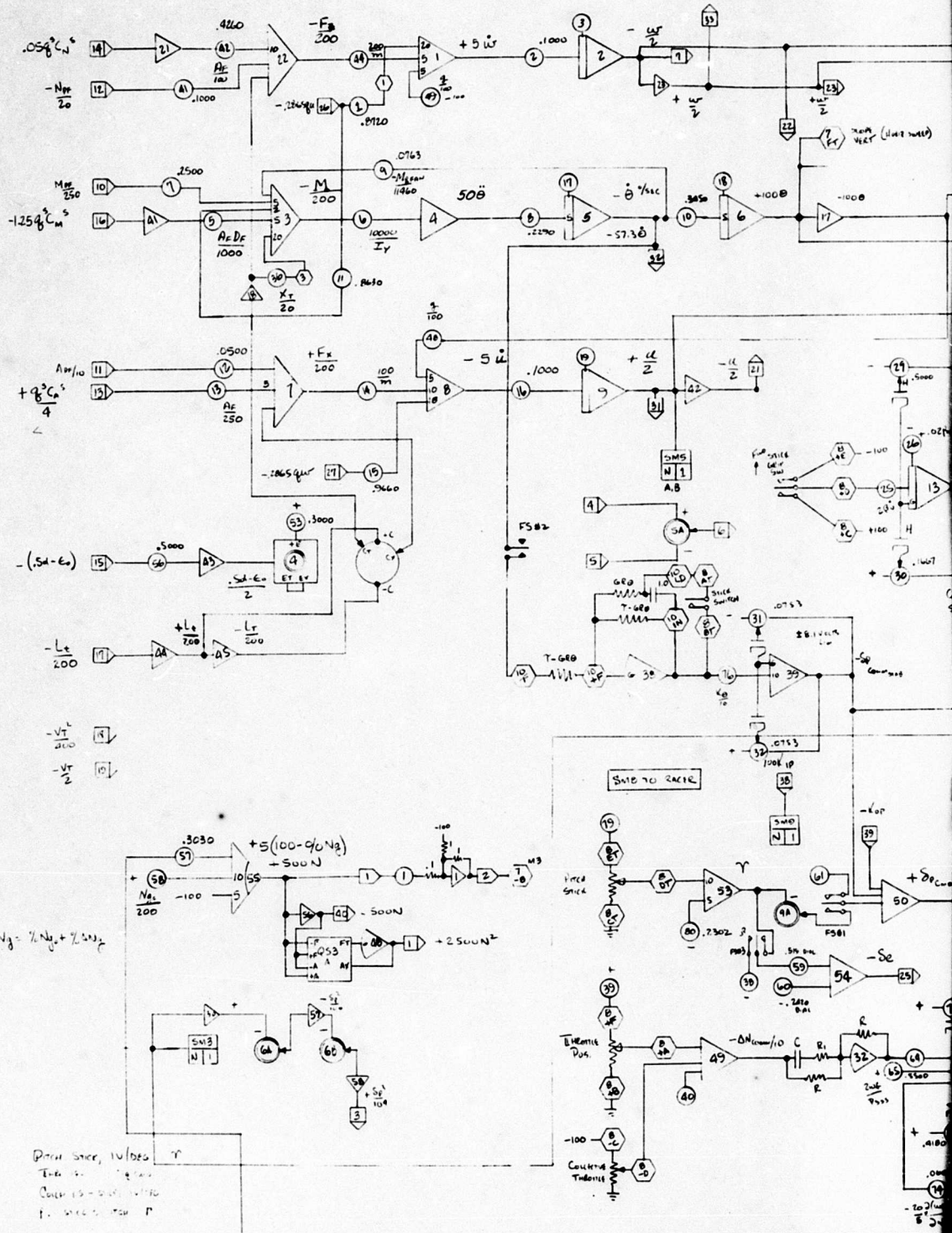
$$I \ddot{\theta} = \Sigma M$$

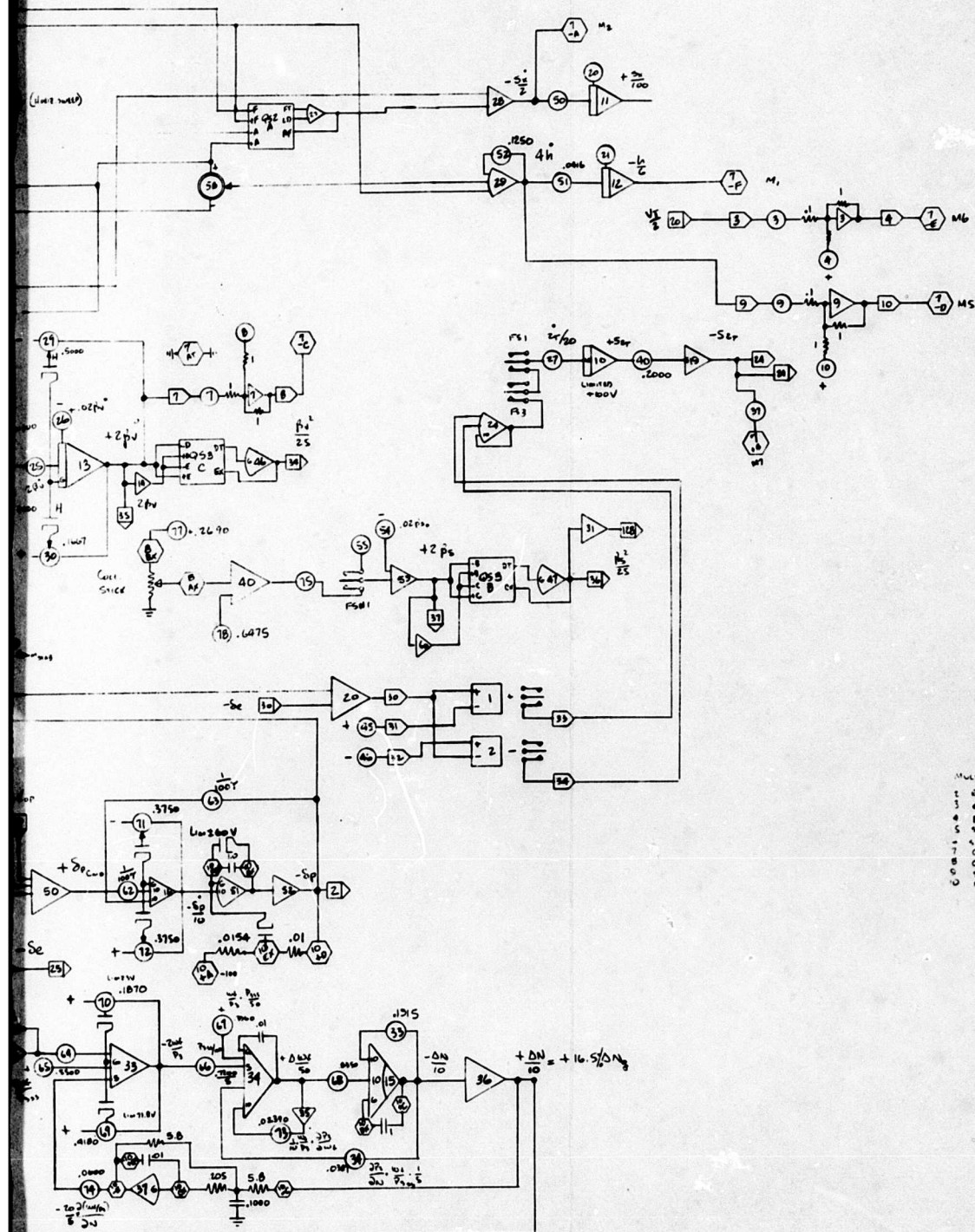
$$q_r = -g \sin \theta$$

$$q_z = g \cos \theta$$

$$F_{\text{on Damper}} = -B \dot{u}$$

$$M_p \text{ TACO-99U}$$



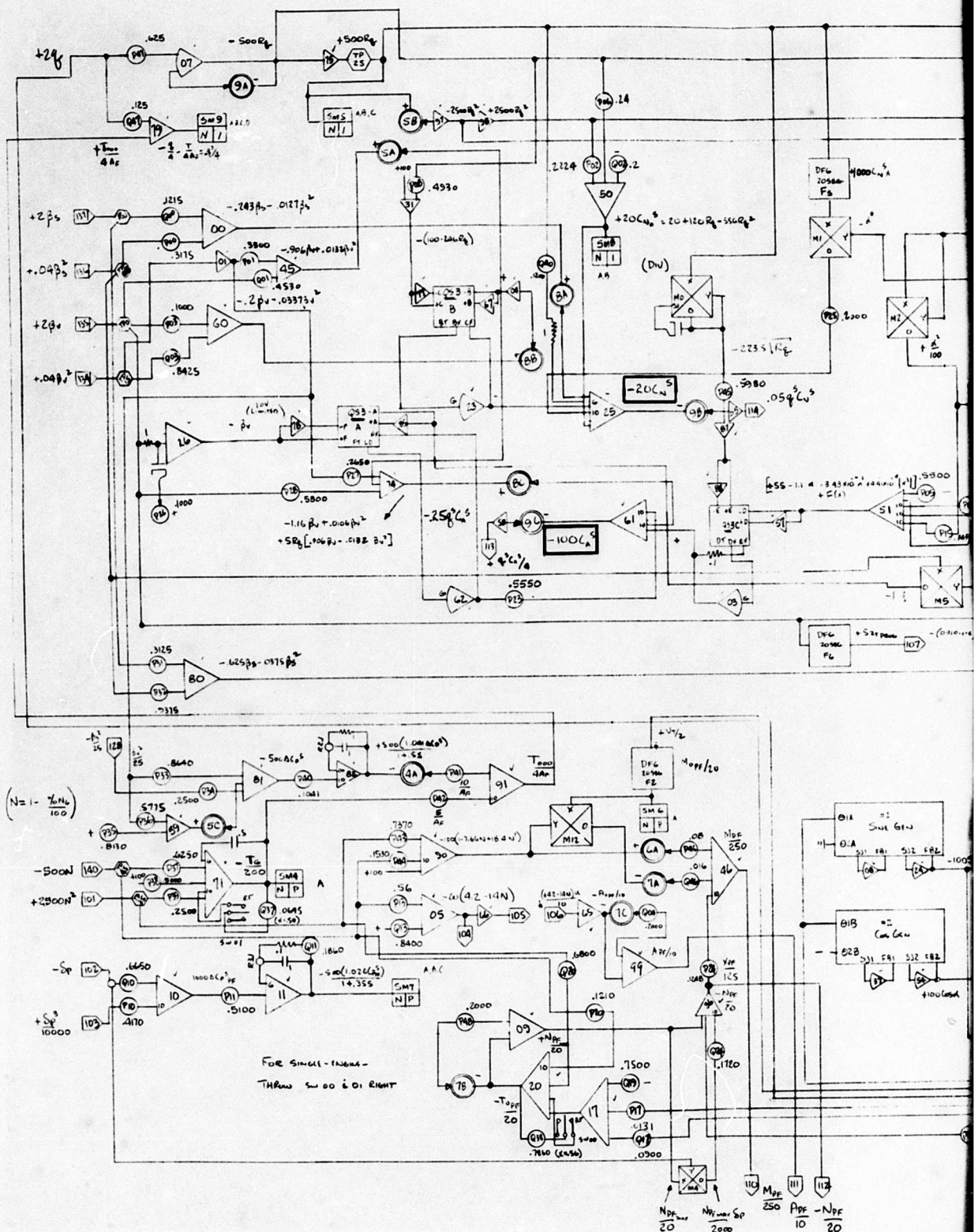


MULT

2	25000
3	45
4	8000
5	9000
6	9000
7	Current
8	Current
9	9000
10	Normal

Figure 31 Computer Diagram, 3° Long Transition

B



A

BLANK PAGE

4.0 LONGITUDINAL THREE DEGREE-OF-FREEDOM CONVERSION SIMULATION

4.1 Discussion

The simulation of the conversion between fan-powered and conventional flight was utilized for several purposes. These were:

1. To provide a check on previously calculated maximum fan-powered flight speed.
2. To determine requirements of tail incidence variation during conversion sequence.
3. To develop conversion sequence to provide smallest transients at conversion.
4. To evaluate handling qualities and piloting techniques before, during, and after the conversion, (below power off stall speed.)
5. To evaluate conversion using one J-85 in jet mode and one in fan mode.

This entire study was conducted using $\beta_v = 50^\circ$, $\delta_f = 45^\circ$, except that later runs were made using the additional 15° aileron droop.

The method of approach to the simulation of the conversion aerodynamic effects deserves mention.

The problem of generating forces and moments during the conversion effectively amounts to the simulation of two separate airplanes. This is further complicated by the fact that during fan door closure the characteristics are for neither of the two configurations.

We have data for pure fan-powered flight, and also data for conventional flight with fan closure doors open and closed. We also have fan run-up and run-down data, plotted versus time from diverter actuation.

The problem is thus presented to determine how to determine the force and moment characteristic at conditions intermediate to the fan-powered and conventional flight regime.

As in previous work, the aerodynamic data was separated into conventional data plus "fan caused" effects. To enable this, the fan doors open-fans off data for lift, drag and moment was converted to slip-stream notation, and subtracted from the fans on data. The difference thus obtained was plotted as a function of T_c^S and angle of attack. These differences were then the net effects of having fan power applied to the aircraft. As fan power was reduced, the differences should then fade gradually away until the conventional flight-fan doors open data remains. In the case of the fan to conventional conversion, it was assumed that during the fan run-down and door closing, there would be practically no effect on fan thrust until the doors were almost closed. At the time the doors closed fan RPM would be down to 40 per cent, and all fan effects would be switched off.

There is another problem concerning the conventional flight doors open and doors closed data. There was no intermediate closure door position data. The closure doors closed data was subtracted from the closure doors open data to obtain increments due to the doors. As the doors went from closed to open, and vice-versa, the increments were added in proportion to the percent of door motion from the original position. These increments are relatively small, and the manner of phasing them in and out did not seem to be critical. Due to more recent fan time response data, the rate of door closure after diverter valve actuation was slowed.

The first use of the longitudinal conversion simulation was to check the previously calculated maximum level fan-powered flight speed attainable. Previous rough calculations had indicated the aircraft would trim at 109 knots, but when the computer was turned on, the vehicle slowed down. The addition of the J-85 ram drag aggravated the situation, and for these reasons the new wind-tunnel data for $45^\circ \delta_f$ and drooped ailerons was taken. In addition, data was made available for lower flight speeds (higher T_c^S).

At about this time it was determined that the $C_{D_0}^S$ values obtained on the 1/6 scale fan-powered model were higher than those obtained on the full scale tests, so a $\Delta C_{D_0}^S$ correction was included, derived from comparison of full-scale model test results with the small-scale data. The drag increment due to the landing gear was also evaluated so that the wheels-up and wheels-down trim speeds could be determined.

Before the $\Delta C_{D_0}^s$ increment was included, data was taken from the computer to enable determination of trim speeds. For this purpose, the J-85 RPM was set at 100%, and the lift and pitching moment were trimmed, both wheels-up and wheels-down, for various velocities. The resulting net horizontal force was plotted versus velocity. These curves are shown in Figure 33. The second set of data was taken at 100% J-85 RPM, but with one J-85 in the fan mode and one in the turbojet mode, for wheels-up and wheels-down. A large increase in trim forward speed is noted. This data is presented in Figure 34.

The third set of data have the $\Delta C_{D_0}^s$ correction included, and curves are presented for both wheels-up and wheels-down flight in Figure 35.

For all of the above curves, the J-85 ram drag was taken as $6.25 V_T$. This is the J-85 mass-flow rate at 2500 foot, hot day, vel. ≈ 200 fps, multiplied times the velocity. This value is conservative, since some of this drag is recovered as the J-85 exhaust is directed rearward by the vanes.

To determine the requirements on horizontal tail incidence during conversion, a high-gain autopilot loop was connected around the pitch axis so that the net pitching moment would be zero during the conversion.

All of these automatic conversions showed that an essentially constant tail rate was required as the butterfly doors cycled through their range.

After it had been determined that a constant tail rate during conversion was feasible, pilot controlled conversions using various conversion sequences were performed.

4.2 Development of Conversion Sequence

After it had been determined that a constant tail rate was acceptable during the conversion, there remained only to choose a sequence of events which would cause the least conversion transient.

It is interesting to note that the vehicle gains about 20 fps in velocity during the conversion sequence. This enables conversions from fan to conventional to be started below the stall speed.

The following conditions were obtained prior to conversion for evaluation of the conversion sequencing:-

<u>Prior to Conversion to Fan Mode</u>	<u>Prior to Conversion to Conventional Mode</u>
1. Flaps down full (45°), aileron drooped.	1. Flaps down full, ailerons drooped.
2. Landing gear down.	2. Landing gear up.
3. $\beta_v = 50^\circ$	3. $\beta_v = 50^\circ$.
4. Nose fan inlet and exit open.	4. Nose fan inlet and exit open.
5. Thrust spoilers out.	5. Thrust spoilers retracted.
6. 100% N_g .	6. $N_g = 100\%$.
7. $V_{trim} = 203$ fps EAS	7. $V_{trim} = 170$ fps EAS

The objective was to find a conversion sequence which would cause the least transient and result in the minimum amount of pilot effort.

During the fan to conventional conversion, the aircraft must change attitude from a slightly negative angle of attack up to about a ten degree positive angle of attack. In the conventional to fan conversion, the rotation will be less because the vehicle is at a smaller initial angle of attack due to higher speed. The sequences picked result in a practically hands-off conversion, and changes from the desired flight conditions only require small pilot corrections.

The desired conversion sequences were determined to be as follows:

<u>Function</u>	<u>Conv. to Fan</u>	<u>Fan to Conv.</u>
1. Diverter valve delay time.	.8 Sec.	0
2. Diverter Valve Actuation time.	.4 Sec.	.4 Sec.
3. Fan door delay time.	0	.4 Sec.
4. Horiz. Stab. Delay Time.	.5 Sec.	0

(Continued)

5. Fan door actuation time.	1.5 Sec.	3.0 Sec.
6. Horiz. Stab. actuation rate.	7.5°/Sec.	7.5°/Sec.
7. Final Horiz. Stab. position.	+8°	-5°
8. Horiz. Stab. travel	12.6°	16.6°

In general the conversion was easily accomplished as long as the horizontal tail moved in the correct direction, but as the tail sequence departed from the optimum, more pilot control was required.

The conversion from fan to conventional flight was also evaluated at an initial velocity below the power-off stall speed. This conversion is practical because during the 3 seconds of the conversion sequence, the unspoiled J-85 thrust results in an average acceleration of about 10ft/sec², for a velocity gain of 30 fps or 17.75 knots.

Care must be taken, however, because too large an angle of attack can result in sufficient drag to result in no velocity increase.

Figure 36 is a recording of several variables during a nominal fan-conv. conversion (both hands-off and pilot-controlled).

Figure 37 is a recording of a nominal conv.-fan conversion.

Figure 38 and 39 - Single-engine-piloted - both ways.

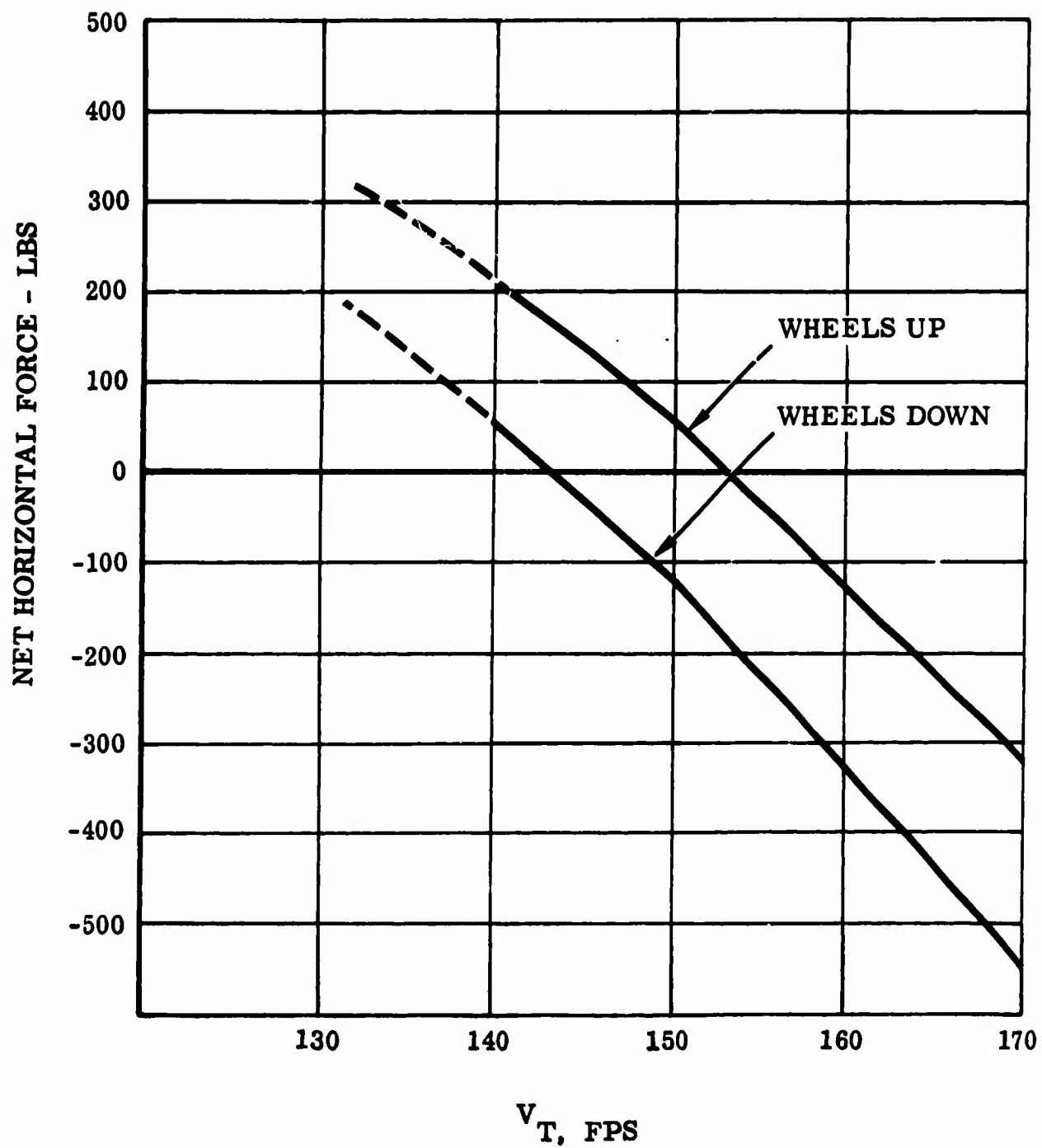


Figure 33 *Net Horizontal Force with Trim Lift and Moment vs Velocity for Both Engines in Fan Mode*

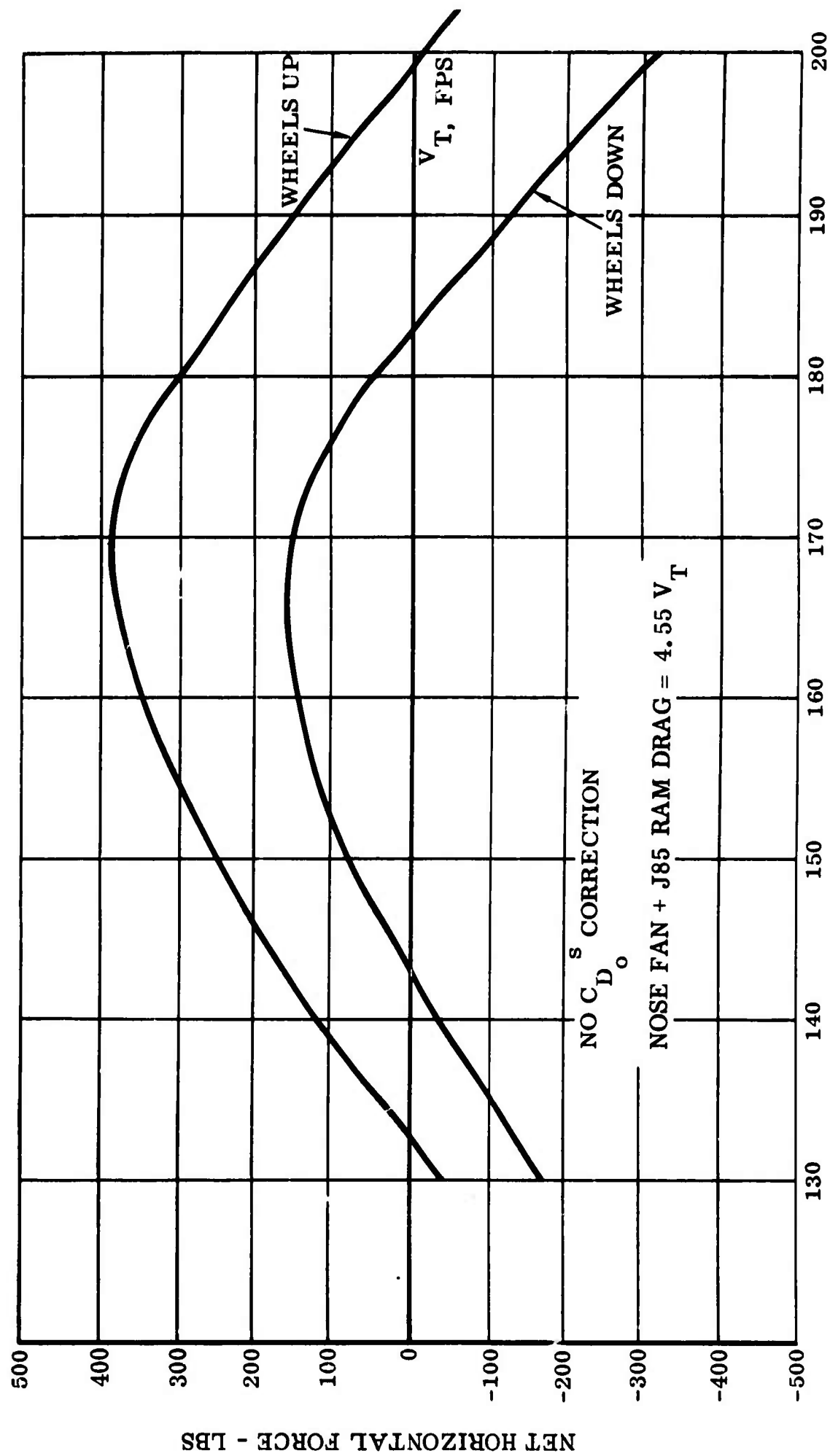


Figure 34 Net Horiz. Force With Trim Lift & Moment Vers. Velocity For One Engine in Turbojet Mode & One Engine in Fan Mode.

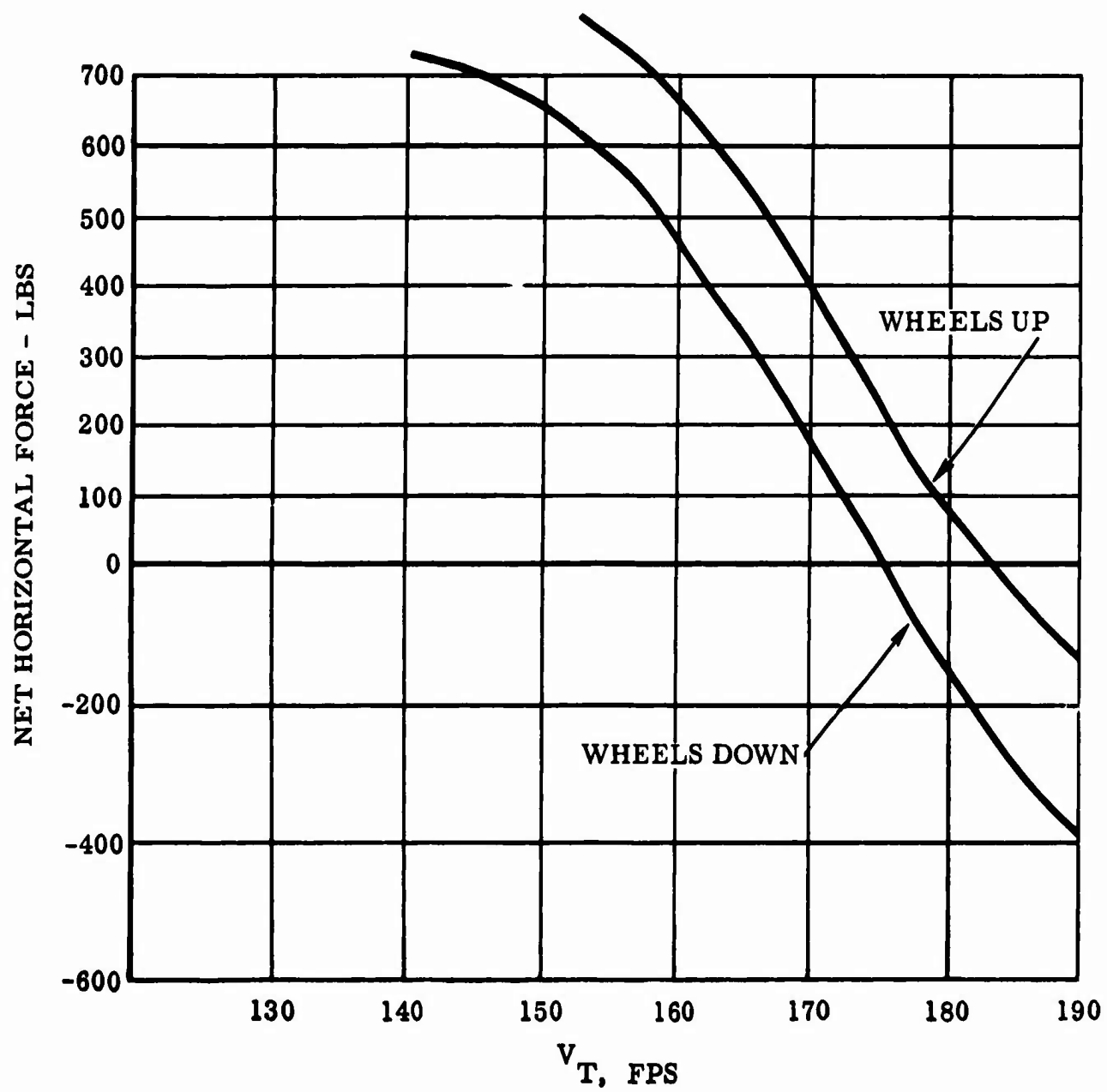


Figure 35 Net Horizontal Force with Trim Lift and Moment vs Velocity for Both Engines in Fan Mode

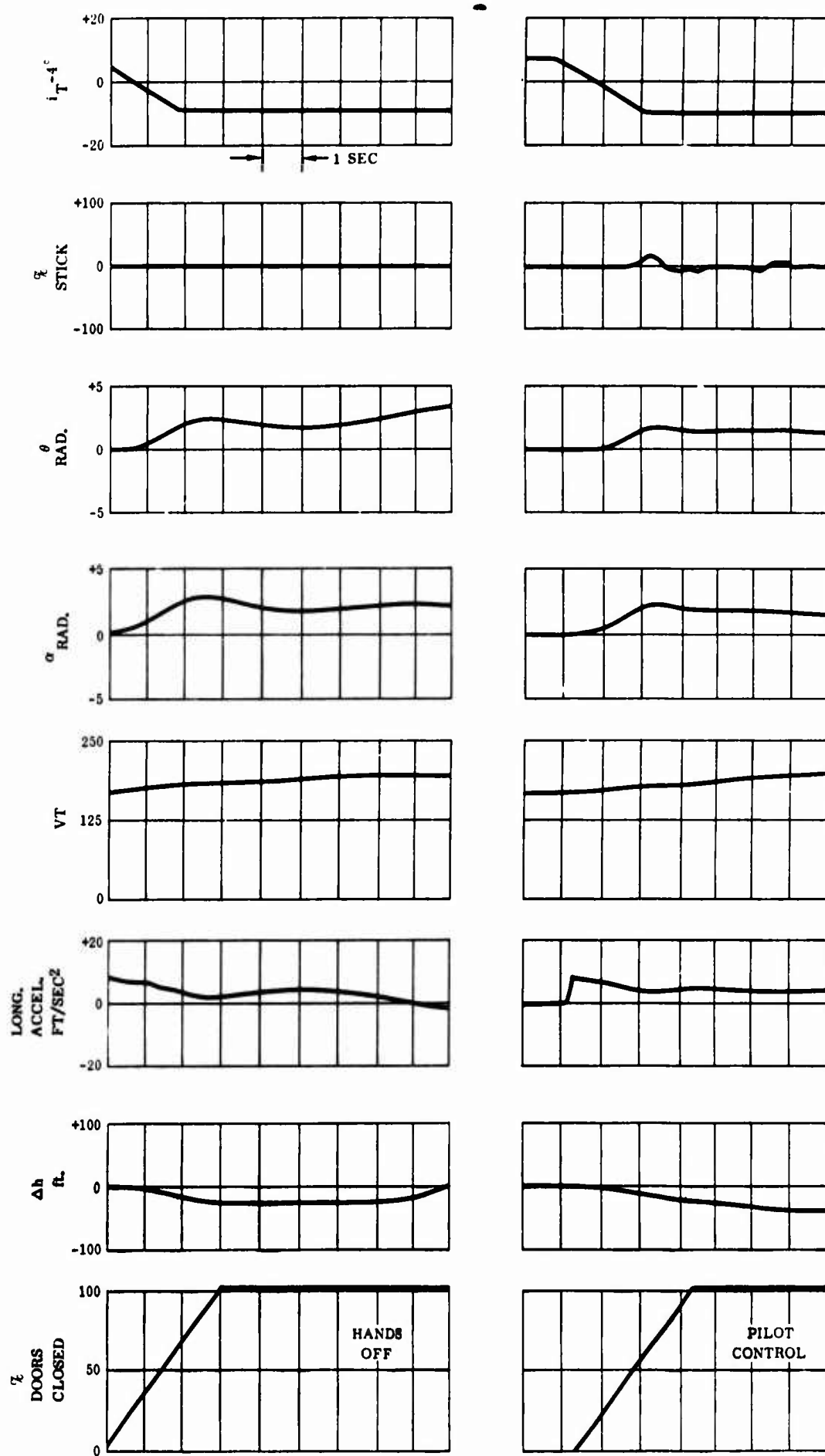


Figure 36 Nominal Fan to Conventional Conversion with and without Pilot Control

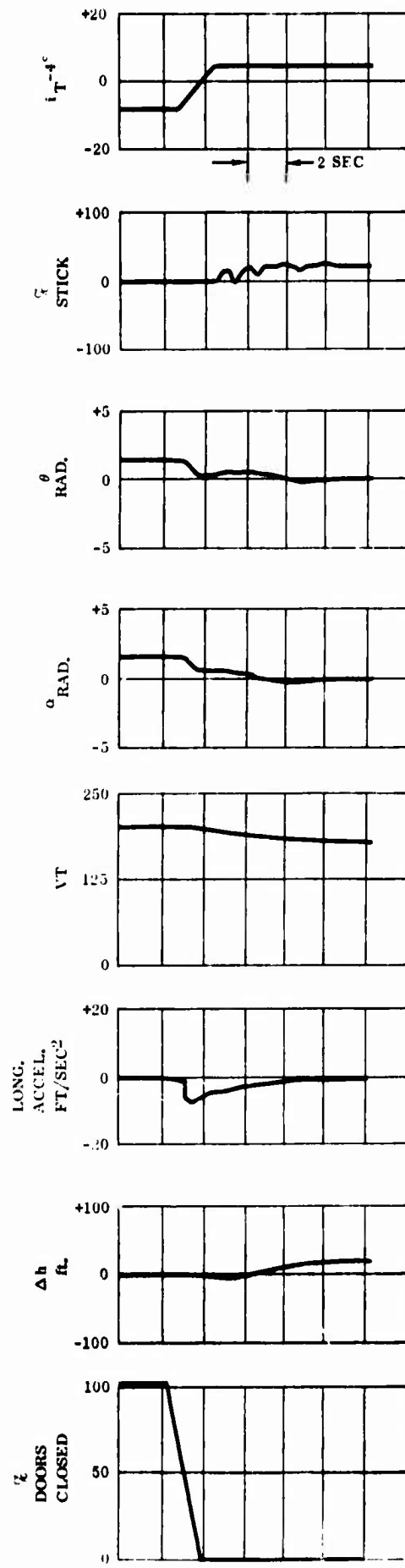


Figure 37 Nominal Conventional to Fan Conversion - Pilot Control

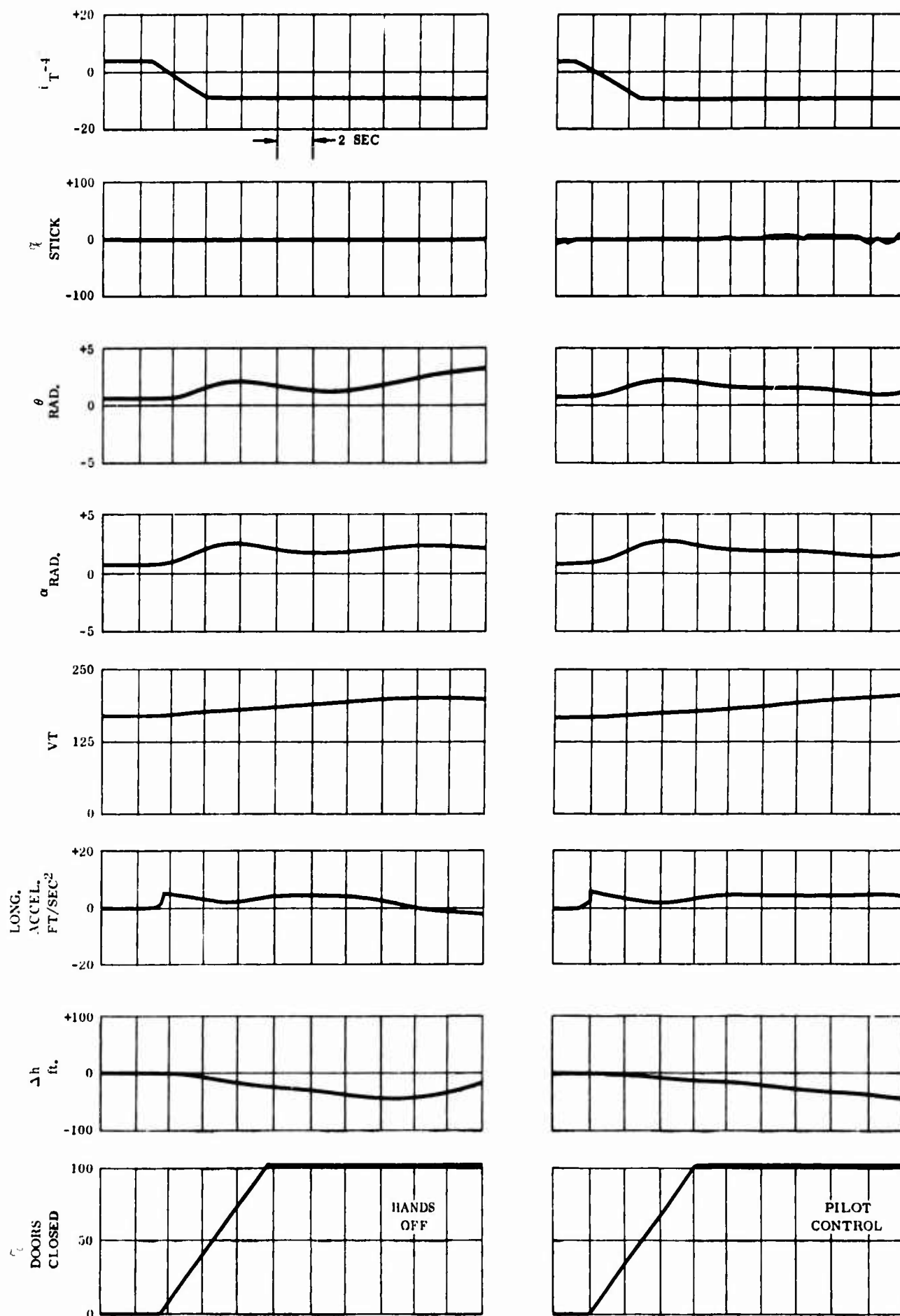


Figure 38 Nominal Single Engine Fan to Conventional Conversion with and without Pilot Control

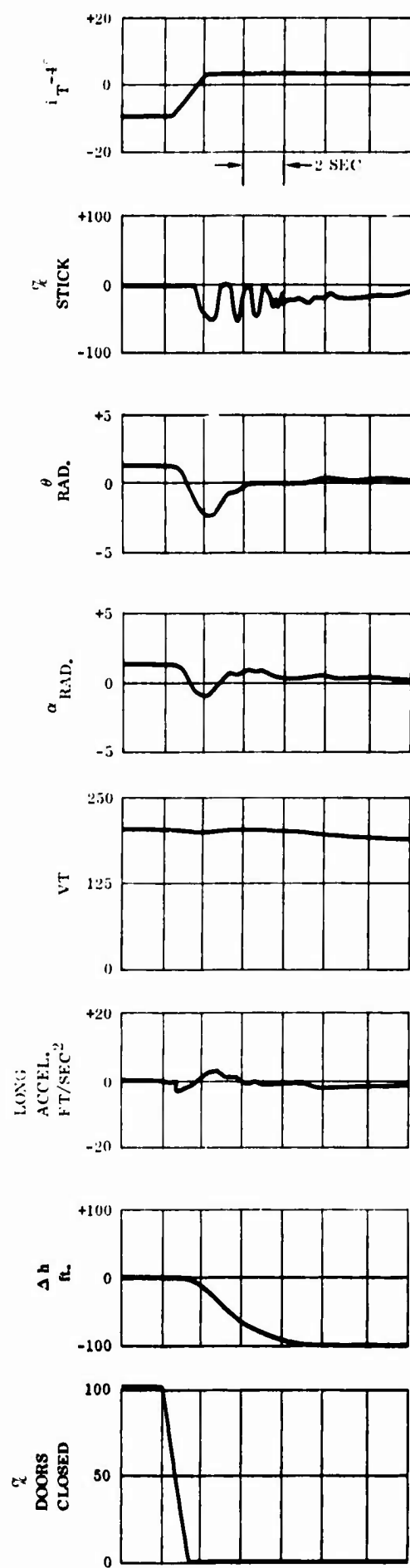


Figure 39 Nominal Single Engine Conventional - Fan Conversion -Pilot Control

4.3 Analysis

Equations of Motion

The conversion maneuver, being restricted to small angles of attack, was simulated using a set of longitudinal stability axis equations of motion. The variables in the stability axis equations are total velocity, flight path angle, and pitch angle. Figure 40 shows the stability axis coordinate system and the three coordinates.

It is seen that:

$$\gamma = \theta - \alpha \quad (1)$$

X and Z are the body axes, rotated through the angle α from the velocity vector.

The lift is perpendicular to the velocity vector, and the drag is parallel to the velocity vector.

We can thus write the equations of motion:

$$\dot{V}_T = g \sin \gamma - \frac{D}{m} - \frac{D_{NF}}{m} + \frac{T_j}{m} \quad (2)$$

$$\dot{\alpha} = - \frac{g \cos \gamma}{V_T} + \frac{L}{m V_T} + \frac{L_t}{m V_T} \quad (3)$$

$$\dot{\theta} = \frac{\Sigma M}{I_y} \quad (4)$$

Where:

$$D = C_D^s q^s A_f$$

$$D_{NF} = \text{Nose fan drag}$$

$$T_j = \text{Turbojet thrust}$$

$$L = C_L^s q^s A_f$$

$$L_t = \text{horiz. tail lift} = .0486 \left[i_t - 4^\circ + \frac{\delta e}{2} \right] q S_t$$

$$\Sigma m = C_m^s q^s A_f D_f - .02 \left[i_t - 4^\circ + \frac{\delta e}{2} \right] q S_w \bar{c} - 66 V_T \dot{\theta}$$

$$A_f = 42.6 \text{ ft.}^2$$

$$D_f = 5.22 \text{ ft}$$

$$S_t = 50.6 \text{ ft}^2$$

$$S_w = 260 \text{ ft}^2$$

$$\rho = .00205 \text{ slugs/cu. ft}$$

$$m = 9200/g \text{ slugs}$$

$$g = 32.2 \text{ ft/sec}^2$$

$$\bar{c} = 9.4 \text{ ft}$$

$$\epsilon_o = \text{downwash at tail at zero angle of attack, degrees.}$$

$$T_{ooo}/A_f = \text{Wing fan thrust loading, psf.}$$

$$q^s = q + T_{ooo}/A_f$$

$$i_t = \text{tail incidence, deg.}$$

$$q = \frac{\rho}{2} V_T^2$$

$$\delta_e = \text{Elevator Pos. deg.}$$

$$T_c^s = \frac{T_{ooo}/A_f}{q + T_{ooo}/A_f}$$

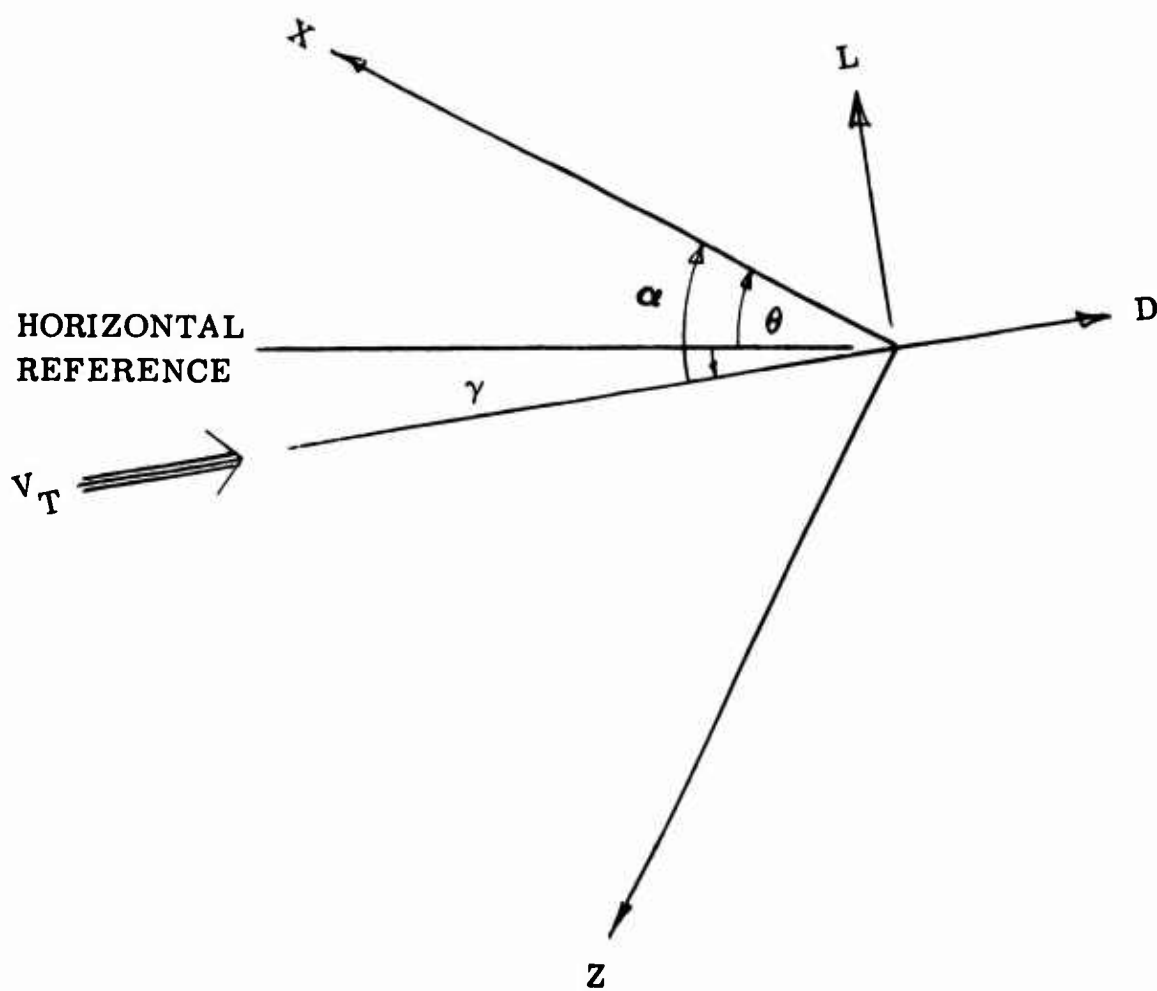
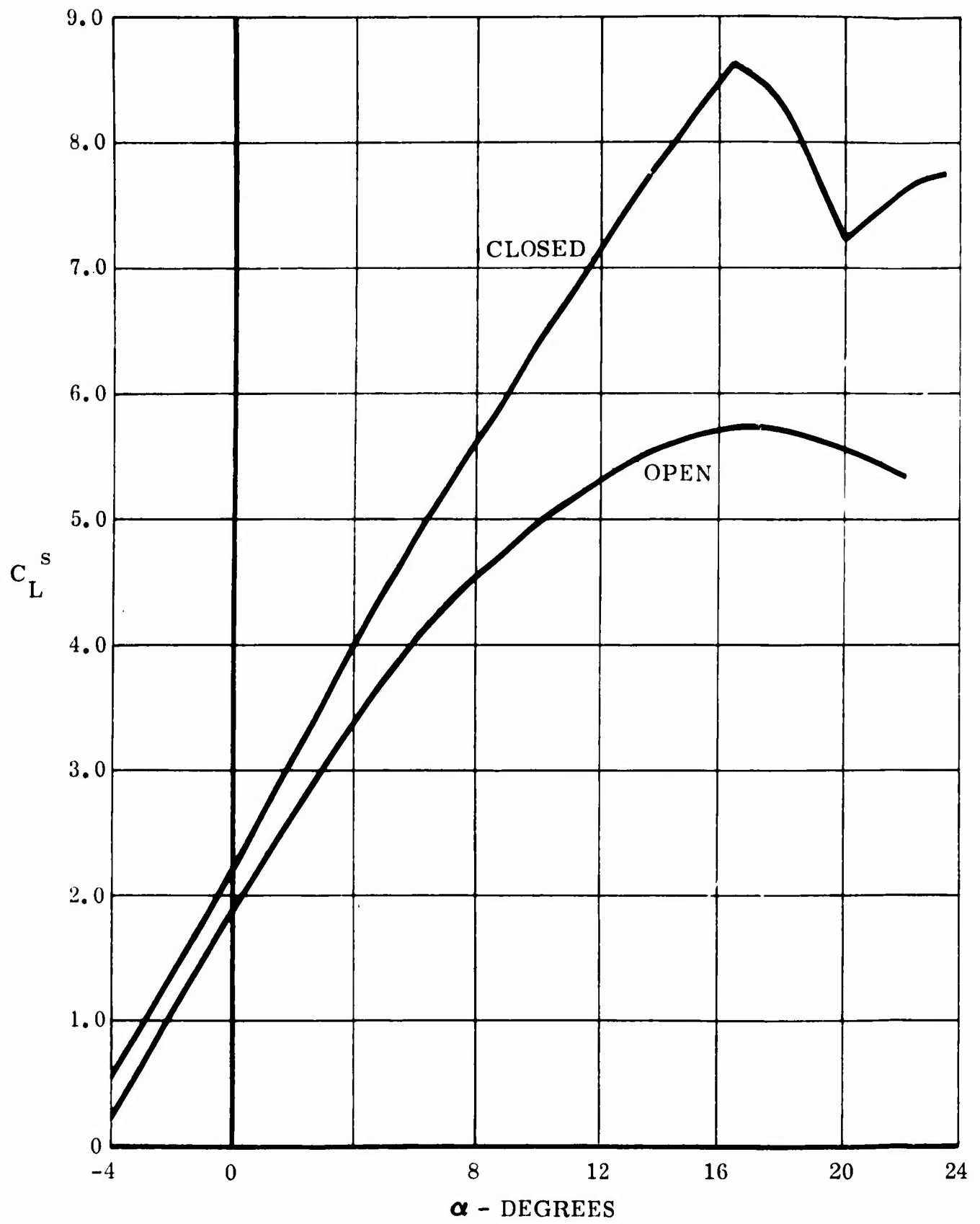
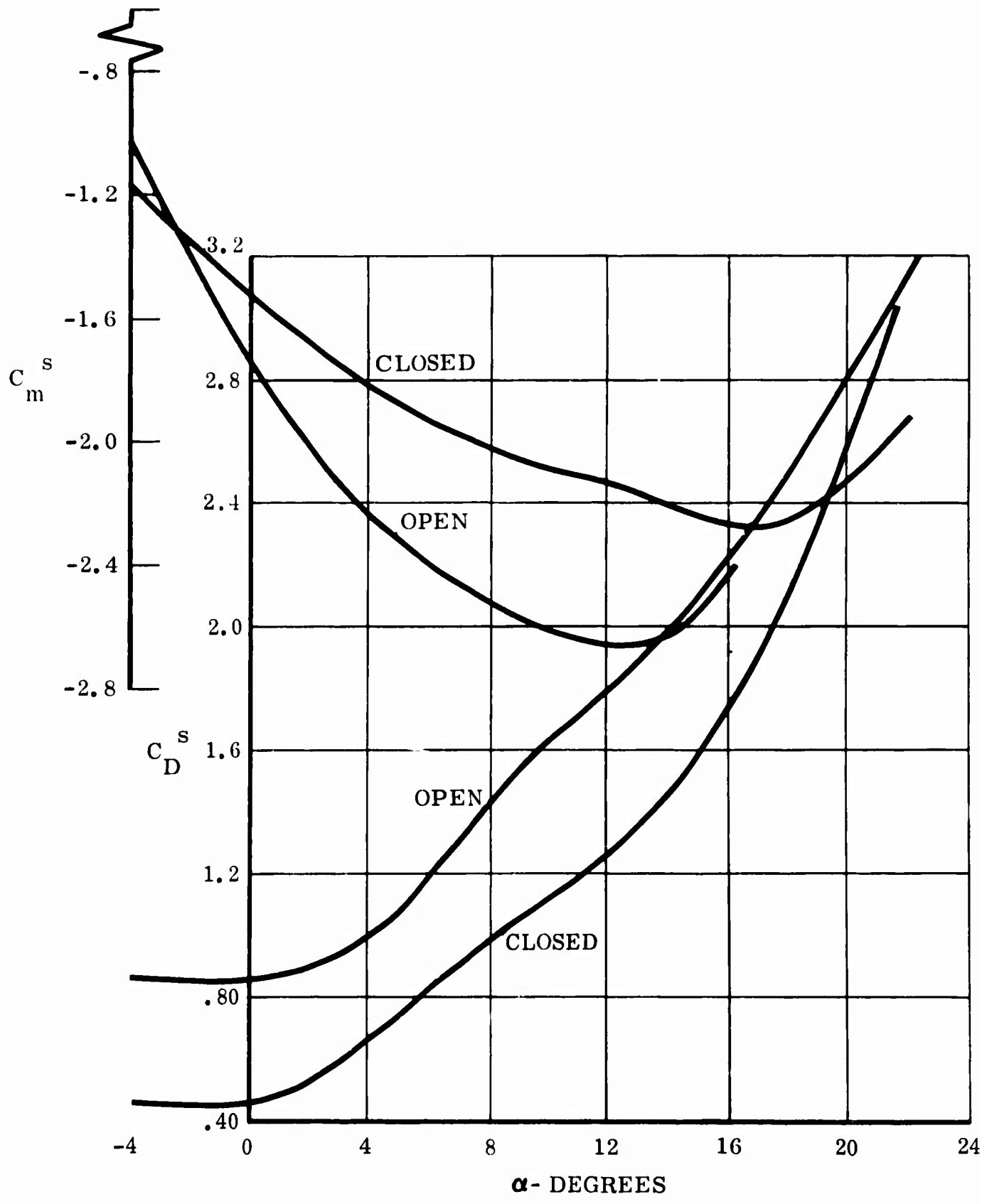


Figure 40 Stability Axis Coordinate System

$\delta_f = 45^\circ, \beta_v = 50^\circ,$



50°, $i_t = 4^\circ$, $\delta_{\text{DROOP}} = 15^\circ$



B

Figure 41 Effect of Wing Closure Doors - Power Off

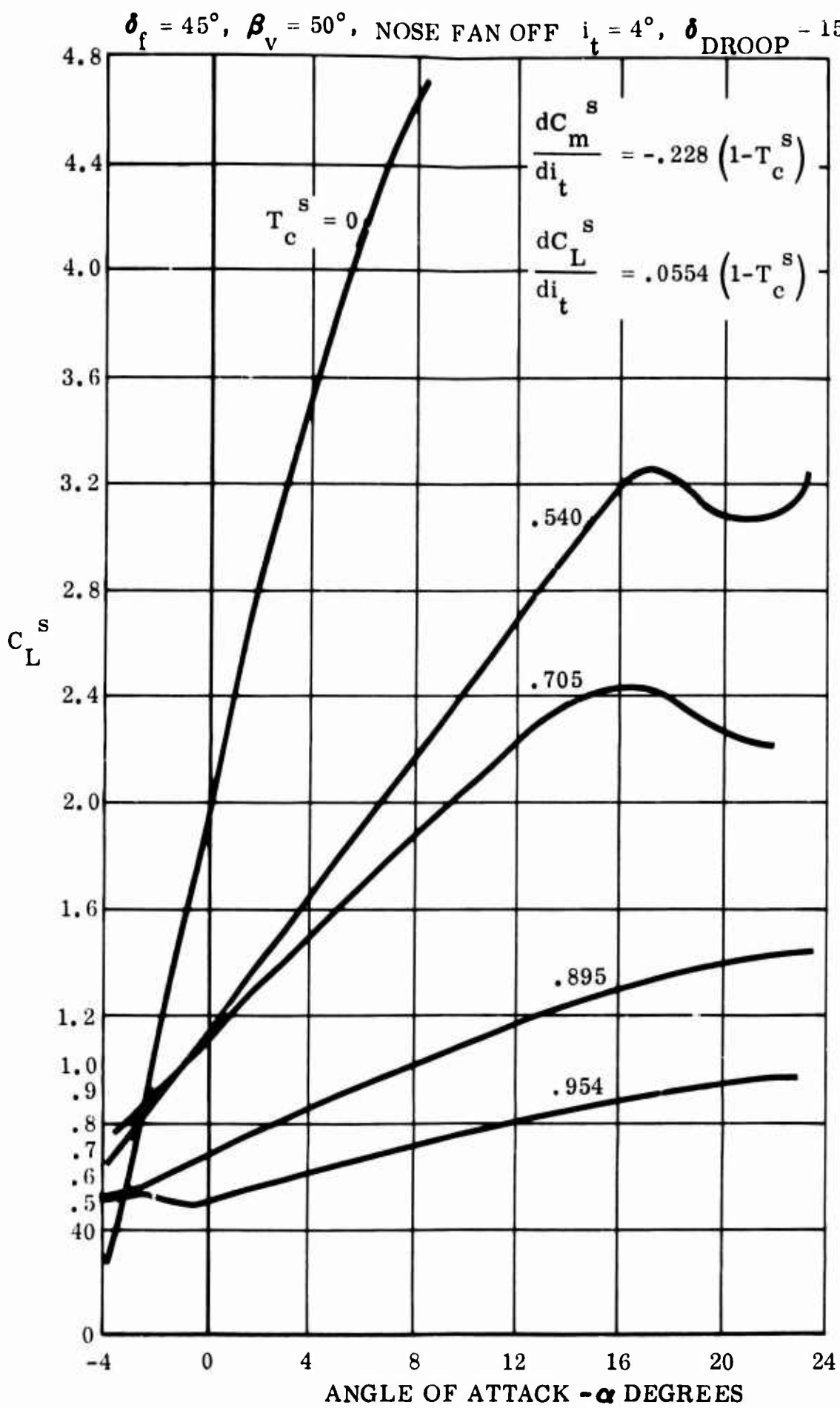


Figure 4

A

$\delta_{\text{DROOP}} = 15^\circ$

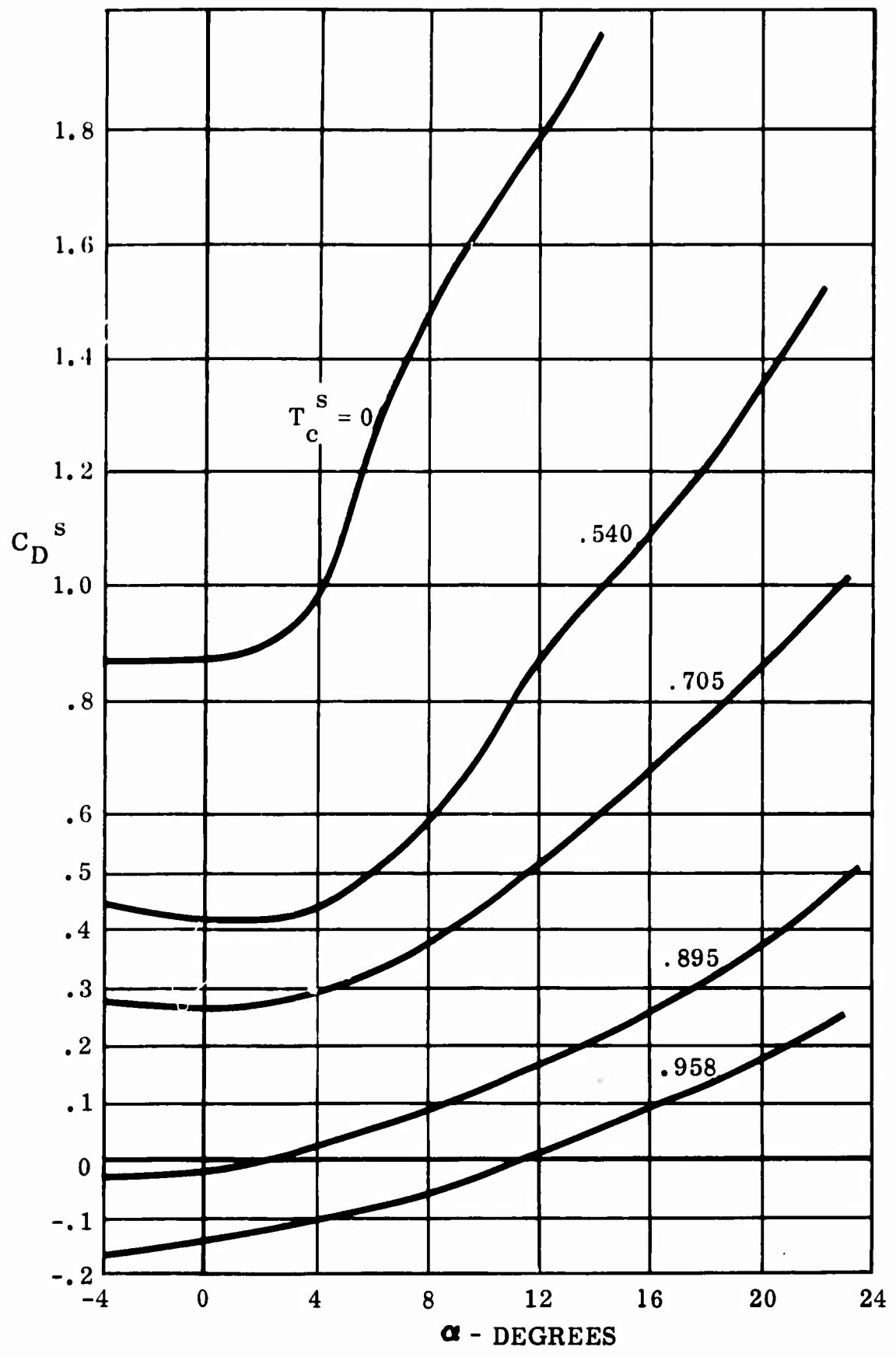
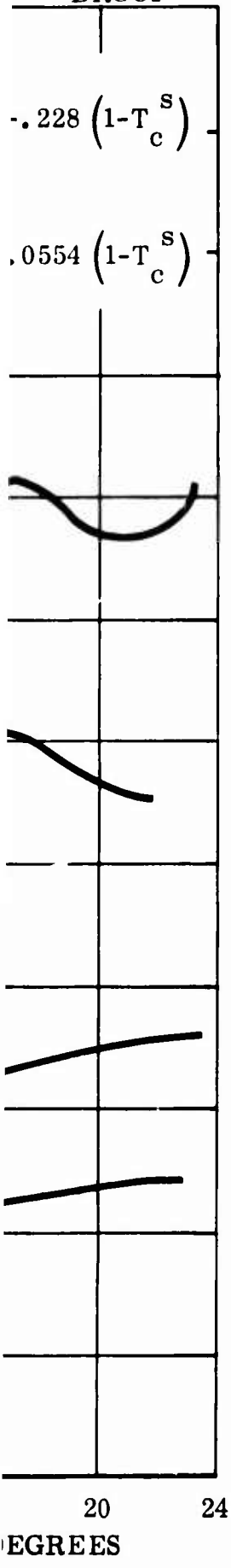


Figure 42 Longitudinal Characteristics During Conversion

B

BLANK PAGE

$$\Delta C_{D_{\text{GEAR}}} = +.029 \text{ ON WING AREA}$$

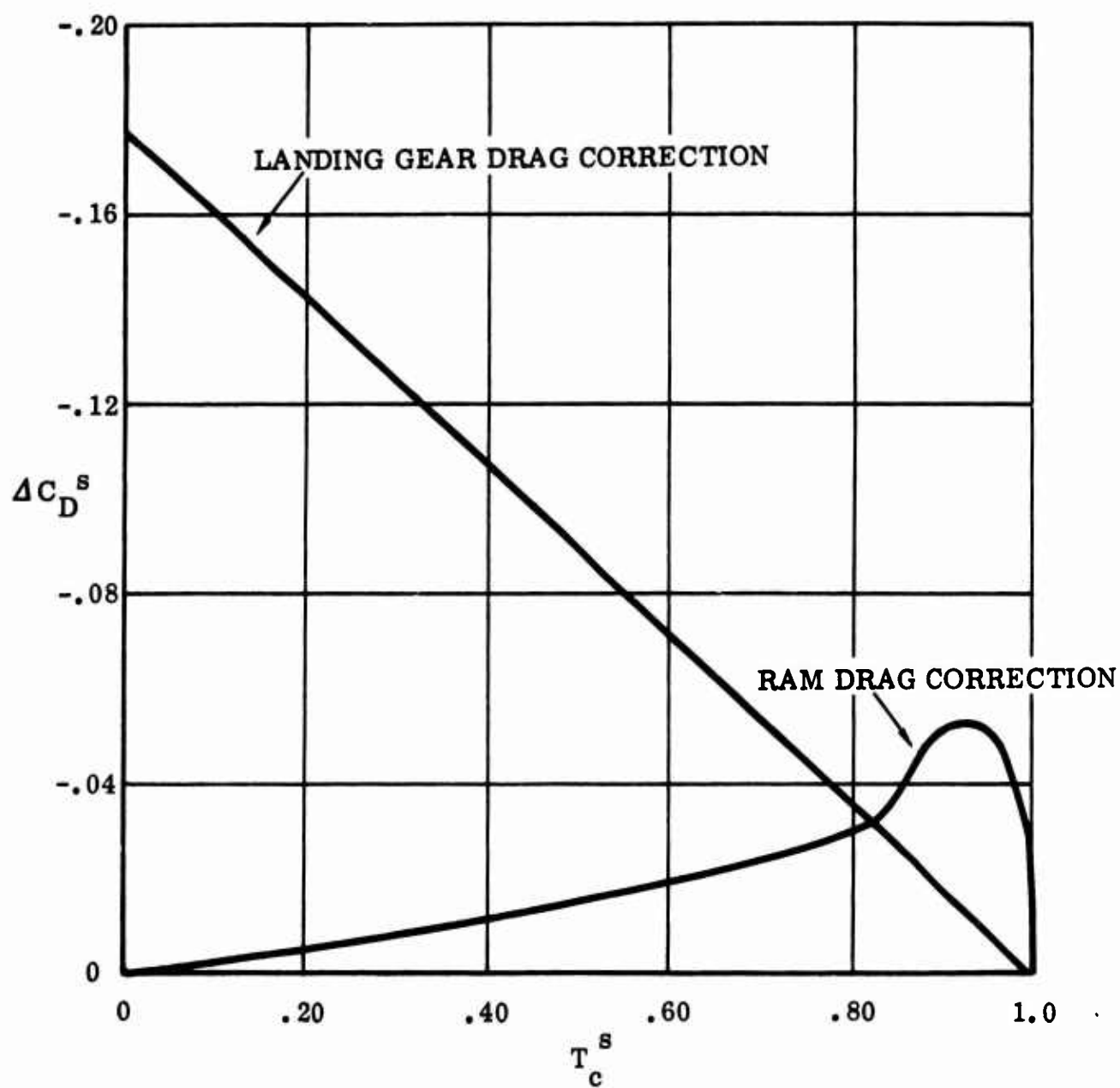


Figure 43 Corrections to Drag for Ram Drag and Landing Gear

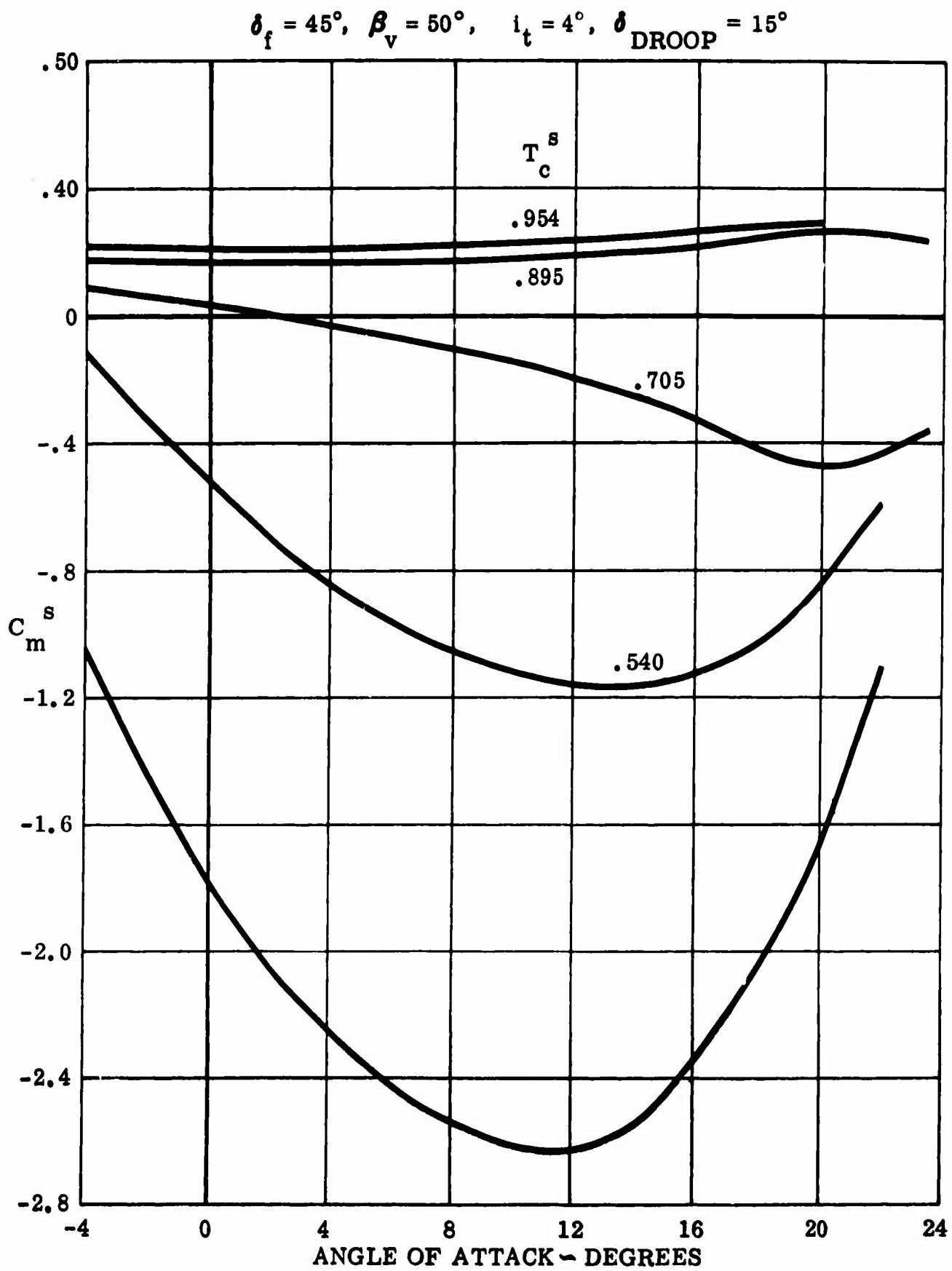


Figure 44 Longitudinal Characteristics in Conversion

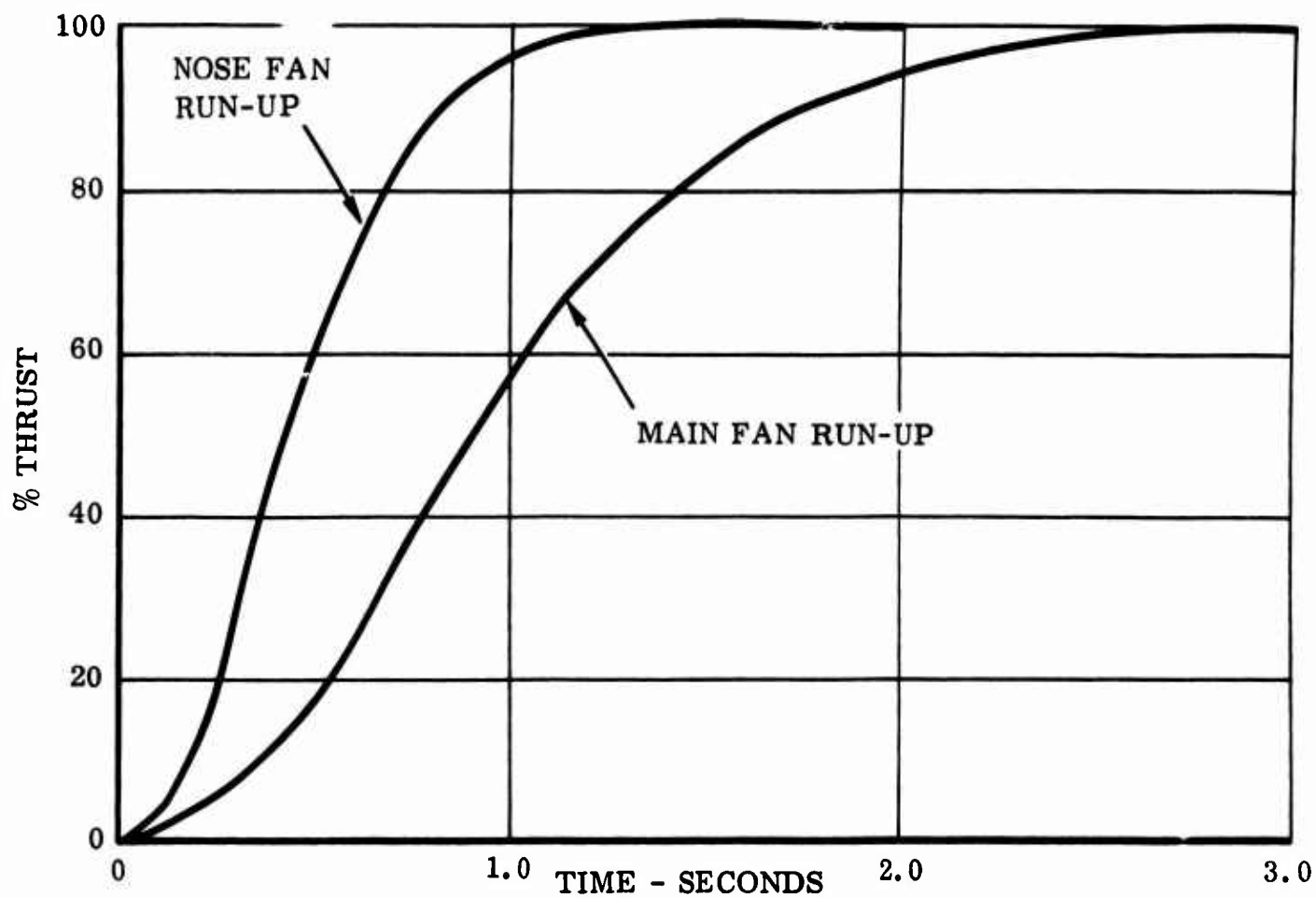


Figure 45 Thrust vs Time from Diverter Actuation for Nose Fan and Main Fan Runup

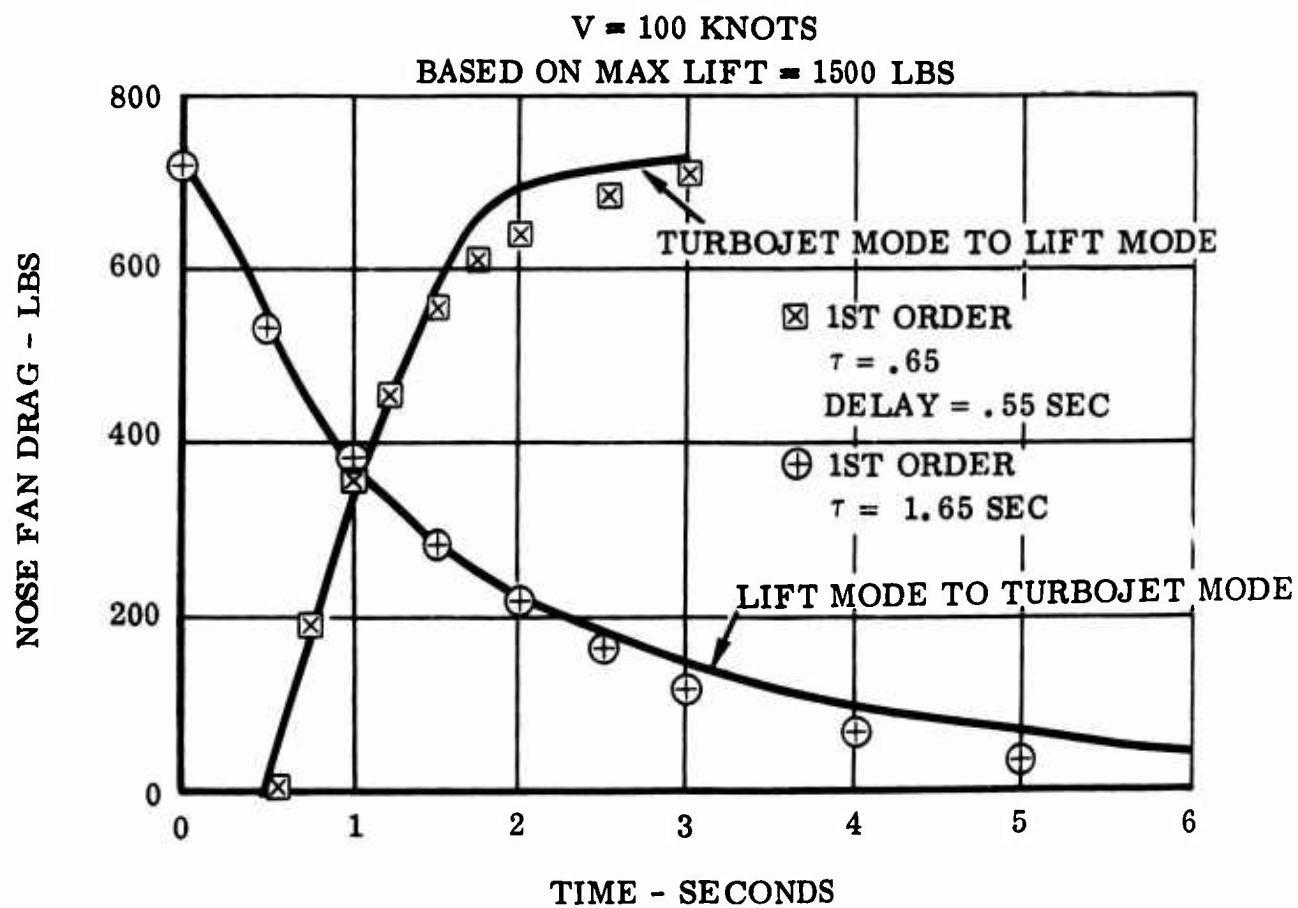


Figure 46 Variation of Nose Fan Ram Drag Following Diverter Valve Operation

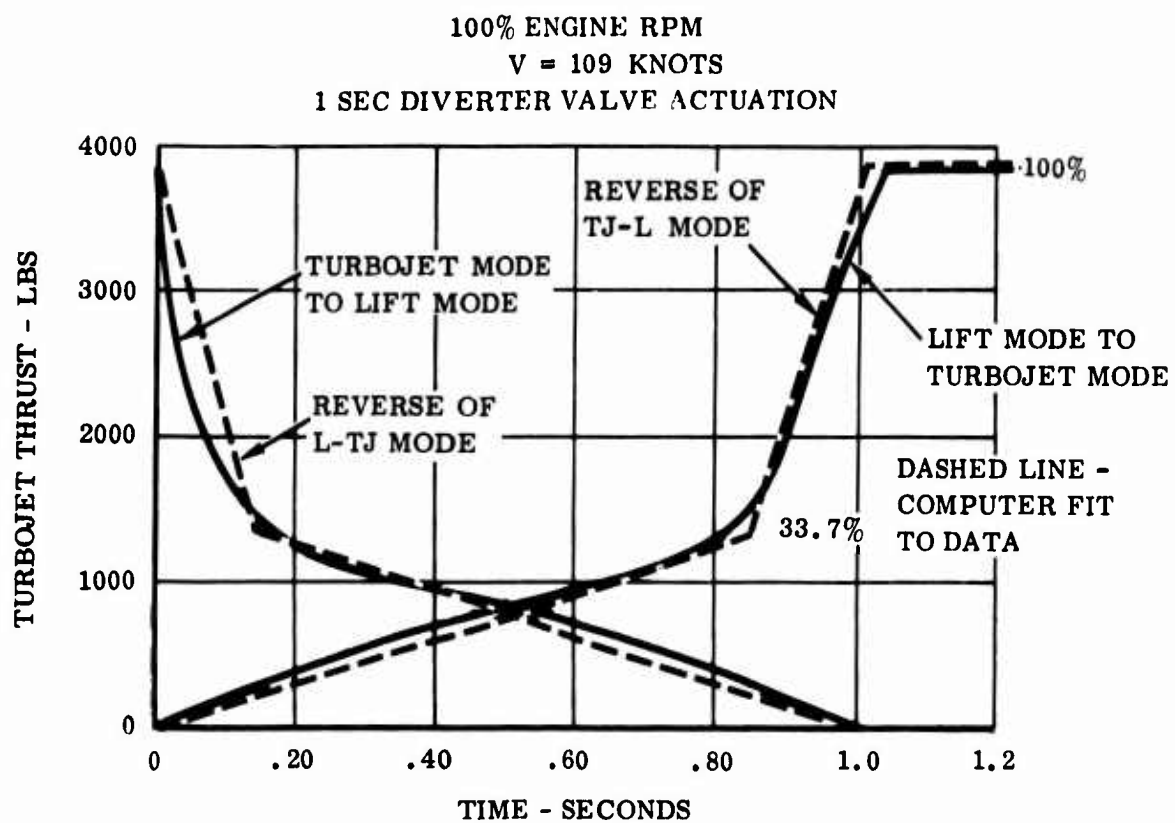


Figure 47 J-85 Thrust Transient Following Diverter Valve Switch

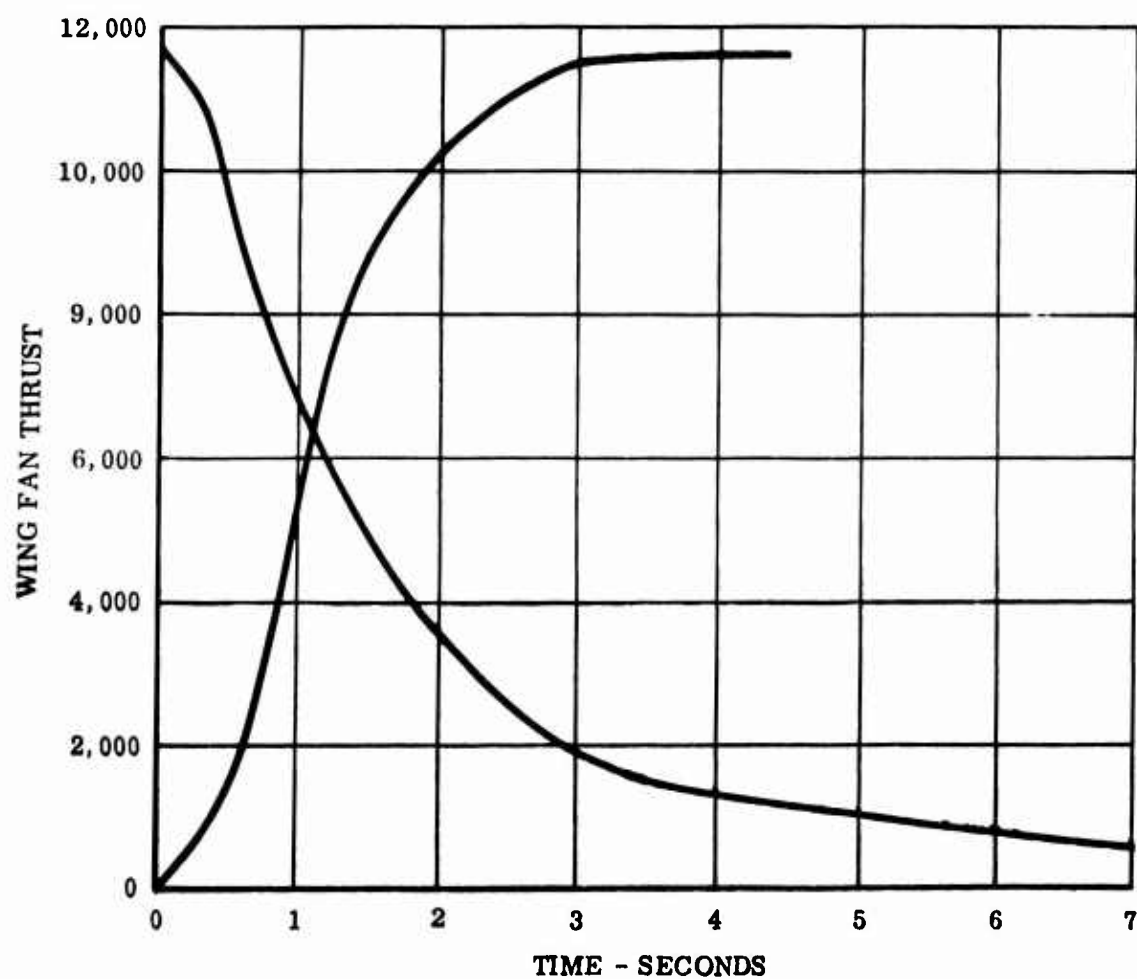


Figure 48 Wing Fan Thrust vs Time for 1 Sec. Diverter Switch

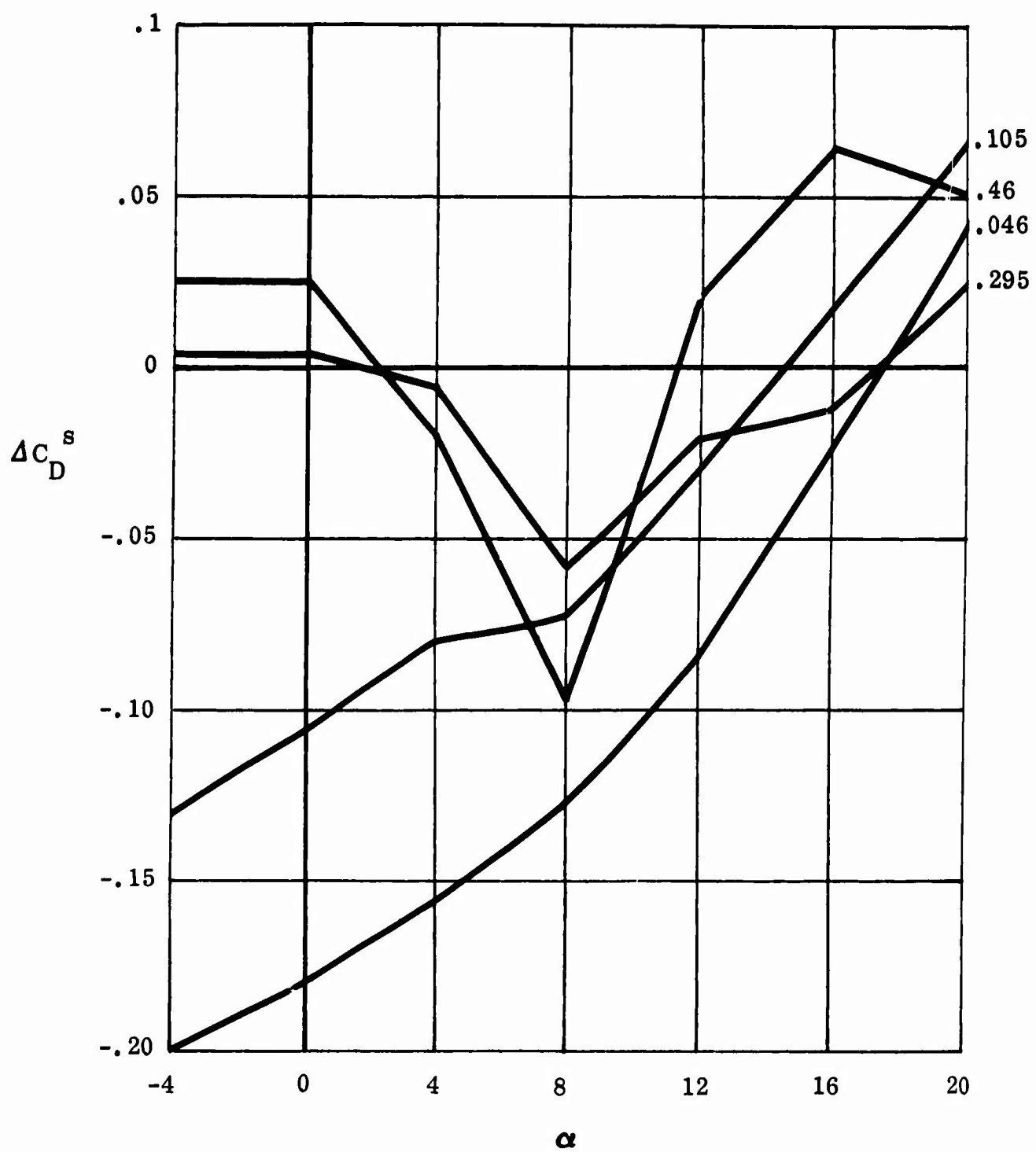


Figure 49 Drag Coefficient Increment Due to Fan Thrust at
 $R_q = .046, .105, .295$ and $.46$

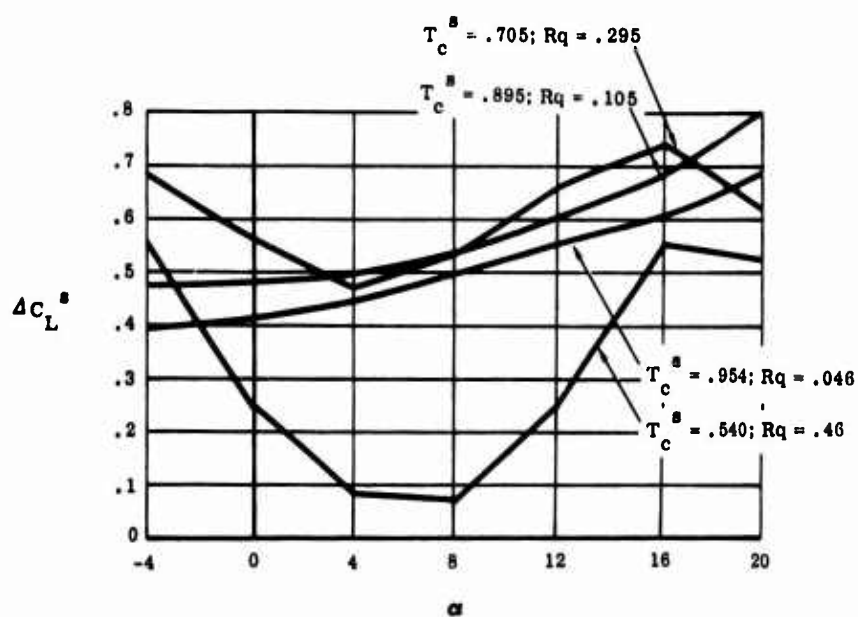


Figure 50 Lift Coefficient Increment Due to Fan Thrust at $R_q = .046, .105, .295$ and $.46$

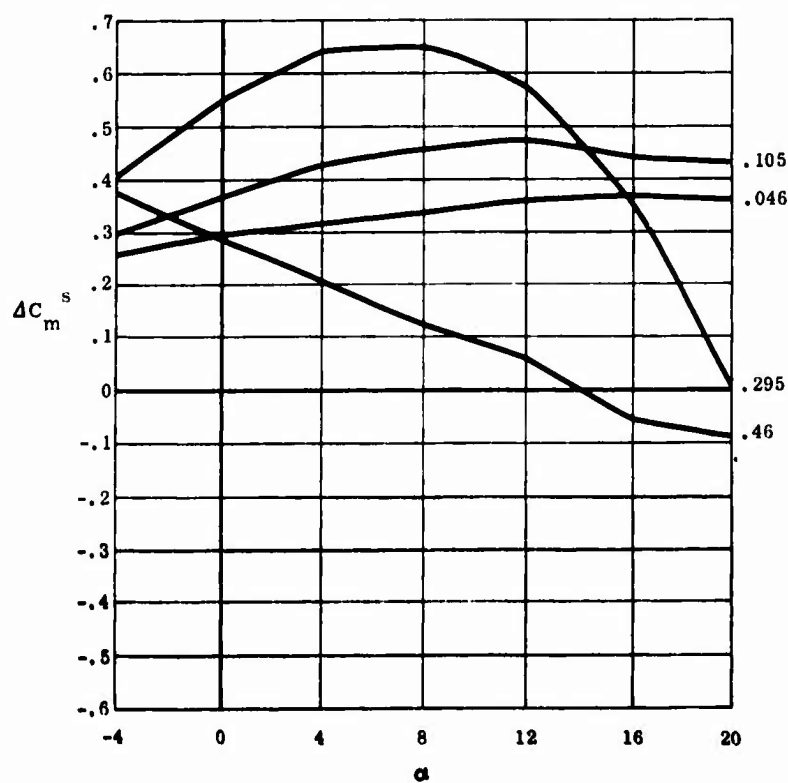


Figure 51 Pitching Moment Coefficient Increment Due to Fan Thrust at $R_q = .046, .105, .295$ and $.46$

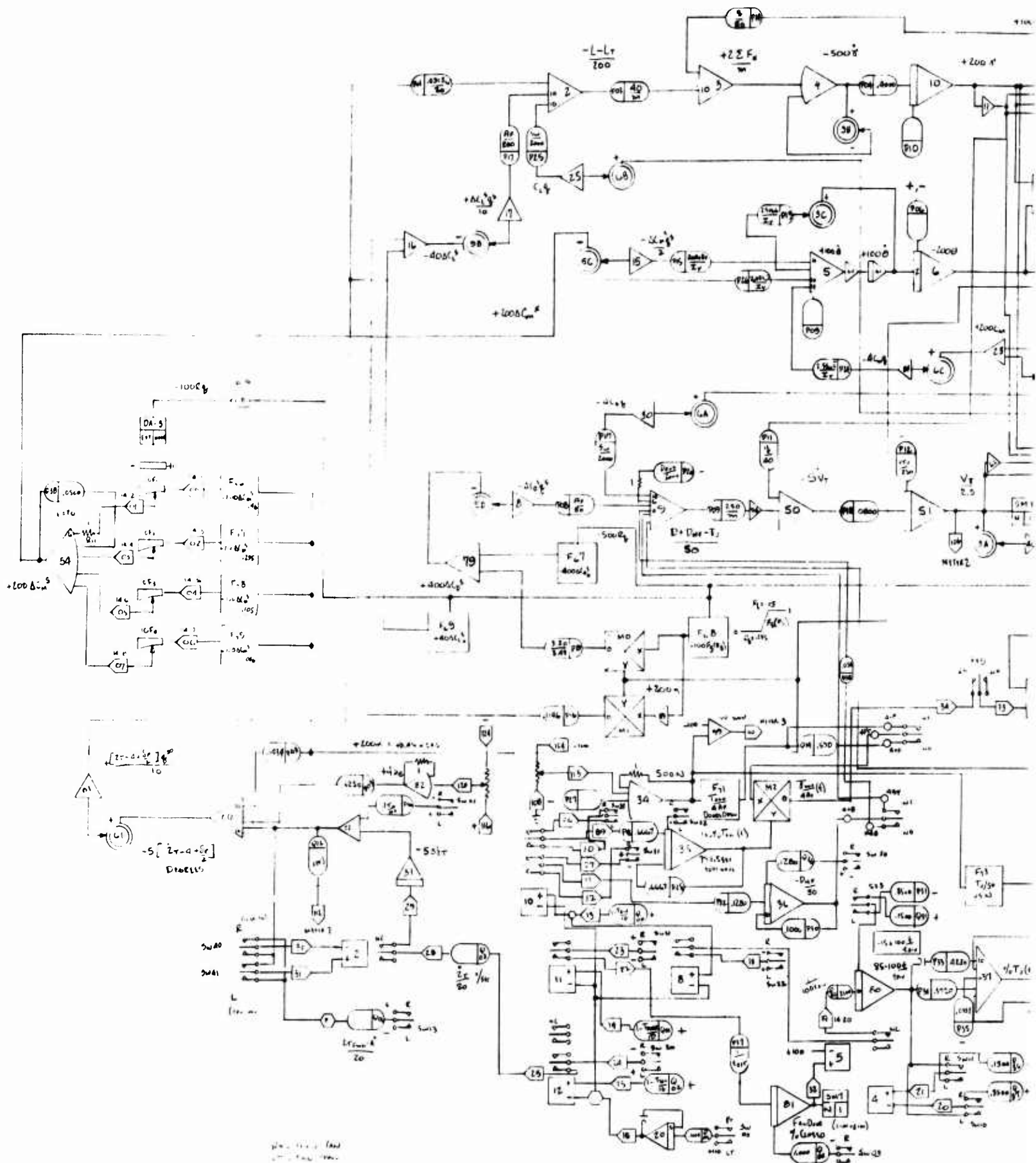


Figure 51A 3° Conversion Lor

A

(A. 86. 0 446)

$$C_k = 1 - T_c^2 \cdot \frac{1}{R^2}$$

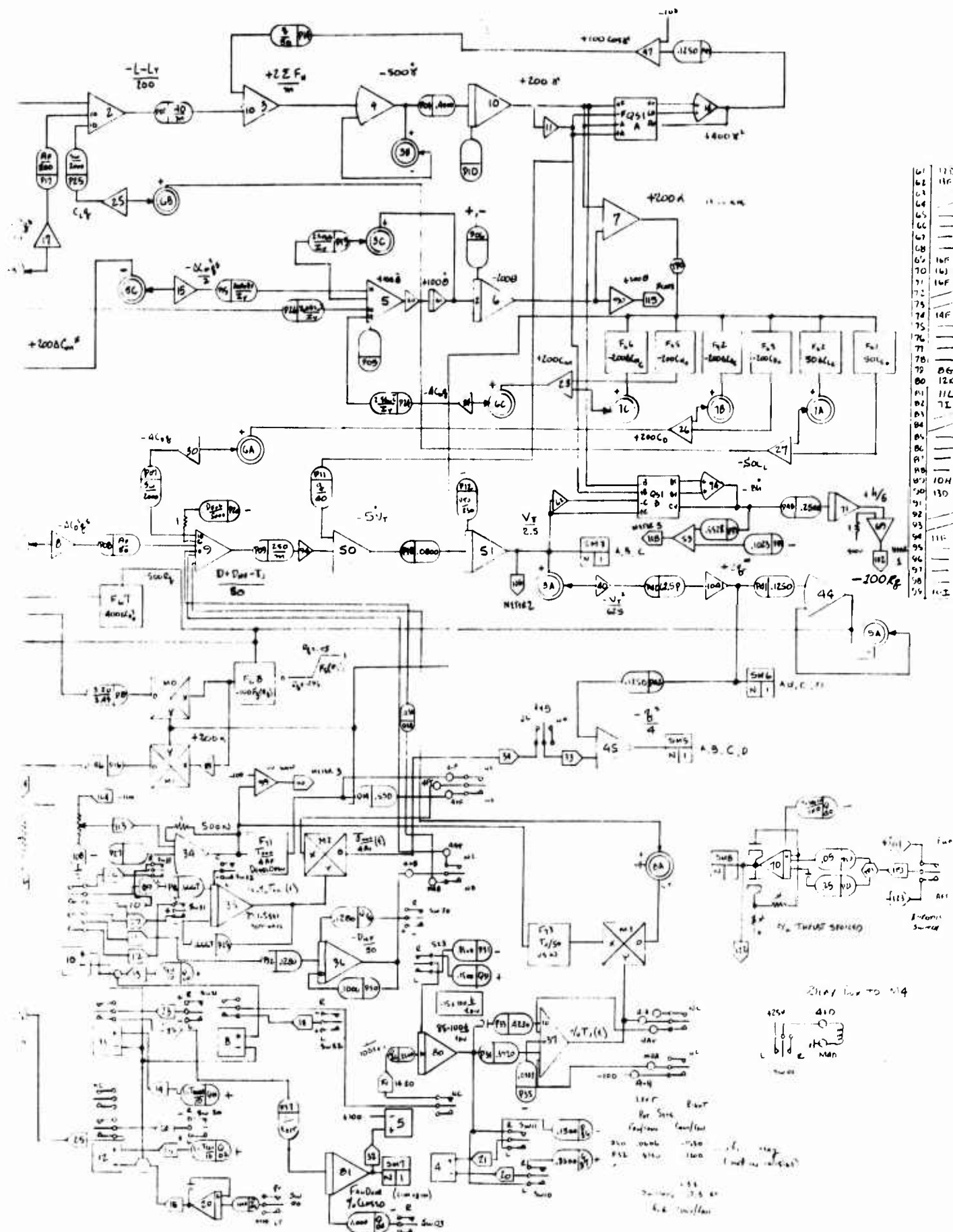


Figure 51A 3° Conversion Longitudinal Computer Diagram

B

$$R_q = 1 - T_c^s = q/q^s$$

C_L^s = Slipstream lift coefficient
(includes tail lift for $i_t = 4^\circ$) Fig. 41 and Fig. 42

C_D^s = Slipstream drag coefficient Fig. 41, Fig. 42 and Fig. 43

C_m^s = Slipstream Pitching moment coefficient Fig. 44 and Fig. 41
(includes tail moment for $i_t = 4^\circ$)

The set-up of this data required the simulation to cover the T_c^s range of about .9 to zero, wing fan doors open and closed.

The curves of Figure 41 depict the variation in the longitudinal aerodynamics due to the position of the wing fan closure doors, in the power off, or $T_c^s = 0$, configuration.

The curves of Figure 42 and 44 show the variation of the longitudinal aerodynamics with the wing fan closure doors open and at various T_c^s values applicable to the conversion regime.

In addition, the curves of figures 45, 46, 47, and 48 were used to simulate the effect of fan speed-up and run-down during the conversion maneuver.

The data was simulated by subtracting the doors open, $T_c^s = 0$, data of Figures 42 and 44. This remainder was considered to be the fan-caused effects, and the effect of fan run-down was applied to these increments. These ΔC_D^s , and ΔC_L^s , and ΔC_m^s are shown in Figures 49, 50 and 51, plotted at constant T_c^s values and zero angle of attack.

(Example) The component of C_L^s from $T_c^s = 0$ reflected to the $T_c^s = .954$ curve on Figure 42 is equal to the C_L^s at $T_c^s = 0$ value multiplied by $(1 - T_c^s)$. These differences, then, are plotted in Figures 49, 50 and 51. As the fan thrust decays during conversion, T_c^s changes and the increments due to fan operation automatically phase out. When the doors close, the remaining small increment is simply turned off.

During the door closing (or opening) period, the increments obtained from Figure 41 are phased in or out proportional to door position.

The 3rd conversion longitudinal computer diagram is shown in Figure 51A.

5.0 SIX-DEGREE-OF-FREEDOM PERTURBATION CONVENTIONAL FLIGHT SIMULATION

5.1 Discussion

The simulated handling qualities of the XV-5A aircraft were investigated for a range of flight conditions and aircraft configurations considered representative of the conventional flight regime. The aerodynamic data used represent the present best estimate of the aircraft aerodynamic characteristics based on wind tunnel data and standard estimating procedures where data were lacking.

Handling qualities were evaluated using the Cooper rating system and the results are presented in Tables I and II following. Characteristics were investigated for gross weights of 7500 and 12,500 pounds; center of gravity at fuselage stations 240 and 246 inches; altitudes of sea level, 20,000 and 32,000 feet and a speed range from 85 to 500 knots ($M = .13$ to $.84$). Table I presents a complete list of conditions studied and Table II gives the evaluation of each condition for a series of maneuvers in terms of Cooper pilot ratings.

An overall evaluation of the XV-5A flying qualities in the conventional flight mode would be Cooper Rating 3, "satisfactory," but with some mildly unpleasant characteristics. The "mildly unpleasant" refers to weakening dihedral effect during conditions of zero or slight negative angle, such as conditions 2 and 4, flaps down, 180 knots and flaps up 500 knots respectively. The problem appears when the aircraft develops a slight left bank while developing a right yawing velocity, due to a right rudder input in the absence of co-ordinating aileron during the maneuver "rudder-S-turns".

This problem is in some degree a result of adverse roll due to rudder $C_{l\delta_r}$ which was verified by removing $C_{l\delta_r}$ and thereby achieving satisfactory dihedral effect. $C_{l\beta}$ for angle of attack zero is $-.00127/\text{deg}$. and $C_{l\delta_r}$ is $.00025/\text{deg}$. The pilot rates this specific maneuver between 5 and 6 "unacceptable for normal operation" and the condition rates 4.

This lack of dihedral effect at these conditions is not apparent during any of the coordinated maneuvers.

Low speed flaps down or condition 1 was studied extensively. The overall rating for condition 1 was 3. Considering the flight speed of 85 knots or 15% over stall speed, the aircraft "flies well". To further investigate this condition the longitudinal stability was increased and decreased by varying C_{m_α} and C_{m_q} . It was found that even large changes

in C_{m_α} or C_{m_q} (50%) had little effect on the pilot's ability to fly the simulator. Reducing C_{m_α} or C_{m_q} to zero made less than 1 change in Cooper rating. However, reducing both C_{m_α} and C_{m_q} had a much more deleterious effect on handling qualities and Cooper rating jumped to 6. This study indicates that any loss in static longitudinal stability associated with flight at low speeds and high angle of attack would not be a threat to flight safety.

At the high speed condition some studies were conducted to establish the aircraft's sensitivity to certain parameters which might change as a means of improving handling qualities or due to possible errors in the aerodynamic data used. Increases in C_{l_β} of 50 and 100% greatly improves the handling characteristics particularly "wing dropping" tendencies. Increases of this magnitude in C_{n_β} do not greatly change the handling qualities. Very large changes in $C_{n_{\delta_a}}$, yawing moment due to aileron, (as much as 1000%) in either direction positive or negative had little or no effect on general handling qualities.

Changes in altitude, gross weight, and center of gravity did not greatly affect handling qualities. For example, changes to high altitude or heavier weight were evaluated as "same as before or maybe a little less". That is to say, if a maneuver got a Cooper rating of 3 at a given condition, it would not vary more than one-half for other altitudes, gross weights, or centers of gravity. For this reason and due to time considerations, some conditions which were originally scheduled for checks were eliminated.

5.2 Summation

1. Reduced static longitudinal stability during low speed flaps down high angle of attack flight does not present a handling qualities problem.
 2. A 50% change in directional stability does not greatly alter the overall handling qualities.
 3. A 50% increase in lateral stability would improve flying qualities considerably.
 4. Overall flying qualities of the XV-5A, as is, are satisfactory.
 5. Changes in aircraft characteristics which result from changes in altitude, gross weight, and center of gravity do not greatly alter handling qualities.
- * For the purpose of this report a change in handling qualities which changes Cooper rating by more than one is large, whereas less than one-half is small.

TABLE I

SIMULATED FLIGHT CONDITIONS						
FLIGHT CONDITIONS	MACH NUMBER	AIRSPEED KNOTS	ALTITUDE FEET	GROSS WEIGHT	FLAP POSITION	CENTER OF GRAVITY
1	.127	84.	S. L	7,500	45°	246
2	.271	180.	"	"	"	"
3	.199	132.	"	"	0°	"
4	.755	500.	"	"	"	"
8	.838	490.	32,000	"	"	"
9	.495	290.	"	12,500	"	"
11	.127	84.	S. L	7,500	45°	240
15	.295	181.	20,000	"	0°	"
16	.828	510.	"	"	"	"

BLANK PAGE

TABLE II-RESULTS

TABLE II - RESULTS										
FLIGHT CONDITION	1	2	3	4	8	9	11	15	16	
MANEUVER										
General Handling	3	4	3	4	4	3	3	3	4	
Steady Turns	2 1/2	3	2	4	3	3	3	2 1/2	3	
Rudder S Turns	3	6	2 1/2	6	4	3	4	3	5	
Aileron S Turns	4	4	2	4	4	3	3	3	4	
Adverse Yaw	3 1/2	3	2	3 1/2	3	2 1/2	3	3	3 1/2	
Steady Sideslip	3	5	3 1/2	5 1/2	3	4	3	3	5	
Lat. -Dir. Oscillations	3 1/2	6	3 1/2	6	4	3	2 1/2	3	4	
Pitch Due to Yaw	3	3	3	3	3	3	3	3	3	
Spiral Stability	2	3	3	3	3	3	2	2	4	
Long. Short Period	3 1/2	3	3	3	3	3	3	2 1/2	2	

5.3 Analysis

The following are the standard small - perturbation lateral-directional and longitudinal three-degree-of-freedom uncoupled equations of motion used throughout the industry.

5.3.1 Longitudinal Perturbation Equations

The longitudinal perturbation equations are:

$$\dot{u} = X_u u + X_w \dot{w} + X_w w + X_q \dot{\theta} + X_{\delta e} \delta_e - g(\cos \gamma_o) \theta \quad (1)$$

$$\dot{w} = Z_u u + Z_w \dot{w} + Z_w w + (U_o + Z_q) \dot{\theta} + Z_{\delta e} \delta_e - g(\sin \gamma_o) \theta \quad (2)$$

$$\ddot{\theta} = M_u u + M_w \dot{w} + M_w w + M_q \dot{\theta} + M_{\delta e} \delta_e \quad (3)$$

Changing all angles to degrees, and letting $w = U_o \alpha / 57.3$

$$\dot{u} = A_u u + A_{\dot{\alpha}} \dot{\alpha} + A_{\alpha} \alpha + A_{\dot{\theta}} \dot{\theta} + A_{\delta e} \delta_e - \frac{g}{57.3} (\cos \gamma_o) \theta \quad (4)$$

$$\dot{\alpha} = B_u u + B_{\dot{\alpha}} \dot{\alpha} + B_{\alpha} \alpha + B_{\dot{\theta}} \dot{\theta} + B_{\delta e} \delta_e - \frac{g}{U_o} (\sin \gamma_o) \theta \quad (5)$$

$$\ddot{\theta} = C_u u + C_{\dot{\alpha}} \dot{\alpha} + C_{\alpha} \alpha + C_{\dot{\theta}} \dot{\theta} + C_{\delta e} \delta_e \quad (6)$$

Where

$$A_u = X_u \quad B_u = Z_u (57.3/U_o) \quad C_u = 57.3 M_u$$

$$A_{\dot{\alpha}} = X_w U_o / 57.3 \quad B_{\dot{\alpha}} = Z_w \quad C_{\dot{\alpha}} = U_o M_w$$

$$A_{\alpha} = X_w U_o / 57.3 \quad B_{\alpha} = Z_w \quad C_{\alpha} = U_o M_w$$

$$A_{\dot{\theta}} = X_q / 57.3 \quad B_{\dot{\theta}} = 1 + Z_q / U_o \quad C_{\dot{\theta}} = M_q$$

$$A_{\delta e} = X_{\delta e} / 57.3 \quad B_{\delta e} = Z_{\delta e} / U_o \quad C_{\delta e} = M_{\delta e}$$

5.3.2 Lateral Perturbation Equations

$$\begin{aligned} \dot{\beta} = & Y_{\beta} \beta + Y_p \dot{\phi} + Y_r \dot{\psi} + Y_{\delta a} \delta_a + Y_{\delta r} \delta_r - \dot{\psi} + \frac{g}{U_o} (\cos \gamma_o) \phi \\ & + \frac{g}{U_o} (\sin \gamma_o) \psi \end{aligned} \quad (7)$$

$$\dot{\phi} = L_{\beta} \beta + L_p \dot{\phi} + L_r \dot{\psi} + L_{\delta a} \delta_a + L_{\delta r} \delta_r + \frac{I_{xz}}{I_x} \ddot{\psi} \quad (8)$$

$$\ddot{\psi} = N_{\beta} \beta + N_p \dot{\phi} + N_r \dot{\psi} + N_{\delta a} \delta_a + N_{\delta r} \delta_r + \frac{I_{xz}}{I_z} \ddot{\phi} \quad (9)$$

5.3.3 Determination of C_{L_u} , C_{D_u} , $C_{D_{\delta e}}$ and C_{m_u}

$$\text{If } C_L = C_{L_{\alpha}} (\alpha - \alpha_{oL}) + C_{L_{\delta e}} \delta_e + \frac{\bar{c}}{2U} (C_{L_{\dot{\alpha}}} \dot{\alpha} + C_{L_{\dot{\theta}}} \dot{\theta}) \quad (10)$$

$$C_D = f_1 + f_2 C_L^2 + f_3 C_L |\delta_e| \quad (11)$$

$$C_m = C_{m_o} + C_{m_{\alpha}} \alpha + C_{m_{\delta e}} \delta_e + \frac{\bar{c}}{2U} (C_{m_{\dot{\alpha}}} \dot{\alpha} + C_{m_{\dot{\theta}}} \dot{\theta}) \quad (12)$$

where

$f_1 = f_1(C_L, M)$ is the untrimmed drag polar

$f_2 = f_2(M)$ is the trim drag coefficient $\frac{C_{D\delta e}}{C_L^2}$

$f_3 = f_3(M)$ is the trim drag coefficient $\frac{C_{D\delta e}}{C_L}$

then

$$C_{L_u} = \frac{M}{2} \left[\left(\frac{\partial C_{L\alpha}}{\partial M} \right) (\alpha_o - \alpha_{oL}) - C_{L\alpha} \left(\frac{\partial \alpha_{oL}}{\partial M} \right) + \left(\frac{\partial C_{L\delta_e}}{\partial M} \right) \delta_{eo} \right] \quad (13)$$

$$C_{D_u} = C_{L_u} \left[\frac{\partial f_1}{\partial C_L} + 2f_2 C_L \left| \delta_{eo} \right| + f_3 \left| \delta_{eo} \right| \right] \quad (14)$$

$$+ \frac{M}{2} \left[\frac{\partial f_1}{\partial M} + \left(\frac{\partial f_2}{\partial M} \right) C_L^2 \left| \delta_{eo} \right| \right] + \frac{M}{2} \left(\frac{\partial f_3}{\partial M} \right) C_L \left| \delta_{eo} \right|$$

$$C_{D_\alpha} = C_{L_\alpha} \left[\frac{\partial f_1}{\partial C_L} + 2f_2 C_L \left| \delta_{eo} \right| + f_3 \left| \delta_{eo} \right| \right] \quad (15)$$

$$C_{D_{\delta_e}} = C_{L_{\delta_e}} \left[\frac{\partial f_1}{\partial C_L} + 2f_2 C_L \left| \delta_{eo} \right| + f_3 \left| \delta_{eo} \right| \right] + f_2 C_L^2 + f_3 C_L \quad (16)$$

$$C_{m_u} = \frac{M}{2} \left[\frac{\partial C_{m_o}}{\partial M} + \left(\frac{\partial C_{m_\alpha}}{\partial M} \right) \alpha_o + \left(\frac{\partial C_{m_{\delta_e}}}{\partial M} \right) \delta_{eo} \right] \quad (17)$$

Provided $\dot{\alpha}_o = \dot{\theta}_o = 0$

5.3.4 Dimensional Stability Derivatives in Terms of Non-Dimensional Stability Derivatives

Longitudinal

$$\begin{aligned} X_u &= \frac{\rho S U}{m} (-C_D - C_{D_u}) & Z_u &= \frac{\rho S U}{m} (-C_L - C_{L_u}) & M_u &= \frac{\rho S U \bar{c}}{I_y} (C_m + C_{m_u}) \\ &+ \frac{1}{m} \left(\frac{\partial T}{\partial u} \right) \cos(\alpha_T + \alpha_o) & & - \frac{1}{m} \left(\frac{\partial T}{\partial u} \right) \sin(\alpha_T + \alpha_o) & & + \frac{z_T}{I_y} \left(\frac{\partial T}{\partial u} \right) \end{aligned}$$

$$X_w = \frac{\rho S U}{2m} (C_L - C_{D_\alpha}) \quad Z_w = \frac{\rho S U}{2m} (-C_{L_\alpha} - C_D) \quad M_w = \frac{\rho S U \bar{c}}{2I_y} (C_{m_\alpha})$$

$$X_{\delta_e} = \frac{\rho S U^2}{2m} (-C_{D_{\delta_e}}) \quad Z_w = \frac{\rho S \bar{c}}{4m} (-C_{L_{\dot{\alpha}}}) \quad M_w = \frac{\rho S \bar{c}^2}{4I_y} (C_{m_{\dot{\alpha}}})$$

$$Z_q = \frac{\rho S U \bar{c}}{4m} (-C_{L_q}) \quad M_q = \frac{\rho S U \bar{c}^2}{4I_y} (C_{m_q})$$

$$Z_{\delta_e} = \frac{\rho S U^2}{2m} (-C_{L_{\delta_e}}) \quad M_{\delta_e} = \frac{\rho S U^2 \bar{c}}{2I_y} (C_{m_{\delta_e}})$$

Lateral

$$Y_\beta = \frac{\rho S U}{2m} C_{y_\beta} \quad L_\beta = \frac{\rho S U^2 b}{2I_x} C_{l_\beta} \quad N_\beta = \frac{\rho S U^2 b}{2I_z} C_{n_\beta}$$

$$Y_{\dot{\beta}} = \frac{\rho S b}{4m} C_{y_{\dot{\beta}}} \quad L_{\dot{\beta}} = \frac{\rho S U b^2}{4I_x} C_{l_{\dot{\beta}}} \quad N_{\dot{\beta}} = \frac{\rho S U b^2}{4I_z} C_{n_{\dot{\beta}}}$$

$$Y_p = \frac{\rho S b}{4m} C_{y_p} \quad L_p = \frac{\rho S U b^2}{4I_x} C_{l_p} \quad N_p = \frac{\rho S U b^2}{4I_z} C_{n_p}$$

$$Y_r = \frac{\rho S b}{4m} C_{y_r} \quad L_r = \frac{\rho S U b^2}{4I_x} C_{l_r} \quad N_r = \frac{\rho S U b^2}{4I_z} C_{n_r}$$

$$Y_{\delta_a} = \frac{\rho S U}{2m} C_{y_{\delta_a}} \quad L_{\delta_a} = \frac{\rho S U^2 b}{2I_x} C_{l_{\delta_a}} \quad N_{\delta_a} = \frac{\rho S U^2 b}{2I_z} C_{n_{\delta_a}}$$

$$Y_{\delta_r} = \frac{\rho S U}{2m} C_{y_{\delta_r}} \quad L_{\delta_r} = \frac{\rho S U^2 b}{2I_x} C_{l_{\delta_r}} \quad N_{\delta_r} = \frac{\rho S U^2 b}{2I_z} C_{n_{\delta_r}}$$

Definitions

T	Thrust, lbs
α_T	Angle between thrust axis and body x-axis
α_o	Initial angle of attack
z_T	Thrust moment arm, ft

5.3.5 Conversion of Inertia Data From Body Axes to Stability Axes

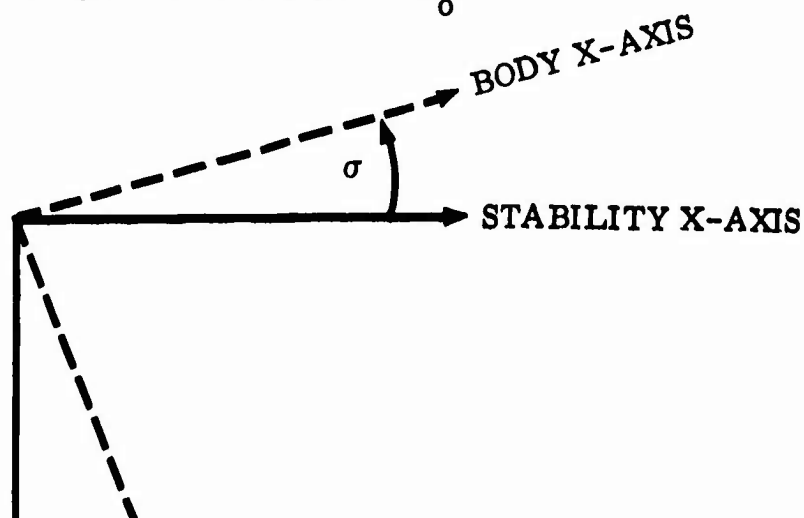
If I_{xb} , I_{zb} , and I_{xzb} are the moments and product of inertia expressed in body axes, and σ is the angle between the body x-axis and the stability x-axis, then the moments of inertia and product of inertia in the stability axis system (I_x , I_z , and I_{xz}) are:

$$I_x = (I_{zb} + I_{xb})/2 - (I_{zb} - I_{xb}) (\cos 2\sigma)/2 - I_{xzb} (\sin 2\sigma) \quad (18)$$

$$I_z = (I_{zb} + I_{xb})/2 + (I_{zb} - I_{xb}) (\cos 2\sigma)/2 + I_{xzb} (\sin 2\sigma) \quad (19)$$

$$I_{xz} = I_{xzb} (\cos 2\sigma) - (I_{zb} - I_{xb}) (\sin 2\sigma) \quad (20)$$

NOTE: If conventional body axes are used $\sigma = \alpha_o$



Equations (1), (2), (3), (7), (8), and (9) were modified to include coupling terms from the lateral to the longitudinal modes. In addition, the gravity components were computed using the Yaw-Roll-Pitch direction cosine relationships. The gravity perturbation values were then computed by subtracting the gravity values, obtaining at the initial flight altitude.

The modified equation of motion became as follows:

$$\dot{u} = X_u u + X_w w + X_{\delta e} \delta e + (g_x - g_{x_0}) + rv - qW_0 \quad (21)$$

$$\dot{w} = Z_u u + Z_{\dot{w}} \dot{w} + Z_w w + Z_q q + Z_{\delta e} \delta e + (g_z - g_{z_0}) + qU_0 - pv \quad (22)$$

$$\dot{q} = M_u u + M_{\dot{w}} \dot{w} + M_w w + M_q q + M_{\delta e} \delta e - p^2 \frac{(I_x)}{I_y} - \frac{rH_x}{I_y} - pr \frac{(I_x - I_z)}{I_y} \quad (23)$$

$$\dot{p} = L_{\beta} \beta + L_{\delta a} \delta a + L_{\delta r} \delta r + L_r r + L_p p + \frac{rI_{xz}}{I_x} qr \frac{(I_z - I_y)}{I_x} \quad (24)$$

$$\dot{r} = N_{\beta} \beta + N_{\delta a} \delta a + N_{\delta r} \delta r + N_p p + N_r r + \frac{pI_{xz}}{I_z} - \frac{(I_y - I_x)}{I_z} pq + \frac{qH_x}{I_z} \quad (25)$$

$$\beta = Y_{\beta} \beta + Y_{\delta a} \delta a + Y_{\delta r} \delta r + Y_r p - r + \frac{(g_y - g_{y_0})}{U_0} + p\alpha_0 \quad (26)$$

Where:

$$g_{x_0} = g_{\ell_{z_0}} = -g \sin \theta_0 \cos \phi_0$$

$$g_{y_0} = g_{m_{\ell_{z_0}}} = g \sin \phi_0$$

$$g_{z_0} = g_{n_{\ell_{z_0}}} = g \cos \theta_0 \cos \phi_0$$

and

$$\dot{\phi} = r$$

$$\dot{\phi} = p$$

$$\dot{\theta} = q$$

U_o = initial x axis velocity component

W_o = initial z axis velocity component

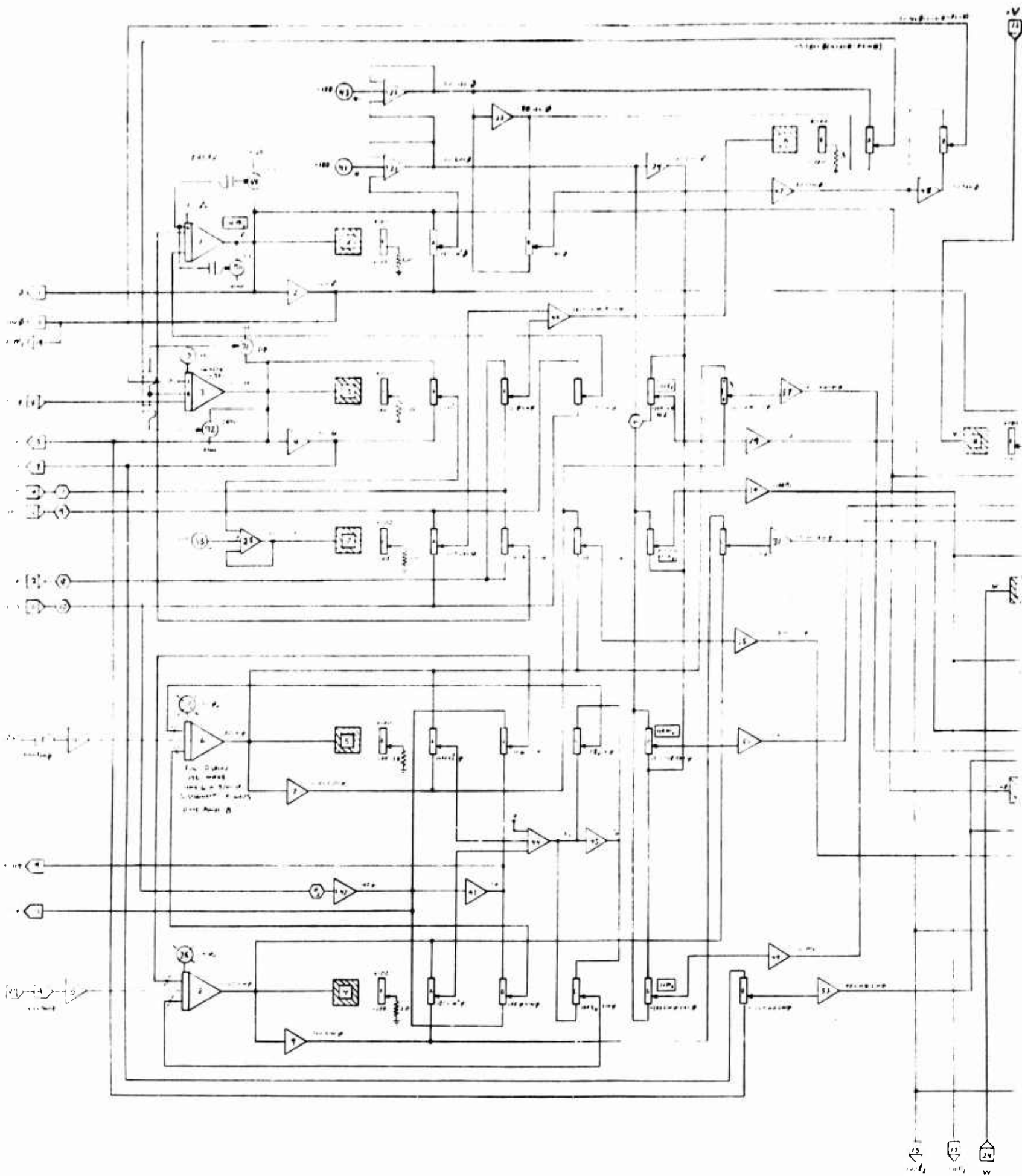
H_x = x axis component of power plant angular momentum

H_z = z axis component of power plant angular momentum

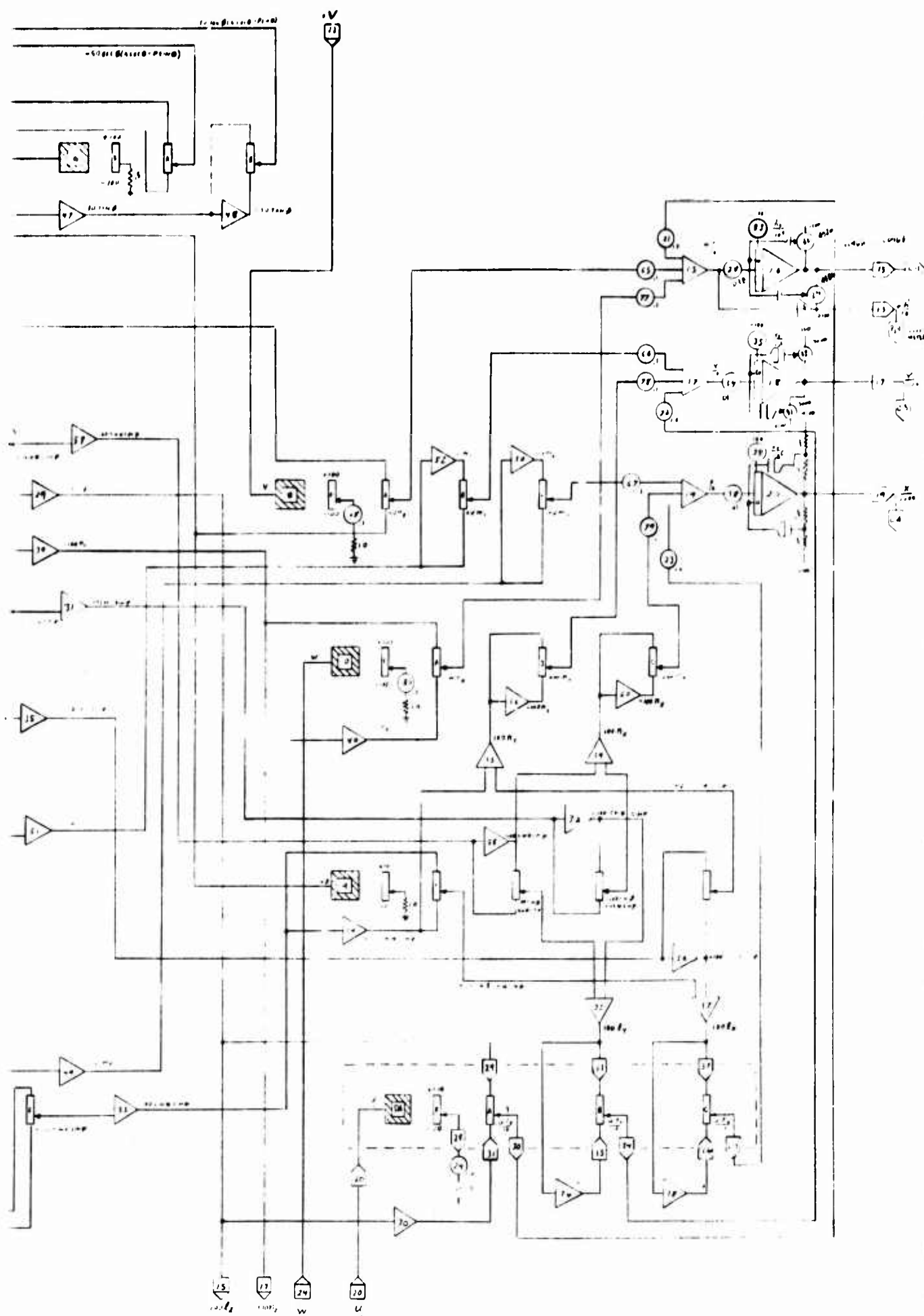
The computer diagrams used to mechanize these equations are shown in Figures 52, 53 and 54.

,

o



A



C3	B5	I4
C4	B6	I5
D3	B6	I6
E4	B7	I7
H3		D5
H4		
I3	A3	I1
K4		I2
		I3
		I4
		I5
		I6
		I7
		I8
		I9
		I10
		I11
		I12
		I13
		I14
		I15
		I16
		I17
		I18
		I19
		I20
		I21
		I22
		I23
		I24
		I25
		I26
		I27
		I28
		I29
		I30
		I31
		I32
		I33
		I34
		I35
		I36
		I37
		I38
		I39
		I40
		I41
		I42
		I43
		I44
		I45
		I46
		I47
		I48
		I49
		I50
		I51
		I52
		I53
		I54
		I55
		I56
		I57
		I58
		I59
		I60
		I61
		I62
		I63
		I64
		I65
		I66
		I67
		I68
		I69
		I70
		I71
		I72
		I73
		I74
		I75
		I76
		I77
		I78
		I79
		I80
		I81
		I82
		I83
		I84
		I85
		I86
		I87
		I88
		I89
		I90
		I91
		I92
		I93
		I94
		I95
		I96
		I97
		I98
		I99
		I100

Figure 52 Axis Transformation

8

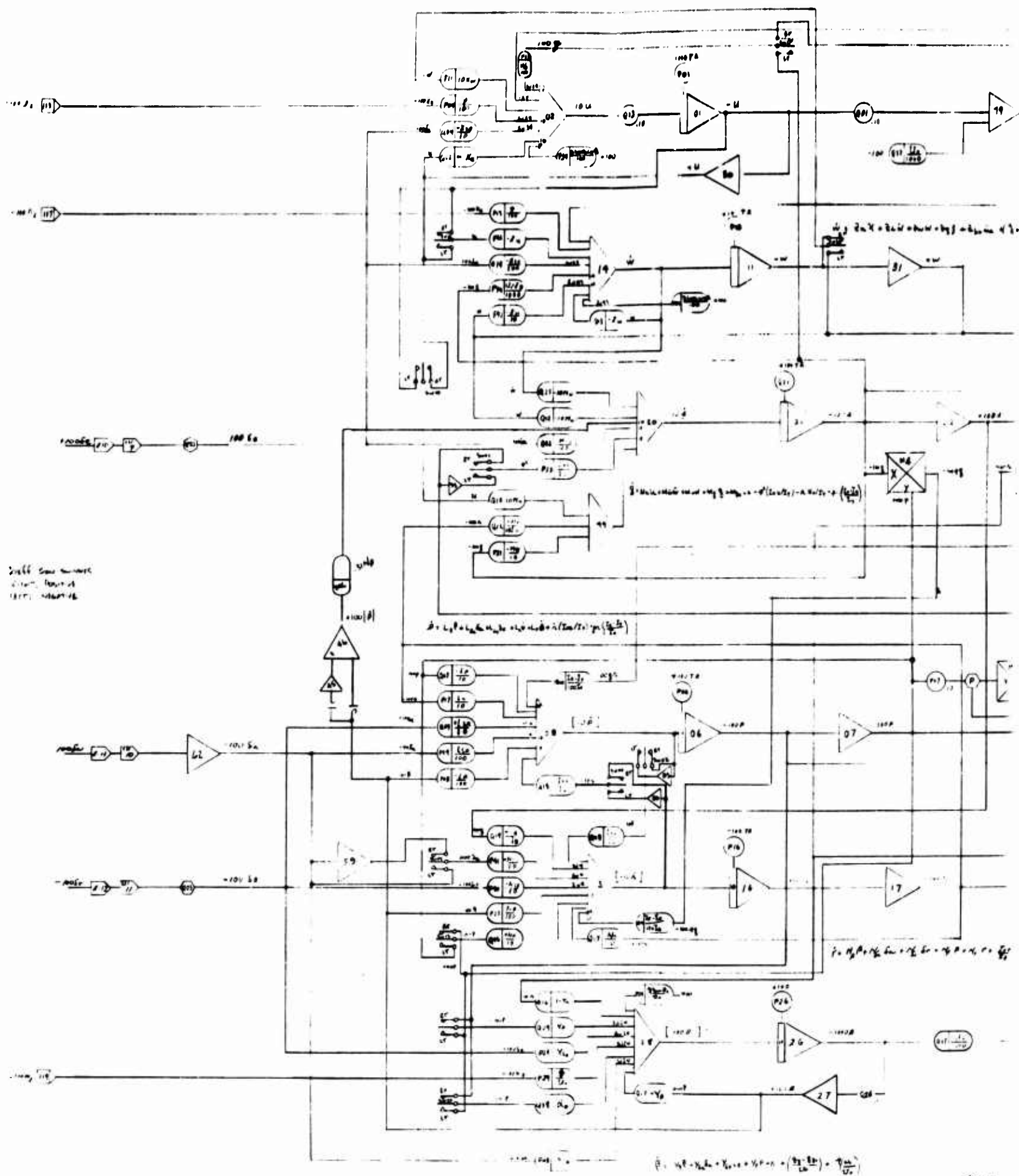
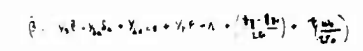


Figure 5

$$= \cancel{V_1} \cdot \cancel{I_1} + \cancel{V_2} \cdot \cancel{I_2} + V_3 \cdot I_3 + (V_1 - V_2) \cdot \Delta V - I_3 \Delta V$$



HIS
HIS
LIS
FIS
IIS
IIS

GI
CI
KI
SIS
KIS
DIS

B

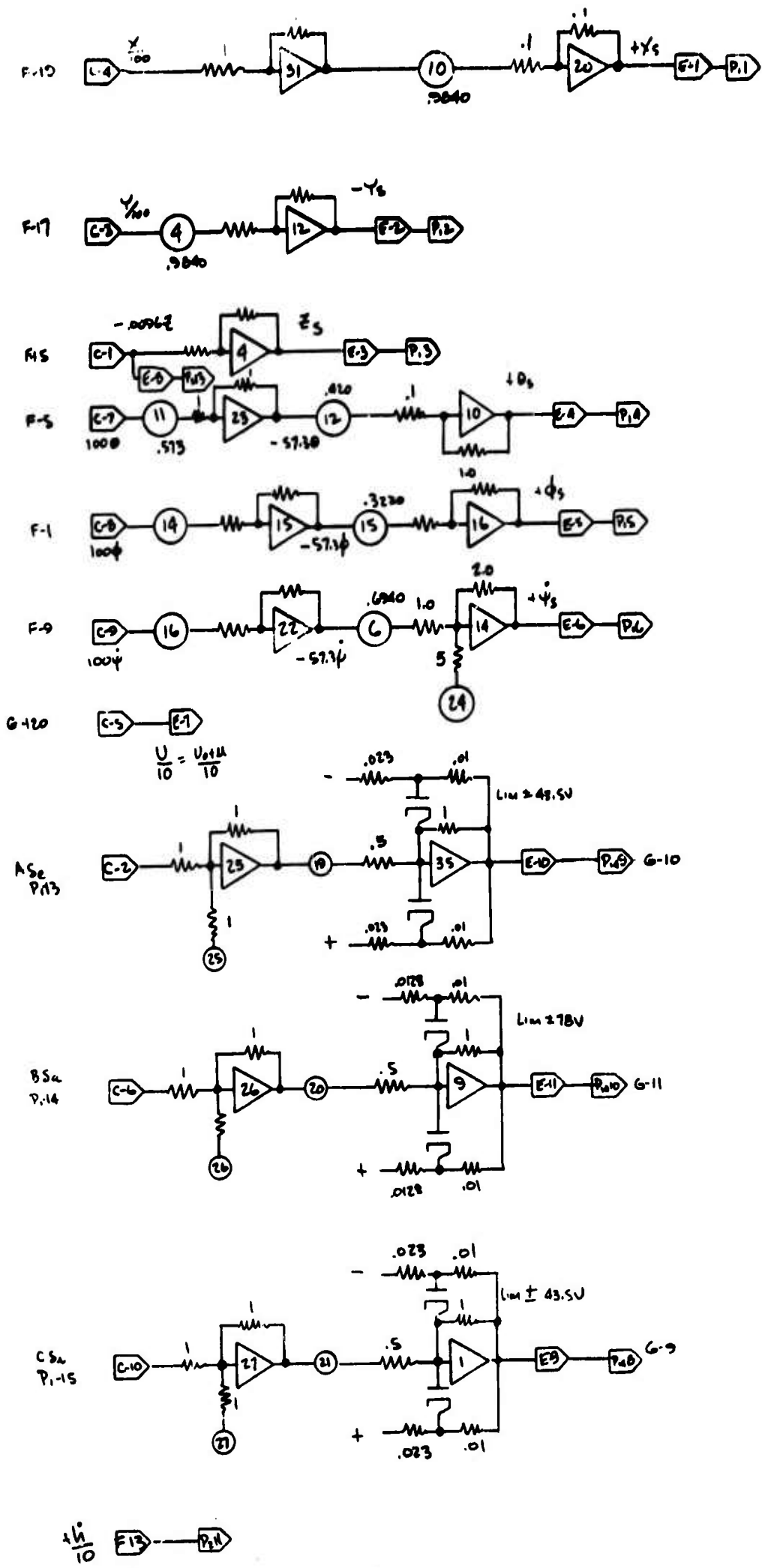


Figure 54 DeFlores Display Input Computer Diagram

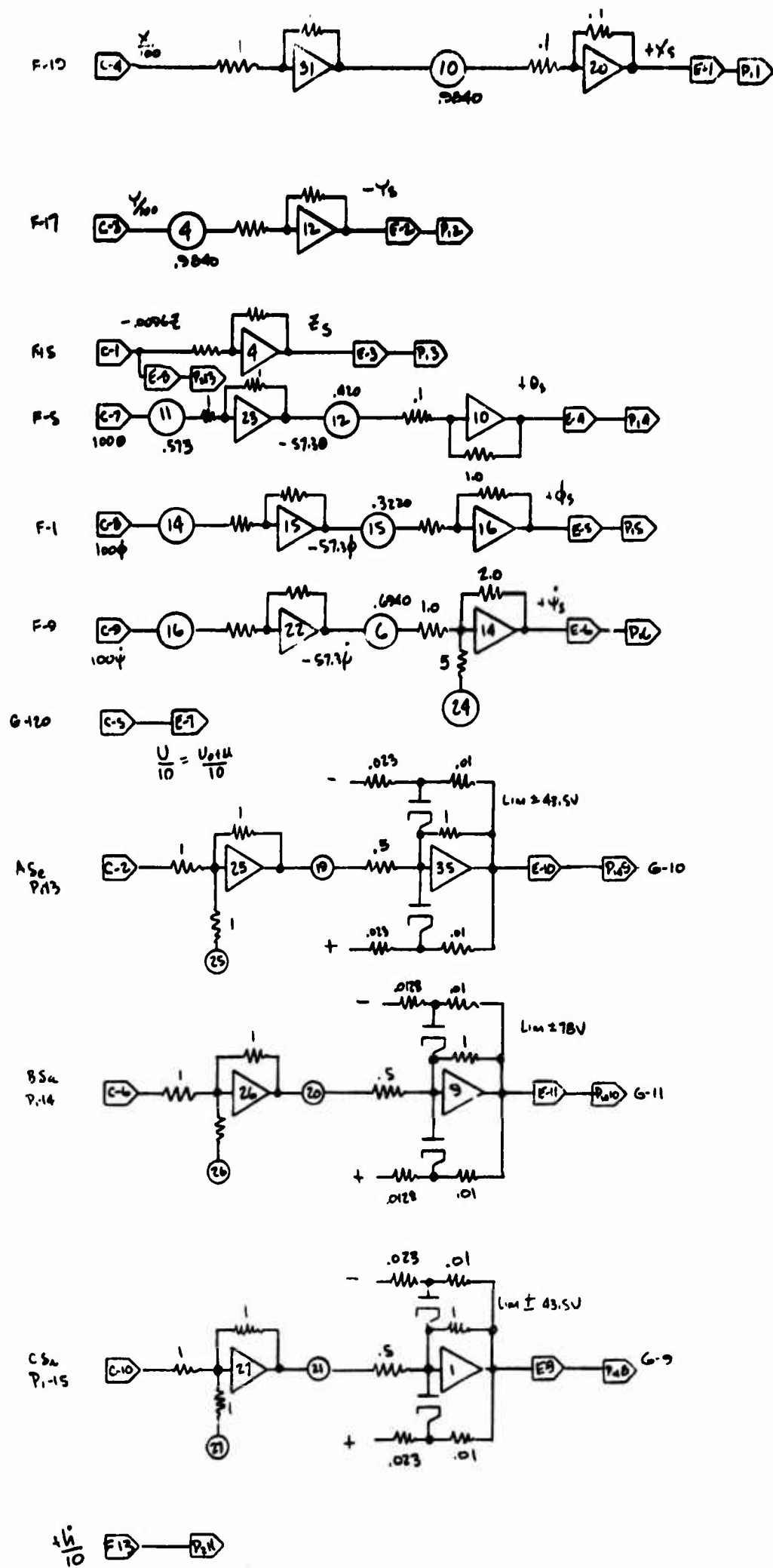


Figure 54 DeFlorez Display Input Computer Diagram

6.0 GAS GENERATOR CONTROL ANALYSIS

6.1 Discussion

The possibility of using J-85 RPM alone for hovering thrust control was investigated concurrently with the hovering simulation. The fan response was approximated by an equivalent first order lag of $\tau = .6$ seconds at the fan speed necessary to enable hovering at 2500 feet on a hot day. The J-85 response was simulated using a small-perturbation analysis around 98% J-85 RPM, and including the limiting effects of the fuel-control system. The computer wiring for the J-85/Fan combination is shown in Figures 56 and 57 following.

Let us assume for the moment that the combined engine-fan response can be approximated by the transfer function

$$\frac{\text{Thrust}}{\text{Thrust Command}} = \frac{1}{(1 + .6S)(1 + \tau_e S)}$$
 the .6 second time constant being the fan equivalent fan lag and the engine being represented by a first order lag of τ_e . This is not a true representation of the engine, but it will suffice for this discussion.

If we can introduce a transfer-function between the throttle and engine of $\frac{1 + \tau_1 S}{1 + \tau_2 S}$, it would be possible to make $\tau_1 = .6$ second, and thus cancel the engine .6 second lag.

This transfer function may be written also as $\frac{E_o}{E_{IN}} = K_1 \frac{(1 + K_2 \tau S)}{1 + \tau S}$,

where τ is fixed at an arbitrary value and K_2 is called the "magnification factor". The response of this transfer function to a step input shown in Figure 57, assuming $K_1 = 1.0$ and $K_2 = 4$.

An example of an electrical network to realize the transfer function is also shown in Figure 57.

This network has the transfer function $\frac{E_o}{E_{in}} = \frac{R_2}{R_1 R_2} \times \frac{(1 + R_1 C S)}{\left(1 + \frac{R_1 R_2 C S}{R_1 + R_2}\right)}$,

where we can let $K_1 = \frac{R_2}{R_1 + R_2}$, $\tau = \frac{R_2 R_1 C}{R_1 R_2}$, and

$$K_2 = \frac{R_1 + R_2}{R_2}.$$

A passive hydraulic unit could be mechanized to give the same transfer function.

By applying this transfer function between the throttle and fuel control, we obtain the complete system transfer function

$\frac{\text{Thrust}}{\text{Thrust}_{\text{pilot command}}} = \frac{K_1 (1 + K_2 \tau S)}{(1 + .6S)(1 + \tau_e S)(1 + \tau S)}$. It is seen that we can choose K_2 and τ so that the $1 + .6S$ term is cancelled, and the resulting transfer function has the engine lag plus a new lag which has a shorter time constant than the fan lag. In this manner the system response can be improved.

However, there is a limit on how large K_2 can be, and this therefore limits the value of τ . Due to the fuel-flow limiting effects of the acceleration cam in the J-c fuel control, increasing K_2 to a large value does not necessarily result in improved system response.

Assuming 98% gas generator RPM is required for hovering flight at 2500 feet hot day conditions, two separate conditions of fuel-flow limiting were investigated. A set of data was taken with a 100% N_g throttle limit, using a step 1% ΔN_g command starting at 98% N_g . Another set of data was taken under the same conditions but using a 102% N_g throttle command limit. The parameter measured was the time for the thrust to rise to 90% of the final thrust change, with the restriction that the overshoot should be less than 20% of the thrust change. Figure 58 is a plot of settling time VS magnification factor and τ for 100% N_g command limit, and Figure 59 is the same plot for a 102% N_g command limit.

The improvement in response tapers off as the magnification factor goes up, because an increased input to the fuel control does not result in an increase in fuel flow once the throttle command limit or acceleration cam unit is reached. Thus, beyond a reasonable value, an increase in the magnification factor does little good. If, however, the gas generator is able to operate well below the acceleration cam limit, such as at S.L. standard day, increased magnification can be utilized to advantage. It is desirable to limit the engine speed by limiting the throttle input, because excessive use of the acceleration cam limit can cause a decrease in engine life due to higher average turbine temperature.

As a result of the computer runs used to develop Figures 58 and 59, a τ of .15 second and a magnification factor of 5 have been chosen as optimum. The time to 90% of final value is reduced from 1.4 second to .6 and .5 seconds for throttle command limits of 100% and 102% respectively.

Representative computer records are shown in Figures 60, 61 and 62 for the bare engine and fan, and for the recommended jazzer values and 100% and 102% throttle input limits.

In addition to the computer runs, which include the non-linear effects of the fuel control and throttle input limit, the linearized block diagram furnished by General Electric was solved for the small-perturbation linear J-85 response.

The J-85 block diagram and small perturbation analysis are given in Section 6.2, with pertinent engine data.

The J-85 closed-loop response for small inputs at 100% RPM was thus derived as

$$\frac{\Delta N}{\Delta \left(\frac{W_f}{P_3} \right)} = \frac{55.1 (S/100 + 1) \left(\frac{S^2}{29^2} + \frac{1.8S}{29} + 1 \right)}{\left(\frac{S}{180} + 1 \right) \left(\frac{S^2}{99.7^2} + \frac{1.76S}{99.7} + 1 \right) \left(\frac{S^2}{46.3^2} + \frac{1.84S}{46.3} + 1 \right) \left(\frac{S^2}{12.24^2} + \frac{.986S}{12.24} + 1 \right)}$$

This hand analysis was used to check the computer mechanization of the J-85.

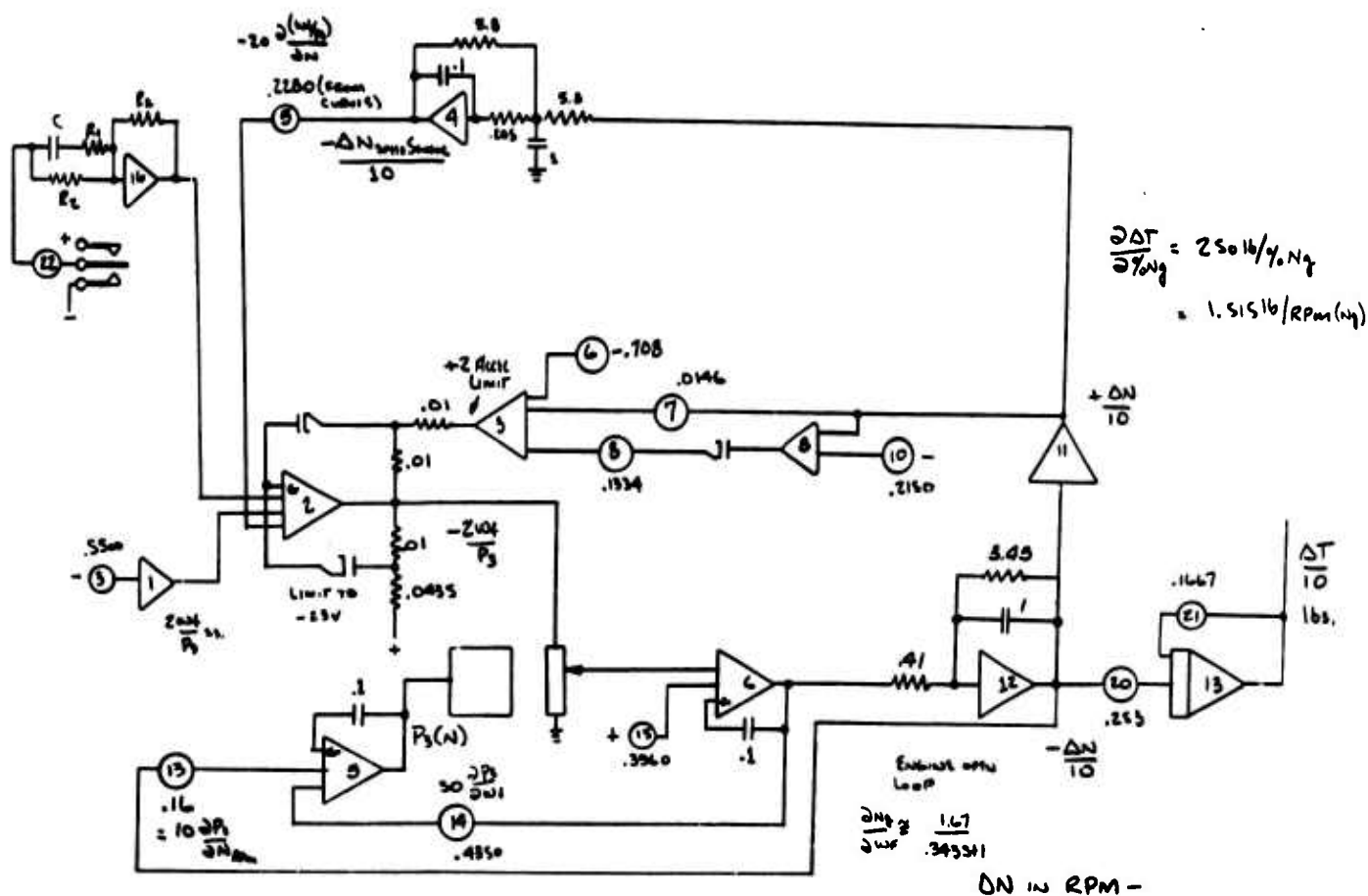


Figure 55 Simplified J-85 Computer Wiring

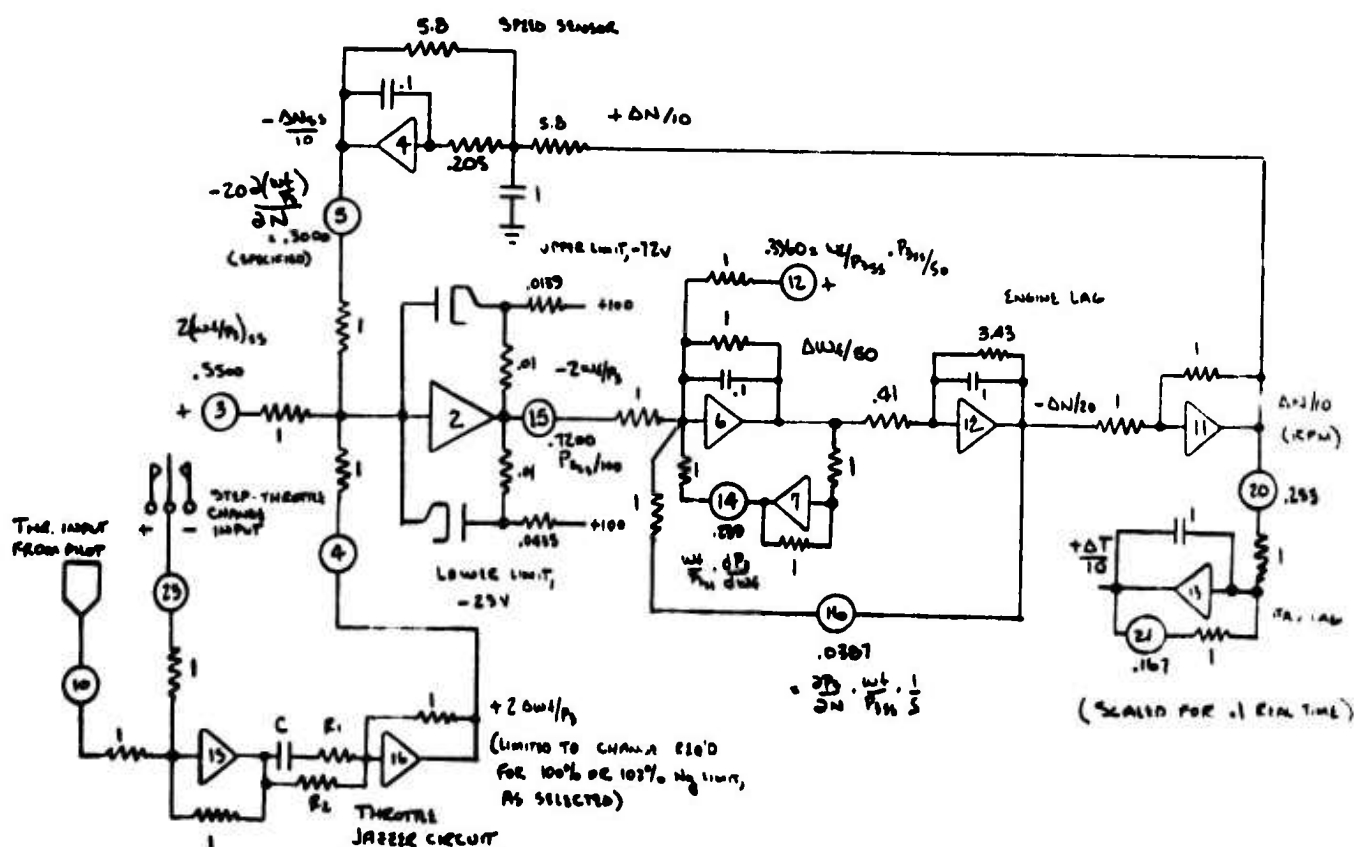


Figure 56 Further Simplified J-85 Computer Wiring

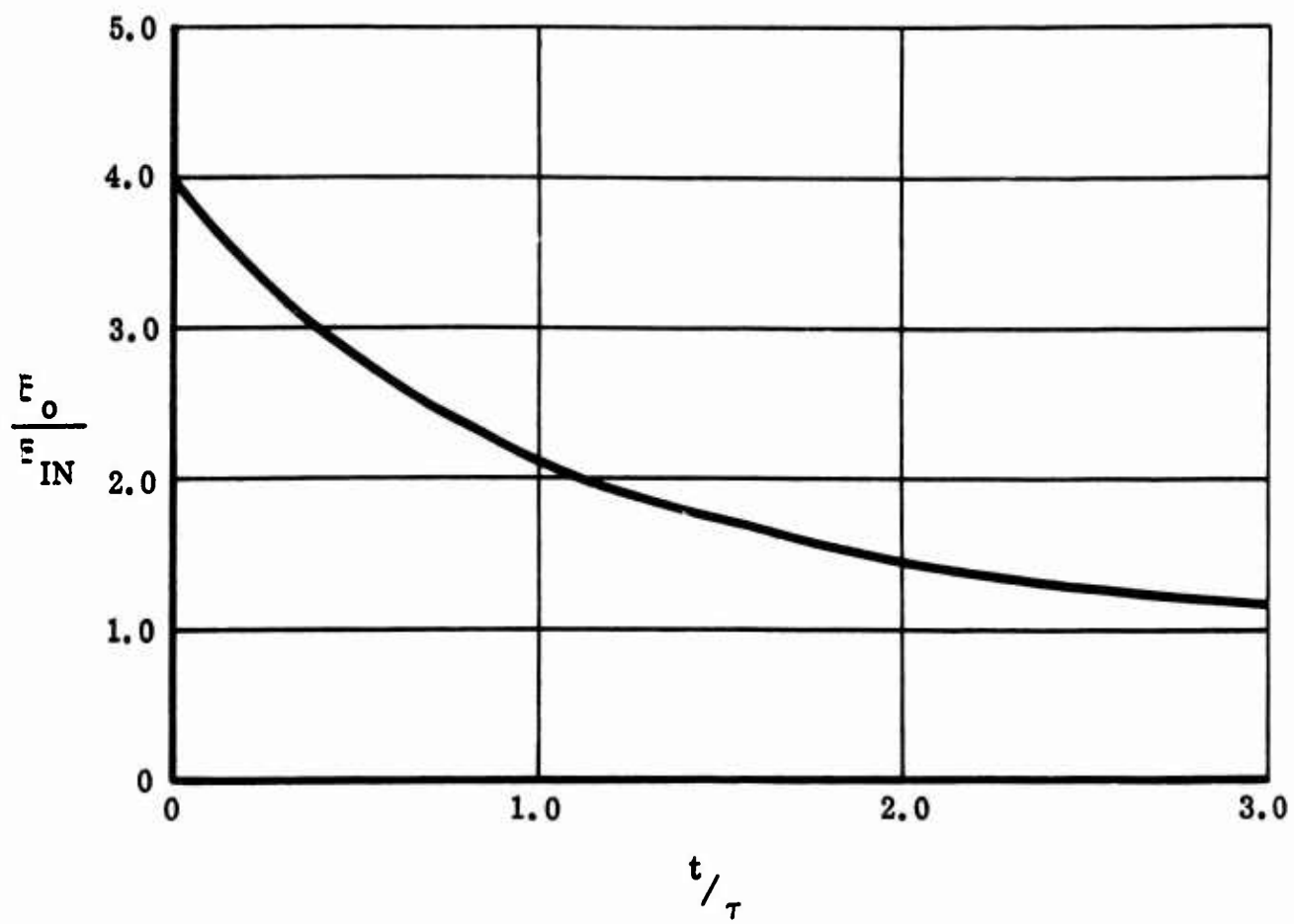


Figure 57A Step Response of Network for $R_2 = \frac{R_1}{3}$

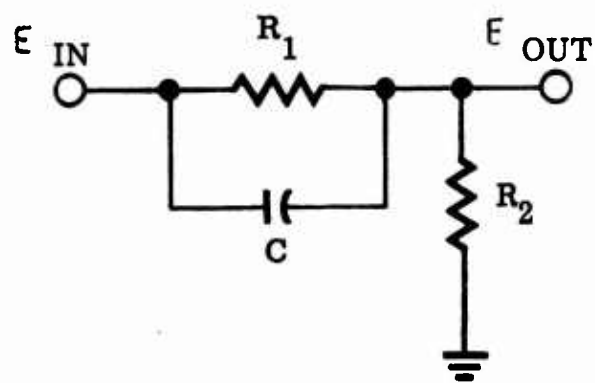


Figure 57B Schematic Diagram of Lead Network

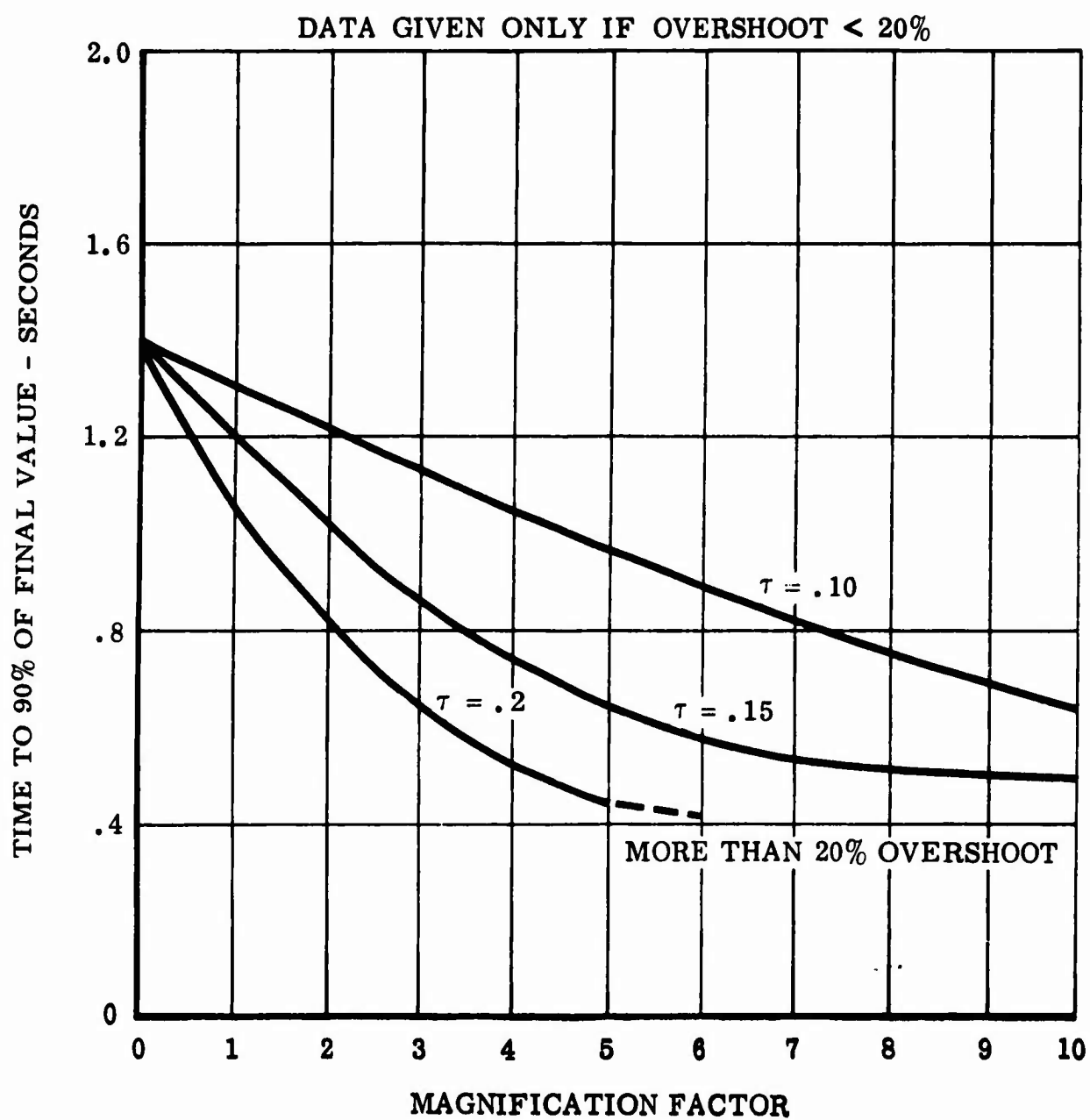


Figure 58 Step Input Response with 100% N_g Command Limit for 1% ΔN_g Input

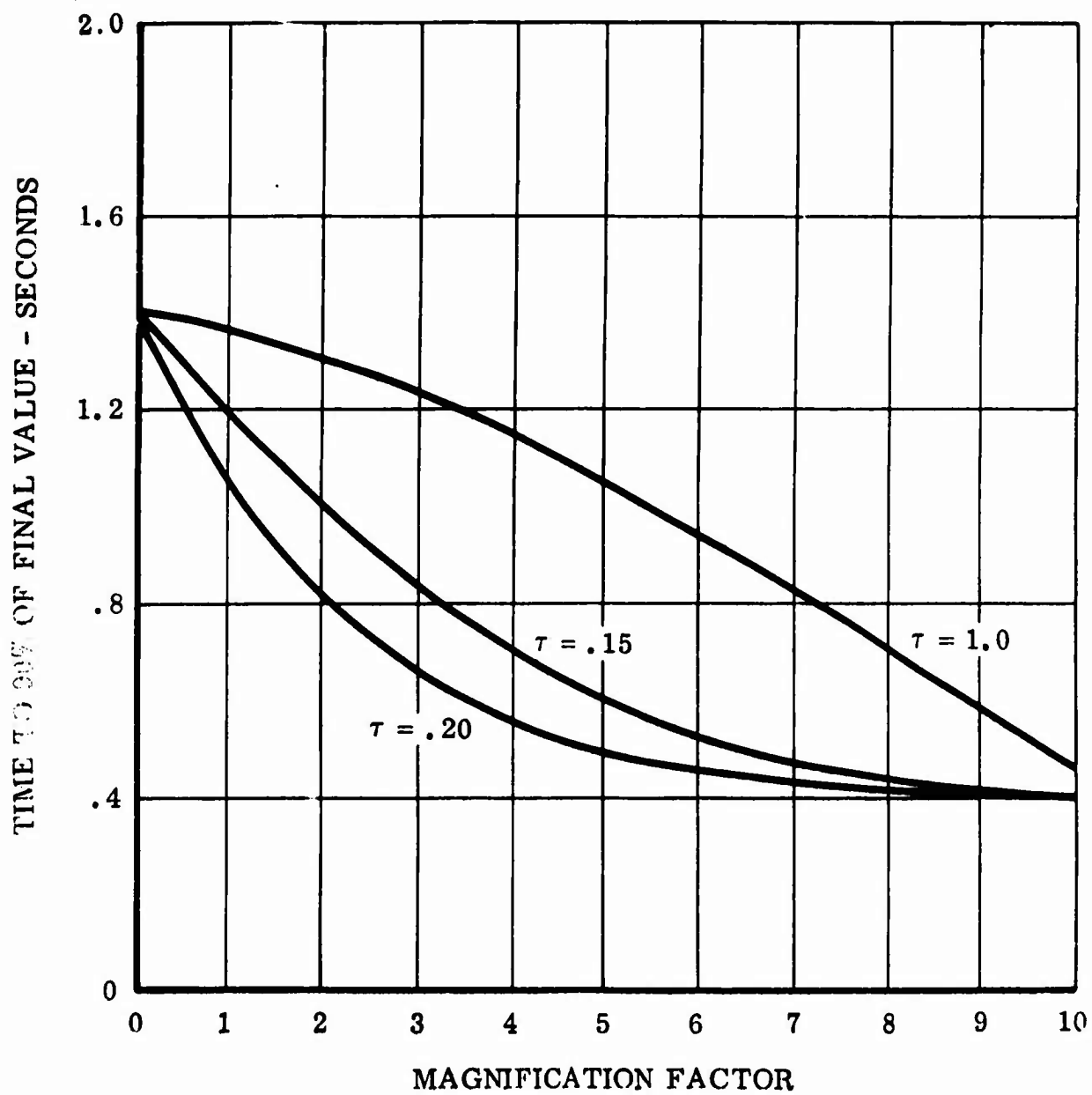


Figure 59. Step Input Responses with 102% Ng Command Limit for 1% Δ Ng Input

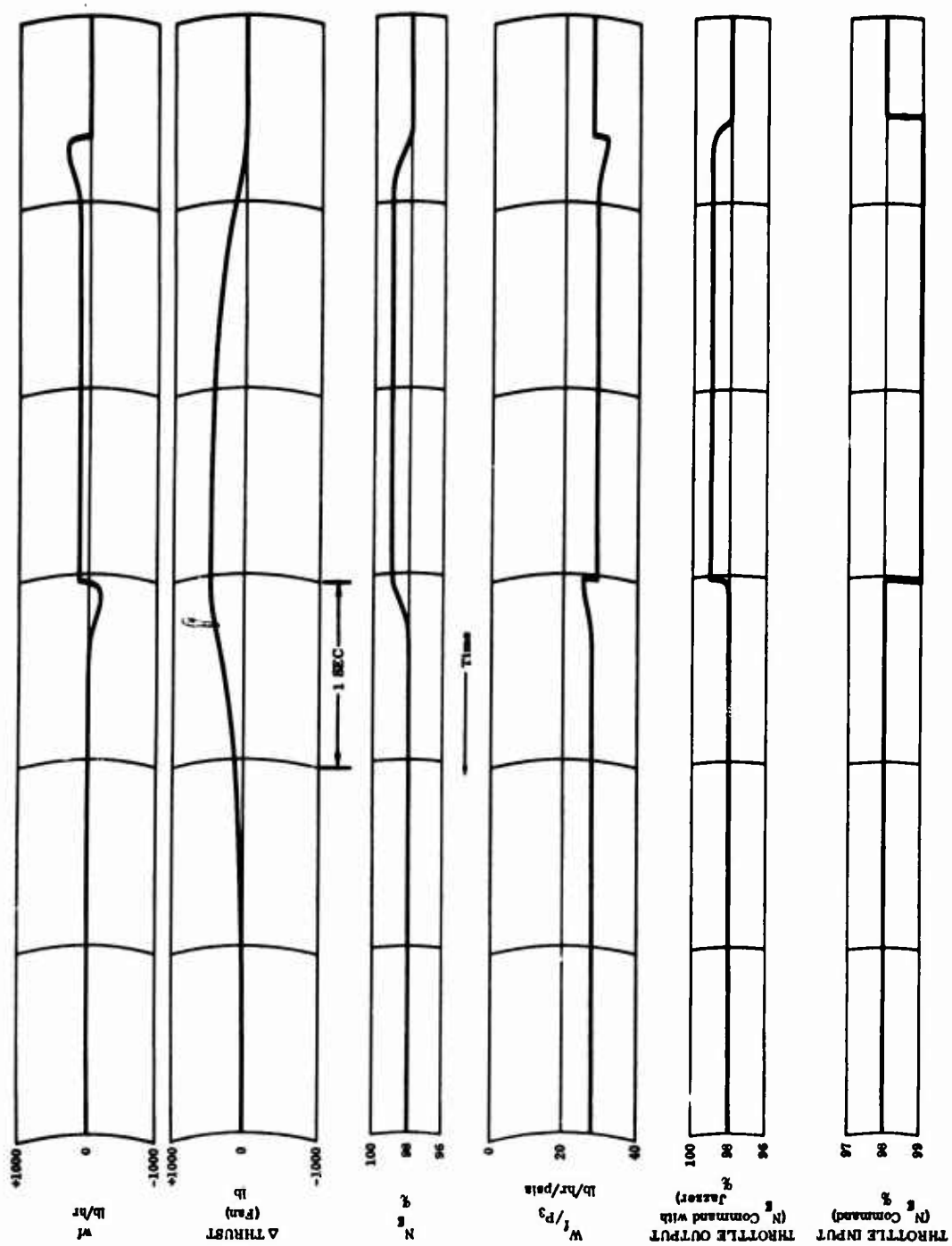


Figure 60 Computer Output Records for Bare EnginePlus Fan Response for 1% ΔN_g Input

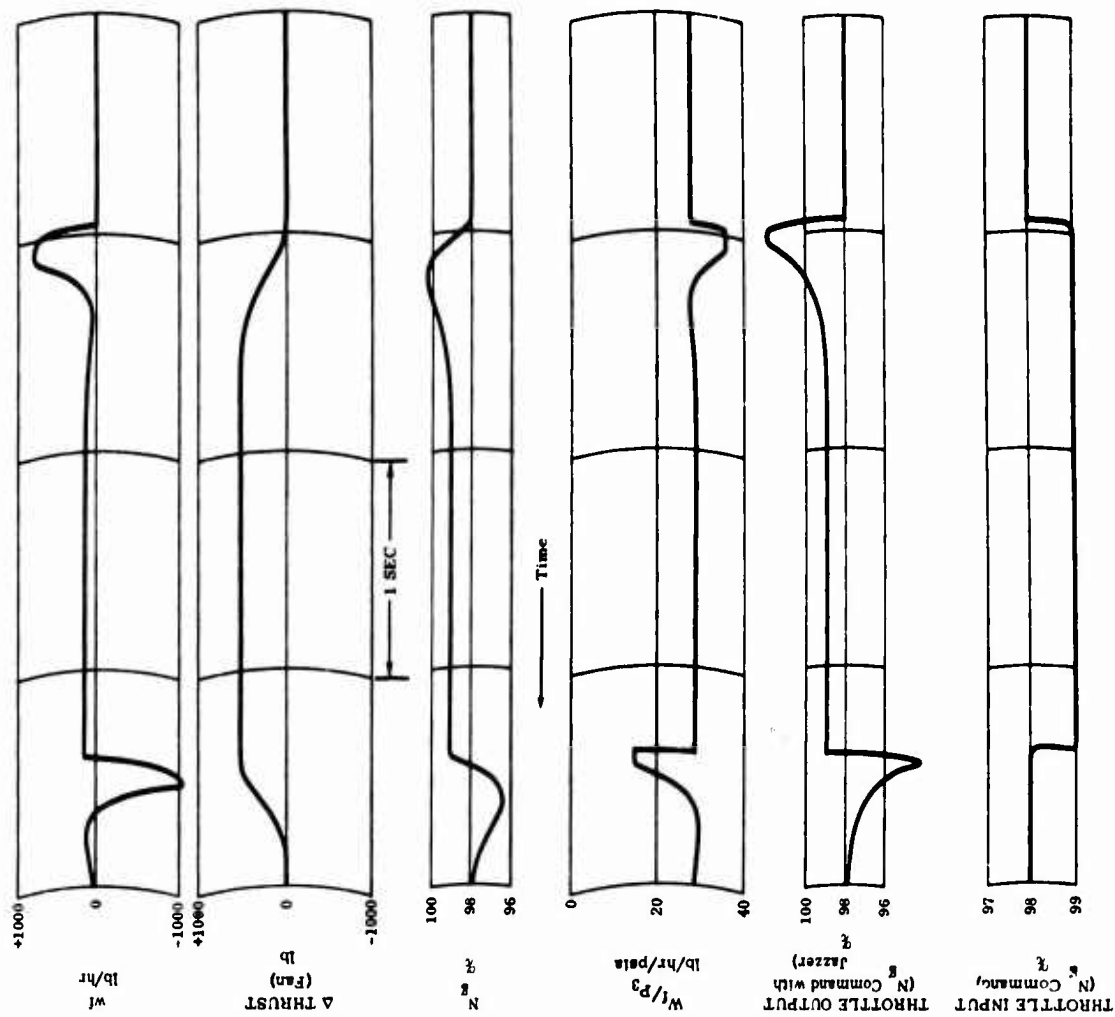


Figure 61 Computer Output Records for 100%
Ng Limit and 1% ΔNg Command

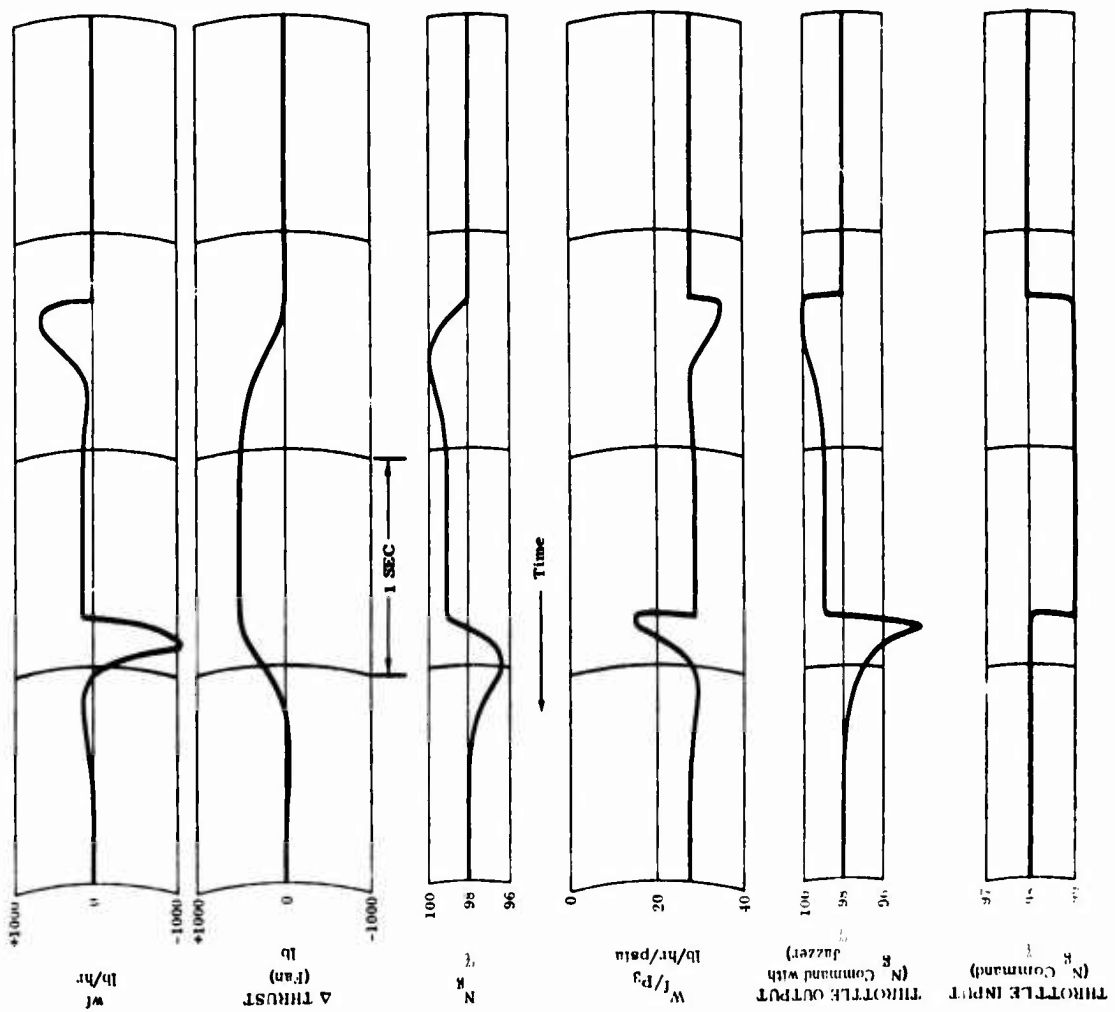


Figure 62 Computer Output Records for 102%
Ng Limit and 1% ΔNg Command

6.2 Analysis

The data used for the small-disturbance hand-calculation of J-85 response are given in Sections 6.2.1 and 6.2.2. Figures 63, 64, and 65 are plots of the data of Section 6.2.1. Figure 66 is a plot of the 95° F, 2500 foot altitude acceleration cam limits on $\frac{W_F}{P_{S3}}$, as well

as the steady state operation line from Section 6.2.1.

Figure 67 is a copy of the original block diagram of the engine and fuel control system as furnished by General Electric. The following Figures 68 through 73 show the successive reductions of this block diagram to a single block, giving the linear closed-loop J-85 response to throttle inputs.

6.2.1 W_f and P_{S3} Values

St'd. Sea Level: $P_{\text{ambient}} = 14.7 \text{ psia}$, $T_{\text{ambient}} = 518.7^\circ \text{ R}$

Mach	J-85 %RPM	P_{S3}	W_f	Mach	J-85 %RPM	P_{S3}	W_f
0	100%	90.08 psia	2679 lb./hr.	0.20	100%	91.96	2734
0	95%	78.62	2082	0.20	95%	79.84	2083
0	90%	62.41	1451	0.20	90%	63.26	1447
0	85%	51.91	1122	0.20	85%	52.48	1116

ANA-421 St'd 2500 Foot Hot Day: $P_{\text{ambient}} = 13.518 \text{ psia}$; $T_{\text{ambient}} = 553.4^\circ \text{ R}$

Mach	J-85 %RPM	P_{S3}	W_f	Mach	J-85 %RPM	P_{S3}	W_f
0	100%	77.23 psia	2258 lb./hr.	0.20	100%	78.56	2286
0	95%	63.97	1609	0.20	95%	64.58	1614
0	90%	51.75	1196	0.20	90%	52.26	1189
0	85%	43.80	989	0.20	85%	43.58	908

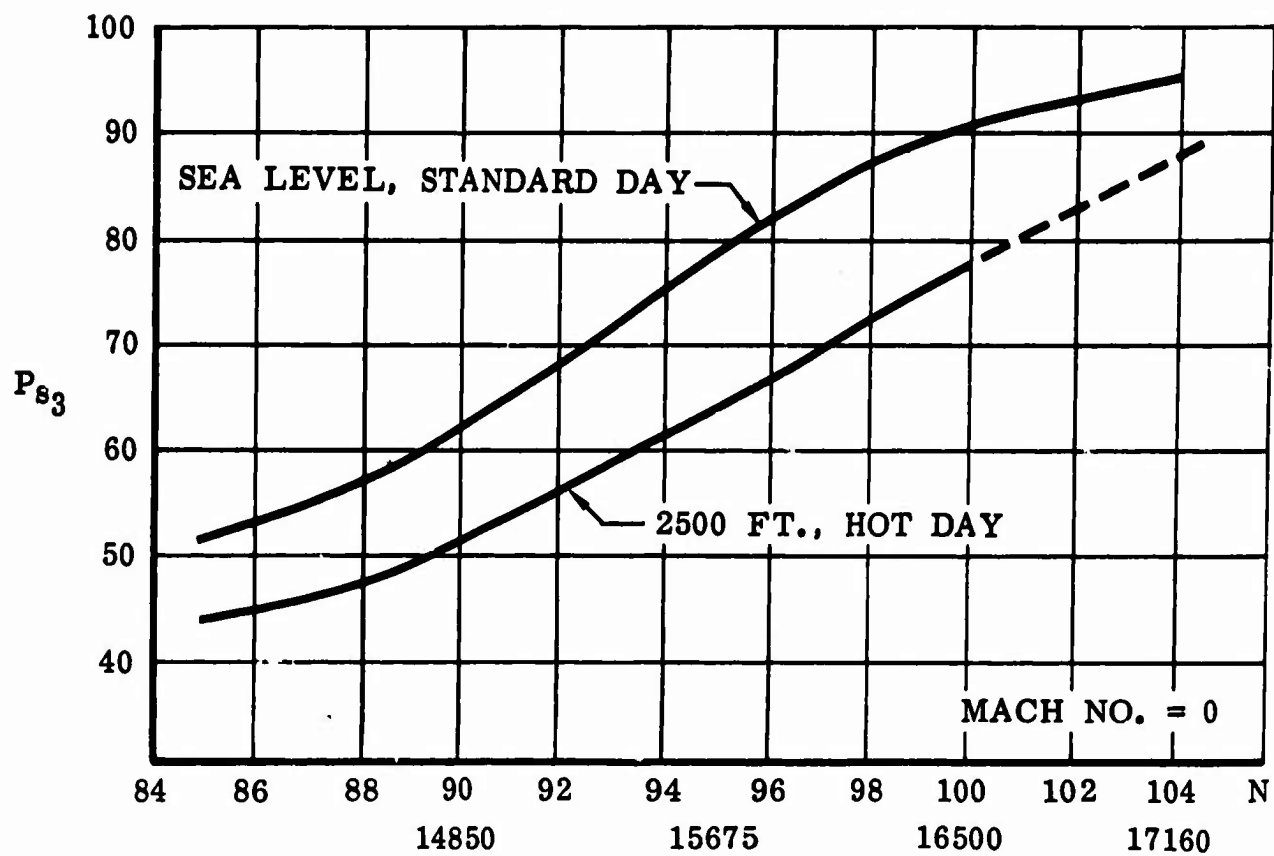


Figure 63 P_{s3} vs N (% RPM)

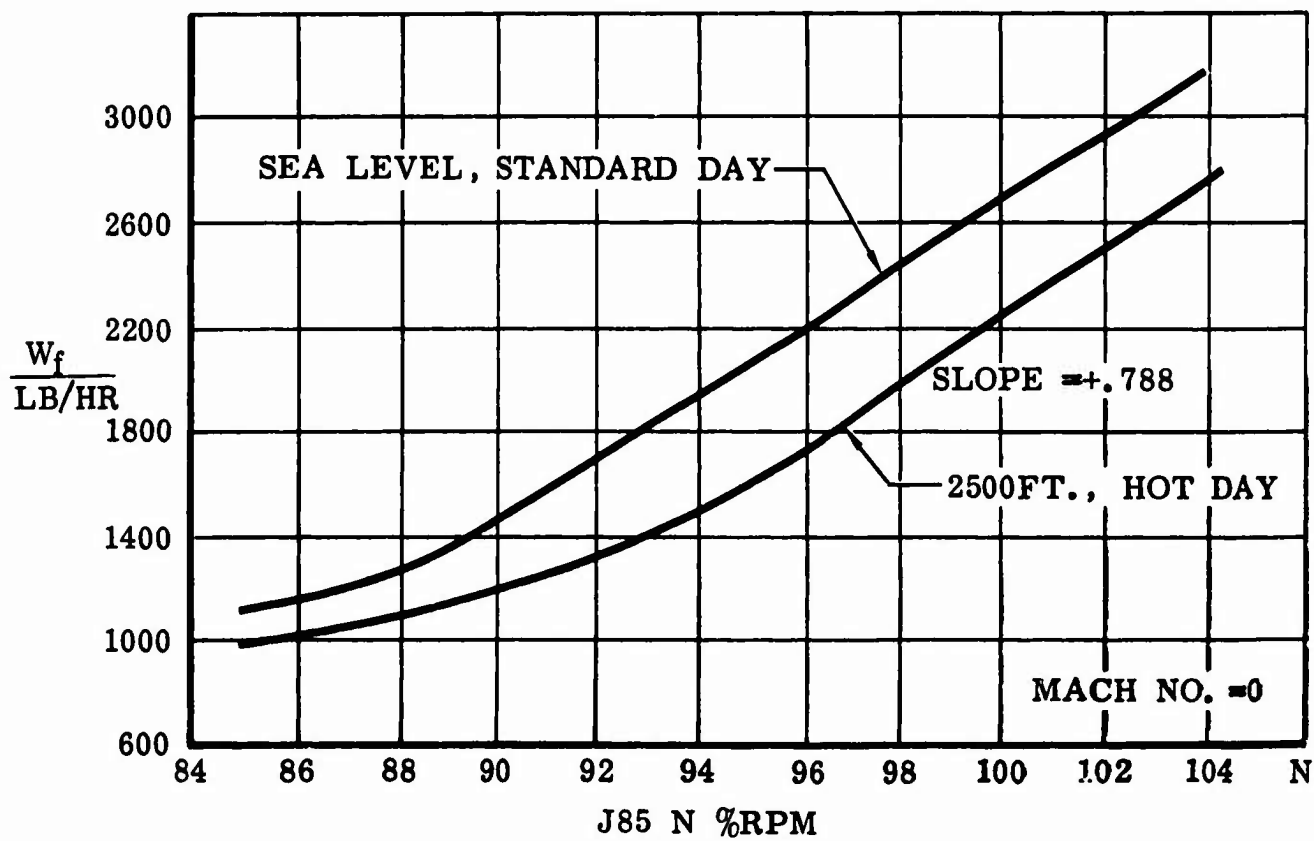


Figure 64 W_f vs N (% RPM)

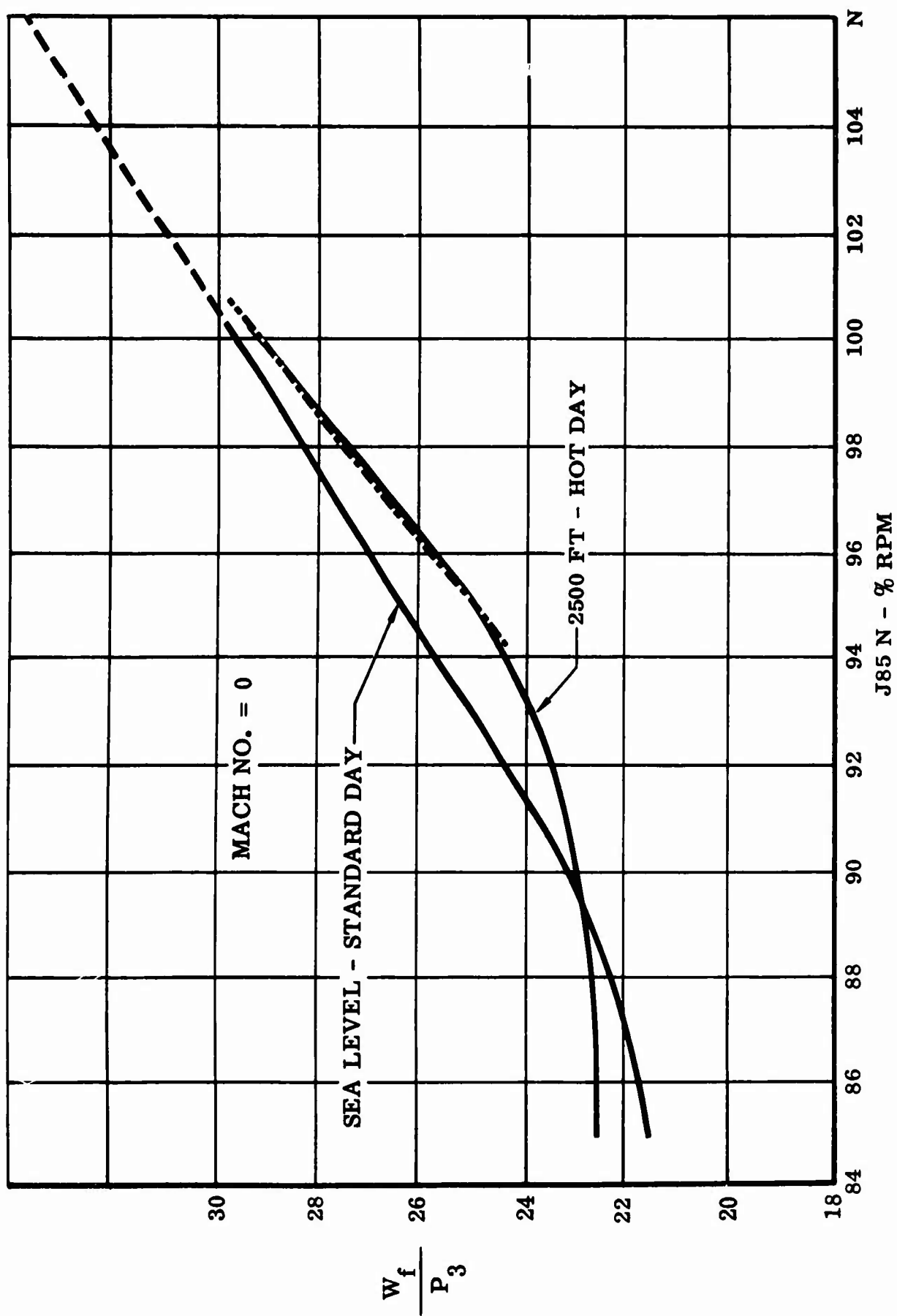


Figure 65 $\frac{W_f}{P_3}$ vs N (% RPM)

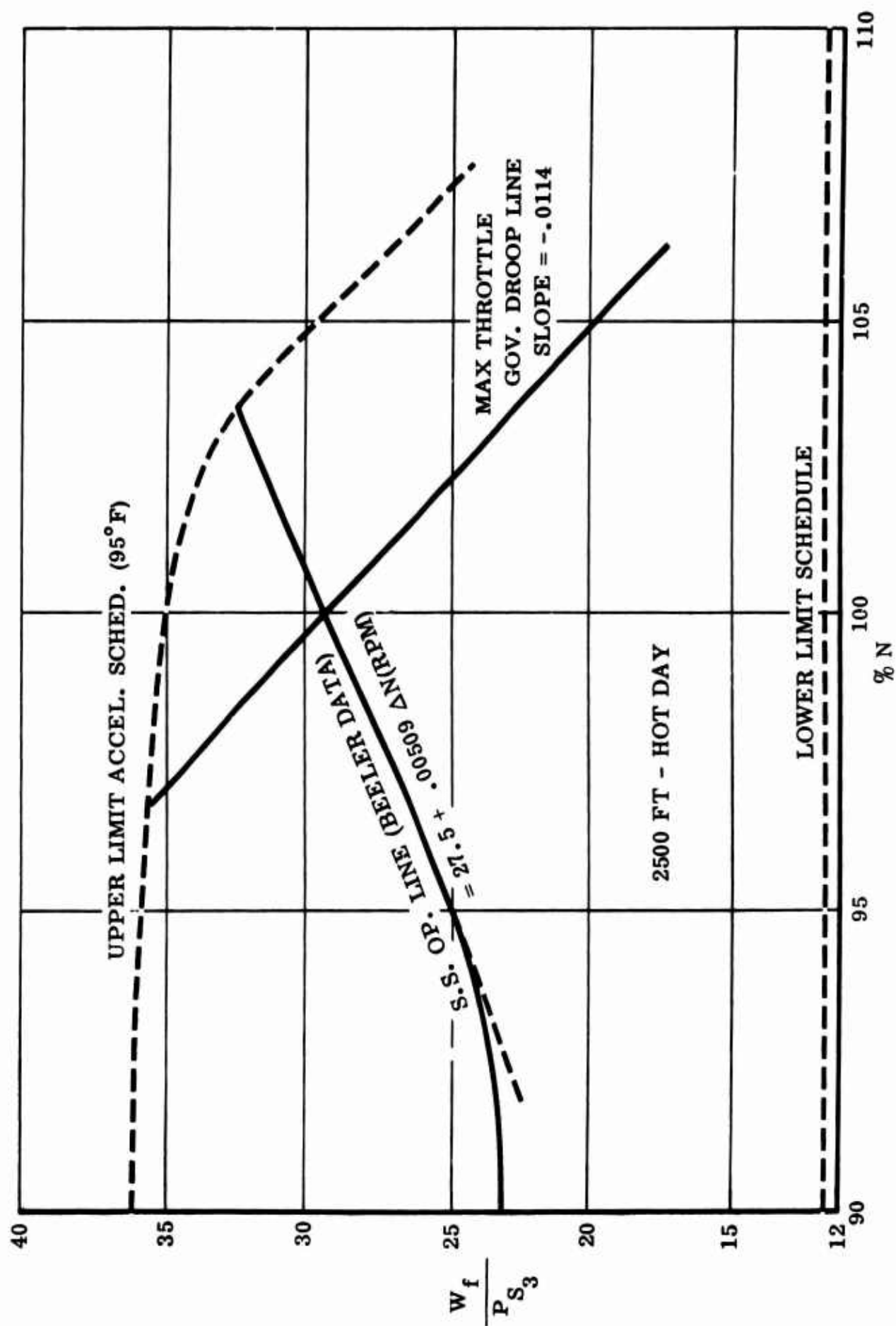


Figure 66 Operational Line and Schedule for 2500' Hot Day

BLANK PAGE

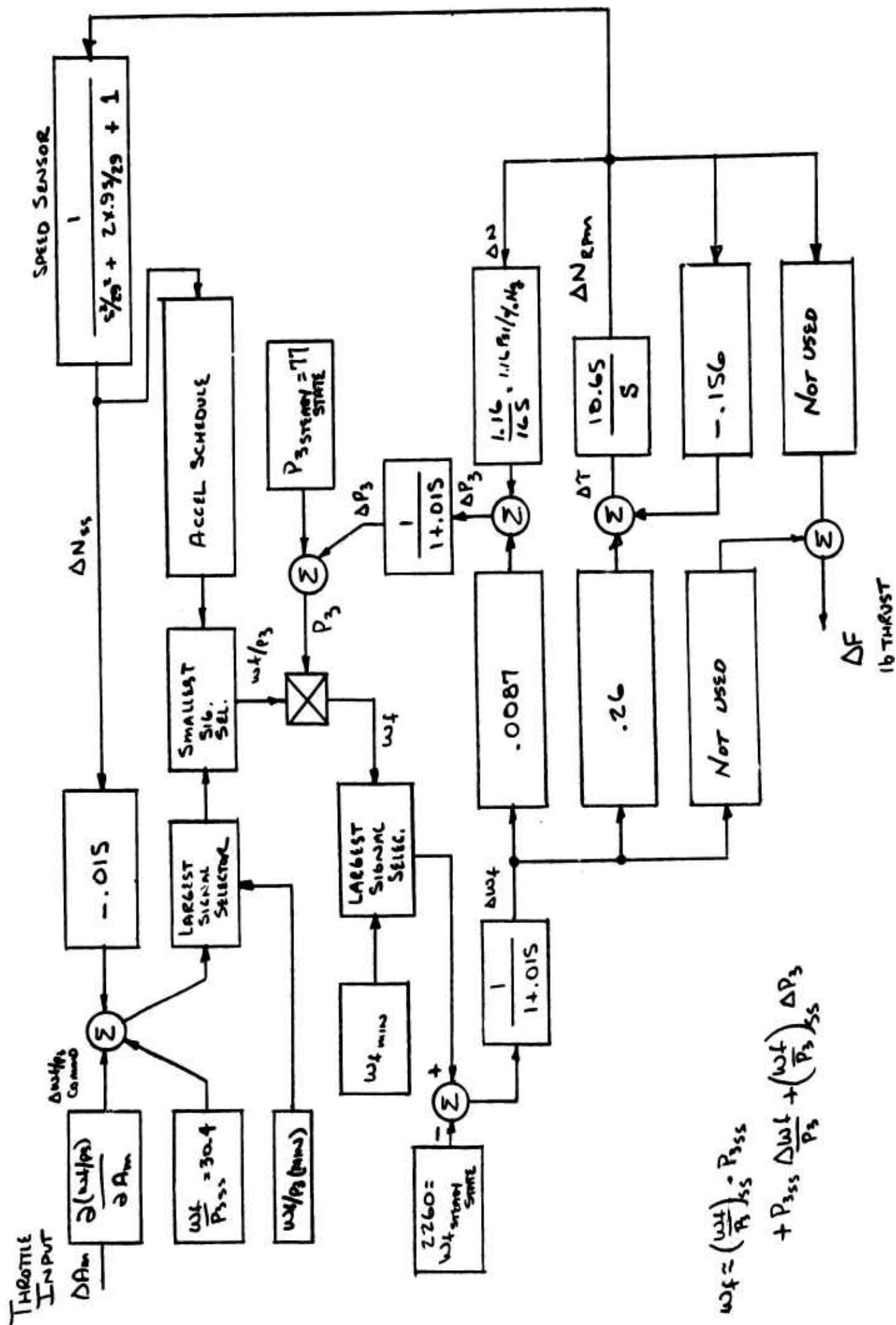


Figure 67 Block Diagram of J-85 Engine and Fuel Control System

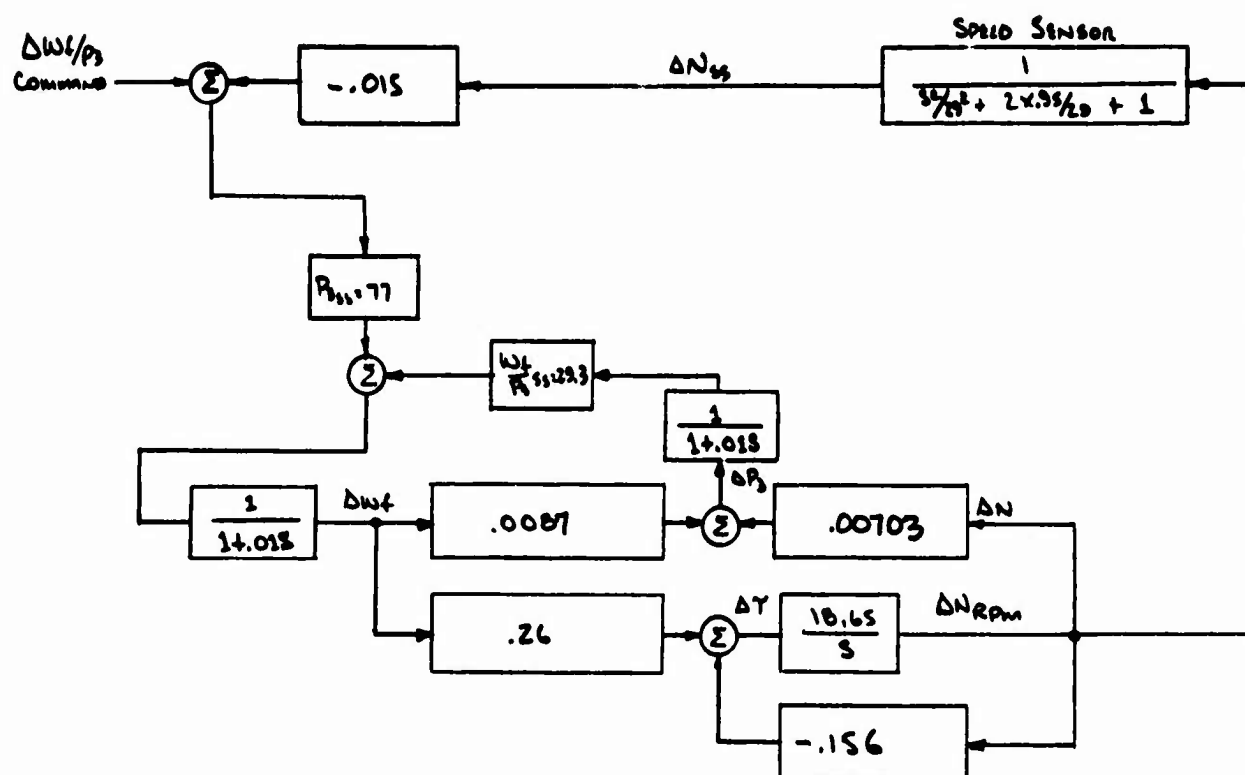


Figure 68 Reduced Block Diagram of J-85 Engine and Fuel Control System

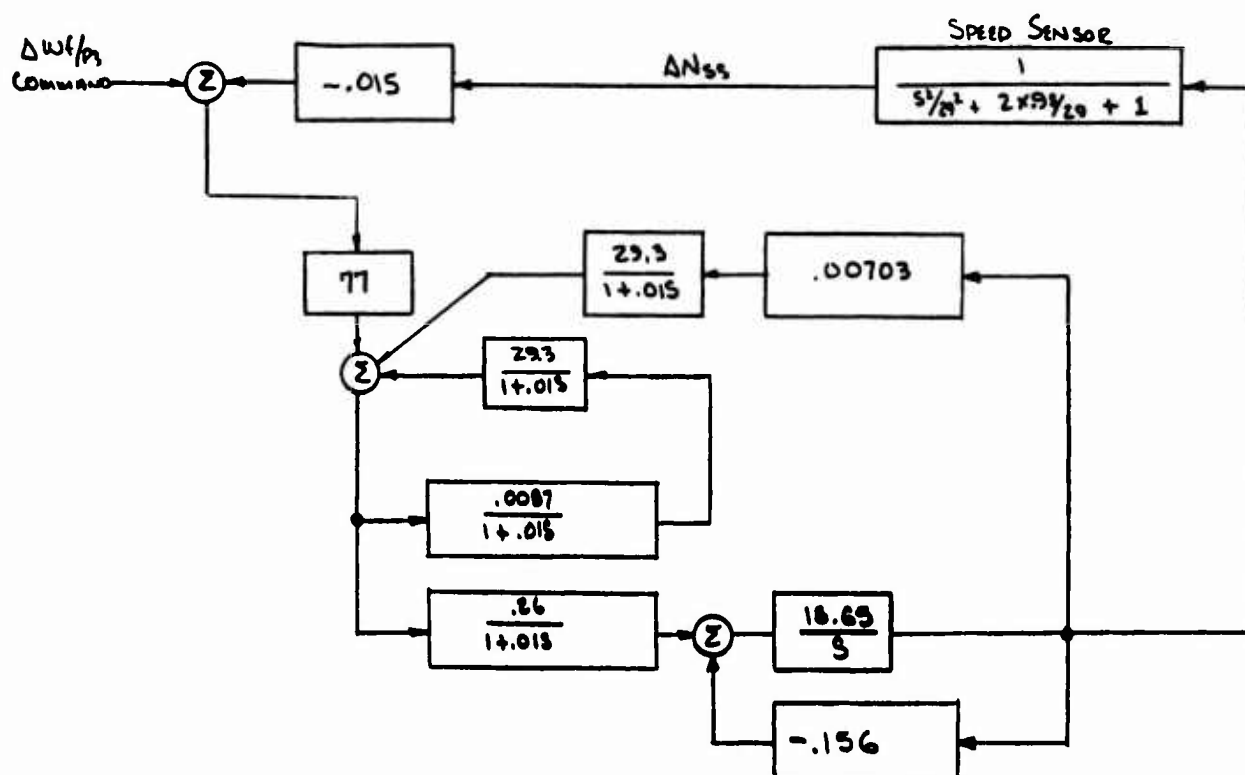


Figure 69 Further Reduced Block Diagram of J-85 Engine and Fuel Control System

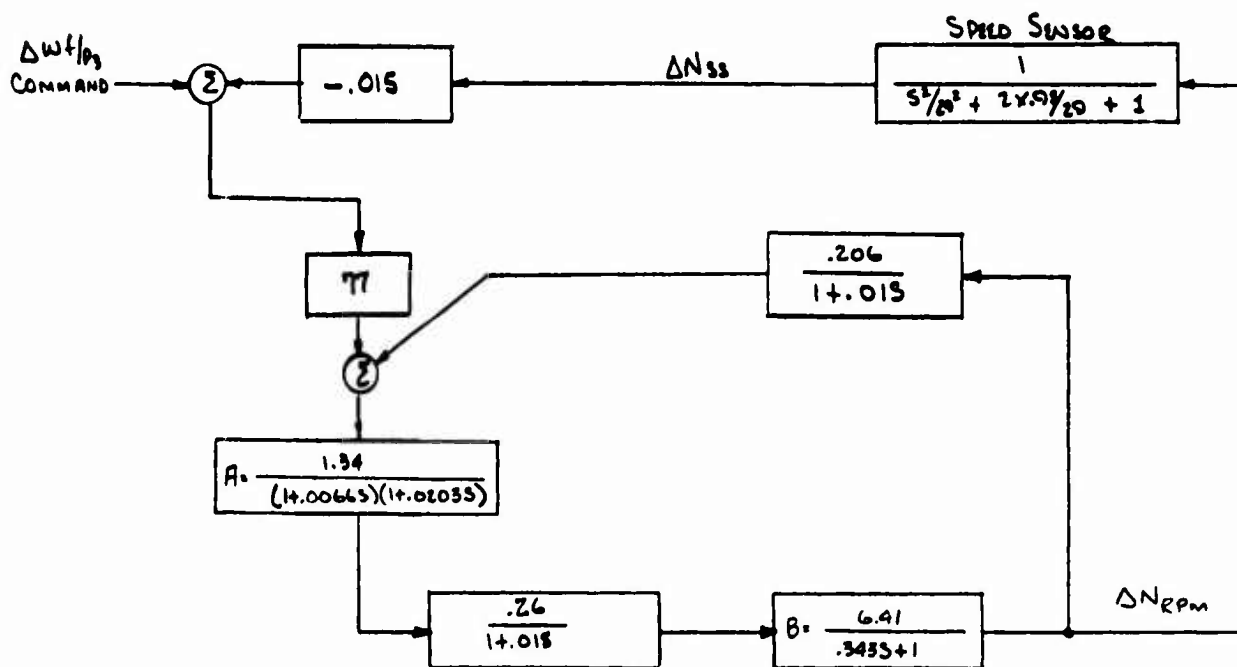


Figure 70 Further Reduced Block Diagram of J-85 Engine and Fuel Control System

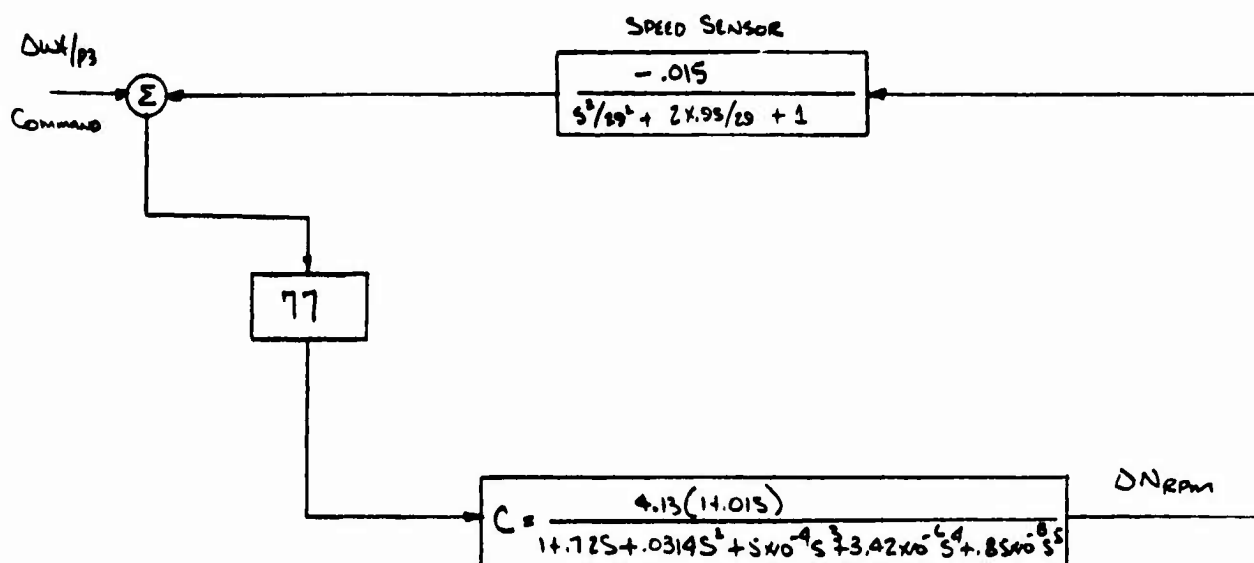


Figure 71 Further Reduced Block Diagram of J-85 Engine and Fuel Control System

$$\begin{array}{c}
 \Delta u_{cl}/p_3 \\
 \text{COMMAND}
 \end{array}
 \rightarrow
 \boxed{
 D = \frac{55.1 (1 + 0.01s) (s^2/29^2 + 1.8s/29 + 1)}{1 + 0.0144s + 0.0134s^2 + 5.77 \times 10^{-4}s^3 + 12.4 \times 10^{-6}s^4 + 1.4 \times 10^{-8}s^5 + 7.56 \times 10^{-10}s^6 + 1.75 \times 10^{-12}s^7}
 }
 \rightarrow \Delta N$$

Figure 72 Final Engine Closed-Loop Small Disturbance Transfer Function

$$\begin{array}{c}
 \Delta u_{cl}/p_3 \\
 \text{COMMAND}
 \end{array}
 \rightarrow
 \boxed{
 \frac{55.1 (s/100 + 1) (s^2/29^2 + 1.8s/29 + 1)}{(s/180 + 1) (s^2/52.7^2 + 1.76s/52.7 + 1) (s^2/46.3^2 + 1.84s/46.3 + 1) (s^2/12.24^2 + 0.986s/12.24 + 1)}
 }
 \rightarrow \Delta N$$

Figure 73 Final Engine Closed-Loop Small Disturbance Transfer Function (Factored)

6.2.2 Engine Partial and Control Data

Engine Data

N = Constant

A. Standard Day S, L, E.				B. 2500' Hot Day $T_{T2} = 93$, $P_{T2} = 13.5$, static			
	90%N	95%N	100%N	90%N	95%N	100%	
$\delta \tau / \delta W_f$.37	.32	.295	.36	.32	.26 FT#/PPH	
$\delta F_n / \delta W_f$.43	.445	.46	.39	.41	.45 #/PPH	
$\delta P_{s3} / \delta W_f$.00975	.0088	.00915	.0090	.0083	.0087 Psi/PPH $N = \text{Constant}$	
<u>$W_f = \text{constant}$</u>							
$\delta \tau / \delta \%N$	-28.22	-41.7	-32.09	-21.41	-33.25	-25.68 FT#/%RPM	
$\delta F_n / \delta \%N$	55.84	93.19	20.08	65.37	67.27	53.36 #/%RPM	
$\delta P_{s3} / \delta \%N$	1.45	2.19	.57	1.86	1.76	1.16 Psi/%RPM $W_f = \text{Constant}$	
$(P_3/\delta) \text{ s. s.}$	<div><div></div><div>Available via J-85 deck at Evendale</div></div>						$F_N = \text{Net Turbojet Thrust}$
$(W_f/P_3 \dot{\theta}^{.718}) \text{ s. s.}$							
$(W_f/\delta \dot{\theta}^{.718}) \text{ s. s.}$							
$J = 16.5 \text{ lb} - \text{ft}^2$							

Control Data

Constants

ξ s.s.	$\approx .9$	Damp. Ratio
ω s.s.	≈ 29 rad/sec	Natural Freq. - Governor
τ mv	≤ 0.01 sec	Metering Valve Lag
$(W_f/P_3)_{min}$	= 11.5 pph/psia	Lean Blowout Fuel Sked
$(W_f)_{min}$	= 220 pph	Starting Fuel Flow
τ_P	≤ 0.01 sec	P ₃ Servo Lag

Reduction of Block A

$$\frac{\theta_o}{\theta_{IN}} = \frac{1}{1 - \frac{29.3 (.0087)}{(1+.01S)^2}} = \frac{1}{1 - .255 \frac{1}{(1+.01S)^2}}$$

$$= \frac{1.34}{1+.0269S + .000134S^2}$$

$$\frac{\theta_o}{\theta_{IN}} = \frac{1.34}{(1 + .0066S) (1 + .0203S)}$$

Reduction of Block B

$$\frac{\theta_o}{\theta_{IN}} = \frac{\frac{18.65}{S}}{1 + \frac{(18.65) .156}{S}} = \frac{18.65}{S + 2.91} = \frac{6.41}{.343S + 1}$$

Reduction of Block C

$$\text{Fwd Loop} = \frac{1.34 \times .26 \times 6.41}{(1 + .01S) (1 + .343S) (1 + .0066S) (1 + .0203S)}$$

$$\text{FB Loop} = \frac{.206}{1 + .015S}$$

$$\frac{\theta_o}{\theta_{IN}} = \frac{\frac{2.23}{(1 + .01S) (1 + .343S) (1 + .0066S) (1 + .0203S)}}{1 - \frac{2.23}{(1 + .01S) (1 + .343S) (1 + .0066S) (1 + .0203S)}} \times \frac{.206}{1 + .015S}$$

$$= \frac{2.23 (1 + .01S)}{(1 + .01S)^2 (1 + .343S) (1 + .0066S) (1 + .0203S) - .459}$$

$$= \frac{2.23 (1 + .01S)}{1 + 38.99 \times 10^{-2} S + 168.7 \times 10^{-4} S^2 + 270.4 \times 10^{-6} S^3 + 185 \times 10^{-8} S^4 + .46 \times 10^{-8} S^5 - .459}$$

$$= \frac{2.23 (1 + .01S)}{.541(1 + 72 \times 10^{-2} S + 312 \times 10^{-4} S^2 + 500 \times 10^{-6} S^3 + 342 \times 10^{-8} S^4 + .85 \times 10^{-8} S^5)}$$

Block C

$$\frac{\theta_o}{\theta_{IN}} = \frac{4.13 (1 + .01S)}{1 + .72S + .0314S^2 + 5 \times 10^{-4} S^3 + 3.42 \times 10^{-6} S^4 + .85 \times 10^{-8} S^5}$$

Reduction of Block D

$$\frac{\Delta N}{\Delta wf/p3} = \frac{\frac{318 (1 + .01S)}{(1 + .72S + .0314S^2 + 5 \times 10^{-4} S^3 + 3.42 \times 10^{-6} S^4 + .85 \times 10^{-8} S^5)}}{318 (1 + .01S) (.015)}$$

$$1 + \frac{1}{(\text{Block C Denom.}) (S^2/29^2 + 1.8S/29 + 1)}$$

$$\frac{\Delta N}{\Delta wf/p3} = \frac{318 (1 + .01S) (S^2/29^2 + 1.8S/29 + 1)}{(\text{Block C Denom.}) (S^2/29^2 + 1.8S/29 + 1) + 4.77 (1 + .01S)}$$

$$\frac{\Delta N}{\Delta wf/p3} = \frac{318 (1 + .01S) (S^2/29^2 + 1.8S/29 + 1)}{1 + .782S + .0773S^2 + 3.07 \times 10^{-4} S^3 + 71.72 \times 10^{-6} S^4 + 81.35 \times 10^{-8} S^5 + 45.98 \times 10^{-10} S^6 + 1.01 \times 10^{-11} S^7 + 4.77 + .048S}$$

$$= \frac{318 (1 + .01S) (S^2/29^2 + 1.8S/29 + 1)}{5.77 (1 + .144S + .0134S^2 + 5.72 \times 10^{-4} S^3 + 12.4 \times 10^{-6} S^4 + 14 \times 10^{-8} S^5 + 7.96 \times 10^{-10} S^6 + .175 \times 10^{-11} S^7)}$$

$$= \frac{55.1 (1 + .01S) (S^2/29^2 + 1.8S/29 + 1)}{(1 + .144S + .0134S^2 + 5.72 \times 10^{-4}S^3 + 12.4 \times 10^{-6}S^4 + 14 \times 10^{-8}S^5 + 7.96 \times 10^{-10}S^6 + .175 \times 10^{-11}S^7)}$$

$$= \frac{55.1 (1 + .01S) (S^2/29^2 + 1.8S/29 + 1)}{(S/180 + 1) (S^2/99.7^2 + 1.76S/99.7 + 1) (S^2/46.3^2 + 1.84S/46.3 + 1) (S^2/12.24^2 + .986S/12.24 + 1)}$$

7.0 LIFT-FAN ROLL-YAW CONTROL COUPLING ANALYSIS

7.1 Discussion

Coupling from roll to yaw and yaw to roll is induced for control inputs at other than zero collective vector angle. This effect is most serious in the yaw mode, where a yaw control input can result in a larger rolling moment than yawing moment. Coupled with the fact that the roll moment of inertia is about 1/5 the yaw moment of inertia, it is seen that yaw control inputs can cause large roll accelerations.

This effect has been compensated for in the mechanical mixer located between the control stick and the exit louver inputs. Yaw due to roll input is not compensated, because the effect is less, due to the higher yaw inertia, and furthermore, the effect is in the direction of the roll, so that a right roll induces a right yaw. The roll-due-to yaw, on the other hand, is in the adverse direction.

The compensation of roll due to yaw consists of cross-coupling the yaw and roll signals, while gradually phasing the yaw louver inputs to zero at $45^\circ \beta_v$. At this vector setting, all yaw control moments are caused by rudder deflections alone, as far as pilot inputs are concerned.

As far as the SA system is concerned, no mixing of yaw and roll signals has been decided upon, since the effects of this cross-coupling (in the SA system) on flying qualities has not as yet been determined. If the system behavior, as determined below is deemed objectionable to the pilot, then either an electrical mixer and/or phasing out of yaw will be necessary.

The effect of vectoring on the roll and yaw moments caused by differential stagger and differential vector is shown in Figure 74. Essentially, as the collective vector angle increases, the effective axes of moments for roll and yaw inputs rotate with the vector angle, and approximately proportionally. Fortunately, this rotation is in such a direction that it results in a stable system. Rotation in the opposite direction can result in a divergent system.

The rate gyros are fixed in the vehicle, and thus measure the angular rates in an axis system displaced from the axis of application of corrective signals.

As is shown in Section 7.2 following, a simple inertial two-degree-of-freedom system was investigated which allowed only yaw and roll angles to occur. No translations were included. This two-degree-of-freedom representation results in a 4th order characteristic equation, which has as a solution, two sets of second order roots. One pair of roots would be the "roll" mode, and the other pair the "yaw" mode.

At $35^\circ \beta_v$ the characteristics of the response have been determined for roll gains of 1 and 10, using a compensation ratio setting of .1 for both axis. The yaw gain, K_y , was varied over the range of 1 to 20.

Figure 75 is a plot of the damping ratios and natural frequencies for $K_R = 2$, and variable K_y .

Figure 76 is the same plot with roll gain, $K_R = 20$.

It can be seen that the variation of the yaw gain results in a variation of the characteristics of both the roll and yaw modes, since both natural frequencies vary.

This is not desirable, but may be tolerable. This must be determined from pilot evaluation tests.

It would be most desirable to have the roll gain affect only the roll axis, and the yaw gain the yaw axis. In this manner, the handling qualities for a given set of roll and yaw gains would be unique and determinable. If this coupling is present, the handling qualities for a given set of gains would not necessarily be unique, and it is very likely that essentially the same characteristics could be arrived at with several different gain combinations.

With this in mind, and realizing that the axis of moments from the roll and yaw louver inputs approximately rotates with collective vector, an analysis was made whereby the rate gyros were rotated with vector also, such that gyros and controls would act in the same coordinate system. Figures 77 and 78 show the effects of rate gyro rotation.

In Figure 77, the roll gain is 2, and it is seen that ω_{N_1} seems not at all affected by K_y .

In Figure 78 the roll gain is 20, and both ω_N values vary over about the same range for the yaw gain variation from 2 to 40.

An open-loop compensation of the effects described above can be made, similar to those accomplished in the mechanical mixer box. It is hoped that, if the above effects prove objectionable, the problem can be minimized by simply turning the yaw SA system axis off when β_v becomes greater than 15 to 20 degrees. This would be the most reliable modification to the present system.

7.2 Analysis

Figures 79 and 80 are plots of ΔC_L^s and ΔC_D^s due to β_s and β_v inputs.

This analysis is restricted to angle of-attack = 0, which aligns the body and stability axes. Assume trimmed flight prior to small incremental louver inputs, β_s and β_v .

Assuming the forces due to louver inputs act at the fan hubs, the resultant rolling and yawing moment expressions, in terms of changes in fan lift and drag are:

$$\text{Rolling Moment} = \mathcal{L} = (\Delta L_{\ell t} - \Delta L_{rt}) Y_f \quad (1)$$

$$\text{Yawing Moment} = \mathcal{N} = (\Delta D_{rt} - \Delta D_{\ell t}) Y_f \quad (2)$$

Where Y_f = wing fan moment arm from fuselage center line, L = lift, D = drag.

It is necessary to determine the variations of lift and drag on the fans due to louver inputs.

Using Figures 79 and 80 we define ΔL , the incremental change in lift, as:

$$\Delta L = \Delta C_L^s q^s A_f \quad (3)$$

which holds for both wings.

For example, to calculate the incremental lift change on the right wing:

$$\Delta L_{rt} = \Delta C_{L_{rt}}^s q^s \frac{A_f}{2} \quad (4)$$

Going one step further, we can expand the expression for $\Delta C_{L_{rt}}^s$ as:

$$\Delta C_{L_{rt}}^s = \frac{\partial C_{L_{rt}}^s}{\partial \beta_v} \beta_{v_{rt}} + \frac{\partial C_{L_{rt}}^s}{\partial \beta_s} \beta_{s_{rt}} \quad (5)$$

and

$$\Delta C_{D_{rt}}^s = \frac{\partial C_{D_{rt}}^s}{\partial \beta_v} \beta_{v_{rt}} + \frac{\partial C_{D_{rt}}^s}{\partial \beta_s} \beta_{s_{rt}} \quad (6)$$

The same expressions hold for the left wing.

For a positive rolling moment, $\beta_{s_{rt}}$ is positive and $\beta_{s_{lt}}$ is negative, and they are assumed equal in magnitude.

For a positive yawing moment, $\beta_{v_{lt}}$ increases and $\beta_{v_{rt}}$ decreases.

With the above knowledge at hand, it is possible to determine the roll and yaw characteristics of both differential stagger and differential vector inputs to the louvers.

If we define β_s as the differential stagger variation on the right wing, and β_v as the differential vector variation on the left wing, a positive β_s results in a positive rolling moment, and a positive β_v results in a positive yawing moment.

For a positive roll input:

$$\mathcal{Z}(\beta_s) = \left[\Delta L_{lt}(\beta_s) - \Delta L_{rt}(\beta_s) \right] Y_f \quad (4)$$

$$\mathcal{N}(\beta_s) = \left[\Delta D_{rt}(\beta_s) - \Delta D_{lt}(\beta_s) \right] Y_f \quad (5)$$

$$\mathcal{L}(\beta_s) = Y_f q^s A_f \frac{1}{2} \left[\frac{\partial C_L^s}{\partial \beta_s} \beta_{s_{lt}} - \frac{\partial C_L^s}{\partial \beta_s} \beta_{s_{rt}} \right] \quad (6)$$

Knowing $\beta_{s_{lt}} = -\beta_{s_{rt}} = -\beta_s$

$$\mathcal{L}(\beta_s) = Y_f q^s A_f \frac{1}{2} \left[-2 \frac{C_L^s}{\partial \beta_s} \beta_s \right] \quad (7)$$

$$\mathcal{L}(\beta_s) = -Y_f q^s A_f \frac{\partial C_L^s}{\partial \beta_s} \beta_s \quad (8)$$

$$\frac{\partial \mathcal{L}(\beta_s)}{\partial \beta_s} = -Y_f q^s A_f \frac{\partial C_L^s}{\partial \beta_s} = \mathcal{L}_{\beta_s}$$

(9)

Now, calculating the yawing moment effect of a positive β_s input

$$\mathcal{N}(\beta_s) = Y_f (\Delta D_{rt}(\beta_s) - \Delta D_{lt}(\beta_s)) \quad (10)$$

$$\mathcal{N}(\beta_s) = Y_f q^s A_f \frac{1}{2} \left[\frac{\partial C_D^s}{\partial \beta_s} \beta_{s_{rt}} - \frac{\partial C_D^s}{\partial \beta_s} \beta_{s_{lt}} \right] \quad (11)$$

Knowing $\beta_{s_{LT}} = -\beta_{s_{rt}} = -\beta_s$

$$\mathcal{N}(\beta_s) = Y_f q^s A_f \frac{1}{2} \left[+2 \beta_s \frac{\partial C_D^s}{\partial \beta_s} \right] \quad (12)$$

$$\mathcal{N}(\beta_s) = +Y_f q^s A_f \beta_s \frac{\partial C_D^s}{\partial \beta_s} \quad (13)$$

$$\frac{\partial \mathcal{N}(\beta_s)}{\partial \beta_s} = +Y_f q^s A_f \frac{\partial C_D^s}{\partial \beta_s} = \mathcal{N}_{\beta_s} \quad (14)$$

Similarly for positive yaw inputs:

$$\mathcal{N}(\beta_v) = Y_f \left[\Delta D_{rt}(\beta_v) - \Delta D_{lt}(\beta_v) \right] \quad (15)$$

$$\mathcal{N}(\beta_v) = Y_f q^s A_f \frac{1}{2} \left[\frac{\partial C_D^s}{\partial \beta_v} \beta_{v_{rt}} - \frac{\partial C_D^s}{\partial \beta_v} \beta_{v_{lt}} \right] \quad (16)$$

Knowing $\beta_{v_{rt}} = -\beta_{v_{lt}} = -\beta_v$

$$\mathcal{N}(\beta_v) = -Y_f q^s A_f \beta_v \frac{\partial C_d^s}{\partial \beta_v} \quad (17)$$

$$\boxed{\frac{\partial \mathcal{N}(\beta_v)}{\partial \beta_v} = \mathcal{N}_{\beta_v} = -Y_f q^s A_f \frac{\partial C_D^s}{\partial \beta_v}} \quad (18)$$

$$\mathcal{L}(\beta_v) = Y_f \left[\Delta L_{lt}(\beta_v) - \Delta L_{rt}(\beta_v) \right] \quad (19)$$

$$\mathcal{L}(\beta_v) = Y_f q^s A_f \frac{1}{2} \left[\frac{\partial C_L^s}{\partial \beta_v} \beta_{v_{lt}} - \frac{\partial C_L^s}{\partial \beta_v} \beta_{v_{rt}} \right] \quad (20)$$

$$\mathcal{L}(\beta_v) = Y_f q^s A_f \beta_v \frac{\partial C_L^s}{\partial \beta_v} \quad (21)$$

$$\frac{\partial \mathcal{L}(\beta_v)}{\partial \beta_v} = \mathcal{L}_{\beta_v} = Y_f^s A_f \frac{\partial C_L^s}{\partial \beta_v} \quad (22)$$

The following Table is a listing of $\frac{\partial C_L^s}{\partial \beta_s}$, $\frac{\partial C_D^s}{\partial \beta_s}$, $\frac{\partial C_L^s}{\partial \beta_v}$, and $\frac{\partial C_D^s}{\partial \beta_v}$ derived from Figures 79 and 80; for collective $\beta_v = 0, 10, 20, 30, 40$ and 50° , and β_s trim equal to 27° .

The curve of Figure 79 was used to determine the trim T_c^s values for the collective β_v values given above.

β_v	T_c^s	$\frac{\partial C_L^s}{\partial \beta_s}$	$\frac{C_D^s}{\partial \beta_v}$	$\frac{\partial C_L^s}{\partial \beta_v}$	$\frac{\partial C_D^s}{\partial \beta_v}$
0	1	-.0093	0	0	-.0190
10	.98	-.0120	.0048	-.003	-.0155
20	.955	-.0115	.0069	-.0118	-.0128
30	.90	-.0086	.0048	-.0130	-.0098
35	.855	-.0050	.0038	-.0138	-.0086
50	.8	-.005	.0038	-.0140	-.0080

(All partials per degree)

It is desired to determine the axis of moments for differential stagger inputs and differential vane inputs.

Figure 81 shows the axes for roll and yaw moments. A positive rolling moment is along the positive "x" axis, and a positive yawing moment is along the positive "z" axis.

The resultant of a rolling and a yawing moment, \mathcal{R} , has a magnitude of $\sqrt{\mathcal{L}^2 + \mathcal{N}^2}$, and is oriented in the xz plane at an angle $\delta = \tan^{-1} \mathcal{N}/\mathcal{L}$ with the x axis.

Since \mathcal{N} and \mathcal{L} are proportioned to the $\frac{\partial C^s}{\partial \beta}$ values, the angle of the resultant δ , may be computed from the coefficients alone.

Thus

$$\mathcal{L}_{\beta_s} \approx - \frac{\partial C_L^s}{\partial \beta_s} \quad (23)$$

$$\mathcal{N}_{\beta_s} \approx - \frac{\partial C_D^s}{\partial \beta_s} \quad (24)$$

$$\mathcal{L}_{\beta_v} \approx - \frac{\partial C_L^s}{\partial \beta_v} \quad (25)$$

$$\mathcal{N}_{\beta_v} \approx - \frac{\partial C_D^s}{\partial \beta_v} \quad (26)$$

These values, as well as the resultant magnitudes and angles are:

β_v	T_c^s	\mathcal{L}_{β_s}	\mathcal{N}_{β_s}	$\mathcal{R}_{\beta_s} \angle \tan^{-1} \mathcal{N}/\mathcal{L}$	\mathcal{L}_{β_v}	\mathcal{N}_{β_v}	$\mathcal{R}_{\beta_v} \angle \tan^{-1} \mathcal{N}/\mathcal{L}$
0	1	.0093	0	.0093 $\angle 0^\circ$	0	.019	.019 $\angle 90^\circ$
10	.98	.0120	.0048	.0129 $\angle 21.8^\circ$	-.008	.0153	.01745 $\angle 117.3^\circ$
20	.96	.0115	.0069	.0134 $\angle 31^\circ$	-.0118	.0128	.01735 $\angle 132.7^\circ$
30	.9	.0086	.0048	.00984 $\angle 29.2^\circ$	-.0130	.0098	.01625 $\angle 142.9^\circ$
35	.86	.0050	.0038	.00627 $\angle 37.3^\circ$	-.0138	.0086	.01625 $\angle 148.2^\circ$
50	.80	.005	.0038	.00627 $\angle 37.3^\circ$	-.014	.008	.0160 $\angle 150$

To convert these coefficients to rolling and yawing moments, we use equations 9, 14, 18 and 22. The coefficients must be multiplied by $Y_f q^s A_f$.

In the transition region, a reasonable value for q^s is 300 psf, and Y_f is equal to 5 feet. A_f is 42.6 ft².

Thus,

$$Y_f q^s A_f = 2 \times 5 \times 300 \times 42.6 = 63,900 \quad (27)$$

For the case of collective $\beta_v = 35^\circ$, the value used in the coupling analysis, we can calculate the values of \mathcal{L}_{β_s} , \mathcal{N}_{β_s} , \mathcal{L}_{β_v} , and \mathcal{N}_{β_v} .

Thus, at $\beta_v = 35^\circ$, $\beta_s = 27^\circ$;

$$\mathcal{L}_{\beta_s} = .005 \times 63,900 = 319.5 \text{ ft lb/deg} = 18,300 \text{ ft lb/rad} \quad (28)$$

$$\mathcal{N}_{\beta_s} = .0038 \times 63,900 = 243 \text{ ft lb/deg} = 13,925 \text{ ft lb/rad} \quad (29)$$

$$\mathcal{L}_{\beta_v} = -.0138 \times 63,900 = -882 \text{ ft lb/deg} = -50,500 \text{ ft lb/rad} \quad (30)$$

$$\mathcal{N}_{\beta_v} = .0086 \times 63,900 = 549.5 \text{ ft lb/deg} = 31,486 \text{ ft lb/rad} \quad (31)$$

Using the values thus derived, we can now develop the characteristics for an inertial two degree-of-freedom (roll and yaw) system with stability augmentation.

The SA system will be connected so that roll rate will be fed into β_s , and yaw rate will be fed into β_v . A 180° phase shift is required for stability.

If we pick a compensation network with the transfer function $\frac{1+S}{1+10S}$, and let K_R = roll gain and K_y = yaw gain, then we can write the equations of motion for the closed-loop system. Also, since the characteristic equation of the system is the desired output, we can write the force-free equation of motion (i. e., no stick inputs) as follows:

$$pS = \frac{I_{xz}}{I_x} rS - \frac{K_R \mathcal{L}_{\beta_s}}{I_x} \left(\frac{1+S}{1+10S} \right) p \frac{K_Y \mathcal{L}_{\beta_v}}{I_x} \left(\frac{1+S}{1+10S} \right) r \quad (32)$$

$$rS = \frac{I_{xz}}{I_z} pS - \frac{K_R \mathcal{N}_{\beta_s}}{I_z} \left(\frac{1+S}{1+10S} \right) p \frac{K_Y \mathcal{N}_{\beta_v}}{I_z} \left(\frac{1+S}{1+10S} \right) r \quad (33)$$

$$p \left[S + \frac{K_R \mathcal{L}_{\beta_s}}{I_x} \left(\frac{1+S}{1+10S} \right) \right] + r \left[- \frac{I_{xz}}{I_x} S + \frac{K_Y \mathcal{L}_{\beta_v}}{I_x} \left(\frac{1+S}{1+10S} \right) \right] = 0 \quad (34)$$

$$p \left[- \frac{I_{xz}}{I_z} S + \frac{K_R \mathcal{N}_{\beta_s}}{I_x} \left(\frac{1+S}{1+10S} \right) \right] + r \left[S + \frac{K_Y \mathcal{N}_{\beta_v}}{I_z} \left(\frac{1+S}{1+10S} \right) \right] = 0 \quad (35)$$

By inspection, and knowing that the characteristic equation must have zero coefficient sign changes to be stable, we can see the value of the constant term will be

$$\left[K_R K_Y \mathcal{L}_{\beta_s} \mathcal{N}_{\beta_v} - K_R K_Y \mathcal{L}_{\beta_v} \mathcal{N}_{\beta_s} \right] \frac{(1+S)^2}{(1+10S)^2} \left(\frac{1}{I_x I_z} \right). \quad (36)$$

For stability, the value of this term must be greater than zero, so the primary criterion for stability is that:

$$\mathcal{L}_{\beta_s} \mathcal{L}_{\beta_v} - \mathcal{N}_{\beta_s} \mathcal{L}_{\beta_v} \geq 0 \quad (37)$$

Substituting in the constants of equation 28, 29, 30 and 31, it is seen that the XV-5A louver system at least satisfies part of the requirements for a stable system.

Using values of $I_x = 3930 \text{ slug ft}^2$, $I_z = 16,180 \text{ slug ft}^2$, and $I_{xz} = 830 \text{ slug ft}^2$, the expansion of equations 34 and 35 result in the characteristic equation:

$$\begin{aligned} & 98.9S^4 + S^3 (19.78 + 96.94 K_R + 25.71 K_Y) \\ & + S^2 (28.3K_Y + 81.06 K_Y K_R + 106.6 K_R + .989) \\ & + S (2.57K_Y + 9.69K_R + 162K_Y K_R) + 81.06K_Y K_R = 0 \end{aligned} \quad (38)$$

Inserting the values of K_Y between 2 and 40 with a value of $K_R = 2$ in equation 38 results in the roots plotted in Figure 75.

Figure 76 is a plot of the same roots for $K_R = 20$.

As seen in Figure 74, and as before noted, the angle between the β_s resultant and the β_v resultant remains approximately 90° . Thus analysis of the effect of rotation of the roll and rate gyros downward with collective β_v was made. This was done for the $\beta_v = 35^\circ$ case.

For this case, the rate measured by the roll rate gyro, p_{gyro} , is equal to: $p_{\text{gyro}} = p \cos \beta_v + r \sin \beta_v$ (39)

Similarly, the rate measured by the yaw rate gyro is:

$$r_{\text{gyro}} = -p \sin \beta_v + r \cos \beta_v \quad (40)$$

These relationships were substituted into the parts of equations 32 and 33 involving the SA system feedback terms. The characteristic equation resulting from this substitution is:

$$98.92S^4 + S^3 (19.78 + 92.2K_R + 164.4K_Y)$$

(continued)

$$\begin{aligned}
& + S^2 (.989 + 101.42K_R + .03K_R^2 + 80.96K_Y K_R + 180.8K_Y) \\
& + S (9.22K_R + .06K_R^2 + 161.3K_Y K_R + 16.44K_Y) \\
& + .03K_R^2 + 80.86 K_Y K_R = 0
\end{aligned} \tag{41}$$

The various values for K_Y and K_R were substituted in equation 41, and the results are plotted in Figures 77 and 78.

For a drill, a 35° upward gyro rotation was investigated, and this resulted in an unstable system.

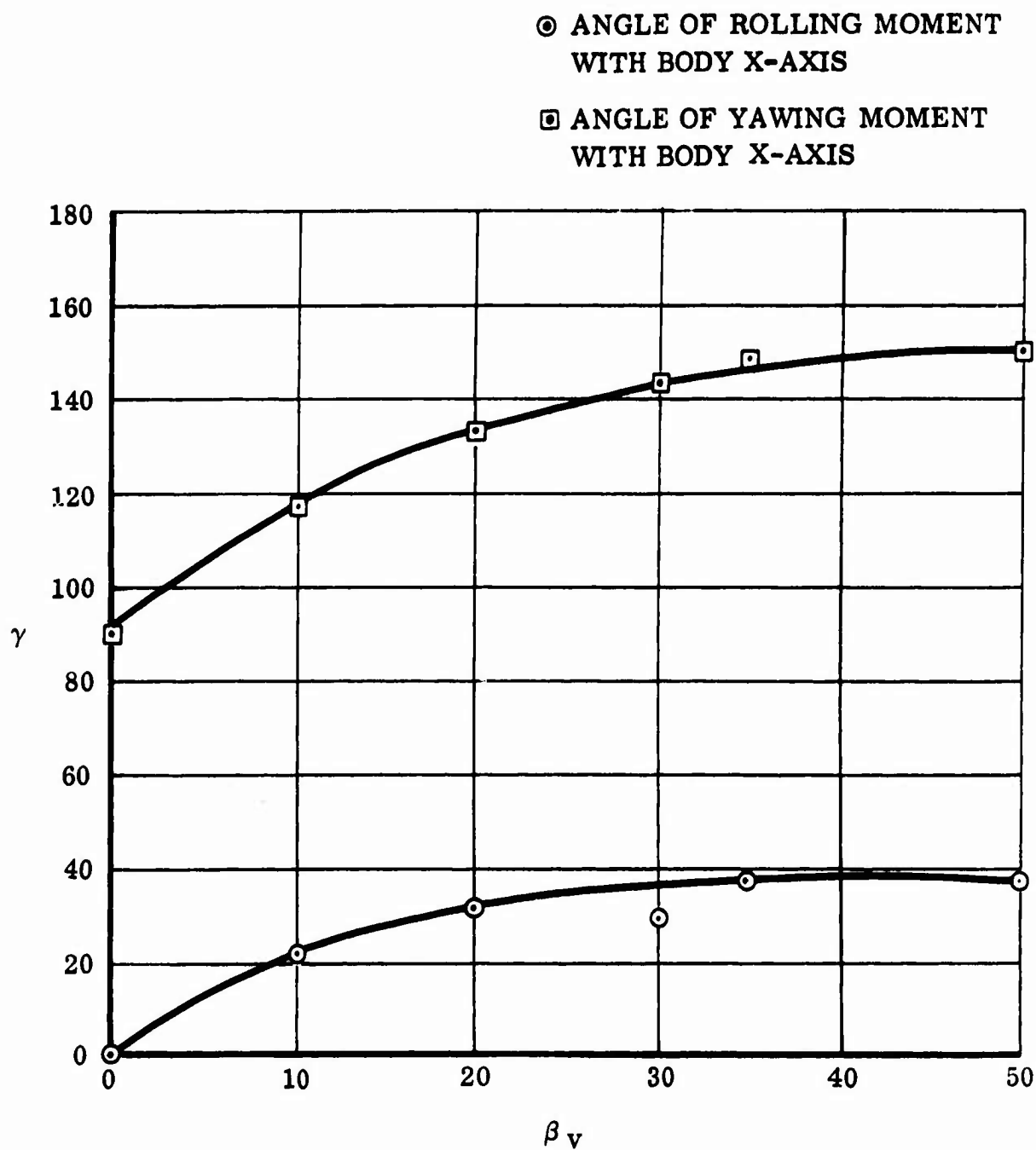


Figure 74 Plot of Angle of Resulting Moments for Roll and Yaw Inputs

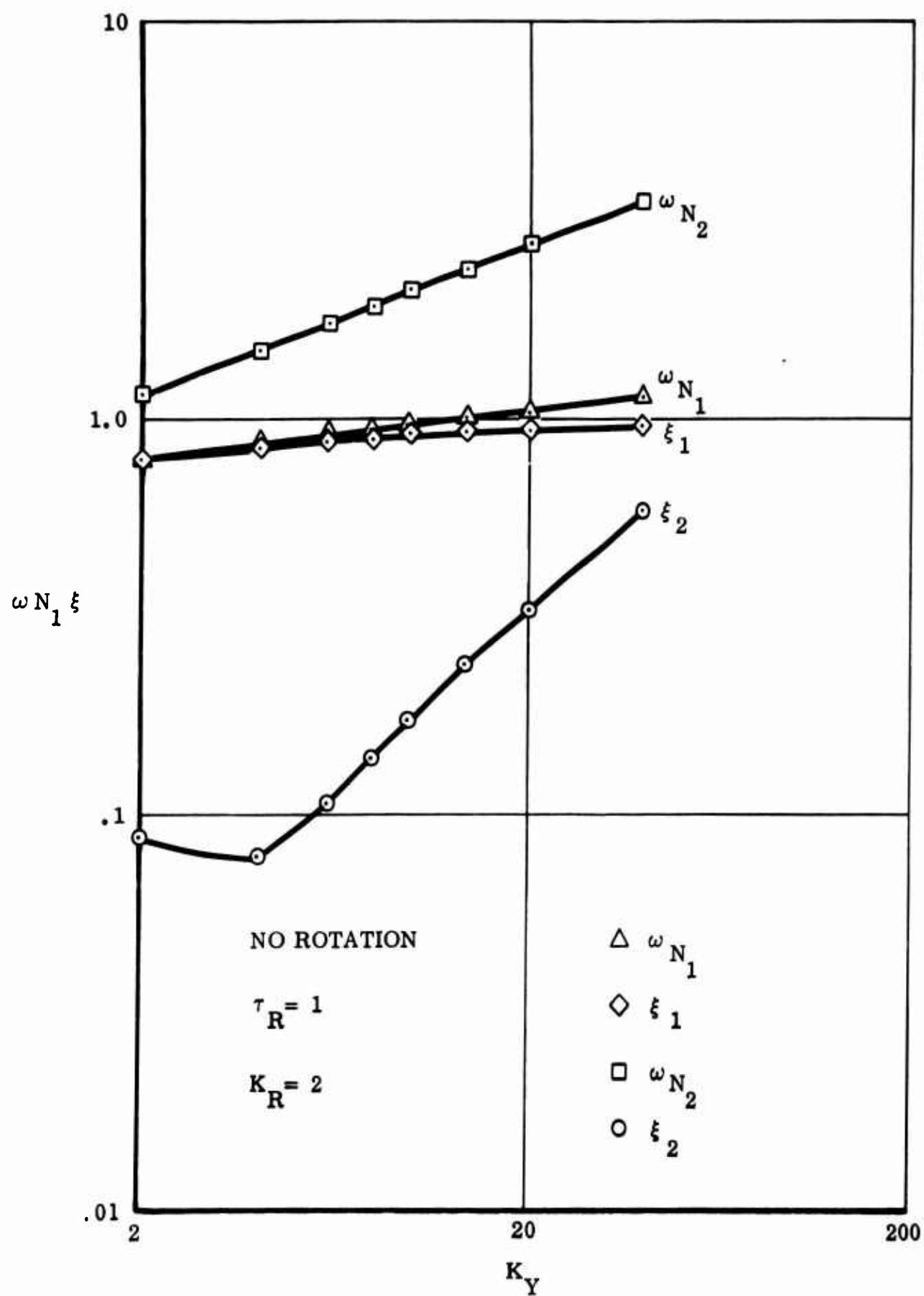


Figure 75 Damping and Natural Frequency vs Yaw Gain

NO GYRO ROTATION

$\tau_R = 1.0$, BOTH AXES

$K_R = 20$

$\triangle \omega_{N_1}$

$\diamond \xi_1$

$\square \omega_{N_2}$

$\circ \xi_2$

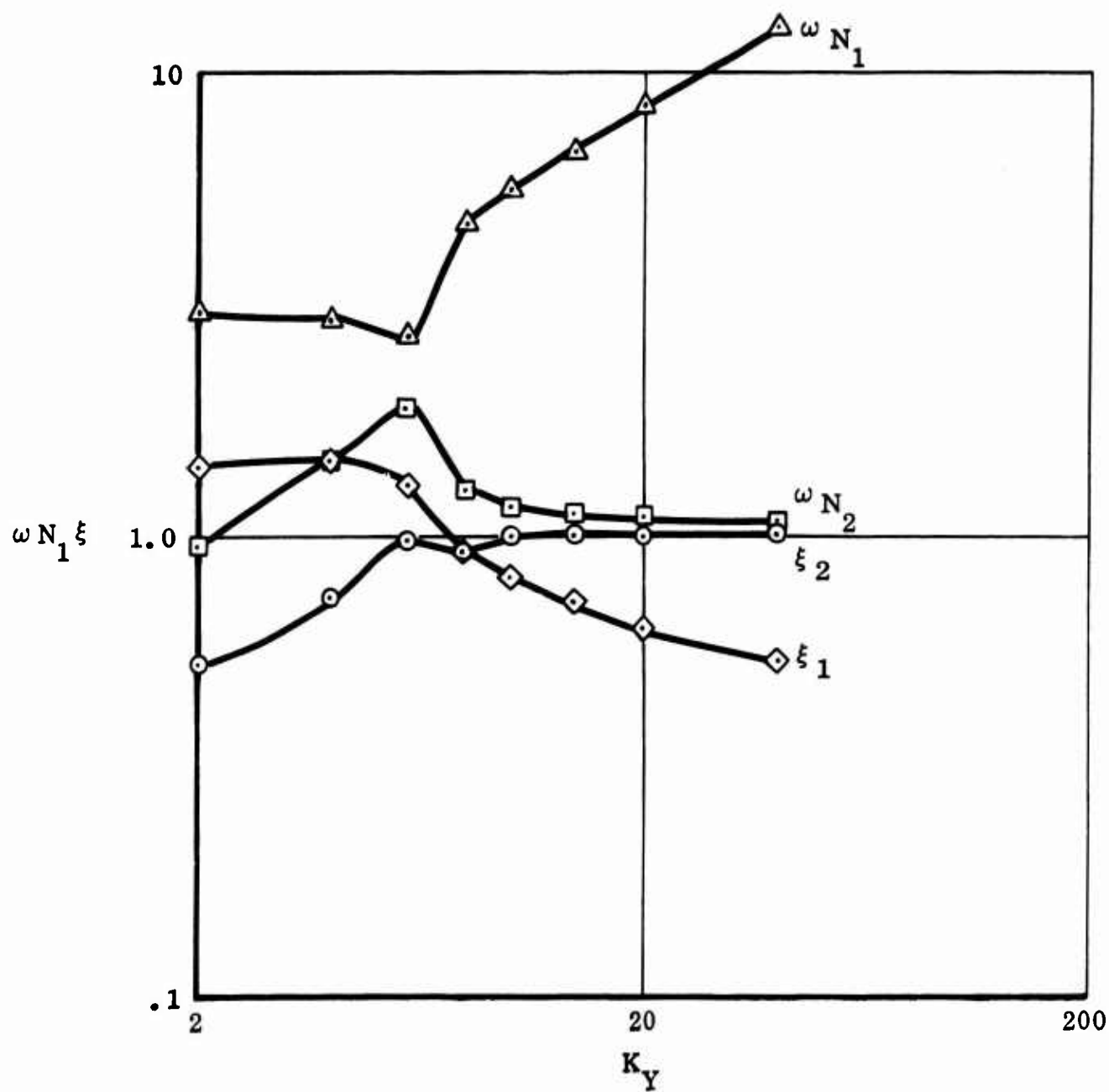


Figure 76 Damping and Natural Frequency vs Yaw Gain

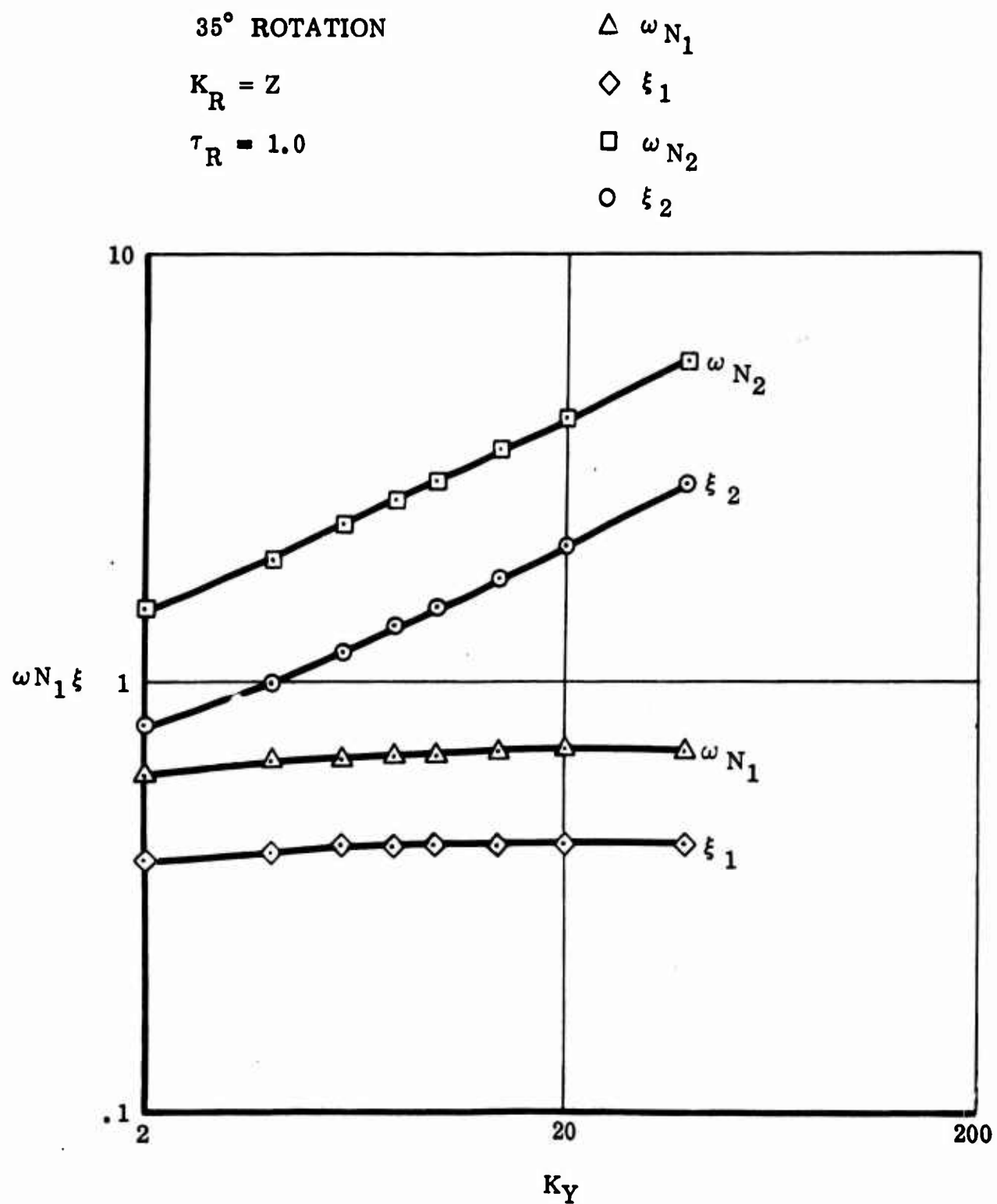


Figure 77 Damping and Natural Frequency vs Yaw Gain

35° ROTATION

$K_R = 20$

$\tau_R = 1.0$

$\triangle \omega_{N_1}$

$\diamond \xi_1$

$\square \omega_{N_2}$

$\odot \xi_2$

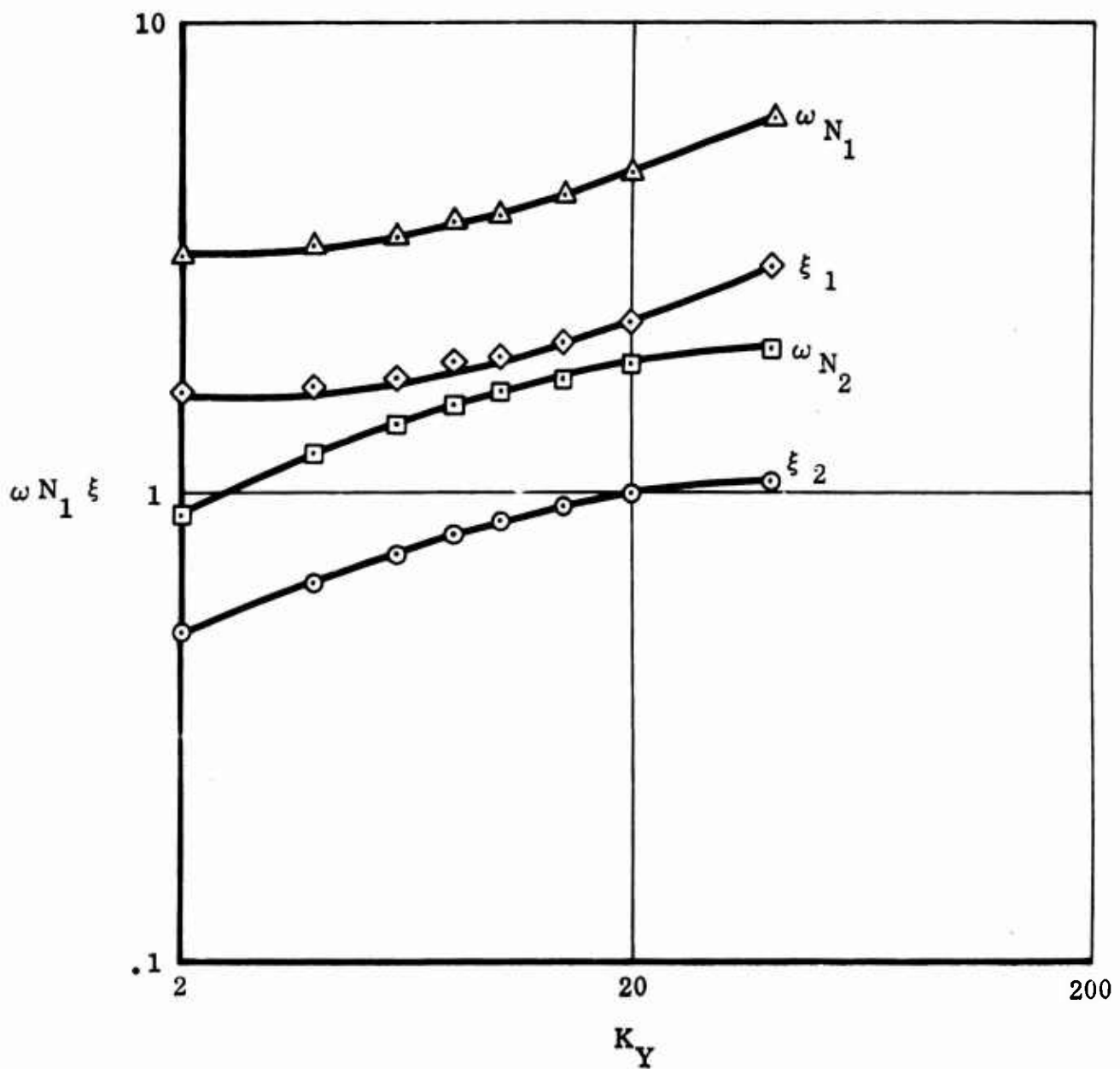


Figure 78 Damping and Natural Frequency vs Yaw Gain

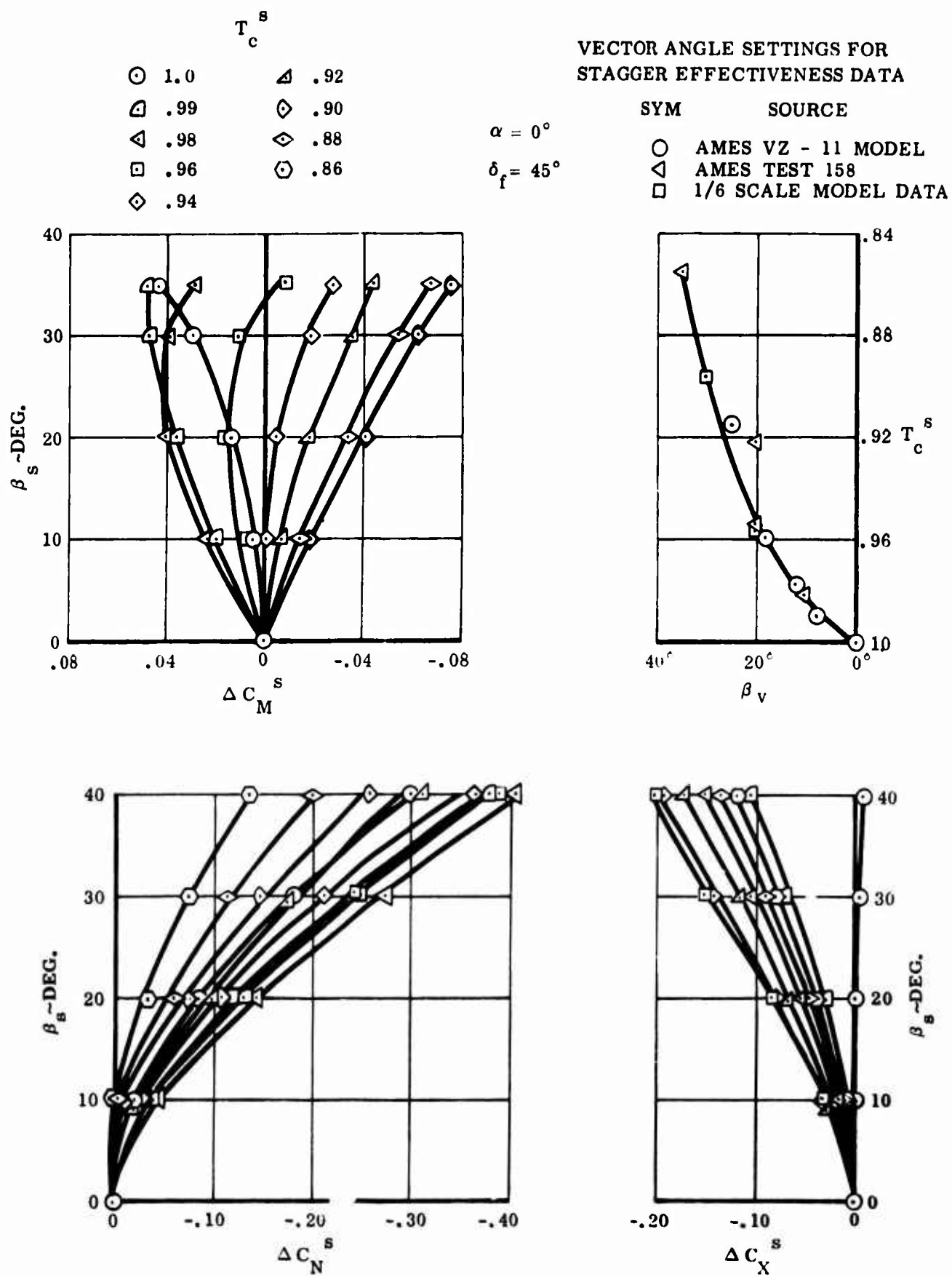


Figure 79 Effect of Exit Louver Stagger on Longitudinal Characteristics

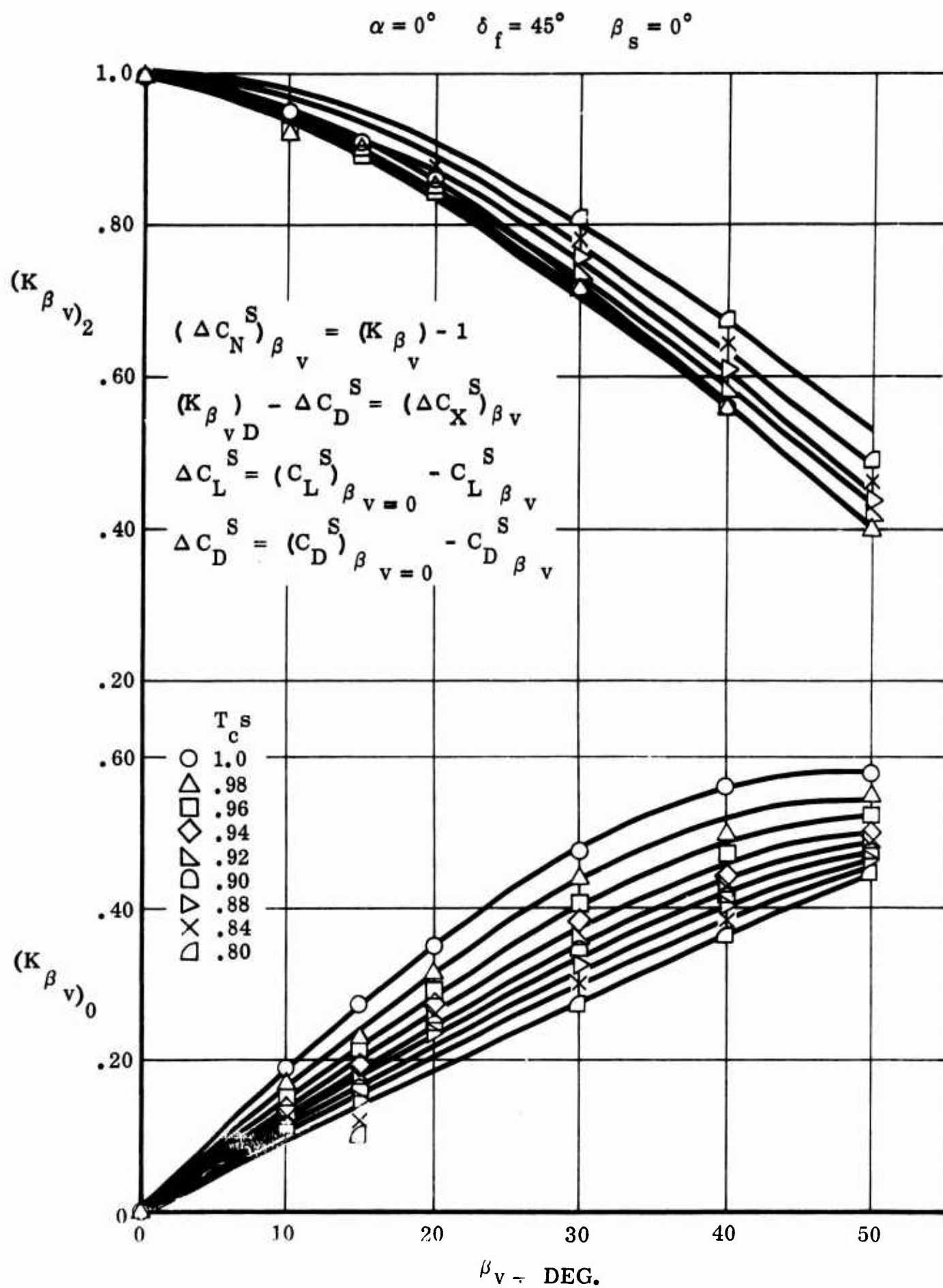


Figure 80 Exit Louver Vector Effectiveness

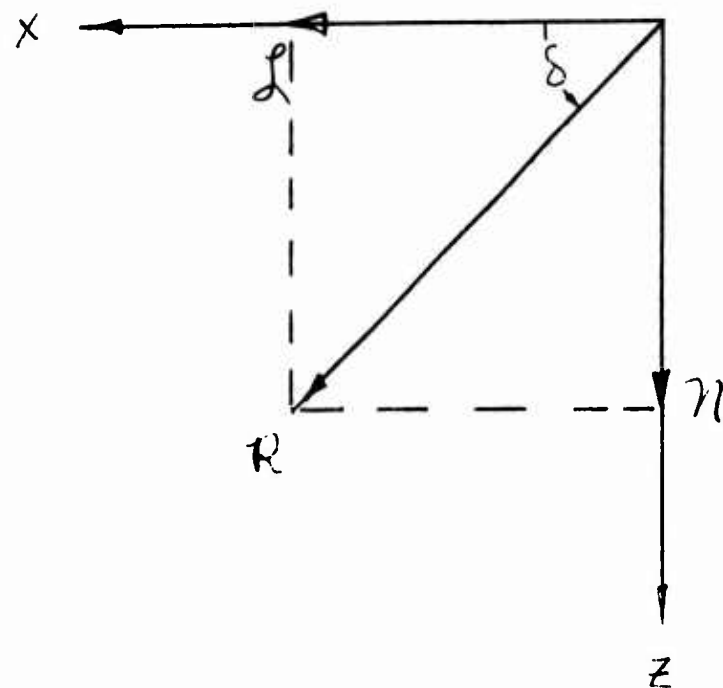


Figure 81 *Determination of Axis of Resultant Moment for a Combination of Rolling and Yawing Moments*

8.0 LIFT-FAN PITCH CONTROL STRUCTURAL FEEDBACK ANALYSIS

8.1 Discussion

When stability augmentation and/or autopilot systems are used in a vehicle which cannot be assumed inelastic, control signals from the sensors can cause autopilot loop instability.

The stabilization system sensors are usually oriented to detect rigid body motion, and their output phasing is based upon rigid body considerations.

Since the vehicle body is a flexible structure, the sensors in reality measure both rigid body motions and elastic body deformations. If the elastic deformations have sufficient magnitude and the wrong phasing, control loop oscillation can result.

The means used to describe the dynamics of the flexible body motion are similar to the use of a Fourier Series to describe an arbitrary periodic wave form.

The motions of a flexible body can be exactly described by the sum of the rigid body motions plus the contribution from an infinite number of "orthogonal body modes". Each of these "orthogonal" or "normal" modes has associated with it a "mode shape" and "modal natural frequency".

One property of these "normal" modes is that the kinetic energy of the body motion will be the sum of the kinetic energies of all of the normal modes plus the kinetic energy of the rigid body modes.

If the flexible body is excited with an impulse of force, the resulting body vibrations will be the sum of contributions from the various normal modes.

With each normal mode is associated a "mode shape", and also a "generalized mass" for the mode. The mode shape is a plot of the modal deflections of points on the body, normalized to any convenient

reference deflection. The generalized mass for a mode is defined as the sum of the differential masses of the body times the square of the modal deflections at the various mass points on the body.

$$m_i = \Sigma dm \left[\phi^{(i)} \right]^2 \quad (1)$$

The equation of motion for the flexible body modes are given as below, in Laplace notation:

$$\Sigma (S^2 + 2\zeta_i \omega_i S + \omega_i^2) q_i = \Sigma \frac{1}{m_i} \left[F \phi_f^{(i)} + M \sigma_m^{(i)} \right] \quad (2)$$

Where

ζ_i = the damping of the i th mode

ω_i = the natural frequency of the i th mode

q_i = the generalized coordinate of the i th mode

m_i = the generalized mass of the i th mode

F = the applied force

M = the applied moment

$\phi_f^{(i)}$ = the normalized deflection of the i th mode at the point of application of the force, F .

$\sigma_m^{(i)}$ = the slope of the normalized deflection curve of the i th mode at the point of application of the moment, M .

In addition, $\Sigma \left[F \phi_f^{(i)} + M \sigma_m^{(i)} \right]$ is defined as the "generalized force".

In general, in autopilot analysis we are interested in solving for the generalized coordinates, because the sum of the generalized coordinates of a point on the body will determine the deflection of that point on the body.

We can show in block diagram form the effect of the rigid + flexible body modes.

Let us assume that we are interested in the effect of the body flexibility upon the pitch rate gyro. Further assume that the pitch rate gyro signal is finally fed to the nose-fan thrust reverser. This is shown in Figure 82.

Thus, the pitch rate gyro, located at station X_g , measures the total pitch rate at this station. This signal is then fed to the nose-fan thrust reverser servo located at approx. X_{nf} , which modifies the body motion in the desired (it is hoped) manner.

This is shown in block diagram form in Figure 83.

θ_g is defined as the total pitch angle at the gyro station, and δ_p is the nose-fan thrust reverser angle, measured from full closed.

In general, an infinite number of flexible body modes are not required to represent the elastic body.

In our case, the first 8 modes were investigated. The effect of the 7th & 8th modes was found to be negligible.

Referring to Figure 83, it is seen how the total pitch angle at the gyro station is computed.

In the case of the XV-5A, the excitation for the symmetrical flexible body modes is provided by the nose-fan force. This force consists of two components. The first is a force due to thrust modulation of the nose-fan by means of thrust reverser door movements. The second is a reaction force due to the acceleration of the thrust reverser doors. Figure 84 shows the rigging of the nose-fan doors.

The door actuating mechanism is such that for sinusoidal inputs to the doors, the reaction due to door acceleration becomes equal to the change in thrust due to door displacement at a frequency of about 5 cps.

Above this frequency the reaction due to door acceleration becomes dominant.

Due to the layout of the door actuation mechanism, essentially zero moment is applied at the nose-fan station due to door operation. The generalized force used to determine the flexible body coordinates, q_i , is thus $\sum \delta_p \phi_{NF}^{(i)}$.

Once the q_i 's have been determined, their contributions to the slope (pitch angle) at the gyro station are found by multiplying the q_i values by the slope of the $\phi^{(i)}$ curves at the gyro station, $\sigma_G^{(i)}$.

The total pitch angle at the gyro station is then the sum of the rigid body pitch angle plus the contributions from the flexible body modes.

The q_i values are functions of S , as is shown in equation (3)

$$\Sigma q_i = \Sigma \left[\frac{F\phi_f^{(i)} + M\sigma_m^{(i)}}{m_i (S^2 + 2\zeta_i \omega_i S + \omega_i^2)} \right] \quad (3)$$

We can then write the total pitch angle, $\Sigma \theta_{q_i}$, at the gyro station due to the flexible body modes and add them to the rigid body θ , as is shown in equation (4).

$$\theta_g = \theta_{\text{rigid}} + \Sigma \frac{(F\phi_f^{(i)} + M\sigma_m^{(i)}) \sigma_G^{(i)}}{m_i (S^2 + 2\zeta_i \omega_i S + \omega_i^2)} \quad (4)$$

or, in our case, assuming the rigid body is inertial, we write:

$$\theta_g = \frac{M_{\delta_p}}{I_y S^2} + \Sigma \frac{F_{\delta_p \phi_{NF}}^{(i)} \sigma_G^{(i)}}{m_i (S^2 + 2\zeta_i \omega_i S + \omega_i^2)} \quad (5)$$

Where:

$$M_{\delta_p} = F_{\delta_p} (X_{NF} - X_{C.G.}) \quad (6)$$

and F_{δ_p} is the force at the nose fan station due to δ_p , and includes the effect of nose fan door inertia.

As is seen, equation (5) is the sum of a series of fractions, and to get the θ_g / δ_p transfer function we must determine the sum of these fractions. The lowest common denominator of these fractions is the product of all the fraction denominators, since they are all different. For each gyro location investigated, X_G , the numerator terms vary, but the denominator terms remain the same.

When this operation is performed, a numerator term results, and this numerator term is a function of S , the Laplace operator. The numerator is then generally a polynomial in S , and as such has roots which result in the polynomial having zero value. These roots are the zeros of the θ_g/δ_p transfer function, while the roots of the denominator cause the transfer function to have an infinite value, and are called the poles of the transfer function. As previously stated, the zeros vary with gyro location, but the poles are invariant.

In general, the θ_g/δ_p transfer function is favorable if the zeros of the transfer function occur at lower frequencies than their associated poles. This is to say, the roots of the transfer function should be aligned zero, pole, zero, pole, etc., as S increases. This configuration of poles and zeros results in a phase characteristic which tends to lead the rigid body phase angle.

The local pitch angle/nose fan force response has been calculated for gyros located at Sta. 90, Sta. 120, and Sta. 150.

Bode plots for these responses are shown in Figures 85, 86 and 87.

Figure 85 is the plot for the Sta. 90 gyro location. This configuration results in a large additional phase lag in the 100-150 rad/sec region.

Figure 86 is for the Station 120 gyro location. It is seen that the phase angle never becomes greater than 180° lagging, which is the phase angle of the assumed rigid body mode.

Figure 87 is the plot for the Station 150 gyro location. This location is in the equipment compartment area, and was the originally selected gyro location. This configuration also has large phase lags around 100 rad/sec.

In order to combine the flexible body with the SA system, several of the parameters were assigned reasonable values.

The rate gyro was given a natural frequency of 26 cps, with a damping ratio of 0.3 critical.

The servo was given a third-order response with the first order time constant of $1/20$ second, and the second order having a natural frequency of 20 cps and damping ratio of 0.3.

The nose wags body transfer function is a double zero at 5 cps, with a gain constant of -1450.

The gyro compensation network has the transfer function

$$\frac{\text{Amplifier input}}{\text{Gyro output}} = \frac{1 + S}{1 + 10S} \quad (7)$$

This corresponds to a ratio of .1, which is the worst case as far as structural feedback is concerned.

Figure 88 is a Bode plot of the response of the servo and nose fan thrust reverser response, $(F/F_o)/\delta_p$

Figure 89 is a Bode plot of the complete system for the Station 120 gyro location. In this case the allowable gain, δ_{p/θ_g} , is 13 degrees/deg/sec.

Figure 90 is the same as Figure 89, with one exception. In this case, a parallel "T" notch network has been added with a null frequency of 100 radians/sec. This network has the transfer function:

$$\frac{1 + \frac{S^2}{\omega_o^2}}{1 + \frac{2S}{\omega_o} + \frac{S^2}{\omega_o^2}}$$

In this case, the allowable gain can be raised to 70, or 37 DB.

Figure 91 is a Bode plot of the complete system less the notch network for the Sta. 150 gyro location. The maximum gain attainable with this configuration is 2.9.

Figure 92 is a Bode plot for the Sta. 150 configuration with the addition of the 100 rad/sec. notch network. Here a maximum gain of 40, or 32DB is attainable.

Figures 93, 94, 95 and 96 show the modal shapes along the fuselage centerline for the first 8 body modes. It is seen that Station 120 is an advantageous gyro location because the slopes of the first two modes

are small, the slopes of the third and fourth modes are small, the slopes of the fifth and sixth modes are zero, and the slopes of the seventh and eighth modes are negligible.

For this work the rigid body was assumed to be purely inertial. This is not true at low frequencies, but at the frequencies of interest in this investigation (10 cps and up) this is a valid assumption.

In general, the vehicle will be flown at various gain and ratio settings, and the objective of this analysis is to ensure that within the gain capabilities of the SA System the rigid body modes will be the limiting factor on system gain. A system gain of about 100 is attainable from the stabilization package, but the short period will go unstable at a gain of around 50. It is thus desirable to be able to attain a gain of over 50 without structural feedback problems.

In addition to relocating the gyros to Station 120, the incorporation of the parallel "T" notch network has been recommended. This network is light and simple, and affords zero transmission at its design frequency. It is useful to reduce the system amplitude at such a point where a troublesome resonant peak occurs.

Preliminary tests on the unloaded nose fan door servo indicate that the damping of the second-order portion of the response might be higher than previously estimated. The addition of the servo inertia load should both lower the frequency of the second-order and the damping.

Figure 97 is a plot of phase and amplitude for: the servo, $\omega_n = 120$, $\zeta = .3$, $\tau = 1/20$ sec.; the rate gyro, $\omega_n = 163$, $\zeta = .3$; the compensation network, $\tau_{\text{numerator}} = 1$ sec., $\tau_{\text{denom}} = 10$ sec.; and the N. W. B. zero, $\omega_N = 31.5$, $\zeta = 0.0$.

Figure 98 is a phase-amplitude plot for the same configuration as Figure 97, plus the addition of a parallel "T" notch network with the null at 100 rad./sec.

Figures 99, 100 and 101 give the complete system block diagram for the Sta. 90, 120 and 150 gyro locations. Due to the large number of second-order terms in the θ_g / δ_p transfer function, a shorthand notation is used. The expression $\frac{\theta_o}{\theta_i} = 1 / \frac{\omega_N = A}{\zeta = B}$ (3) is defined as equivalent

to the expression

$$\frac{\theta_o}{\theta_i} = 1 / \left(\frac{S^2}{A^2} + \frac{2BS}{A} + 1 \right)$$

8.2 Analysis

The inertia of the nose fan doors has considerable bearing on the structural feedback problem. This inertia is reflected back through two bellcranks to the nose fan door actuator, which reacts vertically against the aircraft structure.

The inertia of a nose fan door must first be calculated referred to the door hinge axis.

According to the latest weights data available, the weight of one door is 22 lbs., I_x of a single door is equal to .115 slug ft², the c.g. of the door is at $\bar{X} = 56.8$, $\bar{Y} = 81.9$, and $\bar{Z} = 16.2$. The front hinge is located at $\bar{X} = 34.55$, $\bar{Y} = 12.0$, and $\bar{Z} = 83.16$.

The aft hinge is located at $\bar{X} = 79.8$, $\bar{Y} = 17.34$, $\bar{Z} = 77.82$.

To transfer this inertia to the door hinge line, we must determine the distance from the door c.g. to the hinge line. This is done most easily by means of descriptive geometry, as in Figure 102.

From Figure 102, the distance between the door c.g. and door hinge line is 2 inches. We can thus calculate the door moment of inertia about the door hinge line:

$$I = .115 + \left(\frac{2}{12} \right)^2 \left(\frac{22.2}{32.2} \right) = .115 + .0191 = .134 \text{ slug ft}^2 \quad (1)$$

We must now calculate the effective inertia reflected to the nose fan door actuator, and refer it to δ_p , the door position angle.

Figure 84 is a 1/4 scale layout of the door rigging.

A door position of 33° from full thrust was picked as nominal for this investigation, and this is the position used in Figure 84.

As shown on Figure 84, the force required from the actuator for nose fan door acceleration at $\delta_p = 33^\circ$ is $-5.36 \ddot{\delta}_p I_{\text{DOOR}}$ for each

door. The total is equal to $-10.72 \ddot{\delta}_p I_{\text{DOOR}}$. This force is vertical, and an upward actuator force results in a positive $\ddot{\delta}_p$. The reaction on the airplane is down, which is a negative force for a positive $\ddot{\delta}_p$.

In addition, the reactions on the two hinge points amounts to $-1.34 \ddot{\delta}_p I_{\text{DOOR}}$ for each side of the airplane, for $-2.68 \ddot{\delta}_p I_{\text{DOOR}}$ total. Thus, the total reaction force due to $\ddot{\delta}_p$ is equal to $-13.4 \ddot{\delta}_p I_{\text{DOOR}}$ or $-1.8 \ddot{\delta}_p$

These figures assumed the door c.g. was on the hinge line, whereas it is actually 2" displaced. This effect is negligible on the results.

We have linearized the thrust change due to δ_p such that $75^\circ \delta_p$ results in -1700 lbs. thrust change, or -1300 lbs/rad.

We can thus express the total force from nose fan door deflection:

$$F \text{ lbs.} = 1300 \delta_p - 1.8 \ddot{\delta}_p \quad (2)$$

$$\text{or } F \text{ lbs.} = -1300 \left(\delta_p + \frac{\ddot{\delta}_p}{722} \right) \quad (3)$$

expressing (3) in Laplace notation,

$$\frac{F}{\delta_p} = -1300 \left(1 + \frac{s^2}{722} \right) \text{ lbs/rad.} \quad (4)$$

$$\frac{F}{\delta_p} = -1300 \left(1 + \frac{s^2}{26.9^2} \right) \text{ lbs/rad.} \quad (5)$$

The structural feedback analysis used earlier data, and as a result the transfer function used was:

$$F/\delta_p = -1450 \left(1 + \frac{s^2}{31.5^2} \right) \text{ lbs/rad.} \quad (6)$$

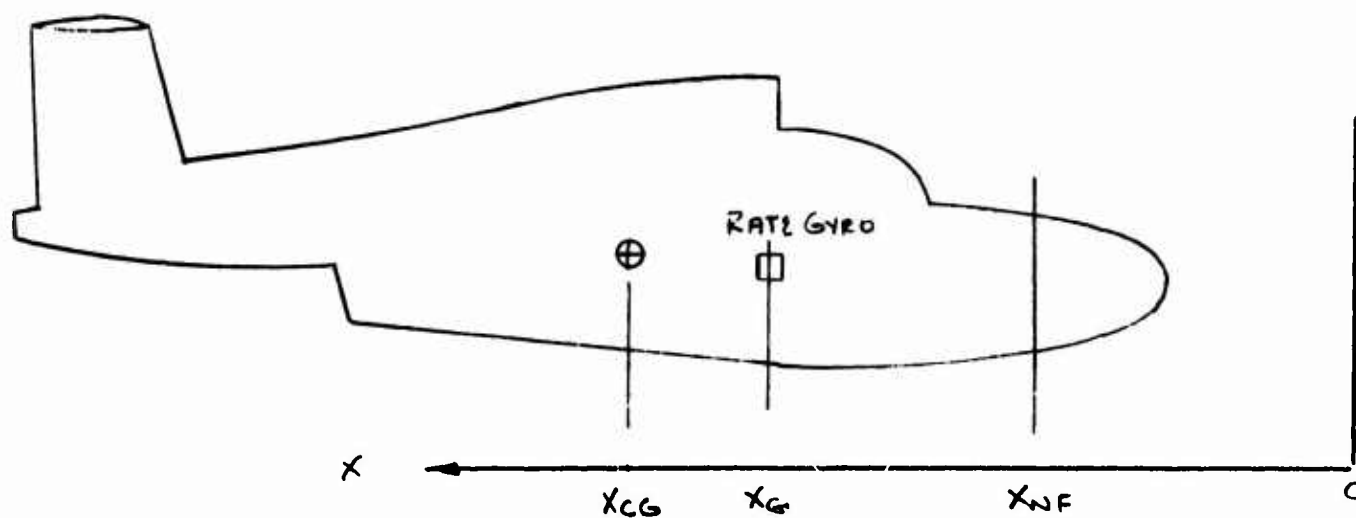


Figure 82 Location of Rate Gyros and Nose Fan with Respect to Airplane C. G.

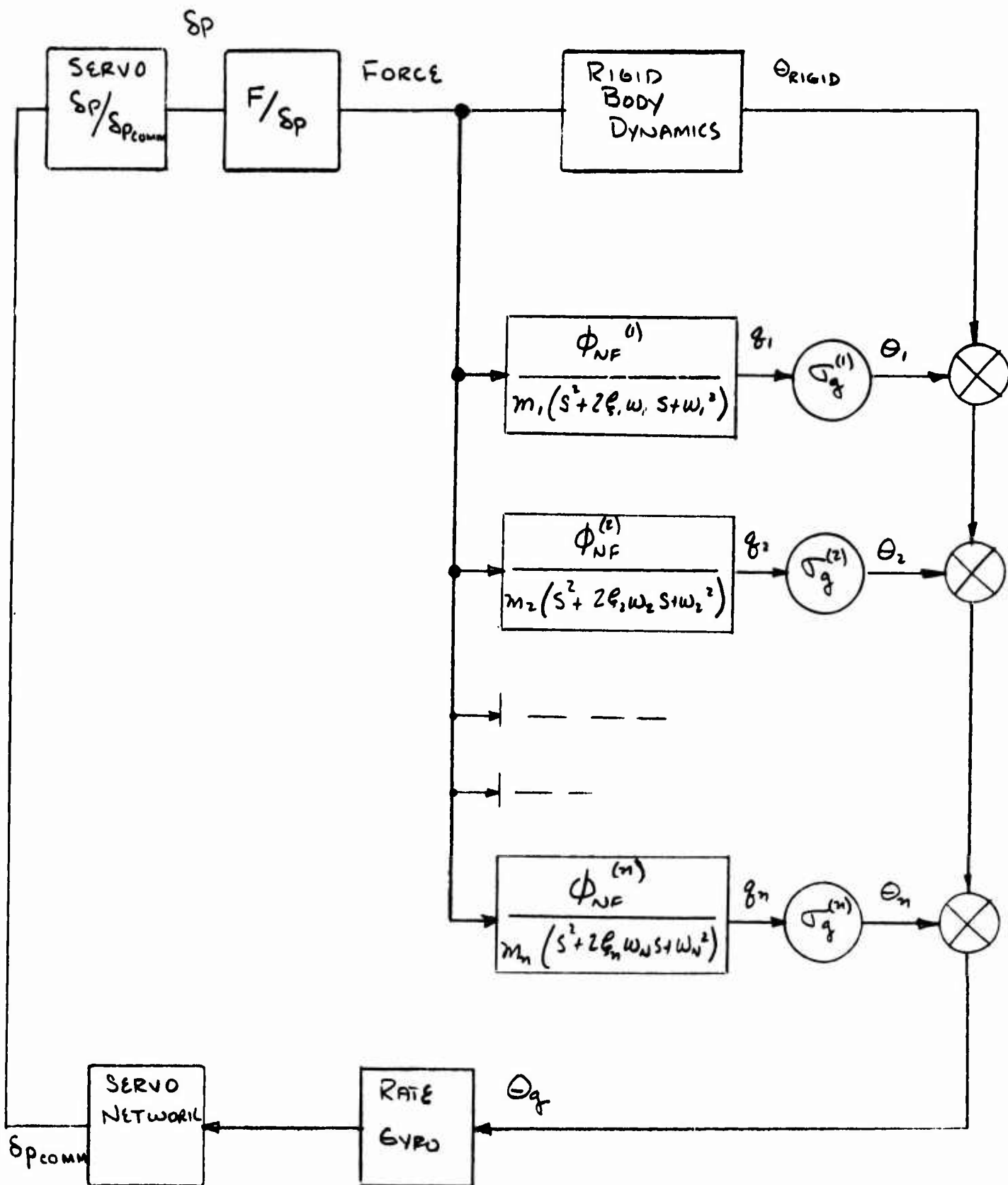


Figure 83 Block Diagram of Flexible Body Plus SA System

BLANK PAGE

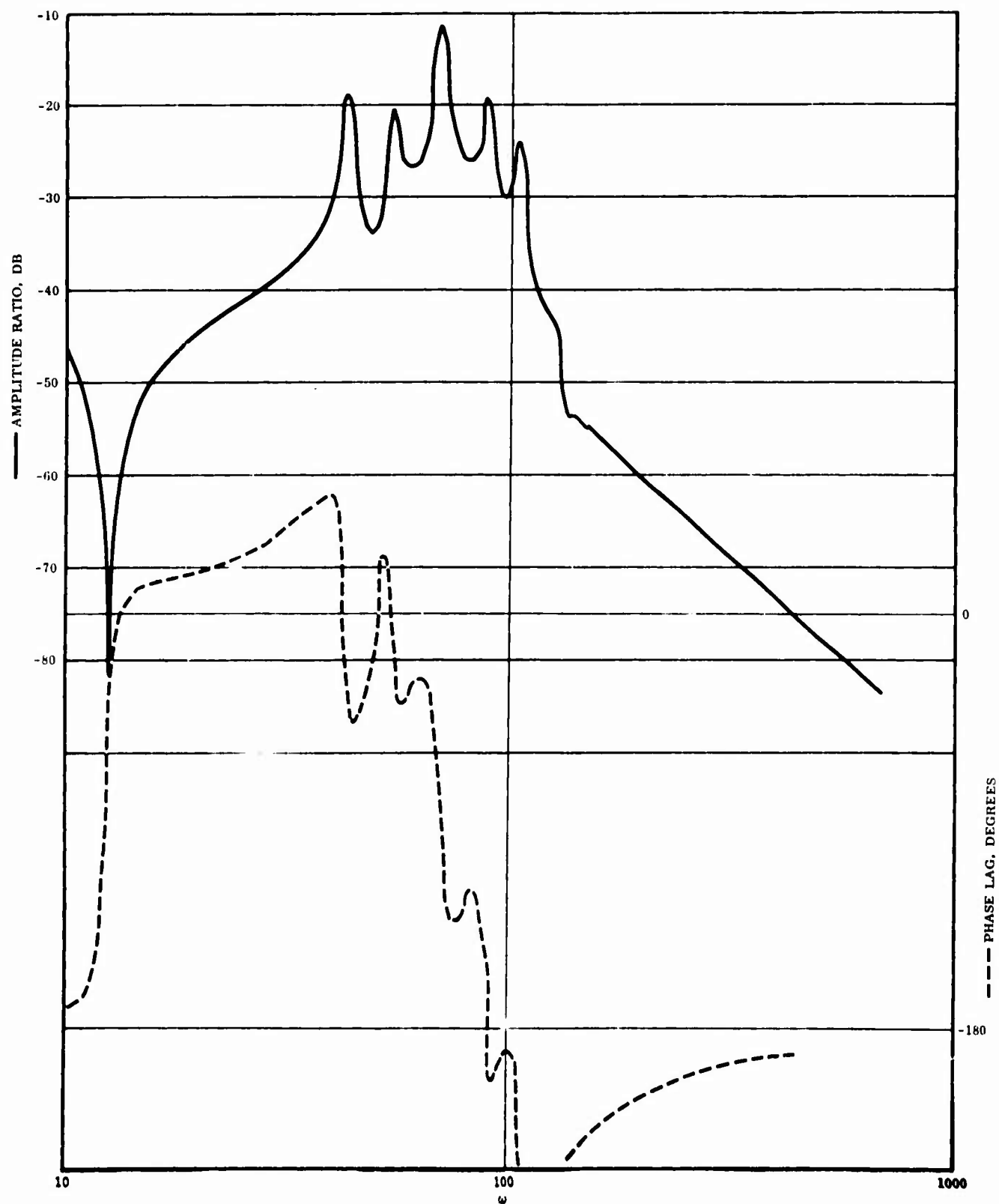


Figure 85 Gyro Station 90, θ_g/δ_p Response Less NWB Response

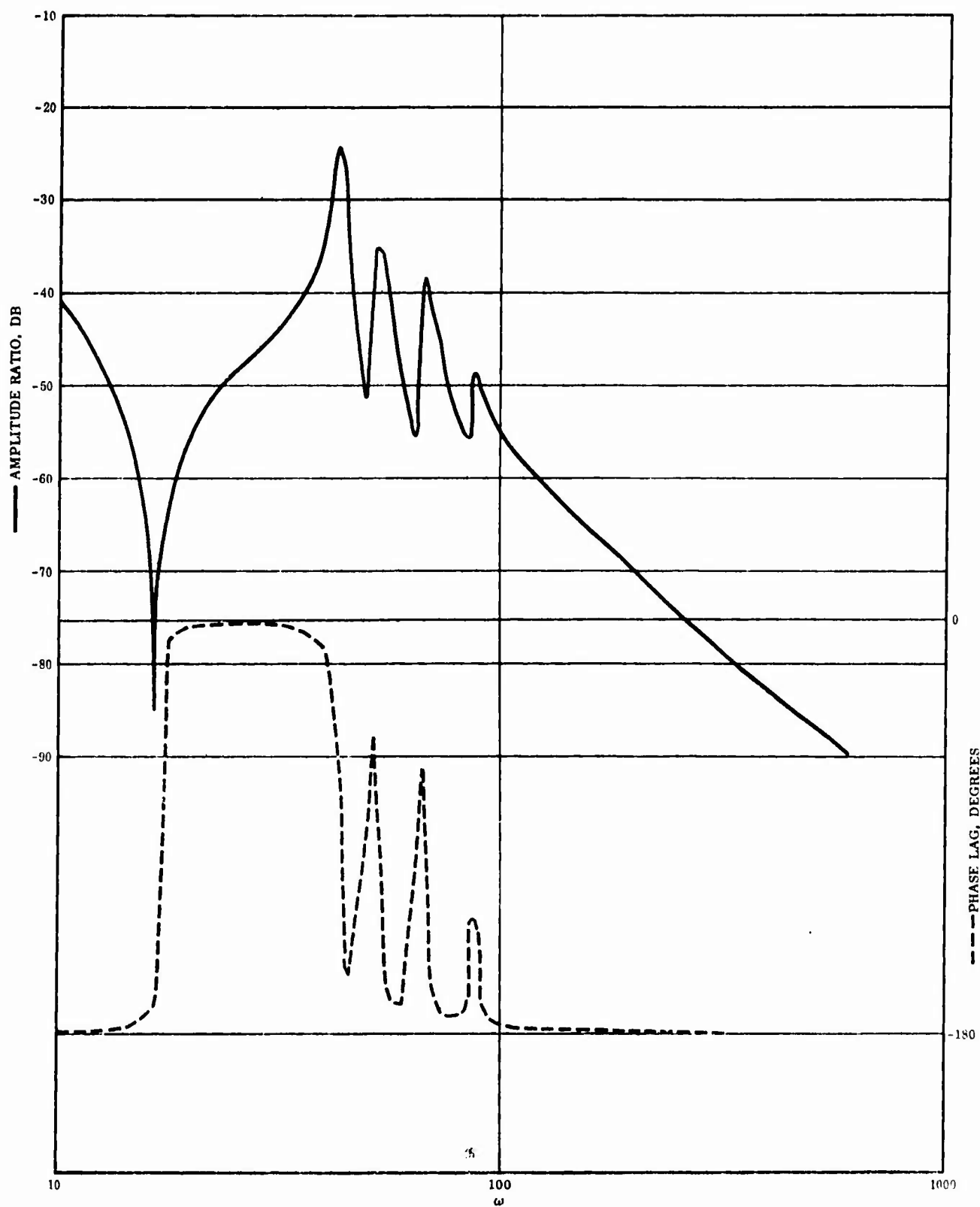


Figure 86 Gyro Station 120, θ_g / δ_p Response Less NWB Response

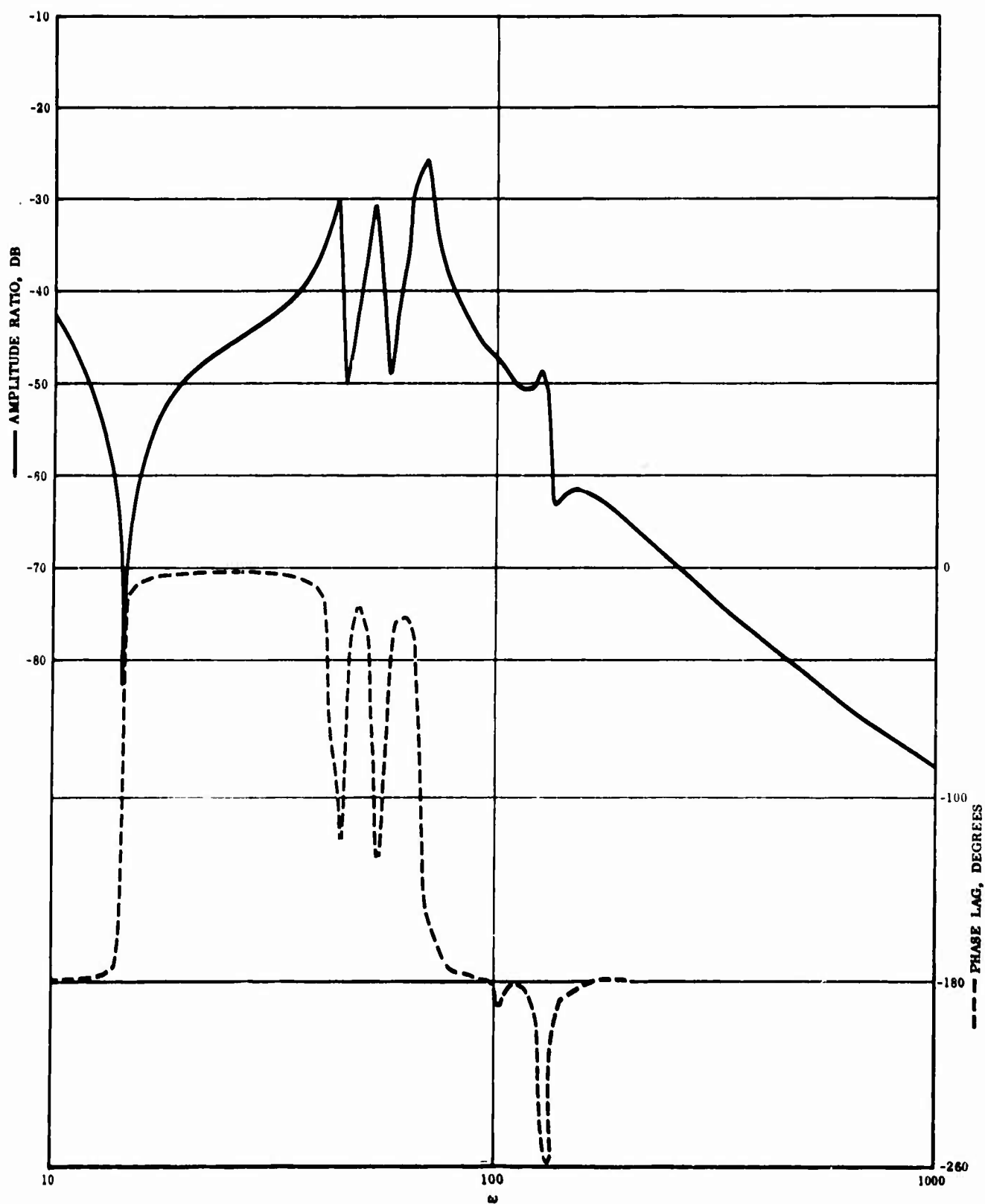


Figure 87 Gyro Station 150, θ_g / δ_p Response Less NWB Response

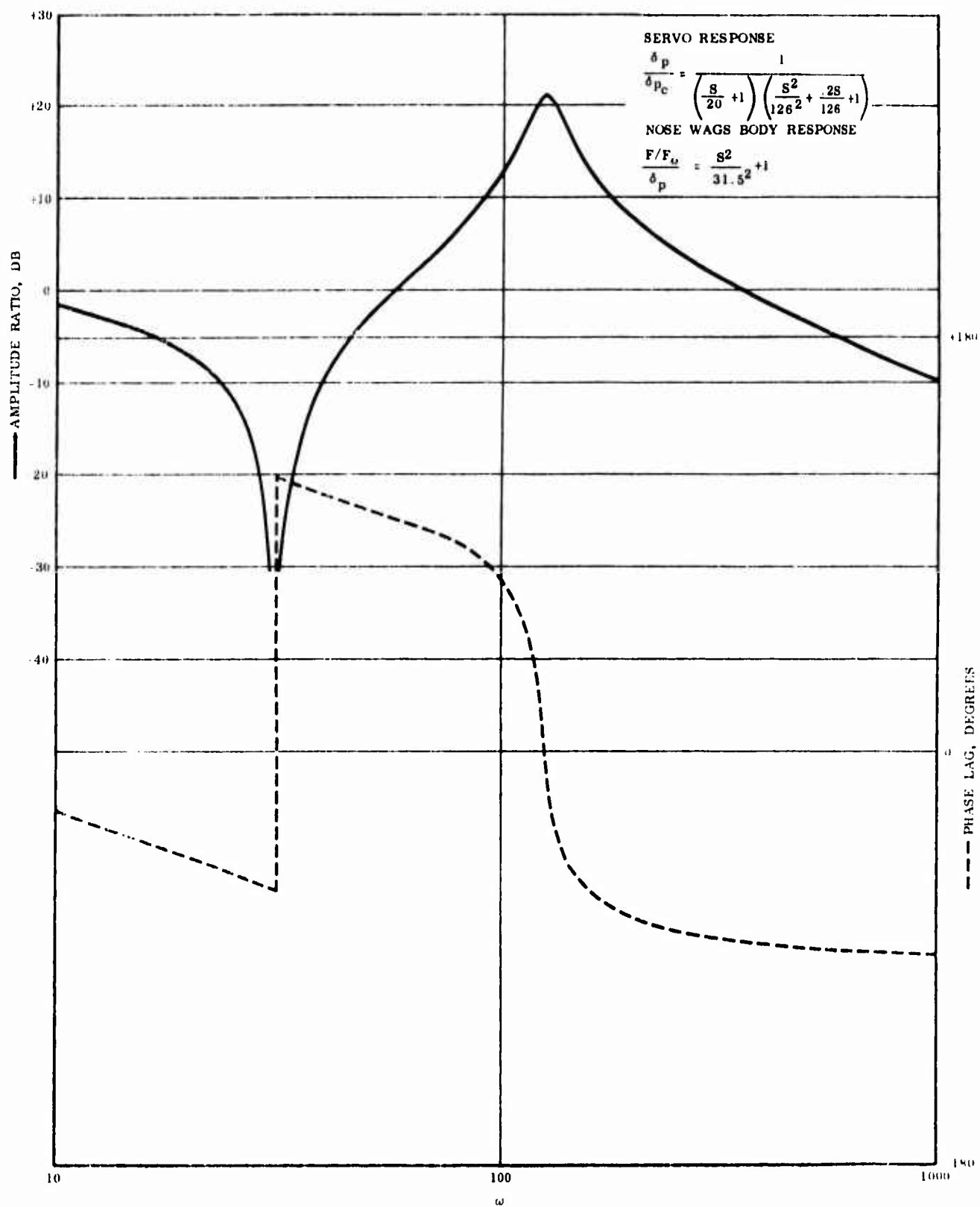


Figure 88 $F/F_0/\delta_{p\text{Command}}$ Response

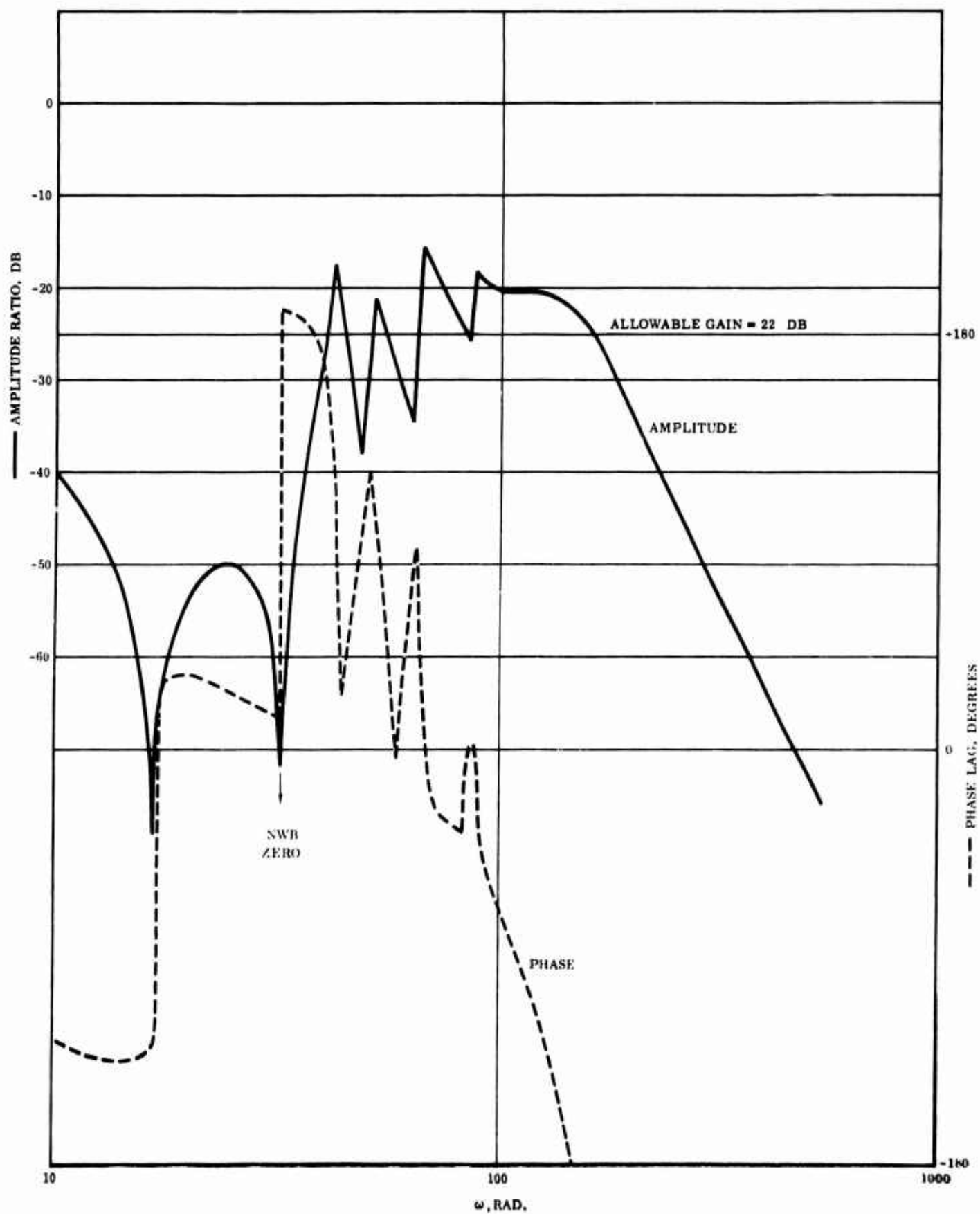


Figure 89 Gyro Station 120 θ_g / δ_p Response, No Notch Network

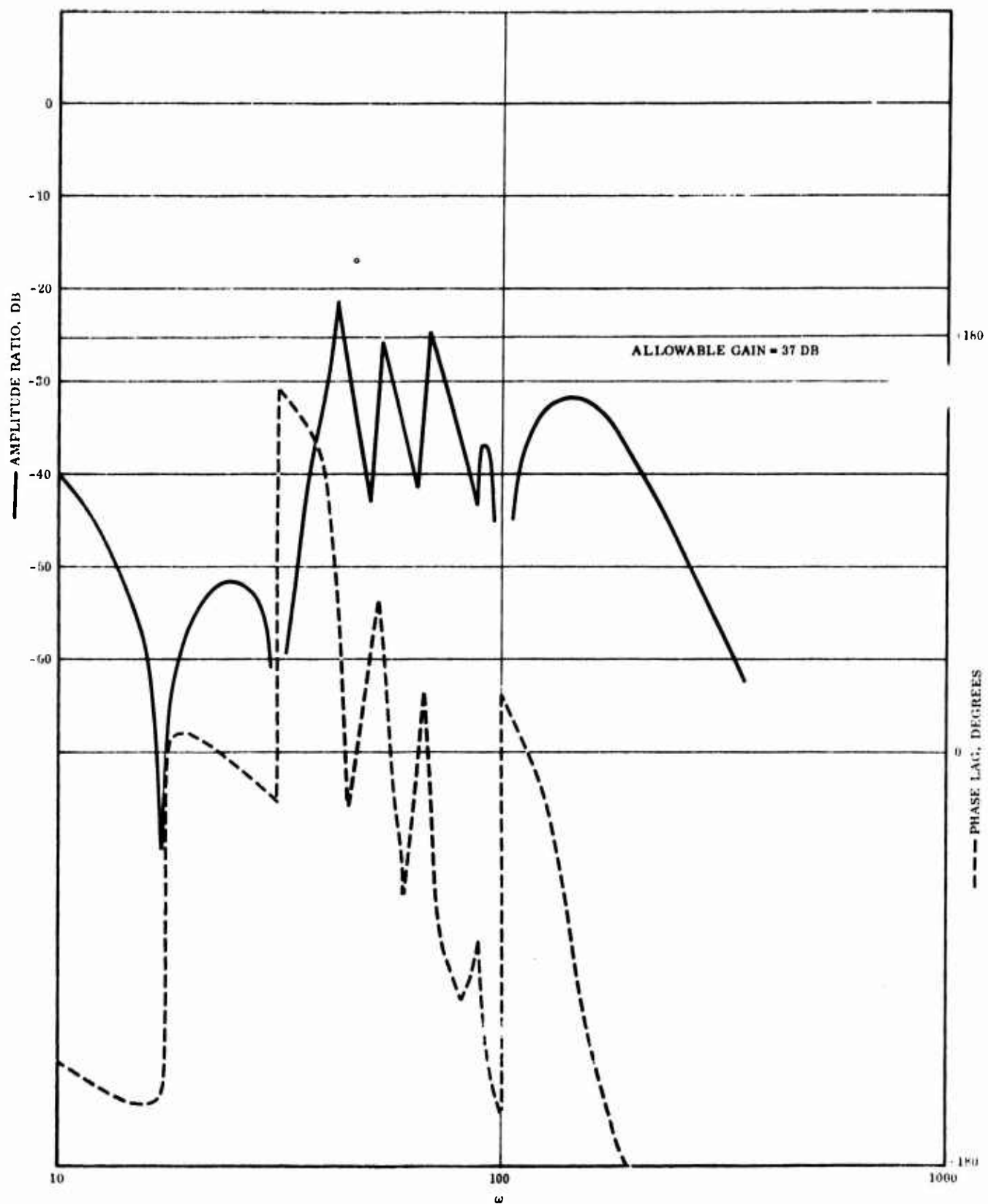


Figure 90 Gyro Station 120, θ_g / δ_p Response Including Notch Network at 100 Rad/Sec

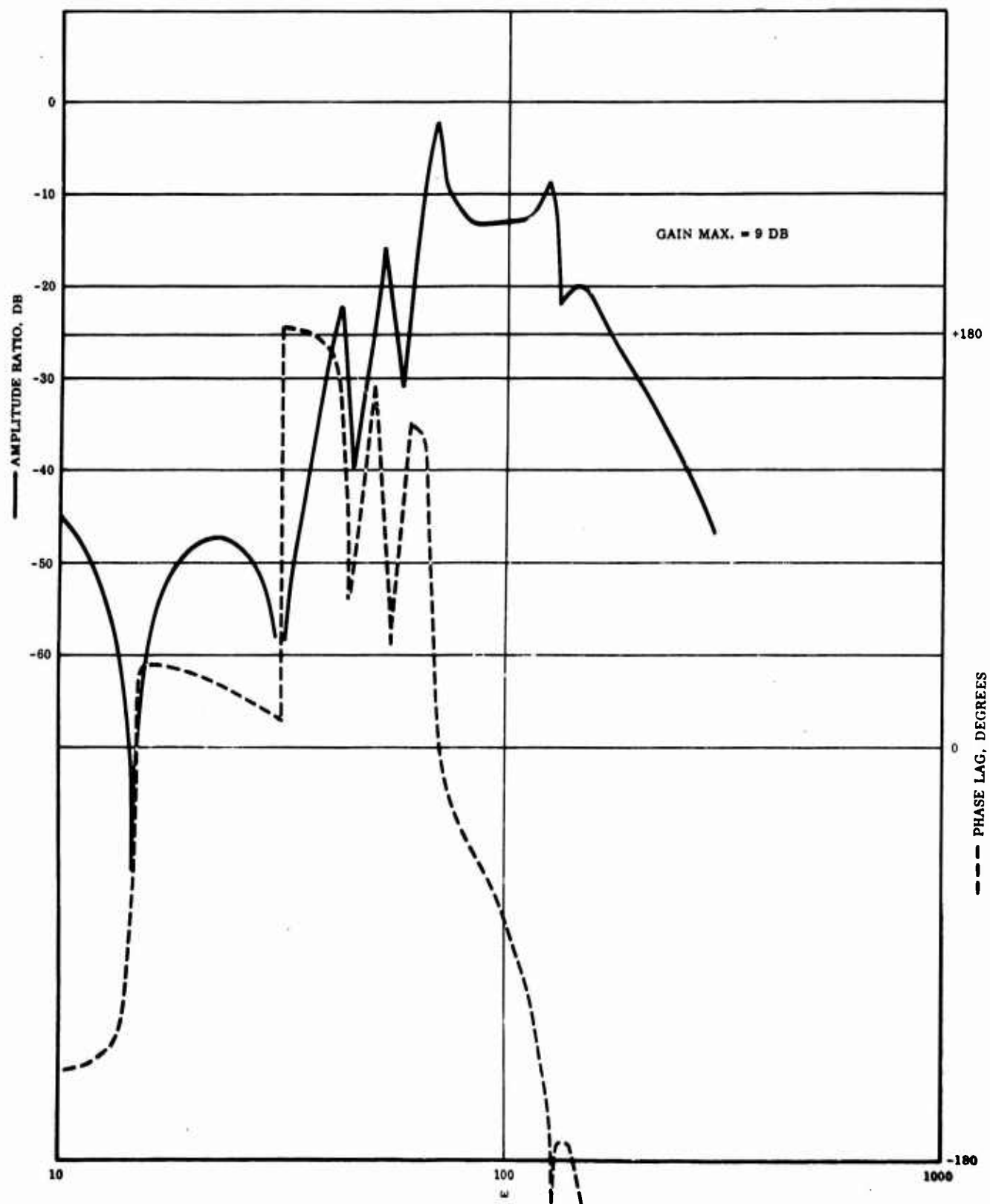


Figure 91 Gyro Station 150, θ_g / δ_p Response, No Notch Network

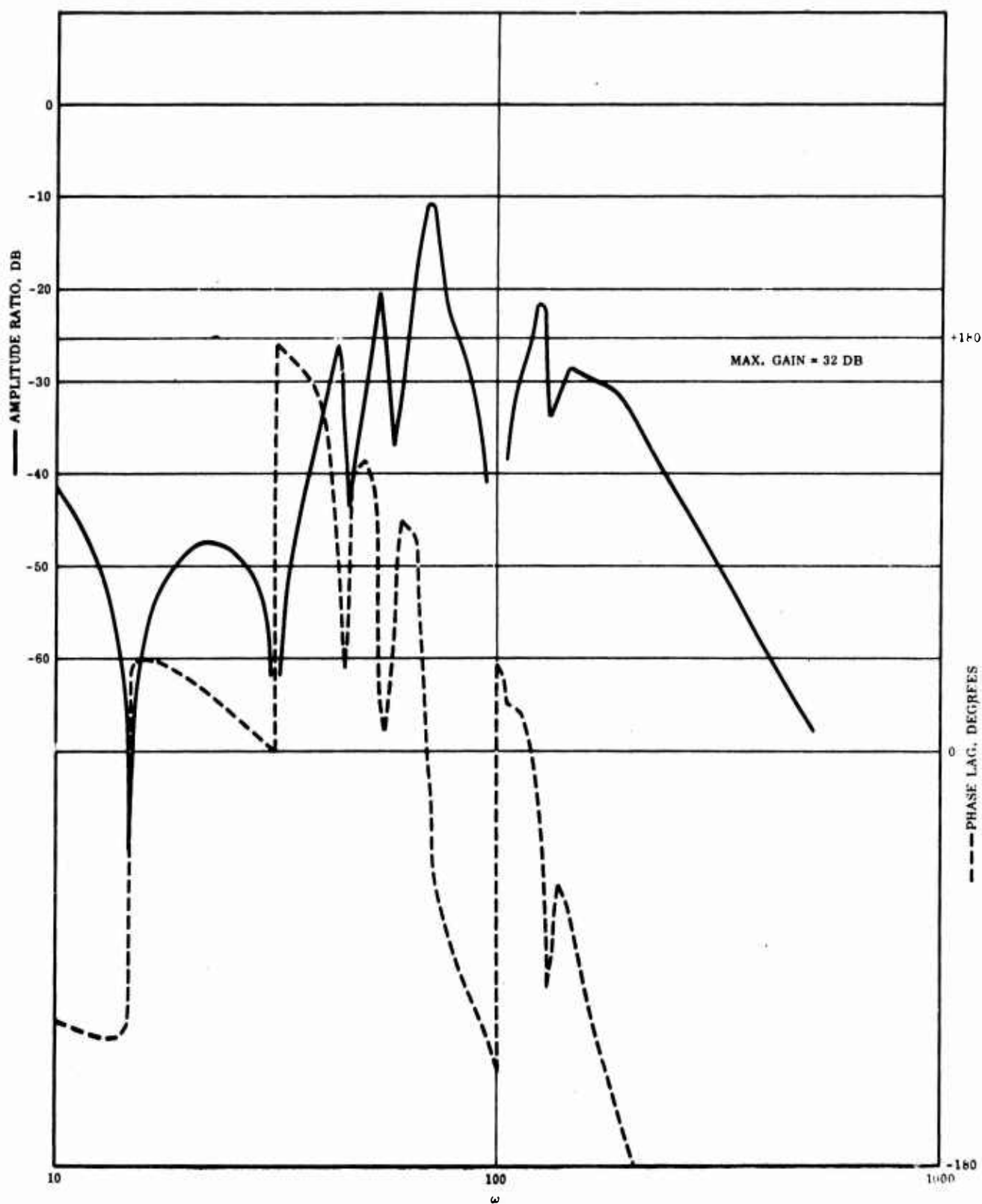


Figure 92 Gyro Station 150, θ_g / δ_p Response Including Notch Network at 100 Rad/Sec

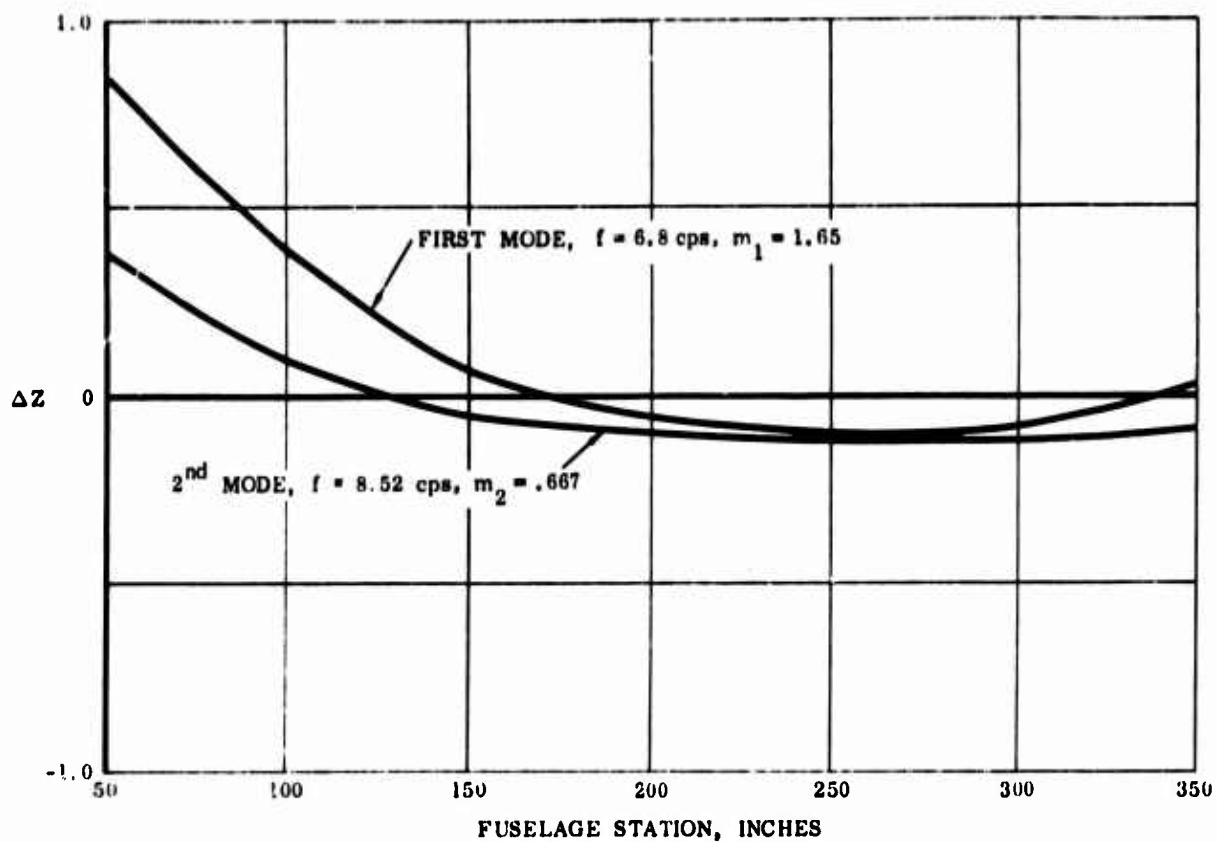


Figure 93 Normalized Deflection vs Fuselage Station for 1st and 2nd Free-Free Body Modes

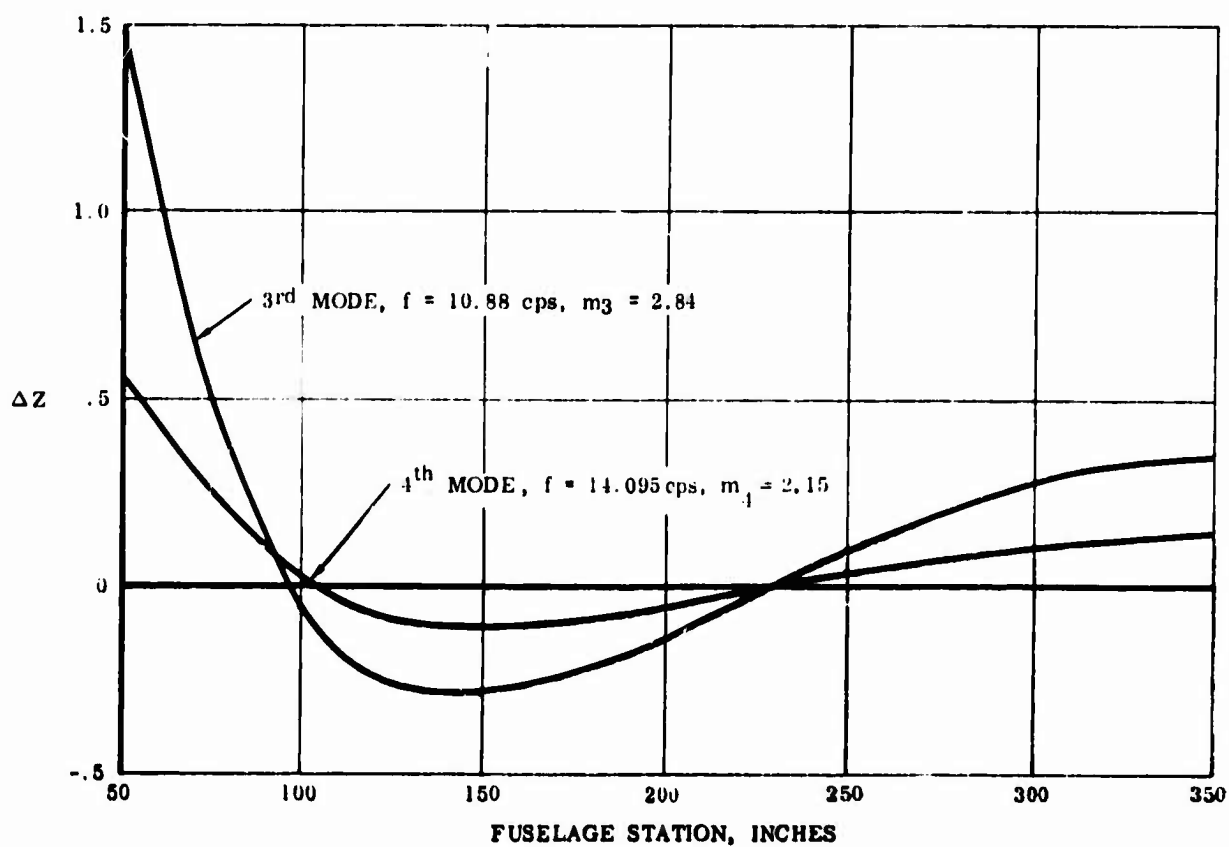


Figure 94 Normalized Deflection vs Fuselage Station for 3rd and 4th Free-Free Body Modes

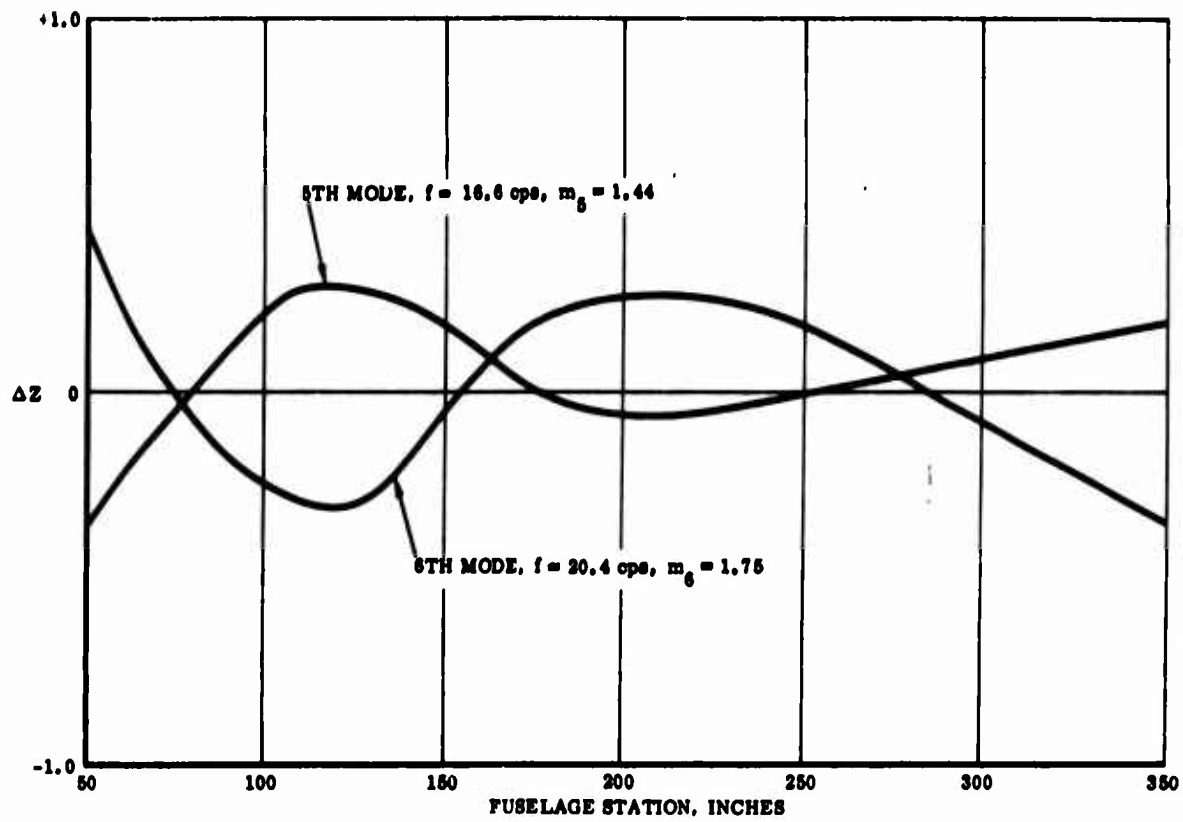


Figure 95 Normalized Deflection vs Fuselage Station for 5th and 6th Free-Free Body Modes

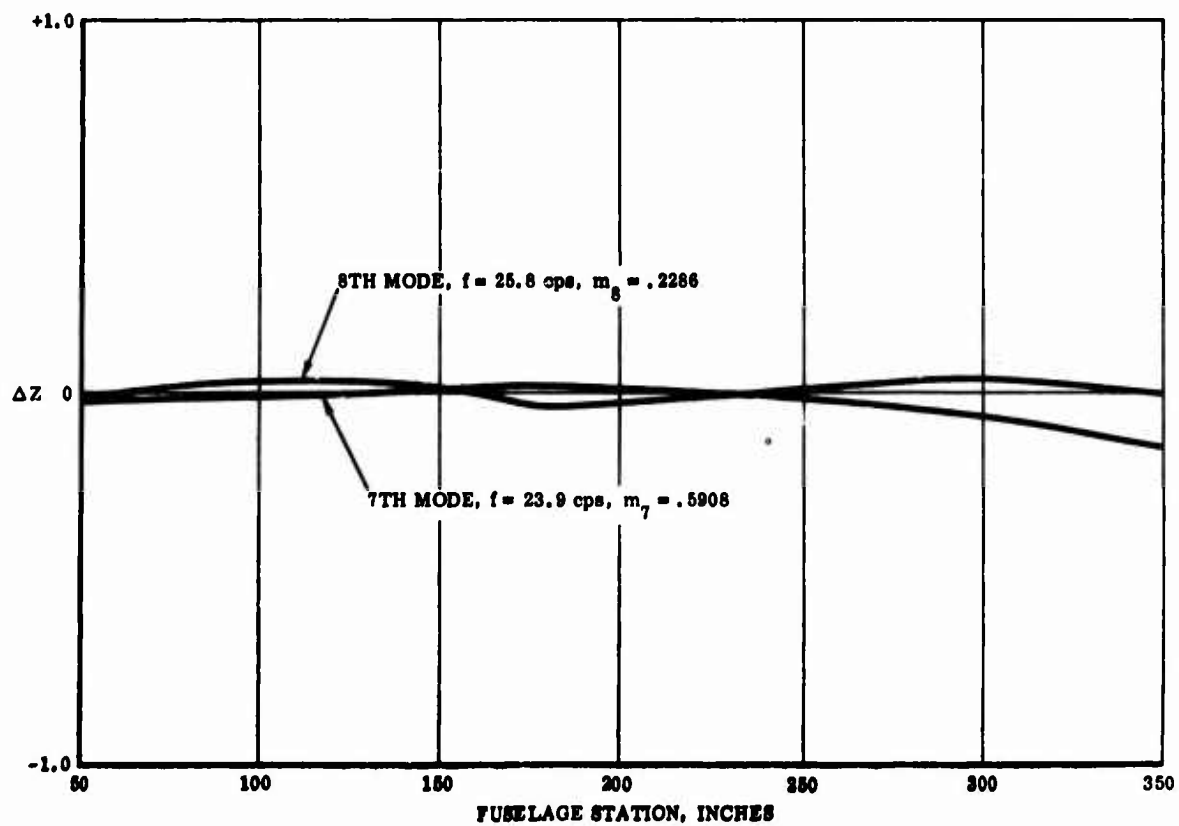


Figure 96 Normalized Deflection vs Fuselage Station for 7th and 8th Free-Free Body Modes

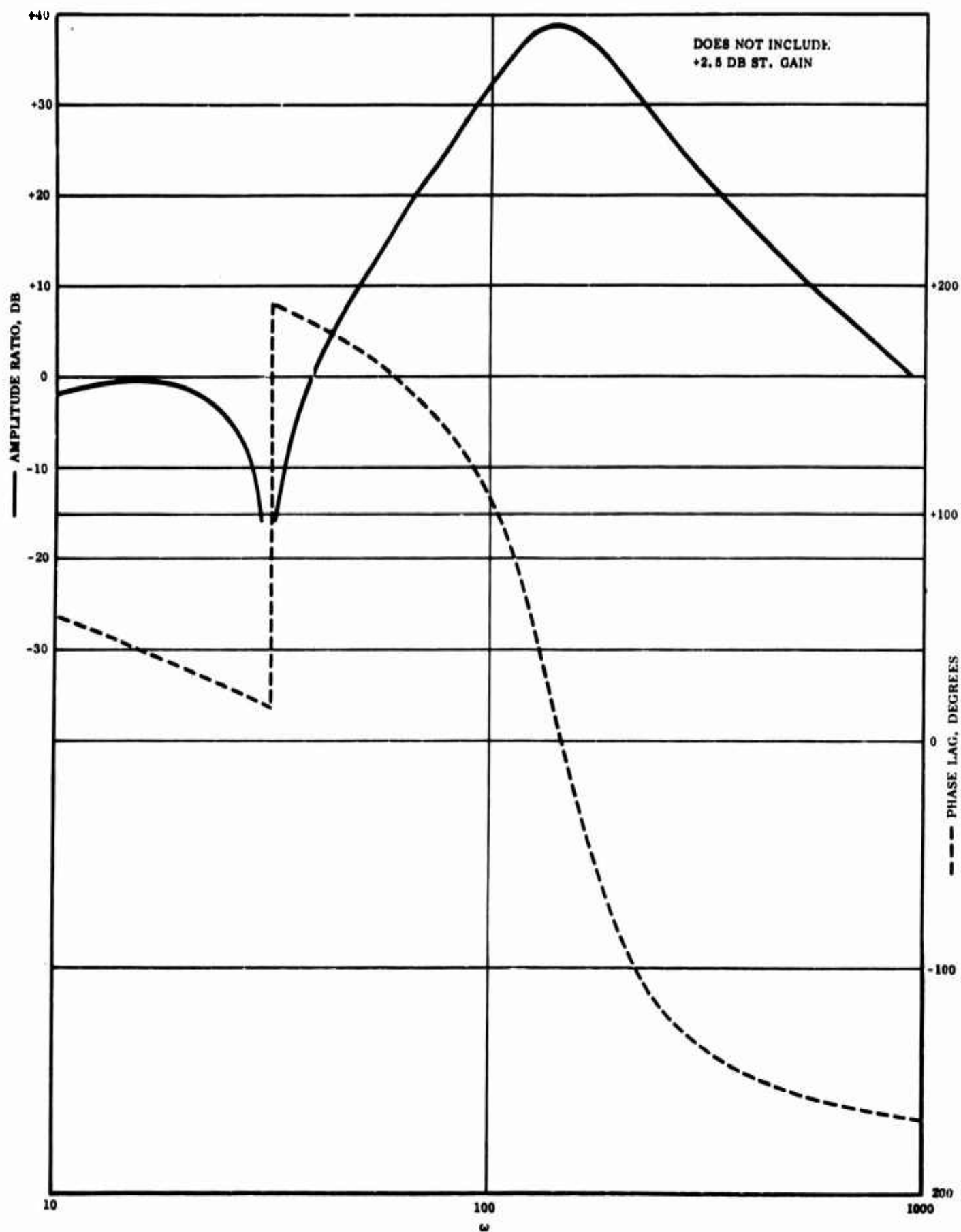


Figure 97 Response of Rate Gyro, Servo and NWB

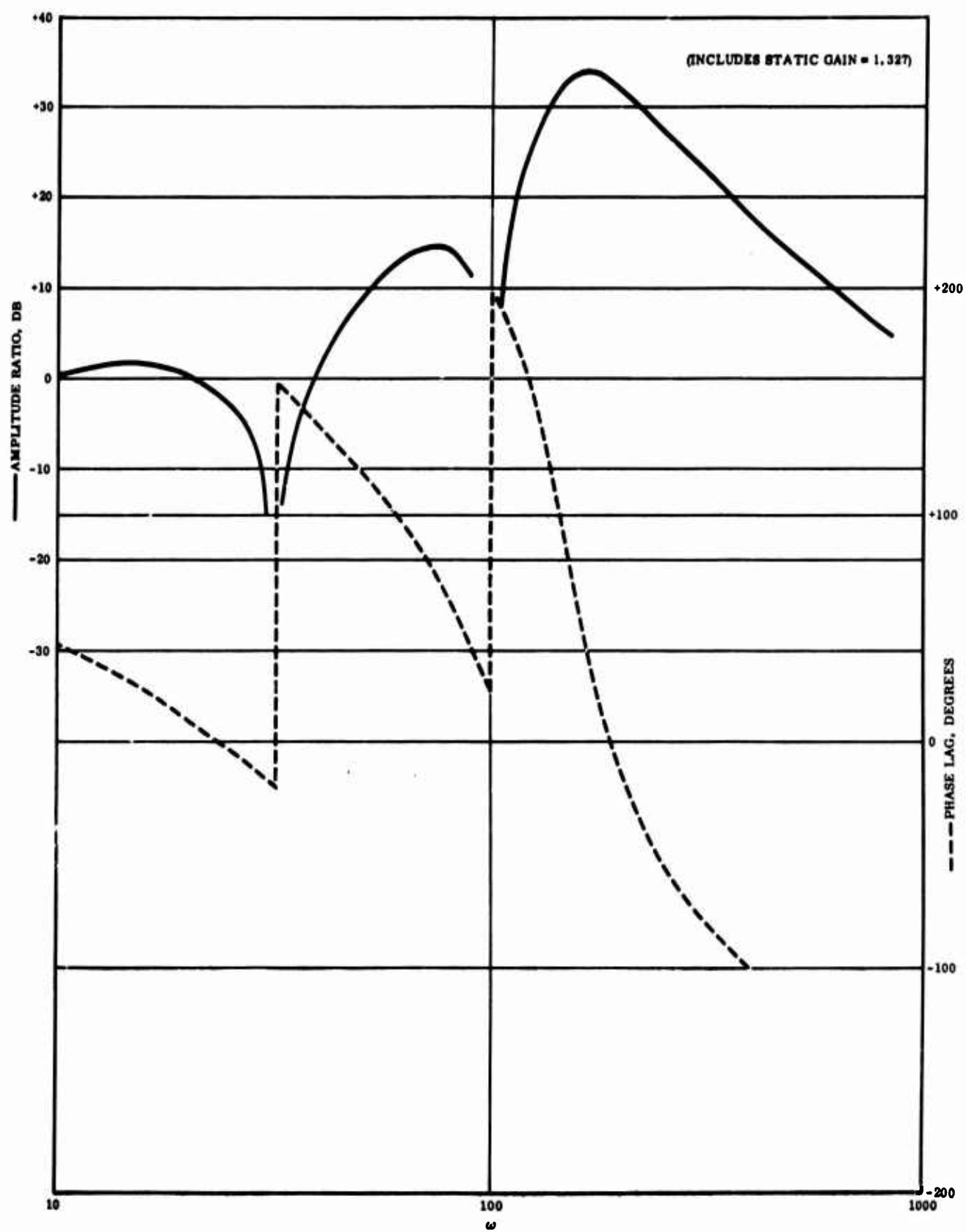


Figure 98 Response of Rate Gyro, Servo, NWB and Notch Network

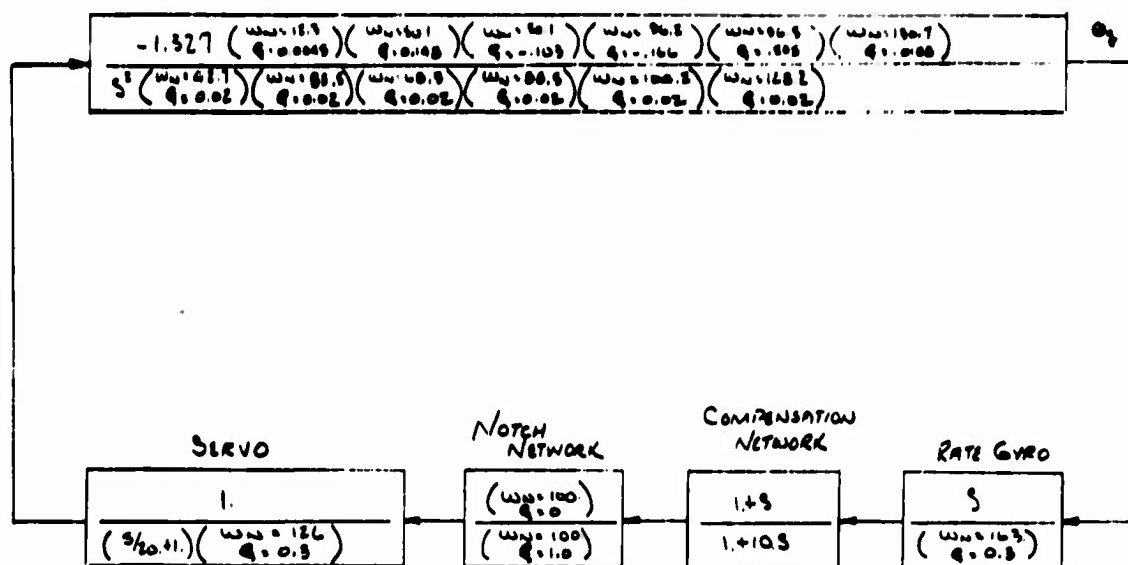


Figure 99 Pitch Loop for Rate Gyro at Station 90

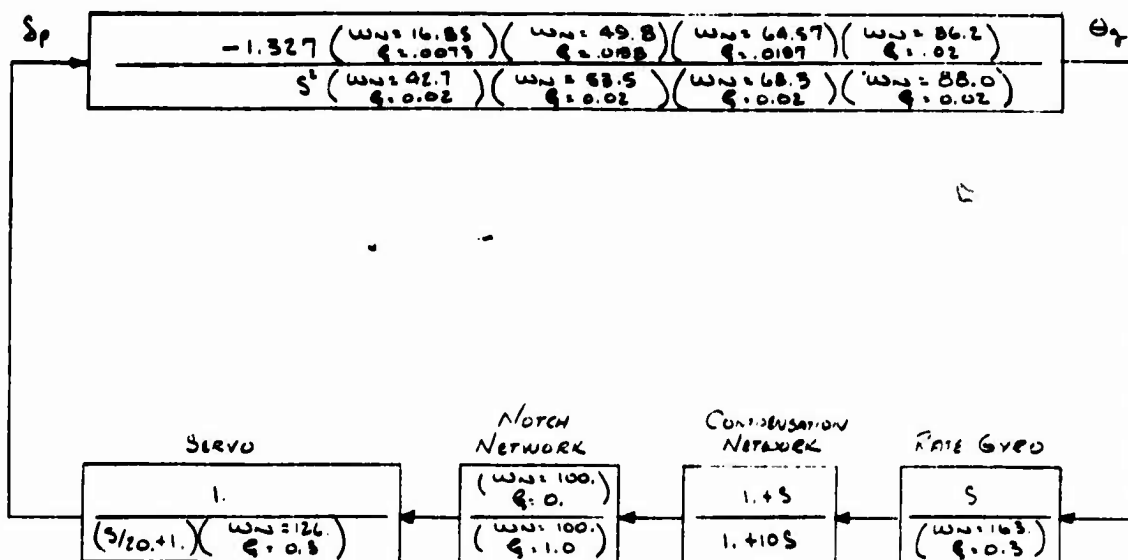


Figure 100 Pitch Loop for Rate Gyro at Station 120

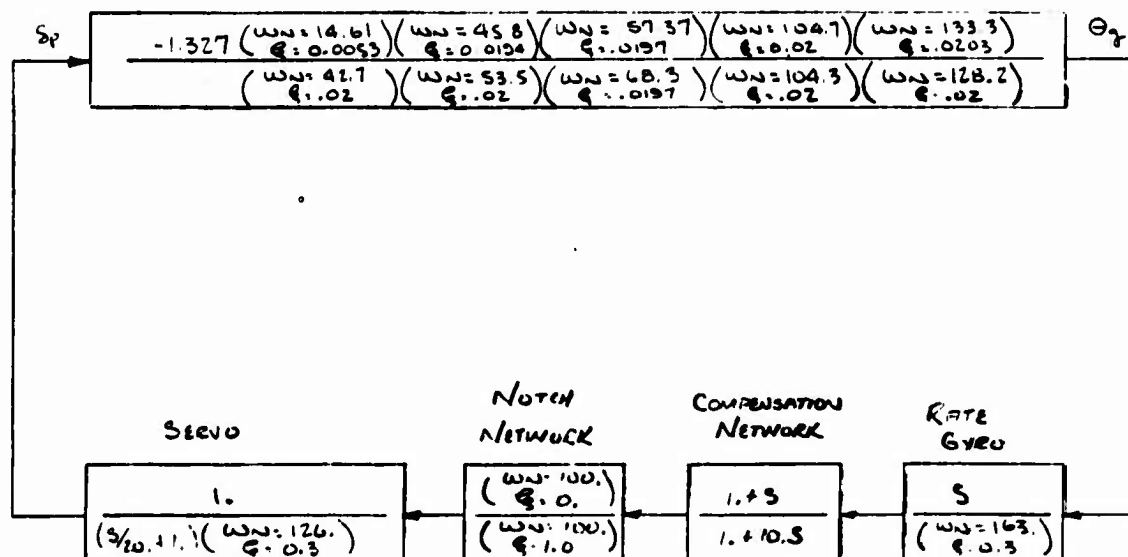


Figure 101 Pitch Loop for Rate Gyro at Station 150

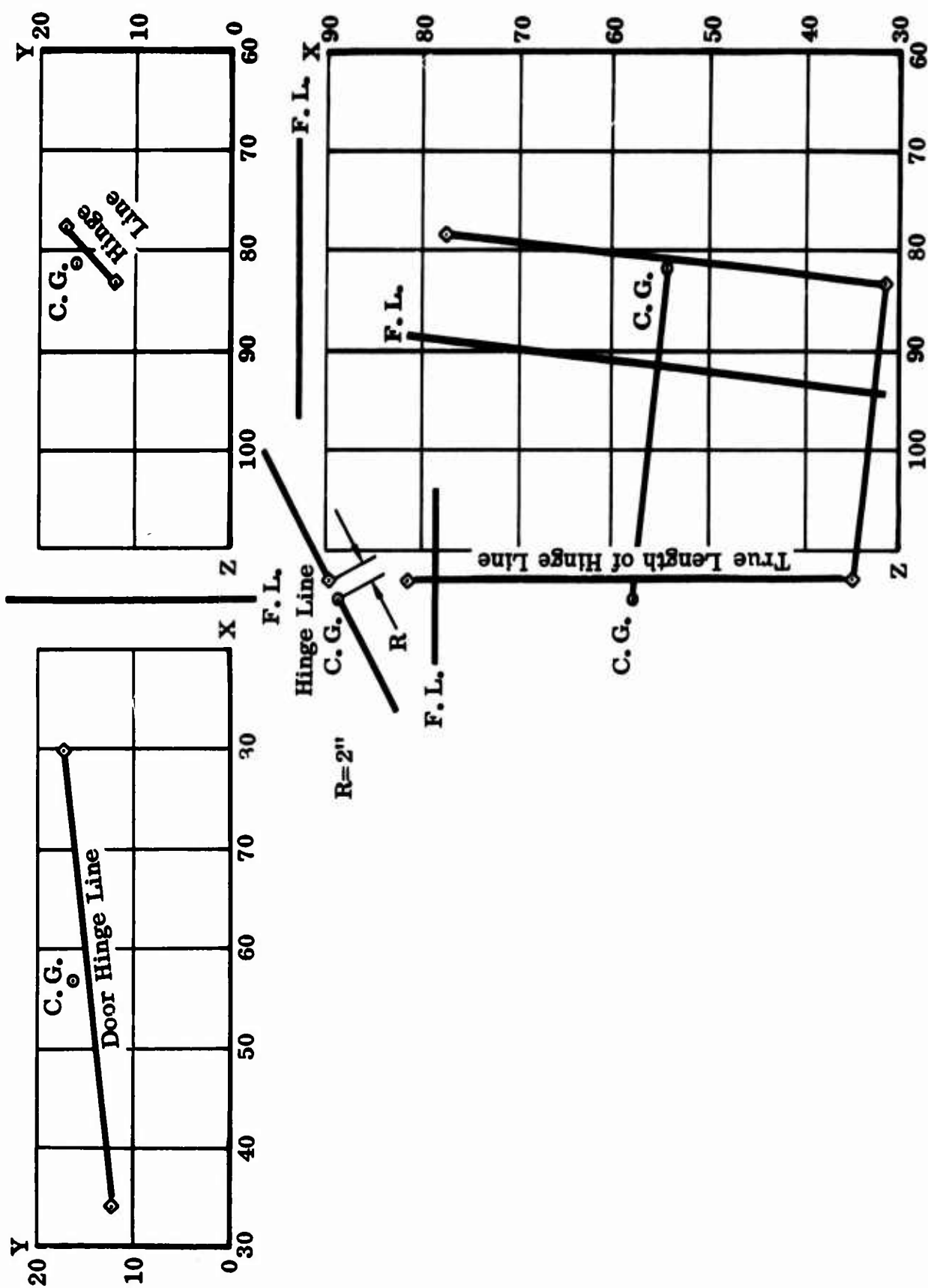


Figure 102 Determination of Distance Between Nose Fan Door C.G. and Hinge Line

BLANK PAGE

9.0 YAW-ROLL-PITCH EULER ANGULAR AND DEFLOREZ DISPLAY RATES DERIVATION

9.1 Discussion

Early in the XV-5A program, the need became apparent for a more realistic visual pilot display if the simulation program was to have meaningful results.

A nationwide survey trip was made to investigate various display concepts, including both fixed and moving base presentations. The most promising system was the point light source system developed by the DeFlorez Company of Englewood Cliffs, New Jersey, a fixed base system.

In this system, a transparency containing the various terrain features is moved about under the light source, and the point source projects through the transparency, resulting in a realistic display on the spherical screen surrounding the simulator cockpit. If the pilot's eyes were at the location of the point source, an exact representation would be afforded. Depending on the radius of the screen, some distance is allowable between the eyes of the pilot and the point light source. Translation of the transparency simulates vehicle translation, and rotation of the transparency simulates vehicle rotations.

A specification for a system such as this containing the various dynamic response requirements was prepared by XV-5A personnel, and the device was constructed by the DeFlorez Company.

The transparency is six feet square, and the active region in X and Y is ± 2 feet. The Z travel of the transparency with respect to the light source is 5 inches total. The active region in roll is approximately $\pm 25^\circ$, and $\pm 17^\circ$ in pitch. Yaw travel is unlimited.

It is thus possible to "scale" the linear motions of the device to any desired ratio, depending upon the vehicle requirements.

One of the limitations of the scale factor chosen is the maximum velocity of the vehicle. If it is desired to be able to fly continuously around the transparency, the radius of turn for the maximum allowable

display device bank angle must be considered. For a coordinated turn, the radius of turn is given in eq. 1.

$$R = \frac{V^2}{g \tan \phi} \quad (1)$$

where R is radius of turn in feet, V is velocity in ft/sec., g is 32.2 ft/sec², and ϕ is the roll angle.

For the display device, ϕ_{\max} is 25°, so equation (1) becomes equation (2).

$$R = \frac{V^2}{15} \quad (2)$$

Now, we know that the maximum circle we can put in a 4 foot square has a 2 foot radius.

If we pick a scale factor K, then we can write equation (3) which is the scaled equation:

$$KR = \frac{V^2}{15} \quad (3)$$

$$\text{or } V_{\max}^2 = K \cdot 15 \cdot 2^2 = 30K. \quad (4)$$

$$\text{or } K_{\min} = \frac{V_{\max}^2}{30} \quad (5)$$

If we thus know the maximum velocity in a given flight regime, we can determine minimum scale factor which allows continuous flight.

In general, it would not be desirable to be required to fly continuously in a circle, so a good value for K_{\min} would allow a circle to be made in 1/2 of the transparency action range, or 1 foot in radius. Then K_{\min} becomes, in equation (6):

$$K_{\min} = \frac{V_{\max}^2}{15} \quad (6)$$

There is another important requirement limiting the scale factor, and this is the required minimum altitude of flight. In a VTOL vehicle, in the low-speed and landing regime, it is desirable to be able to start from ground level, and fly the complete low-speed envelope.

In the case of the XV-5A, the low-speed envelope includes speeds up to conversion speed, or around 100 knots. We may thus determine K_{\min} for 100 Kts TAS. If we are to be able to land, we must be able to attain a minimum altitude equal to the level of the pilot's eye when the airplane is on the ground. In the XV-5A the pilot's eye level is approximately 7 feet.

The limit on display device minimum altitude is a result of the fact that the point light source has a finite diameter, which at close proximity to the transparency causes a loss of resolution of the projected image (fuzziness). This limit has been set at .08 inches. We may thus determine K_{\max} such that this value corresponds to 7' or 84 inches. Thus, in equation (7):

$$.08'' \left(K_{\max} \right) = 84'' \quad (7)$$

$$K_{\max} = \frac{8400}{8} = 1050:1$$

Knowing $V_{\max} = 170$ fps, we calculate

$$K_{\min} = \frac{170^2}{15} = 1900:1$$

In the hovering and transition regime, then, we have two conflicting requirements on scale factor.

We thus compromised by choosing a scale factor of 1500:1, which allows a 10' minimum altitude and still allows continuous flight, although somewhat cramped.

A scale factor of 250:1 was chosen for the hovering regime, and 50,000:1 for conventional flight.

Angles are reproduced exactly, so no conversion is necessary.

Vehicle motions are thus represented by motions of the projection of the point light source through the transparency and onto the screen.

The earth frame of reference is the transparency, and the frame of the device (along with the simulator cockpit) becomes the vehicle. We then have motions of the earth coordinates which look like vehicle motions.

The projector must be driven by the proper computer inputs to truly represent the vehicle motions. The angles through which the projector must rotate are referenced to the earth coordinate system, and are thus Euler angles.

In the projector, the pitch axis is rigidly attached to the support structure. The roll axis is carried by the pitch system, and yaw is attached to roll.

If we start at the transparency, which actually represents the earth, the first rotation is yaw, the second is roll, and the last is pitch.

Thus, we have a set of Yaw, Roll, Pitch Euler angles, and it is necessary to compute the rate-of-change of these Euler angles in terms of the Euler angles and the body angular rates, since body angular rates are computed on the analog computer.

In addition, the Euler angles must be used to calculate ground velocities in terms of body velocities.

Section 9.2 following shows a derivation of the Yaw-Roll-Pitch Euler angles and direction cosines, and the derivation of the ground velocities from body velocities.

These equations are used to generate the Euler angles required to drive the projection device; as well as to generate the S_x , S_y and S_z components for drive of the linear degrees of freedom.

9.2 Analysis

The mechanical layout of the DeFlorez projection device requires the use of Yaw, Roll, Pitch direction cosines and Euler angles.

The derivation of the direction cosine matrix, Euler angular rates, and inertial velocities for this system of Euler angles is given below.

We use a right hand coordinate system, where rotations in the order of X, Y, Z are considered positive. That is, a rotation of X into Y, Y into Z, or Z into X is a positive rotation.

For the Yaw rotation, referring to Figure 103, 104 and 105, we can write,

$$X_{B_1} = X_e \cos \psi + Y_e \sin \psi \quad (1)$$

$$Y_{B_1} = -X_e \sin \psi + Y_e \cos \psi \quad (2)$$

$$Z_{B_1} = Z_e \quad (3)$$

For the Roll rotation

$$X_{B_2} = X_{B_1} \quad (4)$$

$$Y_{B_2} = Y_{B_1} \cos \phi + Z_{B_1} \sin \phi \quad (5)$$

$$Z_{B_2} = -Y_{B_1} \sin \phi + Z_{B_1} \cos \phi \quad (6)$$

and for the Pitch rotation,

$$X_{B_3} = X_{B_2} \cos \theta - Z_{B_2} \sin \theta \quad (7)$$

$$Y_{B_3} = Y_{B_2} \quad (8)$$

$$Z_{B_3} = X_{B_2} \sin \theta + Z_{B_2} \cos \theta \quad (9)$$

We can write these equations in matrix form as below:

$$\begin{bmatrix} X_{B_1} \\ Y_{B_1} \\ Z_{B_1} \end{bmatrix} = \begin{bmatrix} \cos \psi & \sin \psi & 0 \\ -\sin \psi & \cos \psi & 0 \\ 0 & 0 & 1 \end{bmatrix} \begin{bmatrix} X_e \\ Y_e \\ Z_e \end{bmatrix} \quad (10)$$

$$\begin{bmatrix} X_{B_2} \\ Y_{B_2} \\ Z_{B_2} \end{bmatrix} = \begin{bmatrix} 1 & 0 & 0 \\ 0 & \cos \phi & \sin \phi \\ 0 & -\sin \phi & \cos \phi \end{bmatrix} \begin{bmatrix} X_{B_1} \\ Y_{B_1} \\ Z_{B_1} \end{bmatrix} \quad (11)$$

$$\begin{bmatrix} X_{B_3} \\ Y_{B_3} \\ Z_{B_3} \end{bmatrix} = \begin{bmatrix} \cos \theta & 0 & -\sin \theta \\ 0 & 1 & 0 \\ \sin \theta & 0 & \cos \theta \end{bmatrix} \begin{bmatrix} X_{B_2} \\ Y_{B_2} \\ Z_{B_2} \end{bmatrix} \quad (12)$$

Combining the above, and solving for X_{B_3} , Y_{B_3} and Z_{B_3} in terms of

X_e , Y_e , Z_e , there obtains:

$$\begin{bmatrix} X_{B_3} \\ Y_{B_3} \\ Z_{B_3} \end{bmatrix} = \begin{bmatrix} \cos \theta & 0 & -\sin \theta \\ 0 & 1 & 0 \\ \sin \theta & 0 & \cos \theta \end{bmatrix} \begin{bmatrix} 1 & 0 & 0 \\ 0 & \cos \phi & \sin \phi \\ 0 & -\sin \phi & \cos \phi \end{bmatrix} \begin{bmatrix} \cos \psi & \sin \psi & 0 \\ -\sin \psi & \cos \psi & 0 \\ 0 & 0 & 1 \end{bmatrix} \begin{bmatrix} X_e \\ Y_e \\ Z_e \end{bmatrix} \quad (13)$$

or

$$\begin{bmatrix} X_{B_3} \\ Y_{B_3} \\ Z_{B_3} \end{bmatrix} = \begin{bmatrix} \theta \\ \phi \\ \psi \end{bmatrix} \begin{bmatrix} X_e \\ Y_e \\ Z_e \end{bmatrix} \quad (14)$$

Expanding the product $\theta \phi \psi$, we get:

$$\begin{bmatrix} X_{B_3} \\ Y_{B_3} \\ Z_{B_3} \end{bmatrix} = \begin{bmatrix} (\cos \theta \cos \psi - \sin \theta \sin \phi \sin \psi) & (\cos \theta \sin \psi + \sin \theta \sin \phi \cos \psi) & (-\sin \theta \cos \phi) \\ (-\cos \phi \sin \psi) & (\cos \phi \cos \psi) & (\sin \phi) \\ (\sin \theta \cos \psi + \sin \psi \cos \theta \sin \phi) & (\sin \theta \sin \psi - \cos \theta \cos \psi \sin \phi) & (\cos \theta \cos \phi) \end{bmatrix} \begin{bmatrix} X_e \\ Y_e \\ Z_e \end{bmatrix} \quad (15)$$

Or, with the following definitions -

$$\begin{bmatrix} X_{B_3} \\ Y_{B_3} \\ Z_{B_3} \end{bmatrix} = \begin{bmatrix} l_x & l_y & l_z \\ m_x & m_y & m_z \\ n_x & n_y & n_z \end{bmatrix} \begin{bmatrix} X_e \\ Y_e \\ Z_e \end{bmatrix} \quad (16)$$

The various l , m , and n values are the direction cosines of the angles between the body axes and the inertial axes.

Therefore, for example, l_x , m_x , and n_x are the cosines of the angles between the body X, Y, and Z axes and the inertial X axis.

The direction cosine matrix is orthogonal, and thus the inverse is equal to the transposed matrix, and the determinant of the matrix has a value of ± 1 .

We can then modify equation (16) to solve for the earth components in terms of the body components.

$$\begin{bmatrix} X_e \\ Y_e \\ Z_e \end{bmatrix} = \begin{bmatrix} l_x & m_x & n_x \\ l_y & m_y & n_y \\ l_z & m_z & n_z \end{bmatrix} \begin{bmatrix} X_{B_3} \\ Y_{B_3} \\ Z_{B_3} \end{bmatrix} \quad (17)$$

X_{B_3} , Y_{B_3} and Z_{B_3} are the body coordinates after the three revolutions.

We can also use the direction cosine matrix to determine ground rates from body velocities. If S_x , S_y and S_z are the ground velocities along the inertial X, Y and Z axes, and u , v , and w are the body velocities along the body X, Y and Z axis, then:

$$\begin{bmatrix} \dot{s}_x \\ \dot{s}_y \\ \dot{s}_z \end{bmatrix} = \begin{bmatrix} l_x & m_x & n_x \\ l_y & m_y & n_y \\ l_z & m_z & n_z \end{bmatrix} \begin{bmatrix} u \\ v \\ w \end{bmatrix} \quad (18)$$

In order to compute the Euler angles for use with the display, it is necessary to derive the Euler angular rates and then integrate.

If we denote the matrix of direction cosines in equiv. (18) as \tilde{A} , we can write an expression for the rate of change of this matrix as follows:

$$\frac{d}{dt} \begin{bmatrix} \tilde{A} \end{bmatrix} = \omega X \begin{bmatrix} \tilde{A} \end{bmatrix} = 0 \quad (19)$$

This is so because we know the determinant of the matrix has the value ± 1 . Thus the only change possible in the matrix must be due to a rotation.

If we let the body unit vectors equal X, Y and Z, we thus can write:

$$\dot{\tilde{A}} + \omega X \tilde{A} = 0 \quad (20)$$

$$\text{or} \quad \dot{\tilde{A}} = -\omega X \tilde{A} \quad (21)$$

$$\text{and then, if } \omega_{X_B} = p, \omega_{Y_B} = q, \text{ and } \omega_{Z_B} = r, \quad (22)$$

$$\dot{\tilde{A}}_z = \hat{X} \dot{l}_z + \hat{Y} \dot{m}_z + \hat{Z} \dot{n}_z = -\hat{X} \begin{bmatrix} qn_z - rm_z \end{bmatrix} - \hat{Y} \begin{bmatrix} r l_z - pn_z \end{bmatrix} - \hat{Z} \begin{bmatrix} pm_z - q l_z \end{bmatrix} \quad (23)$$

$$\dot{l}_z \Delta = rm_z - qn_z \quad (23)$$

$$\dot{m}_z \Delta = pn_z - r l_z \quad (24)$$

$$\dot{n}_z \Delta = q l_z - pm_z \quad (\text{and ditto for the X and Y values}) \quad (25)$$

using the values for \dot{l}_z , \dot{m}_z and \dot{n}_z from equations (15) and (16) we write:

$$\dot{l}_z = r\dot{m}_z - q\dot{n}_z = \frac{d}{dt} (-\sin \theta \cos \phi) = r \sin \phi - q \cos \theta \cos \phi \quad (26)$$

$$\dot{m}_z = p\dot{n}_z - r\dot{l}_z = \frac{d}{dt} (\sin \phi) = p \cos \theta + r \sin \theta \cos \phi \quad (27)$$

$$\dot{n}_z = q\dot{l}_z - p\dot{m}_z = \frac{d}{dt} (\cos \theta \cos \phi) = -q \sin \theta \cos \phi - p \sin \phi \quad (28)$$

Performing the derivative operation

$$r \sin \phi - q \cos \theta \cos \phi = -\dot{\theta} \cos \theta \cos \phi + \dot{\phi} \sin \theta \sin \phi \quad (29)$$

$$p \cos \theta \cos \phi + r \sin \theta \cos \phi = \dot{\phi} \cos \phi \quad (30)$$

$$-q \sin \theta \cos \phi - p \sin \phi = -\dot{\theta} \sin \theta \cos \phi - \dot{\phi} \cos \theta \sin \phi \quad (31)$$

from equation 30, we see:

$$\dot{\phi} = p \cos \theta + r \sin \theta \quad (32)$$

Using equation (29), and solving for $\dot{\theta}$:

$$\dot{\theta} = \frac{q \cos \theta \cos \phi - r \sin \phi + \dot{\phi} \sin \theta \sin \phi}{\cos \theta \cos \phi} \quad (33)$$

$$\dot{\theta} = q - \frac{r \tan \phi}{\cos \theta} + \dot{\phi} \tan \theta \tan \phi \quad (34)$$

Substituting $\dot{\phi} = p \cos \theta + r \sin \theta$;

$$\dot{\theta} = q - r \tan \phi \sec \theta + p \tan \phi \sin \theta + r \sin \theta \tan \phi \tan \theta \quad (35)$$

$$\dot{\theta} = q + p \tan \phi \sin \theta + r \tan \phi \left[\frac{\sin^2 \theta - 1}{\cos \theta} \right] \quad (36)$$

$$\dot{\theta} = q + (p \sin \theta - r \cos \theta) \tan \phi \quad (37)$$

Now, we can write

$$\dot{m}_y = p \dot{n}_y - r \dot{l}_y \quad (38)$$

$$m_y = \cos \phi \cos \psi \quad (39)$$

$$\begin{aligned} \frac{d}{dt} (\cos \phi \cos \psi) = \\ p (\sin \theta \sin \psi - \cos \theta \cos \psi \sin \phi) \\ - r (\cos \theta \sin \psi + \sin \theta \sin \phi \cos \psi) \end{aligned} \quad (40)$$

$$\begin{aligned} - \dot{\phi} \sin \phi \cos \psi - \dot{\psi} \cos \phi \sin \psi = \\ p (\sin \theta \sin \psi - \cos \theta \cos \psi \sin \phi) \\ - r (\cos \theta \sin \psi + \sin \theta \sin \phi \cos \psi) \end{aligned} \quad (41)$$

and this is solved for $\dot{\psi}$ to give:

$$\dot{\psi} = \sec \phi (r \cos \theta - p \sin \theta) \quad (42)$$

The Euler angular rates are then given in equations (32, (37), and (42), repeated below

$$\dot{\phi} = p \cos \theta + r \sin \theta \quad (43)$$

$$\dot{\theta} = q + (p \sin \theta - r \cos \theta) \tan \phi \quad (44)$$

$$\dot{\psi} = \sec \phi (r \cos \theta - p \sin \theta) \quad (45)$$

and we can also write the direction cosines:

$$l_x = \cos \theta \cos \psi - \sin \theta \sin \phi \sin \psi \quad (46)$$

$$m_x = -\cos \phi \sin \psi \quad (47)$$

$$n_x = \sin \theta \cos \psi + \sin \psi \cos \theta \sin \phi \quad (48)$$

$$l_y = \cos \theta \sin \psi + \sin \theta \sin \phi \cos \psi \quad (49)$$

$$m_y = \cos \phi \cos \psi \quad (50)$$

$$n_y = \sin \theta \sin \psi - \cos \theta \cos \psi \sin \phi \quad (51)$$

$$l_z = -\sin \theta \cos \phi \quad (52)$$

$$m_z = \sin \phi \quad (53)$$

$$n_z = \cos \theta \cos \phi \quad (54)$$

Due to the limited rotation of the visual display in pitch and roll, it is not necessary to compute the direction cosines exactly.

The following approximations are used when driving the visual display:

$$\dot{\phi} = p + r \theta \quad (55)$$

$$\dot{\theta} = q + p \theta \phi - r \phi \quad (56)$$

$$\dot{\psi} = \frac{r - p \theta}{\cos \phi}, \text{ where all angles are in radians} \quad (57)$$

and

$$l_x = \cos \psi - \theta \phi \sin \psi \quad (58)$$

$$m_x = \cos \phi \sin \psi \quad (59)$$

$$n_x = \theta \cos \psi + \phi \sin \psi \quad (60)$$

$$l_y = \sin \psi + \theta \phi \cos \psi \quad (61)$$

$$m_y = \cos \psi \cos \phi \quad (62)$$

$$n_y = \theta \sin \psi - \phi \cos \psi \quad (63)$$

$$l_z = - \theta \cos \phi \quad (64)$$

$$m_z = \phi \quad (65)$$

$$n_z = \cos \phi \quad (66)$$

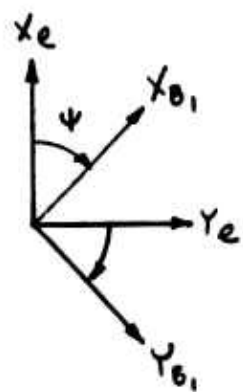


Figure 103 Yaw Rotation

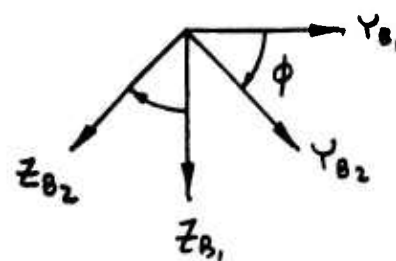


Figure 104 Roll Rotation

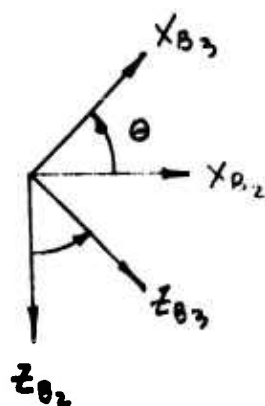


Figure 105 Pitch Rotation

10.0 STABILIZATION SYSTEM BRIDGE NETWORK DEVELOPMENT

10.1 Roll-Yaw Bridge Considerations

The louver and pitch fan thrust reverser hydraulic actuators have dual input valves which allow the summing of electrical and mechanical inputs at the same flapper. The electrical input is designed so that it has 25% of the authority of full mechanical input. The actuators employ mechanical position feedback to the valve spool, so that for a constant electrical input a fixed output displacement will result. The valves have dual 1500 ohm coils, and in the series connection, 4 ma is required for full electrical output. In the parallel coil connection, 8 ma is required for full output, and 8 ma will drive the electrical input to full output through a single coil. Due to the push-pull, push-push type mechanism of developing rolling and yawing moments from the exit louvers, it is possible to connect the valve coils from the four sets of louvers into a bridge circuit such that a single amplifier will drive all four coils in the proper phase for a yaw input, and another single amplifier will independently drive all four coils in the proper phase for a roll input. In addition, if the two coils in each valve are connected into opposite bridge legs, the effects of an open failure of a single coil will be minimized.

A requirement for the amplifiers to drive the bridge is that they have a high output impedance. If they had infinite output impedance, i.e. were current sources, there would be no effect on the system if a single coil opened. This says that if the output load was doubled in resistance, the voltage would double and the current would remain the same.

Amplifier Input Network Considerations

The amplifier input network picked to mechanize the desired transfer function;

$$\frac{\beta}{\beta_{\text{comm.}}} = K_{\beta} \frac{(1 + R \tau S)}{1 + \tau S}, \text{ is shown in Figure 106.}$$

This approach is feasible because rate gyros with high output voltage gradients have been specified. Our rate gyros will have an output gradient of .4 volts/deg/sec.

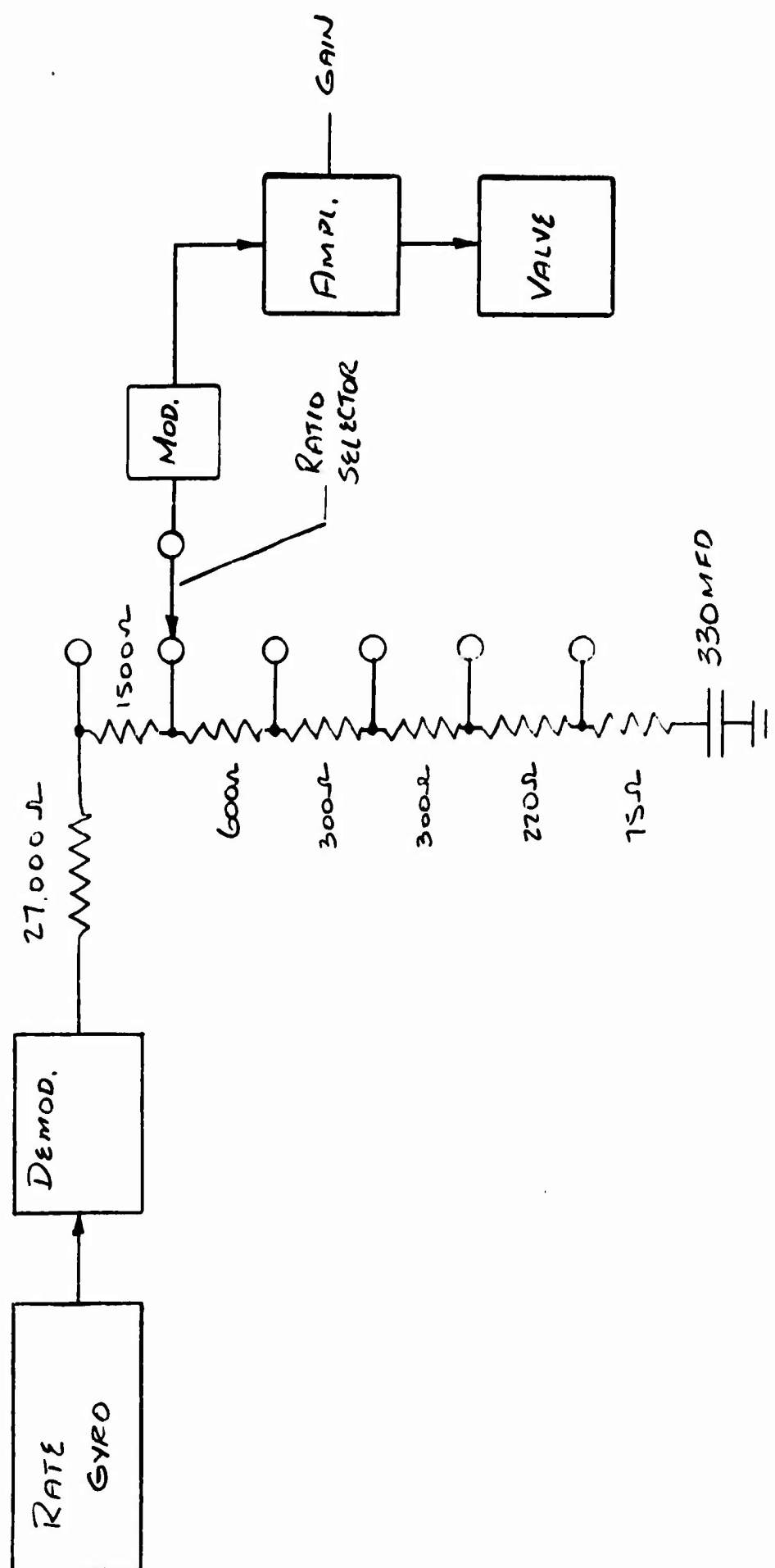


Figure 106 Block Diagram of SA Components and Input Network

K_β is varied by variation of the amplifier gain, and R can be any of six values, which are .1, .05, .03, .02, .01, and .0025.

τ has been chosen as 10 seconds, nominal. The values of τ , and of the six K values are affected by the leakage resistance of the 330 mfd. capacitor.

The transfer function for the circuit of Figure 107, including the effect of leakage is:

$$\frac{E_o}{E_{IN}} = \frac{R_2 + R_L}{R_1 + R_2 + R_L} \left[\frac{1 + \frac{R_2 R_L CS}{R_2 + R_L}}{1 + \frac{R_L (R_1 + R_2) CS}{R_1 + R_2 + R_L}} \right] \quad (1)$$

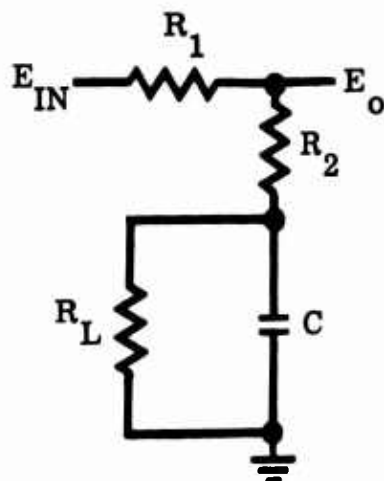


Figure 107 Servo Input Network with Leakage

If we pick position six of the ratio (K) selector switch, $R_2 = 3,000$ ohms, $R_1 = 27,000$ ohms, and $C = 330$ mfd:

thus, writing resistance values in thousands of ohms,

$$\frac{E_o}{E_{IN}} = \frac{3 + R_L}{30 + R_L} \left[\frac{1 + \frac{3R_L CS}{3 + R_L}}{1 + \frac{30R_L CS}{30 + R_L}} \right] \quad (2)$$

We find that the ratio of the time constants, K, is then equal to

$$\frac{3R_L}{3 + R_L} \cdot \frac{30 + R_L}{30 R_L} = \frac{30 + R_L}{10(3 + R_L)} \quad (3)$$

if we further let $R_L = 100,000$ ohms;

The ratio, K, then becomes

$$\frac{130}{10(130)} = \frac{130}{1030} = .126$$

Figure 108 is an amplitude vs frequency plot of one channel of the breadboard stab system package with the selector on position 6.

The best fit to this data indicated that $\tau = 10.6$, and $K = \frac{1.18}{10.6} = .111$.

A further cause of a ratio error is the effect of using a full-wave input demodulator which feeds directly into the compensation network without filtering of the A.C. components.

If we assume a peak demodulator, output of 1V, the RMS value of the output is .707V. The DC value of the output is .636V. The RMS value of the AC components is thus $\sqrt{.707^2 - .636^2} = .308V$. The AC components are operated upon by the network as if the capacitor were short-circuited, and are thus attenuated to a value of .308K volts. At very low frequency, the DC component goes through the network unattenuated. The RMS value of the output at low frequencies then is

$$\sqrt{.636^2 + .308^2 K^2}.$$

At $K = .1$, (our max. value) the RMS output is equal to

$\sqrt{.405 + .00095} = .636V$. At high frequencies, both the AC and DC values are attenuated by the factor K, (.1 in this case) and the RMS value of the output = $.0636^2 + .0305^2 = .0707V$. Thus the ratio is $\frac{.0707}{.636} = .111$. instead of .10. At all K values, this effect changes the ratio by the same percentage. Thus, at $K = .01$, the ratio would be .0111.

It is interesting to note that an R_L of 240K would also give $K = .0111$ at the setting of .01.

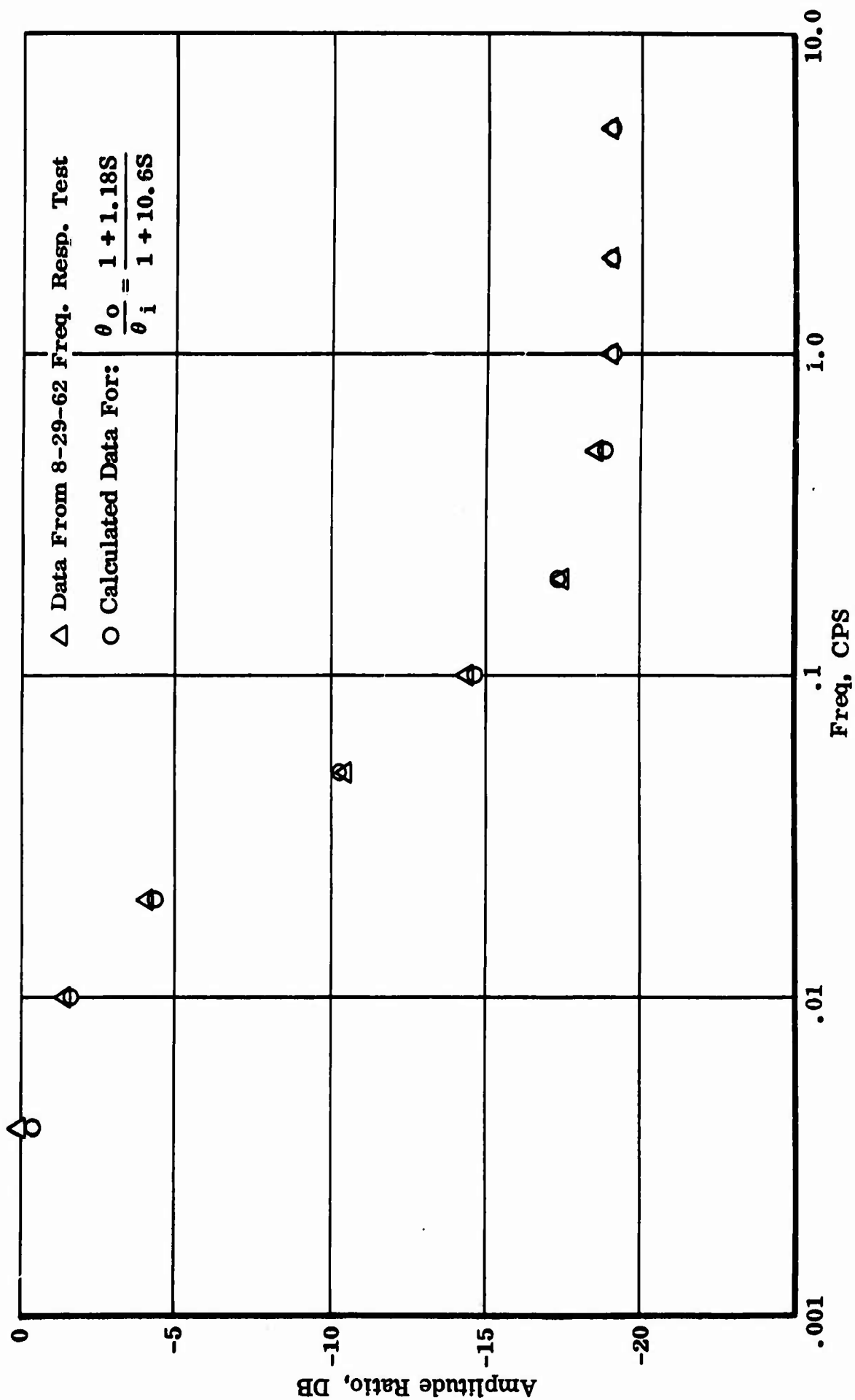


Figure 108 Package Yaw Channel Response, Position #6